AN INVESTIGATION OF UNDOPED AND IMPURITY-ADDED $SrTiO_3$

U. Balachandran
B.E. (Honours), Madras University, 1975
M.E., Indian Institute of Science, 1977

A dissertation submitted to the faculty
of the Oregon Graduate Center
in partial fulfillment of the
requirements for the degree
Doctor of Philosophy
in
Materials Science

December, 1980

The dissertation "An Investigation of Undoped and Impurity-Added $SrTiO_3$" by U. Balachandran has been examined and approved by the following Examination Committee:

Nicholas G. Eror, Thesis Advisor
Associate Professor

John S. Blakemore
Professor

Thomas M. Loehr
Professor

Jack H. Devletian
Associate Professor

ACKNOWLEDGEMENTS

I wish to express my deep gratitude and sincere thanks to Dr. N. G. Eror for his excellent, extensive, and valuable guidance throughout this work. This work would not have been brought to fruition but for his encouragement and assistance, which has always been a constant source of inspiration to me. My thanks are also to Drs. J. S. Blakemore and T. M. Loehr for their expert advice and the numerous discussions I had with them. It is not possible to list all that the above three persons have done on my behalf, but I am extremely grateful for all their efforts. I am thankful to Dr. J. Devletian for reading this dissertation.

I have benefited from discussions with many other friends and colleagues--most notably, Dr. Bahne Cornilsen, Mike Sprinker, Bruce Odekirk, Lawrence J. Willis, P. A. Molian, Tae-Il Oh, and R. Padmanabhan. I thank all of them.

I thank Ms. Nancy A. Fick who typed this long dissertation with intelligence, speed, accuracy, and style which made the production of the dissertation seem so easy. I thank Ms. Barbara Ryall for the excellent drawings and Mr. Allan Ryall for the glass-blowing job he has done for me.

I wish to recognize the students, staff, and faculty of the Oregon Graduate Center for making my stay here truly a memorable one.

Lastly, I would like to thank God. You know better than I do your part in this thesis. You have helped me in ways which I do not recognize or understand. I pray that such understanding will come with time.

This work was supported in part by the Gas Research Institute, Chicago.

DEDICATION

This work is dedicated to all my teachers.

TABLE OF CONTENTS

LIST OF TABLES

LIST OF FIGURES

PREFACE

It is well known that a perfect crystal, i.e., one in which all identical lattice points are occupied by identical ions, no other sites being occupied, cannot exist at temperatures above 0 K. Real crystals always show a number of deviations from ideal crystal structure, a number that increases with rising temperatures. Several kinds of deviations are known. First, the atoms or ions are not stationary at fixed lattice points, but execute vibrations around an equilibrium site. We also find that lattice sites are not occupied, or may be occupied by different atoms. It likewise happens that some locations which should be unoccupied in fact contain atoms. Both lattice vibrations and point defects influence the physical properties of the solid state to a very high degree. We may cite their effects on thermal conductivity, luminescence, diffusion and electrical transport properties.

In the past, our knowledge of defect chemistry was developed and increased by the work of Frenkel,[1] Schottky,[2] Wagner,[3] Kroger and Vink,[4] and a large number of contributions have been published. The most recent work deals with the description of unitary and binary phases while, in the latter, equiatomic compounds MX are usually considered. Schmalzreid and Wagner[5] considered the defect chemistry of ternary systems. However, in their work only little attention was paid to the relations between electrical transport properties and the ambient atmosphere.

Strontium titanate has a cubic perovskite structure, and has technological importance in the photolysis of water, oxygen sensors, and in magneto hydrothermal (MHD) operations. Also, in recent years, strontium titanate has attracted much attention, both experimental and theoretical, due to its many and varied properties, including superconductivity,[6-8] a second-order structural phase transition[9] and a stress-induced phase transition.[10]

The purpose of the present investigation is to study the defect structure of $SrTiO_3$ with different cation-cation ratios and with foreign atoms. The techniques employed are: thermogravimetry, X-ray powder diffraction, laser Raman spectroscopy, scanning electron microscopy (SEM), and high temperature electrical conductivity measurements.

ABSTRACT

The compound $La_xSr_{1-x}TiO_3$ with X up to 40 at.% was observed to be homogeneous by microscopic examination. The observed X-ray powder diffraction pattern corresponds to the cubic perovskite structure. The plot of lattice constant a_o vs X indicated a Vegard's law dependence within experimental error. Gravimetric measurements on pure and lanthanum doped $SrTiO_3$ have shown that the reversible change of oxygen content, between specified states of oxidation and reduction, is proportional to the dopant concentration. These measurements indicate that the donor-dopants are ionically compensated by additional oxygen uptake in the oxidized state. The gravimetrical measurements are explained by a model involving a shear structure. The electrical conductivity of polycrystalline $SrTiO_3$ with different Sr to Ti ratios and with donor- and acceptor-dopants were determined for the oxygen partial pressure range of 10^0 to 10^{-22} atm., and temperature range of 800-1050°C. For $SrTiO_3$ with (Sr/Ti) = 1, the data were found to be proportional to the -1/6 power of the oxygen partial pressure for the oxygen pressure range 10^{-15} - 10^{-22} atm., proportional to $P_{O_2}^{-1/4}$ for the oxygen pressure range 10^{-8} - 10^{-15} atm., and proportional to $P_{O_2}^{+1/4}$ for the oxygen pressure range $>10^{-3}$ atm. These data are consistent with the presence of a very small amount of acceptor impurity in $SrTiO_3$. The deviation from ideal (Sr/Ti) ratio is found to be accommodated by neutral vacancy pairs. For the donor doped $SrTiO_3$, two kinds of charge compensation were observed according to the oxygen partial pressure, via an electronic or a lattice

defect in a $La_xSr_{1-x}TiO_3$ or a $La_xSr_{1-x}TiO_{3+x/2}$ solid solution, respectively. For the acceptor (Fe, Al)-doped samples, the p to n transition is shifted to lower P_{O_2} as compared to the undoped $SrTiO_3$. The conductivities in the acceptor-doped samples are lower in the n-type region, and are higher in p-type region, as compared to the values in the undoped $SrTiO_3$.

The Raman spectra of $SrTiO_3$ were recorded as a function of temperature using an argon-ion laser as exciter. At room-temperature the Raman spectrum was found to be second-order in agreement with the selection rules for the cubic perovskite structure. The bands in the second-order spectrum originate largely from pairs of phonons with wave vectors near the Brillouin zone boundary. On cooling the $SrTiO_3$ below 120K, five additional bands appear in the spectra, which are due to first-order modes of the tetragonal structure. The energies of phonon branches are deduced, and compared with the results of neutron inelastic scattering experiments. It is shown that Raman scattering from polycrystalline solid contains all of the essential features of the Raman single crystal spectrum.

Factor group analysis were made for the Ruddlesden-Popper phases ($nSrTiO_3 \cdot SrO$) up to n = 25. These analysis did not yield a simple band multiplicity, even though the space group D_{4h}^{17}, [I4/mmm] was preserved by stacking the cubic perovskite ($SrTiO_3$) blocks. Not all the Raman active modes predicted by factor group analysis were actually observed for these phases and this may be due to poor coupling of the vibrations between individual segments of the enlarged unit cell.

1. INTRODUCTION

One of the prime interests of scientists working with defect crystals is concern with the control of the concentrations of various defects in crystals, and hence the control of the crystal properties related to these defects.

Generally, six types of primary inperfections are distinguished; namely phonons, dislocations, electrons and holes, excitons, vacant lattice sites (or interstitial atoms or ions), and foreign atoms or ions in either interstitial or substitutional positions.[11] In addition, atoms of the base crystal may be present at lattice sites normally occupied by other atoms (the anti-site disorder).

Five types of primary imperfections will be dealt with here; namely; vacant lattice sites, interstitials, misplaced lattice atoms, foreign atoms, and electrons and holes. Phonons will not be mentioned explicitly, although their presence will be assumed in order to account both for thermal disorder and for the establishment of thermal equilibrium. The first two types of imperfections are shown schematically in Figure 1. The foreign atoms may be present substitutionally or interstitially depending on their atomic size in relation to the size of the various sites. The concentrations of the various imperfections are not independent of each other. It is the purpose of this section to show the type of relations existing between the concentrations of the imperfections.

Figure 1. TYPES OF PRIMARY POINT DEFECTS a) VACANCIES; b) INTERSTITIALS; c) EQUAL NUMBERS OF INTERSTITIALS AND VACANCIES, FRENKEL DISORDER.

1.1 Stability of Crystal Disorder

For purpose of illustration, let us consider an elemental crystal containing vacancies. Let us start with N atoms arranged on N lattice sites in the crystal. The free energy of the perfect crystal will be G*. Let us now remove n atoms from the crystal and place them on the surface. We have, therefore, formed n vacant sites. Each of these vacancies will be associated with an enthalpy of formation, ΔH_v, and vibrational entropy resulting from the disturbance of the nearest neighbors, ΔS_v. There will be a configurational or mixing entropy change associated with the formation of n vacancies given by,

$$\Delta S_c = K \ln \frac{w'}{w}$$

For the perfect crystal w = 1. We may readily find w' since we now have n vacancies and N atoms distributed among (N+n) sites. It can be shown that

$$\Delta S_c = K \ln w' = K \ln \frac{(N + n)!}{N!\ n!}$$

In these expressions w and w' represent the number of ways of distributing the n vacancies in the crystal containing (N+n) sites and K represents the Boltzmann constant. In a perfect crystal there are no vacancies and hence the value of w is taken as unity. The value of w' is obtained from a simple statistical interpretation of theory of randomness. Using Stirling's approximation we find

$$\Delta S_c = -K \left[N \ln \frac{N}{(N+n)} + n \ln \frac{n}{(N+n)} \right] \quad (1)$$

and therefore

$$\Delta G = G - G^* = n \Delta H_v - T \left(\Delta S_c + n \cdot \Delta S_v \right)$$

or

$$G - G^* = n \Delta H_v + KT \left[N \ln \frac{N}{(N+n)} + n \ln \frac{n}{(N+n)} \right] - nT \Delta S_v \quad (2)$$

In Figure 2 is shown a plot of $n(\Delta H_v - T\Delta S_v)$, ΔS_c and G as a function of n. The entropy contribution, ΔS_c, is always negative, and in fact has a slope equal to $-\infty$ at $n = 0$. From Figure 2, therefore, it is observed that introduction of vacancies lowers the free energy of the crystal until an equilibrium concentration is reached, after which G increases again. This equilibrium concentration may be readily calculated in principle since at this concentration, $\partial G/\partial n = 0$. Thus, using equation 2, we find

$$\frac{\partial G}{\partial n} = \Delta H_v - T \Delta S_v + KT \ln \frac{n}{(N+n)} = 0$$

Upon rearrangement,

$$\frac{n}{N+n} = \exp \left[\frac{\Delta S_v}{K} \right] \exp \left[\frac{-\Delta H_v}{KT} \right]$$

The fraction of total sites vacant may be expressed as X_v and

$$X_v = \exp \left[\frac{\Delta S_v}{K} \right] \exp \left[\frac{-\Delta H_v}{KT} \right] = \exp \left[\frac{-\Delta G_v}{KT} \right] \quad (3)$$

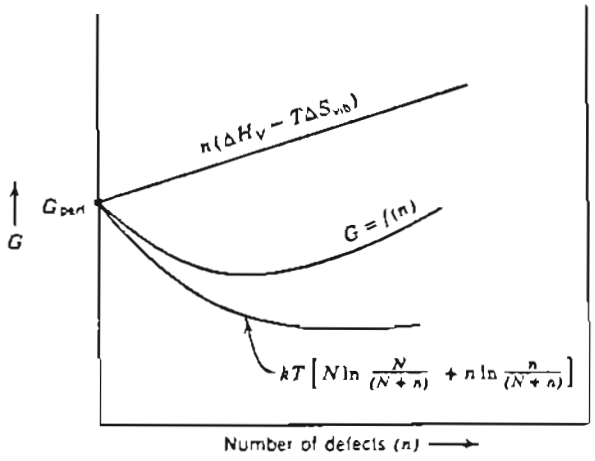

Figure 2. FREE ENERGY OF A CRYSTAL AS A FUNCTION OF DEFECT CONCENTRATION.

From equation (3) we find that vacancies are indeed stable in the crystal at any temperature greater than absolute zero, and that the mole fraction varies exponentially with temperature.

The imperfect crystals may be divided into two classes, namely, stoichiometric and nonstoichiometric.

1.2 Atomic Disorder

In a perfect stoichiometric oxide MO, five primary types of atomic disorder can be distinguished.[1-3]

a) equal number of vacant sites on M sublattice (V_m) and O sublattice (V_o). [Schottky-Wagner defect]

$$MO \rightleftharpoons MO + \delta V_m + \delta V_o \qquad \delta << 1 \tag{4}$$

b) equal numbers of vacancies on the M sublattice (V_m) and M interstitial ions (M_i) [Frenkel defect]

$$MO \rightleftharpoons M_{(1-\delta)}O + \delta V_m + \delta M_i \tag{5}$$

c) equal numbers of vacancies in the O sublattice (V_o) and O interstitial ions (O_i) [Frenkel defect]

$$MO \rightleftharpoons MO_{(1-\delta)} + \delta V_o + \delta O_i \tag{6}$$

d) equal concentrations of M and O interstitials [Anti Schottky-Wagner defect]

$$MO \rightleftharpoons M_{(1-\delta)}\ O_{(1-\delta)} + \delta M_i + \delta O_i \tag{7}$$

e) M ions occupy O sites and O ions occupy M sites

[Antistructural defect]

$$MO \rightleftharpoons M_{(1-\delta)}\ O_{(1-\delta)} + \delta M_o + \delta O_m \tag{8}$$

Combinations of these five types of defects are also possible. We have assumed that $\delta << 1$ so that in writing equilibrium constants for the above reactions we shall consider concentrations of the atoms on normal sites to remain virtually constant. We shall also use the further approximation that the defects are sufficiently dilute to replace their activities by their concentrations. We may now write

$$[V_m]\ [V_o] = K_4 = K_{S_1} \tag{9}$$

$$[V_m]\ [M_i] = K_5 = K_{F_1} \tag{10}$$

$$[V_o]\ [O_i] = K_6 = K_{F_2} \tag{11}$$

$$[M_i]\ [O_i] = K_7 = K_{S_2} \tag{12}$$

where K_{S_1}, K_{F_1}, K_{F_2}, and K_{S_2} are equilibrium constants for reactions (4) through (7) respectively. The antistructural disorder is not considered here. Furthermore, since the equilibrium constant may be written

$$K = \exp\left[\frac{-\Delta G_F^\circ}{RT}\right]$$

$$= \exp\left\{\left[\frac{\Delta H_F^\circ}{-RT}\right] + \left[\frac{\Delta S_F^\circ}{R}\right]\right\} \tag{13}$$

where ΔG_F°, ΔH_F°, and ΔS_F° are respectively the standard Gibbs free energy, enthalpy and entropy of formation for the reaction as written, each of the defect reactions will have thermodynamic formation terms associated with it.

It should also be kept in mind that in addition to the above unassociated defects, associations between defects are possible. Therefore, further defect reactions of the form,

$$[V_m, V_o] = [V_m]\,[V_o] \tag{14}$$

where $[V_m, V_o]$ refers to a metal vacancy-oxygen vacancy complex, may be written. Similarly

$$\frac{[V_m]\,[V_o]}{[V_m, V_o]} = K_{S_3} \tag{15}$$

with its thermodynamic formation terms as in equation (13).

The concentrations of defects expressed in the proceeding equilibrium relations are not independent of one another. We may write

$$\frac{[M_i]}{[V_o]} = \frac{K_{F_1}}{K_{S_1}} = K_{16} \tag{16}$$

as an example of the relationships that exist between the various defect reactions.

Thus far we have only considered those atomic imperfections that preserve stoichiometry. Stoichiometry is a special limiting case of the

phase equilibria, and departures therefrom are likely to occur on either the metal excess or oxygen excess side of the stoichiometry if the limiting case of stoichiometry exists. A departure from stoichiometry on the metal excess side may be expressed as

$$M_g + MO \rightleftharpoons M_i + MO \tag{17}$$

where M_g refers to metal in the gas phase. Equation (17) may be rewritten as

$$M_g \rightleftharpoons M_i \tag{18}$$

Therefore, assuming that M is an ideal gas

$$\frac{[M_i]}{P_m} = K_{18} \tag{19}$$

where P_m refers to the partial pressure of the metal. Metal excess could also have been accommodated by

$$\delta M_g + (1-\delta)\ MO \rightleftharpoons MO_{1-\delta} + \delta V_o \tag{20}$$

or

$$M_g \rightleftharpoons M_m + V_o \tag{21}$$

where M_m refers to a metal atom on a normal sublattice site, such that

$$\frac{[V_o]}{P_m} = K_{21} \tag{22}$$

Similarly for an oxygen excess departure from stoichiometry

$$1/2\ O_2 \rightleftharpoons O_o + V_m \tag{23}$$

where O_2 refers to oxygen gas and O_o an oxygen atom in a normal oxygen sublattice site, or

$$1/2\ O_2 \rightleftharpoons O_i \tag{24}$$

where O_i stands for an interstitial oxygen atom.

The equilibrium constants for reactions (23) and (24) are:

$$\frac{[V_m]}{P_{O_2}^{1/2}} = K_{23} \tag{25}$$

and

$$\frac{[O_i]}{P_{O_2}^{1/2}} = K_{24} \tag{26}$$

We may consider reactions (21) and (23) to express the deviations from stoichiometry. We may express the deviation from stoichiometry in terms of the oxygen pressure only since by combining the relationships between defects,

$$[V_m]\ [V_o] = K_{23}\ P_m\ K_{21}\ P_{O_2}^{-1/2} = K_{S_1} \tag{27}$$

or

$$P_m = K_{28} P_{O_2}^{-1/2} \tag{28}$$

Equation (22) then becomes

$$[V_o]\, P_{O_2}^{1/2} = K_{29} \tag{29}$$

1.3 Electronic Disorder

All electrons in an insulating crystal are in the state of "lowest" energy at low temperatures. At higher temperatures when the entropy plays a role, part of the electrons occupy higher states under equilibrium conditions. This may be considered as a type of defect parallel to atomic disorder and may be called electronic disorder.

Two types of excited electronic states can be distinguished:

a) states not involving atomic imperfections

b) states involving atomic imperfections.

1.3.1 Electronic disorder not involving atomic imperfections.

Electronic disorder not involving atomic imperfections is referred to as intrinsic electronic disorder. As the temperature is increased, thermal excitations can free an electron from the interatomic or valence bonds. This creates simultaneously an electron of higher energy and a hole available for conduction if an electric field is applied. Free electrons and holes generated by thermal motion are free to recombine continuously.

The formation and the annihilation of the quasi-free charge carriers can be described by the following equilibrium equation

$$np \rightleftharpoons n + p \tag{30}$$

where n is a thermally excited electron available for conduction and p, an electron hole which also contributes to the conductivity. Applying the mass-action to the above reaction, one finds the following relation between the concentrations of the electrons (n) and the holes (p),

$$[n]\,[p] \simeq K_i \tag{31}$$

1.3.2 Electronic Disorder Involving Atomic Imperfections. Imperfections may make two kinds of additional excitation processes possible, namely

a) excitation in which electrons associated with the imperfections are brought into states in which they can move freely through the crystal; and

b) excitation in which normal valence electrons of the crystal are transferred to the imperfections.

Excitation (a) corresponds to transitions between the local level and the conduction band. An oxygen vacancy can be ionized once according to the reaction

$$V_o \rightleftharpoons V_o^{\cdot} + n \tag{32}$$

and still further in accordance with the relation

$$V_O^{\cdot} \rightleftharpoons V_O^{\cdot\cdot} + n \tag{33}$$

where $V_O^{\cdot}$ refers to a singly ionized oxygen vacancy, $V_O^{\cdot\cdot}$ refers to a doubly ionized oxygen vacancy and the dots indicate positive charges on the atomic defects. The equilibrium constants for these ionizations are

$$\frac{[V_O^{\cdot}]\ [n]}{[V_O]} = K_{32} \tag{34}$$

and

$$\frac{[V_O^{\cdot\cdot}]\ [n]}{[V_O^{\cdot}]} = K_{33} \tag{35}$$

$$\frac{[V_O^{\cdot\cdot}]\ [n]^2}{[V_O]} = K_{32}\ K_{33} = K_{36} \tag{36}$$

Excitation (b) corresponds to transitions between the valence band and the local levels; free holes are consequently formed in the valence band. Vacancies on the metal sublattice offer an example for this type of excitation. These vacancies may accept valence electrons. For the ionization of a metal vacancy we have

$$V_m \rightleftharpoons V_m' + P \tag{37}$$

and

$$V_m' \rightleftharpoons V_m'' + P \tag{38}$$

where V_m' and V_m'' refer respectively to a singly and doubly ionized metal vacancy and the prime stands for a negative charge on the defect. The

equilibrium constant for these ionizations are

$$\frac{[V_m'] \ [P]}{[V_m]} \cong K_{37} \tag{39}$$

and

$$\frac{[V_m''] \ [P]}{[V_m']} \cong K_{38} \tag{40}$$

or

$$\frac{[V_m''] \ [P]^2}{[V_m]} \cong K_{37} \ K_{38} = K_{41} \tag{41}$$

1.4 Relationship between the various states of atomic and electronic disorder

When considering the relationships between the various imperfections, further simplifications may be derived among the various states of disorder. By combining equations (34), (9), (31), and (39) we may write

$$[V_o^{\cdot}] \ [V_m'] = K_{S_1}' \tag{42}$$

The relations between equations (36), (9), (31), and (41) result in

$$[V_o^{\cdot\cdot}] \ [V_m''] = K_{S_1}'' \tag{43}$$

Now, we shall consider the changes in concentration of the various states of atomic and electronic disorder as a function of oxygen partial pressure in a crystal MO when the native imperfections are Schottky-Wagner type with doubly ionized anion and cation vacancies. There are eight unknown concentrations of the quantities n, P, V_m, V_o, V_m', V_m'', V_o° and $V_o^{\cdot\cdot}$. Therefore, eight equations must be employed to solve for the concentrations of these defects. In addition to equations (42) and (43), the following equations need to be considered:

$$[V_o]\,[V_m] \cong K_{S_1} \tag{9}$$

$$[V_m] \cong K_{23}\, P_{O_2}^{1/2} \tag{25}$$

$$\frac{[V_m']\,[P]}{[V_m]} \cong K_{37} \tag{39}$$

$$\frac{[V_m'']\,[P]^2}{[V_m]} \cong K_{41} \tag{41}$$

$$[n]\,[P] \cong K_i \tag{31}$$

$$[P] + [V_o^{\circ}] + 2\,[V_o^{\cdot\cdot}] = [n] + [V_m'] + 2\,[V_m''] \tag{44}$$

The last relation [equation (44)] is just the condition requiring electrical neutrality in the oxide crystal. When the concentrations of particular defects are dominant, the electrical neutrality condition, equation (44), may be separated into nine limiting cases.

The nine limiting cases of the electrical neutrality condition allow simplification of the seven defect equations involving equilibrium constants so that with eight equations and eight unknowns the concentration of the defects can be calculated as a function of P_{O_2}. The P_{O_2} dependences for the concentrations of the eight defects for each of the nine limiting cases of the neutrality condition are given in Table I. Figures 6 through 9 show the variation of the defect concentration with P_{O_2}, that results from the previous considerations. Arbitrary values for the equilibrium constants are assumed while drawing these plots.

The width of the respective regions in the plots depend upon the relative values of the seven equilibrium constants. The symmetry of the figures depend on the assumption that $K_{32} = K_{33} = K_{38}$ for illustrative purposes.

1.5 Effect of foreign atoms

If an impurity atom is introduced into the MO lattice, the valence state of the impurity must be considered, since the introduction of other than divalent impurities will necessitate the modification of the defect structure to maintain the electrical neutrality of the oxide crystal. Foreign atoms which are incorporated in the crystals are found to influence properties in various ways. Thus, the incorporation of cadmium or calcium in AgCl and AgBr enhances the ionic conductivity.[13,14] Incorporation of lithium in NiO under oxidizing conditions increases the concentration of free holes, and therewith, the p-type conductivity.[15,16]

Table I.

P_{O_2} DEPENDENCE OF DEFECT CONCENTRATIONS FOR EACH OF THE NINE LIMITING CASES OF THE ELECTRICAL NEUTRALITY CONDITION

Defect	Region I $[p]=[V_m^{'}]$	Region II $[p]=2[V_m^{''}]$	Region III $[V_m^{'}]=2[V_O^{\cdot\cdot}]$	Region IV $[p]=[n]$	Region V $[V_m^{'}]=[V_O^{\cdot}]$	Region VI $[V_m^{''}]=[V_O^{\cdot\cdot}]$	Region VII $2[V_m^{''}]=[V_O^{\cdot}]$	Region VIII $[n]=2[V_O^{\cdot\cdot}]$	Region IX $[n]=[V_O^{\cdot}]$
$[n]$	-1/4	-1/6	-1/3	0	-1/2	-1/4	-1/3	-1/6	-1/4
$[p]$	1/4	1/6	1/3	0	1/2	1/4	1/3	1/6	1/4
$[V_m^{'}]$	1/4	1/3	1/6	1/2	0	1/4	1/6	1/3	1/4
$[V_O^{\cdot}]$	-1/4	-1/3	-1/6	-1/2	0	-1/4	-1/6	-1/3	-1/4
$[V_m^{''}]$	0	1/6	-1/6	1/2	-1/2	0	-1/6	1/6	0
$[V_O^{\cdot\cdot}]$	0	-1/6	1/6	-1/2	1/2	0	1/6	-1/6	0
$[V_m]$	1/2	1/2	1/2	1/2	1/2	1/2	1/2	1/2	1/2
$[V_O]$	-1/2	-1/2	-1/2	-1/2	-1/2	-1/2	-1/2	-1/2	-1/2

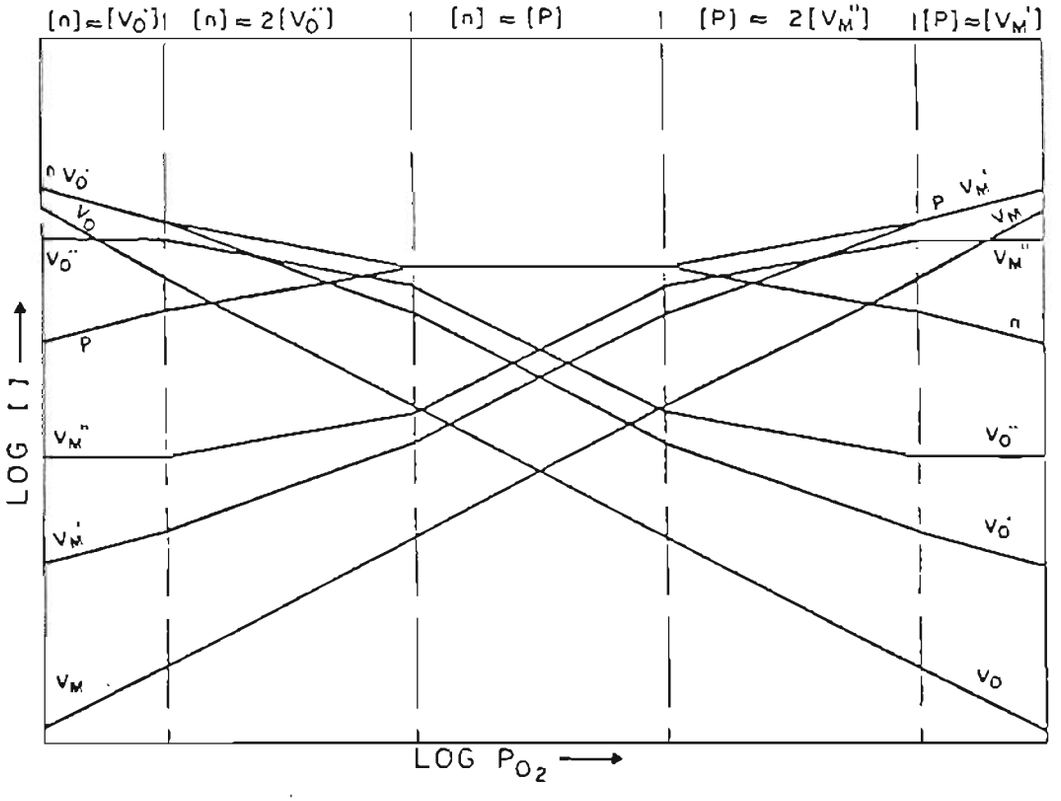

Figure 3. CONCENTRATIONS OF IMPERFECTIONS AS A FUNCTION OF P_{O_2}.

$$K_{38}^2 > K''_{si}, \frac{K_i}{4}, \frac{K'_{si}}{4}\ ;\ K_i > 4K''_{si}\ ;\ K_i > (2\,K'_{si}\,K_{38})^{2/3}$$

$$\text{AND } K_i > \left(\frac{K'_{si}K_{38}}{2K''_{si}}\right)^2$$

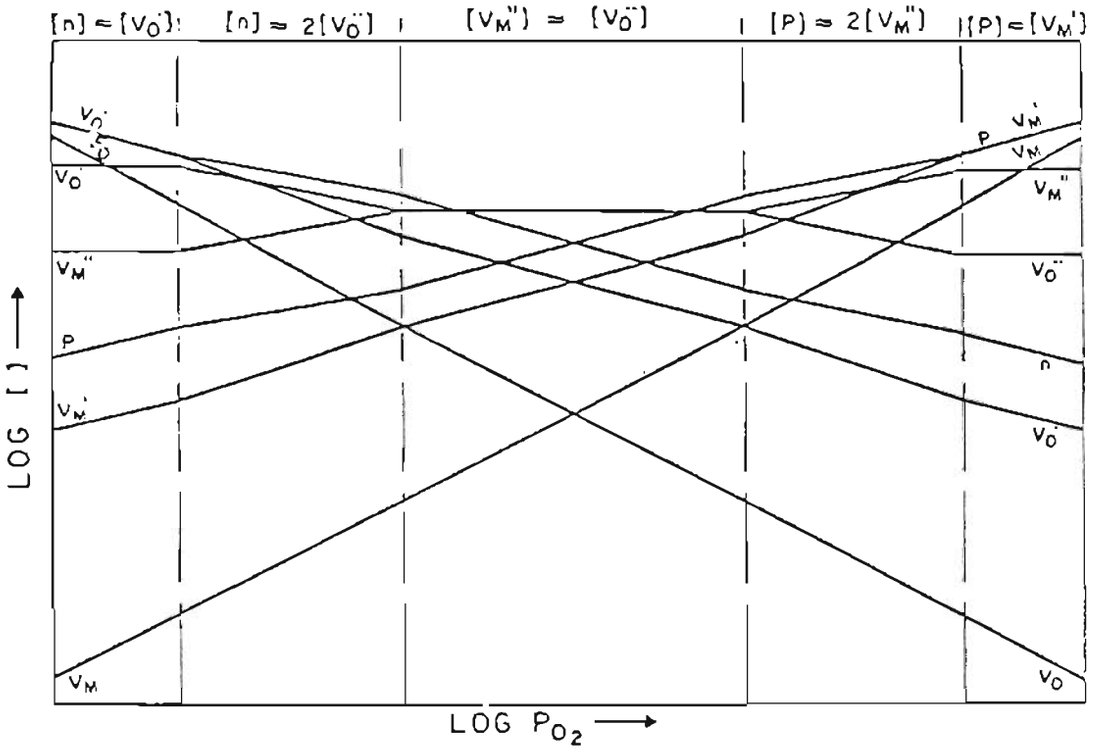

Figure 4. CONCENTRATIONS OF IMPERFECTIONS AS A FUNCTION OF P_{O_2}.

$$K_{38}^2 > K_{si}'' \text{ , } \frac{K_i}{4} \text{ , } \frac{K_{si}'}{4} \text{ ; } K_{si}'' > \frac{K_i}{4} \text{ ; } K_{si}'' > \left(\frac{K_{si}' K_{38}}{4}\right)^{2/3} \text{ AND}$$

$$K_{si}'' > \left(\frac{K_{si}' K_{38}}{K_i}\right)^2 .$$

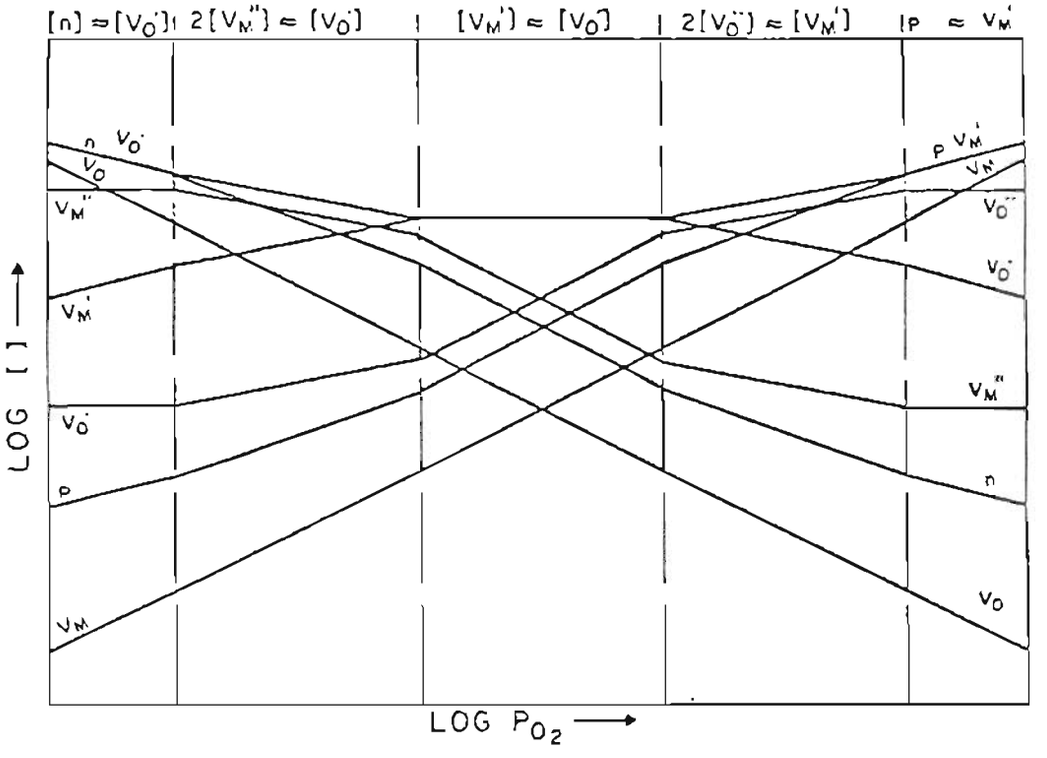

Figure 5. CONCENTRATIONS OF IMPERFECTIONS AS A FUNCTION OF P_{O_2}.

$$K''_{si} > K^2_{38}, \quad \frac{K_{38}K_i}{2}^{1/2}, \quad \frac{K_{38}K_{si}}{2}^{1/2}, \text{ AND } K'_{si} > 4K''_{si},$$

$$\left[\frac{2K_iK''_{si}}{K_{38}}\right]^{2/3}, \left(\frac{K_i}{2K_{38}}\right)^2.$$

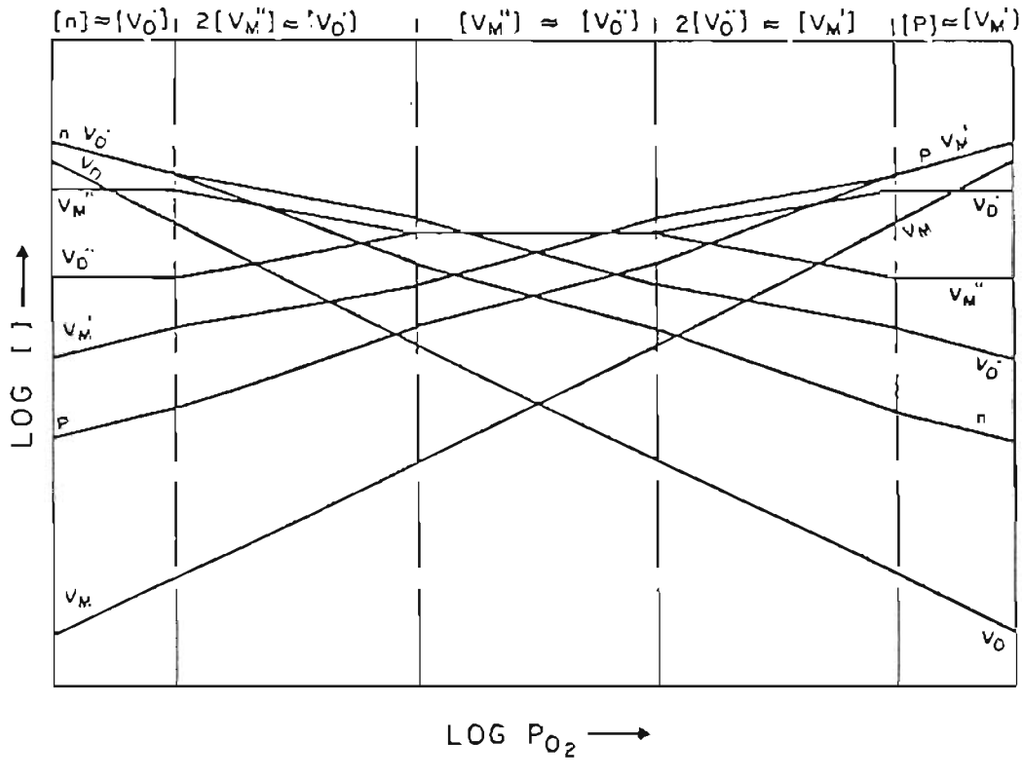

Figure 6. CONCENTRATIONS OF IMPERFECTIONS AS A FUNCTION OF P_{O_2}.

$$4K_{si}'' > K_{38}^2, \frac{K_{38}K_{si}^{1/2}}{2}, \frac{K_{35}K_{si}'^{1/2}}{2}, \frac{K_{si}'}{4}, \frac{K_i^2}{2^4K_{38}^2}$$

$$\text{AND } K_{si}' > \frac{K_iK_{si}''^{1/2}}{K_{38}} .$$

Gallium incorporated in CdS under sulfurizing conditions changes the color of pure CdS from yellow to a bright red. In contrast, the incorporation of gallium under reducing conditions leaves the color unchanged. However, it causes the electronic conductivity to increase substantially.[17] These few examples may suffice to show that the incorporation of foreign atoms may have a variety of consequences which depend on the base crystal, the valence state of the foreign atom and the site at which the impurity atom occupies in the lattice.

The following discussion will be concerned only with the incorporation of the impurity atom on the metal sublattice. This limitation approximates the actual effect of the impurity atoms, since the concentration of electropositive impurities are dominant. If a less electropositive element is an impurity in the MO lattice, then one must consider the ionization,

$$\frac{[I_m'][p]}{[I_m]} \cong K_{45} \tag{45}$$

where I_m' refers to an ionized acceptor impurity ion on a normal metal sublattice site and I_m is an impurity ion on a regular metal site.

The ionization of the impurity requires the inclusion of the new charged defect that is created in the electroneutrality condition. The new electroneutrality condition for the case of a less electropositive element as an impurity is

$$[P] + [V_O^{\cdot}] + 2[V_O^{\cdot\cdot}] = [n] + [V_m'] + 2[V_m''] + [I_m'] \tag{46}$$

Since the total concentration of impurity remains constant, we may write

$$[I_m'] + [I_m] = [I_m]_{total} = \text{constant} \tag{47}$$

and for the case of complete ionization,

$$[I_m'] = [I_m]_{total} = \text{constant} \tag{48}$$

The effect of the addition of the acceptor impurity which is completely ionized on the previous example of nonstoichiometric MO exhibiting Schottky-Wagner disorder given in Figure 3 is shown in Figure 7.

If a donor element is an impurity in the MO crystal, then the ionization

$$\frac{[I_m^{\cdot}]\ [n]}{[I_m]} \cong K_{49} \tag{49}$$

where $I_m^{\cdot}$ and I_m refer respectively to an ionized impurity ion and an impurity ion on normal metal sublattice sites, must be considered. The new charge neutrality condition for this case is

$$[P] + [V_O^{\cdot}] + 2\ [V_O^{\cdot\cdot}] + [I_m^{\cdot}] = [n] + [V_m'] + 2\ [V_m''] \tag{50}$$

Also for the case of complete ionization we may write

$$[I_m^{\cdot}] = [I_m] = \text{constant} \tag{51}$$

The defect concentration diagram is given in Figure 8 for the case of MO containing a donor impurity. It should be noted that the stoichiometry

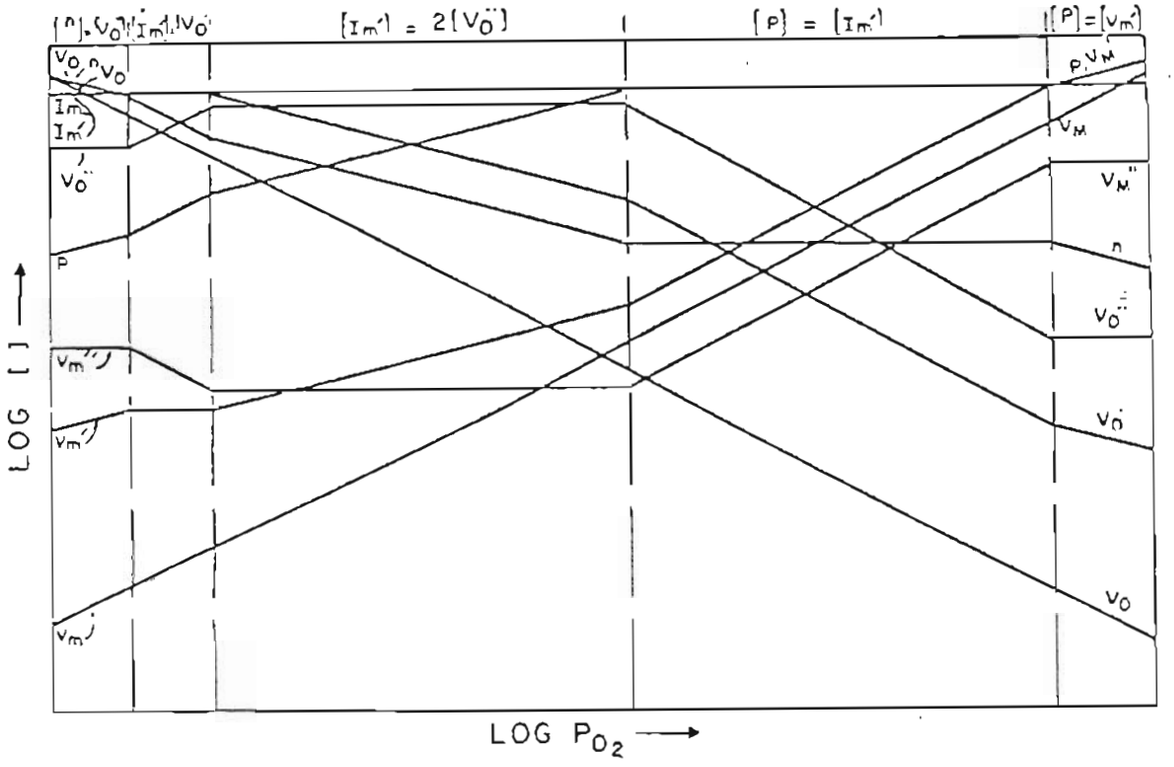

Figure 7 . CONCENTRATIONS OF THE IMPERFECTIONS AS A FUNCTION OF P_{O_2}. SAME AS IN FIGURE 6 BUT THE CRYSTAL NOW CONTAINS SINGLY IONIZED ACCEPTOR IMPURITY $[I'_m]$.

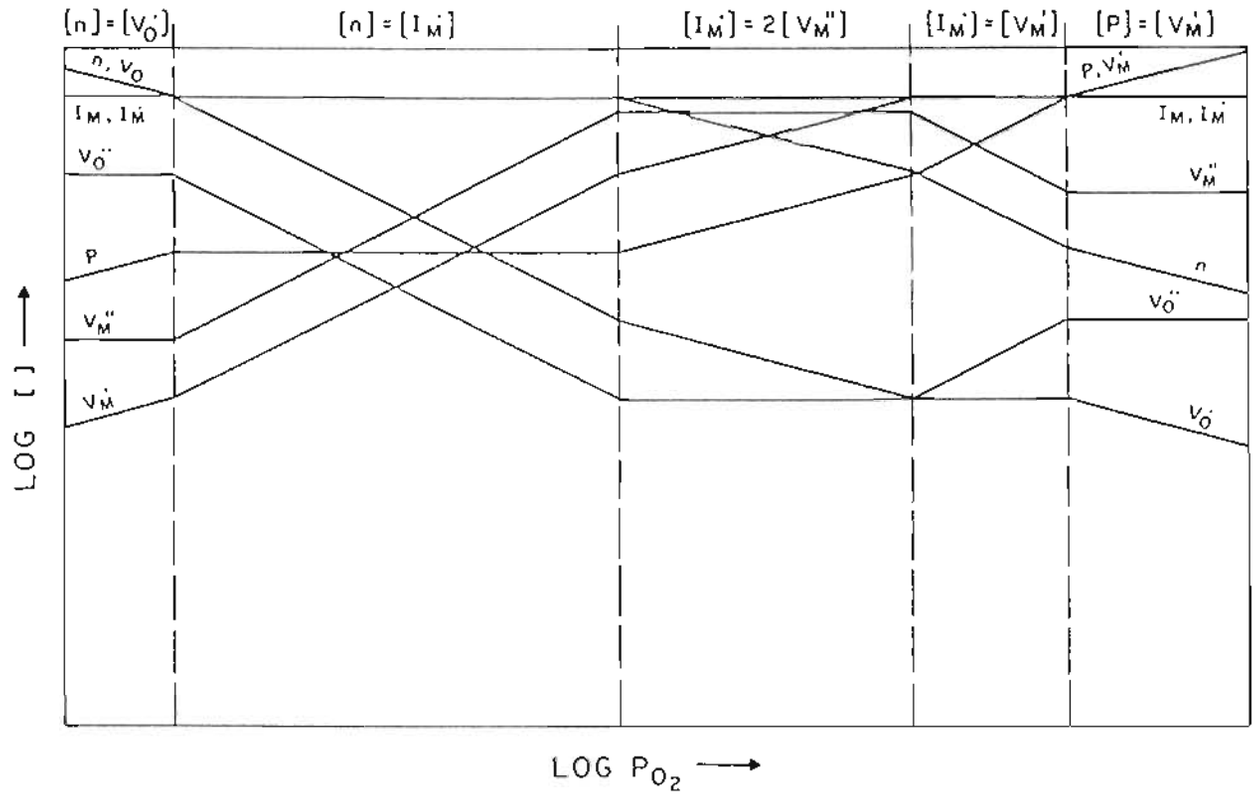

Figure 8 . CONCENTRATIONS OF THE DEFECTS AS A FUNCTION OF P_{O_2} FOR A CRYSTAL MO WITH SCHOTTKY-WAGNER DISORDER CONTAINING A FOREIGN ATOM I_m HAVING MORE VALENCE ELECTRONS THAN M.

indicated from a p to n transition for the pure MO crystal illustrated in Figures 3 through 6 will be shifted to lower oxygen partial pressures when acceptor impurity is added and to higher P_{O_2} for the case of addition of a donor impurity.

1.6 Imperfections in Ternary compound of the type ABO_3

The way in which the dependence of the defect concentrations on the oxygen partial pressure in a ternary compound ABO_3 is found will be illustrated with reference to the simplest case first. Let us suppose that at a certain temperature, the only defects present are V_A, V_B, V_o, V'_A, V'_B, V°_o, n, and P, and further that $[V_A] = [V_B]$ and $[V'_A] = [V'_B]$. The defect equations involved are:

$$[V_A]\,[V_B]\,[V_o]^3 \cong K_s \tag{52}$$

$$[V'_A]\,[V'_B]\,[V^{\circ}_o]^3 \cong K'_s \tag{53}$$

$$[V_o] \cong K_{54}\, P_{O_2}{}^{-1/2} \tag{54}$$

$$[V_A]\,[V_B] \cong K_{55}\, P_{O_2}{}^{3/2} \tag{55}$$

$$\frac{[n]\,[V^{\circ}_o]}{[V_o]} \cong K_{56} \tag{56}$$

$$\frac{[P]\,[V'_A]}{[V_A]} \cong K_{57} \tag{57}$$

$$\frac{[P]\ [V_B']}{[V_B]} \cong K_{58} \tag{58}$$

$$[n]\ [P] \cong K_i \tag{31}$$

and the total charge neutrality condition:

$$[p] + [V_o^{\cdot}] = [n] + [V_A'] + [V_B'] \tag{59}$$

The assumption that $[V_A] = [V_B]$ and $[V_A'] = [V_B']$ further leads to condition corresponding to the case of $K_{57} = K_{58}$. From equation (55) we now get

$$[V_A] = [V_B] = K_{55}^{1/2}\ P_{O_2}^{3/4} \tag{60}$$

For sufficiently large values of the P_{O_2}, $[V_A']$ and $[V_B']$ will be much greater than $[V_o^{\cdot}]$ and $[n]$. Then the neutrality condition reduces to

$$[V_A'] + [V_B'] = [p] \tag{61}$$

Similarly, for low oxygen pressures

$$[V_o^{\cdot}] = [n] \tag{62}$$

For intermediate oxygen pressures, two approximate solutions are possible, depending on the actual values of the equilibrium constants. Those two possible simplified neutrality conditions are

$$[V_o^{\cdot}] = [V_A'] + [V_B'] \tag{63}$$

or

$$[n] = [p] \tag{64}$$

Combinations of equations (54), (60), (61), (62), (63), (64) together with equations (52) to (58) yields expressions for all defect concentrations as a function of P_{O_2}. These expressions are summarized in Table II. Figures 9 and 10 show the variation of defect concentrations as a function of oxygen partial pressure for the two intermediate neutrality conditions.

The example considered is a rather artificial case. It is fairly improbably that the equilibrium constants governing the dissociation of A and B vacancies are the same. The concentrations of V_A' and V_B' will consequently differ and so, too, will the concentrations of V_A, and V_B. Furthermore, the imperfections may have a higher level of ionization.

From these we will consider a case involving defects at a higher level of ionization. With increasing P_{O_2} we may expect the following sequence of charge neutrality conditions:

$[n] \cong [V_O^{\circ}]$

$[n] \cong 2\ [V_O^{\cdot\cdot}]$,

$[V_O^{\cdot\cdot}] \cong [V_A'''] + 2\ [V_B''''']$,

$[p] \cong 2\ [V_A'''] + 4\ [V_B''''']$,

$[p] \cong [V_A'] + 2\ [V_B'']$

For reasons of convenience we omit the description of neutrality conditions such as $[p] = 2\ [V_A''] + 3\ [V_B''']$ and $[p] = [V_A'] + 3\ [V_B''']$. Considera-

tions of these conditions yield comparable results. The calculated oxygen partial pressure dependence of the completely ionized defect concentrations are given in Table III. Figures 11 and 12 illustrate the isothermal pressure dependence of various defect concentrations. Only the totally ionized defects are included in the Figures. The neutrality conditions in the intermediate regions are $[V_O^{\cdot\cdot}] = [V_A''] + 2[V_B'''']$ in Figure 11 and [n] = [p] in the Figure 12. Anticipating the results of the electrical conductivity in $SrTiO_3$, we notice that no region where the conductivity is independent of P_{O_2}. This means that in the investigated ranges of temperature and oxygen partial pressure a neutrality condition $[n] = [p] = K_i^{1/2}$ will not exist (Figure 15) or exist in a very narrow region.

1.7 The Incorporation of Foreign Atoms in a ternary oxide ABO_3

If we dissolve a foreign component in ABO_3, the system changes from three component into a four component system. If the vapor pressure of the dissolved component is low enough, the quantity of the dissolved component in the solid phase is constant and the increase of one degree of freedom is compensated for.

Consider ABO_3 in which acceptor impurity is dissolved and assume that all the acceptor is completely ionized so that

$$[I_m]_{total} = [I_m'] = \text{constant} \qquad (65)\ [\text{Eq. } 48]$$

Again we obtain various possibilities for the sequence of reduced neutrality conditions, such as:

Table II.

RELATIONS BETWEEN DEFECT CONCENTRATIONS AND OXYGEN PRESSURE IN THE TERNARY OXIDE ABO_3.
IN THIS CASE ONLY NEUTRAL AND SINGLY IONIZED DEFECTS ARE CONSIDERED

Defect	$[n] = [V_O^{\cdot}]$	$[V_A'] + [V_B'] = [V_O^{\cdot}]$
$[n]$	$K_{56}^{1/2} K_{54}^{1/2} P_{O_2}^{-1/4}$	$2^{-1/2} K_{56}^{1/2} K_{57}^{-1/2} K_{54}^{5/4} K_s^{-1/4} K_i^{1/2} P_{O_2}^{-5/8}$
$[p]$	$K_i K_{56}^{-1/2} K_{54}^{-1/2} P_{O_2}^{1/4}$	$2^{1/2} K_{56}^{-1/2} K_{57}^{1/2} K_{54}^{-5/4} K_s^{1/4} K_i^{1/2} P_{O_2}^{5/8}$
$[V_O]$	$K_{54}^{-1/2} P_{O_2}^{-1/2}$	$K_{54}^{-1/2} P_{O_2}^{-1/2}$
$[V_A]=[V_B]$	$K_s^{1/2} K_{54}^{-3/2} P_{O_2}^{3/4}$	$K_s^{1/2} K_{54}^{-3/2} P_{O_2}^{3/4}$
$[V_O^{\cdot}]$	$K_{56}^{1/2} K_{54}^{1/2} P_{O_2}^{-1/4}$	$2^{1/2} K_{56}^{1/2} K_{57}^{1/2} K_{54}^{-1/4} K_s^{1/4} K_i^{-1/2} P_{O_2}^{1/8}$
$[V_A']=[V_B']$	$K_{56}^{1/2} K_{57}^{-1} K_{54}^{1/2} K_s^{-1} K_i^{1/2} P_{O_2}$	$2^{-1/2} K_{56}^{1/2} K_{57}^{1/2} K_{54}^{-1/4} K_s^{1/4} K_i^{-1/2} P_{O_2}^{1/8}$

Table II. (cont.)

RELATIONS BETWEEN DEFECT CONCENTRATIONS AND OXYGEN PRESSURE IN THE TERNARY OXIDE ABO_3.
IN THIS CASE ONLY NEUTRAL AND SINGLY IONIZED DEFECTS ARE CONSIDERED

Defect	$[n] = [p]$	$[V_A'] + [V_B'] = [p]$
$[n]$	$K_i^{1/2}$	$2^{-1/2} K_{57}^{-1/2} K_s^{-1/4} K_{54}^{3/4} K_i P_{O_2}^{-3/8}$
$[p]$	$K_i^{1/2}$	$2^{1/2} K_{57}^{1/2} K_s^{1/4} K_{54}^{-3/4} P_{O_2}^{3/8}$
$[V_o]$	$K_{54}^{-1/2} P_{O_2}^{-1/2}$	$K_{54}^{-1/2} P_{O_2}^{-1/2}$
$[V_A]=[V_B]$	$K_s^{1/2} K_{54}^{-3/2} P_{O_2}^{3/4}$	$K_s^{1/2} K_{54}^{-3/2} P_{O_2}^{3/4}$
$[V_o^{\cdot}]$	$K_{56} K_{54}^{-1/2} K_i^{-1/2} P_{O_2}^{-1/2}$	$2^{1/2} K_{56} K_{57}^{1/2} K_s^{1/4} K_m^{1/4} K_i^{-1} P_{O_2}^{-1/8}$
$[V_A']=[V_B']$	$K_{57} K_s^{1/2} K_{54}^{-3/2} K_i^{-1/2} P_{O_2}^{3/4}$	$2^{-1/2} K_{57}^{1/2} K_s^{1/4} K_{54}^{-3/4} P_{O_2}^{3/8}$

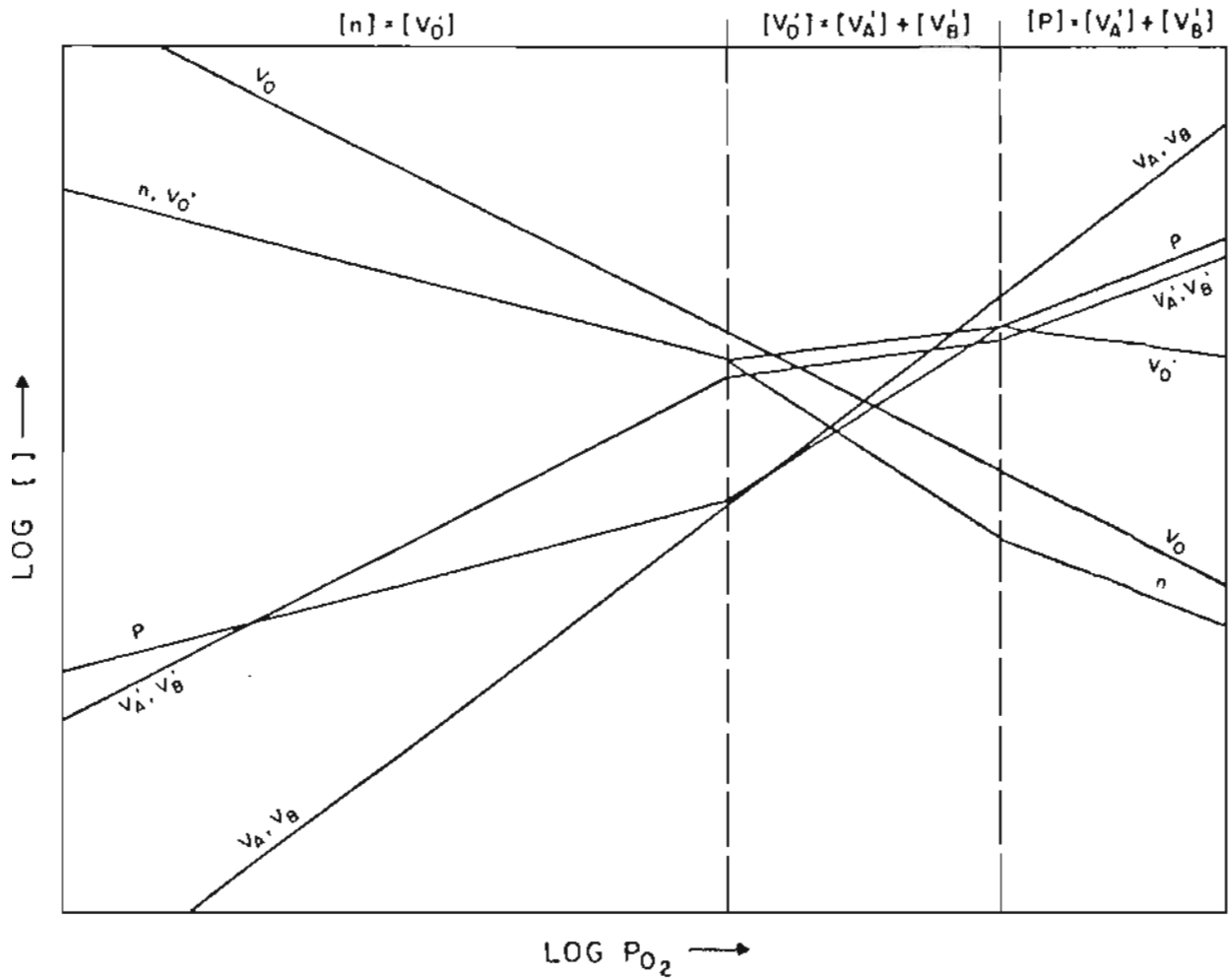

Figure 9. CALCULATED DEFECT CONCENTRATIONS IN ABO_3 AS A FUNCTION OF OXYGEN PRESSURE. NEUTRAL AND SINGLY IONIZED DEFECTS ONLY ARE CONSIDERED. THE CONCENTRATIONS OF THE TWO CATIONS ARE EQUAL. INTERMEDIATE NEUTRALITY CONDITION IS $[V_O^{\cdot}] = [V_A^{'}] + [V_B^{'}]$.

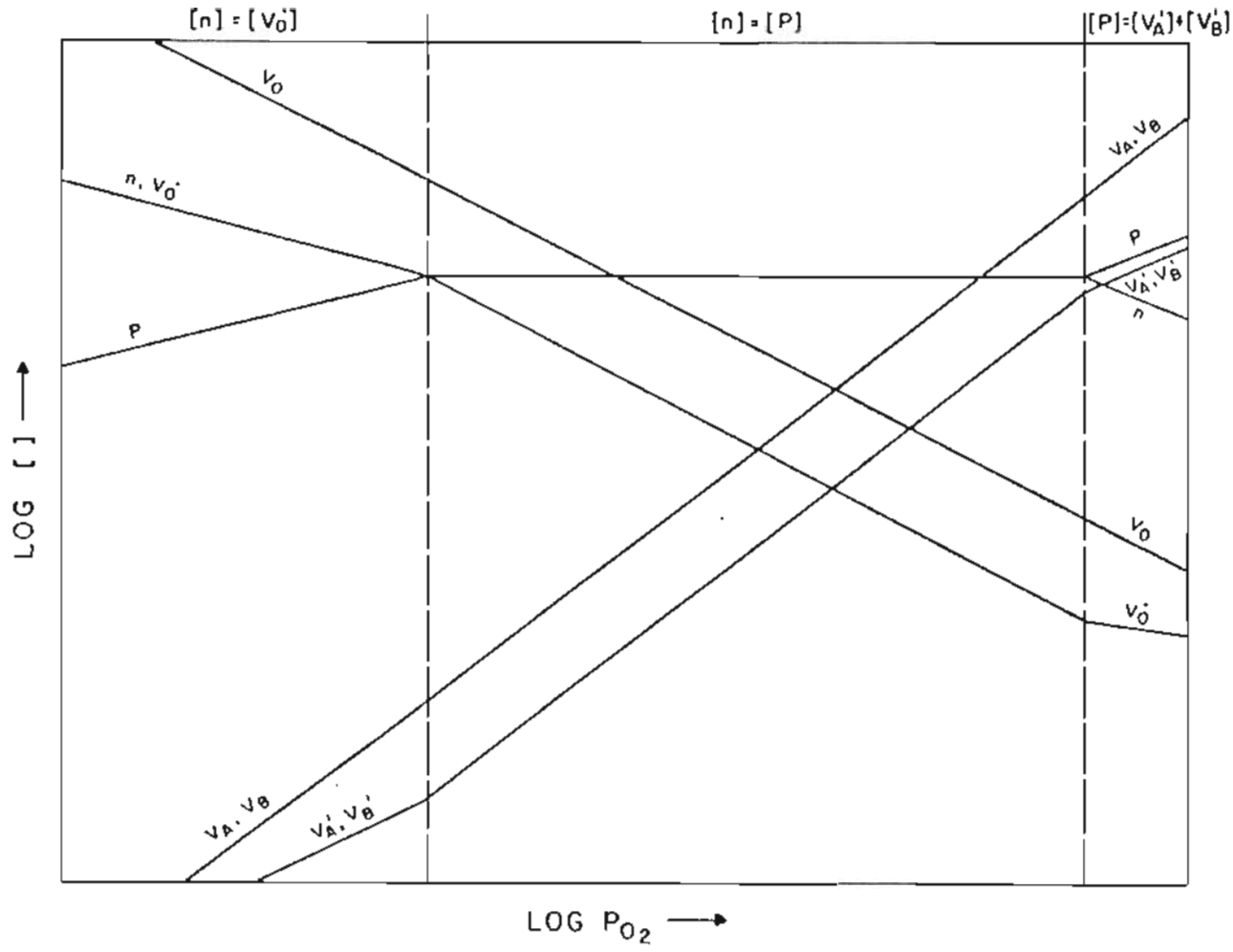

Figure 10. CONCENTRATIONS OF DEFECTS AS IN Figure 12, BUT WITH INTERMEDIATE NEUTRALITY CONDITION [n] = [p].

Table III.

P_{O_2} DEPENDENCE OF COMPLETELY IONIZED DEFECT CONCENTRATIONS IN THE TERNARY OXIDE ABO_3

Defect	$[n]=2[V_O^{\cdot\cdot}]$	$[V_O^{\cdot\cdot}]=[V_A'']+2[V_B'''']$	$[n]=[p]$	$[p]=2[V_A'']+4[V_B'''']$
$[n]$	-1/6	-1/4	0	-3/16
$[p]$	1/6	1/4	0	3/16
$[V_O^{\cdot\cdot}]$	-1/6	0	-1/2	-1/8
$[V_A'']=[V_B'''']$	5/12	0	3/4	3/16

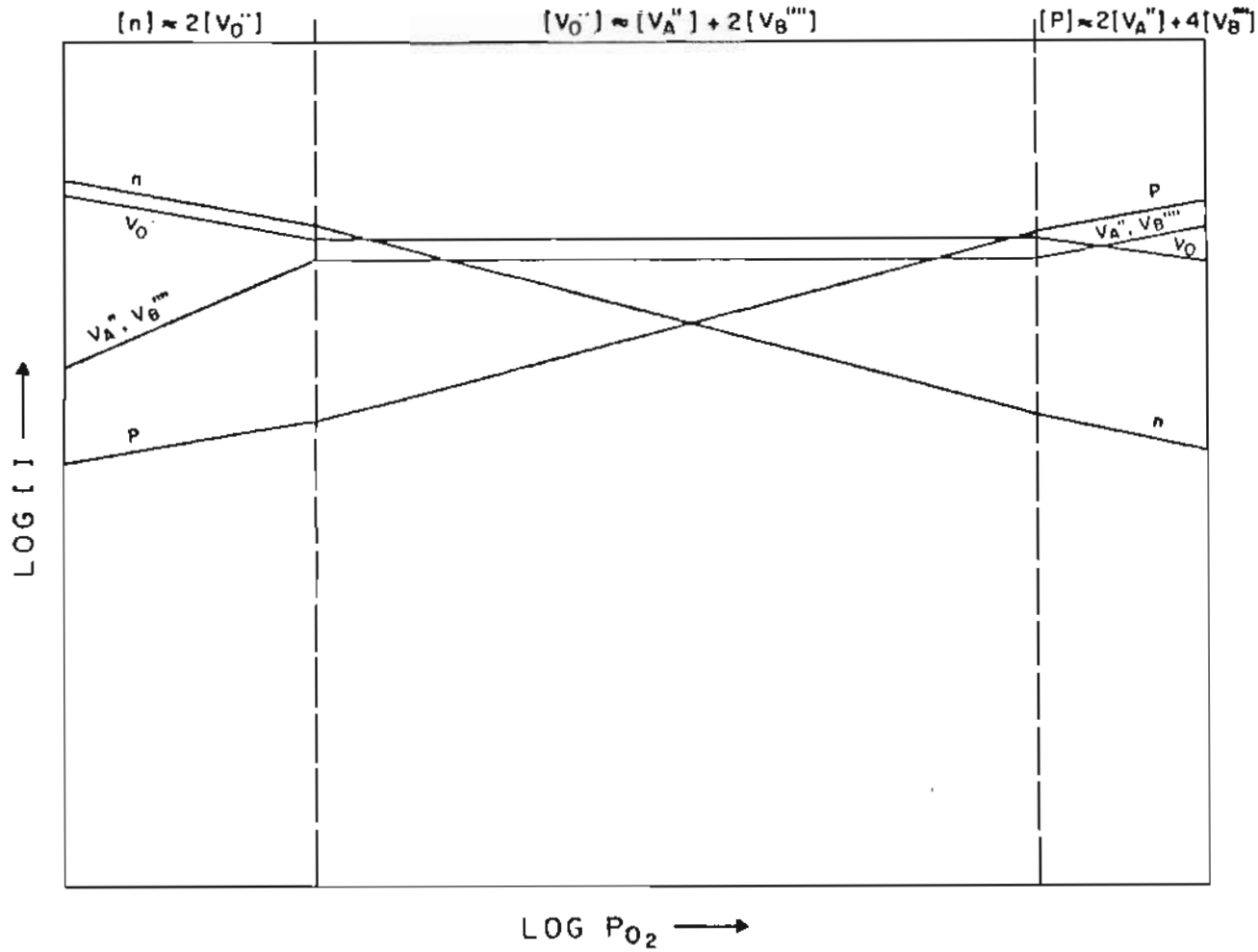

Figure 11. CALCULATED DEFECT CONCENTRATIONS VS. THE OXYGEN PRESSURE IN ABO_3. THE A AND B CONTENTS OF THE MATERIAL ARE ASSUMED TO BE THE SAME.

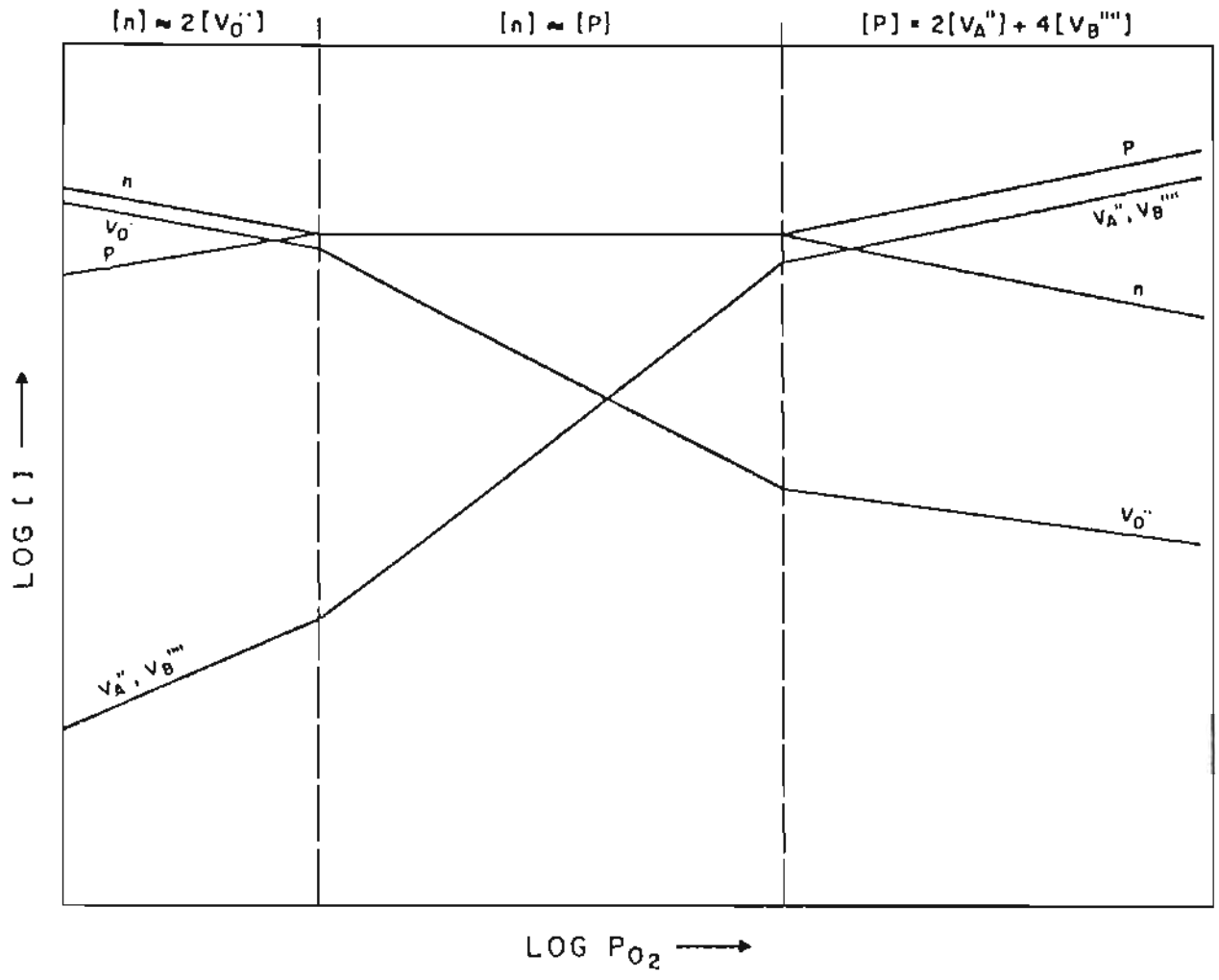

Figure 12. CONCENTRATIONS OF THE DEFECTS AS IN Figure 14, BUT INTERMEDIATE NEUTRALITY CONDITION READS [n] = [p].

$$[n] \cong [V_o^{\circ}],\ [n] \cong 2[V_o^{\cdot\cdot}],\ 2[V_o^{\cdot\cdot}] \cong [I_m'],$$

$$[p] \cong [I_m'],\ [p] \cong 2[V_A''] + 4[V_B''''],$$

$$[p] \cong [V_A'] + 3[V_B'''];\qquad (66)$$

$$[n] \cong [V_o^{\circ}],\ [n] \cong 2[V_o^{\cdot\cdot}],\ [n] \cong [p]$$

$$[p] \cong 2[V_A''] + 4[V_B''''];$$

$$[p] \cong [V_A'] + 3[V_B'''] \qquad (67)$$

The variation of the defect concentrations are calculated as before and the slopes for the log [ ] vs log P_{O_2} plots (see Figure 13) are given in Table IV. The p-n intersection point is moved to lower P_{O_2} value in the diagram for the acceptor doped ABO_3 (Figure 13) as compared with Figures 11 and 12, which are for the pure ABO_3 compound.

In Figure 13 the pressure range with neutrality condition $2[V_o^{\cdot\cdot}] = [I_m']$ is of main interest. In this region,

$$n \propto P_{O_2}^{-1/4} \qquad \text{and,}$$

$$p \propto P_{O_2}^{1/4}$$

The concentration of holes, [p] increases and finally becomes equal to I_m'. But before that condition is reached we have [p] > [n] and hence the conductivity changes to p-type with +1/4 dependence on P_{O_2}. In the region with charge neutrality condition

$$2[V_o^{\cdot\cdot}] \cong [I_m'],$$

Table IV.

P_{O_2} DEPENDENCE OF THE DEFECT CONCENTRATIONS IN THE ACCEPTOR DOPED ABO_3 [see Fig. 13].

Defect	$[n]=2[V_O^{\cdot\cdot}]$	$[I_m']=2[V_O^{\cdot\cdot}]$	$[I_m']=[p]$
$[n]$	-1/6	-1/4	0
$[p]$	1/6	1/4	0
$[V_O^{\cdot\cdot}]$	-1/6	0	-1/2
$[V_A'']=[V_B''''']$	5/12	0	+3/4

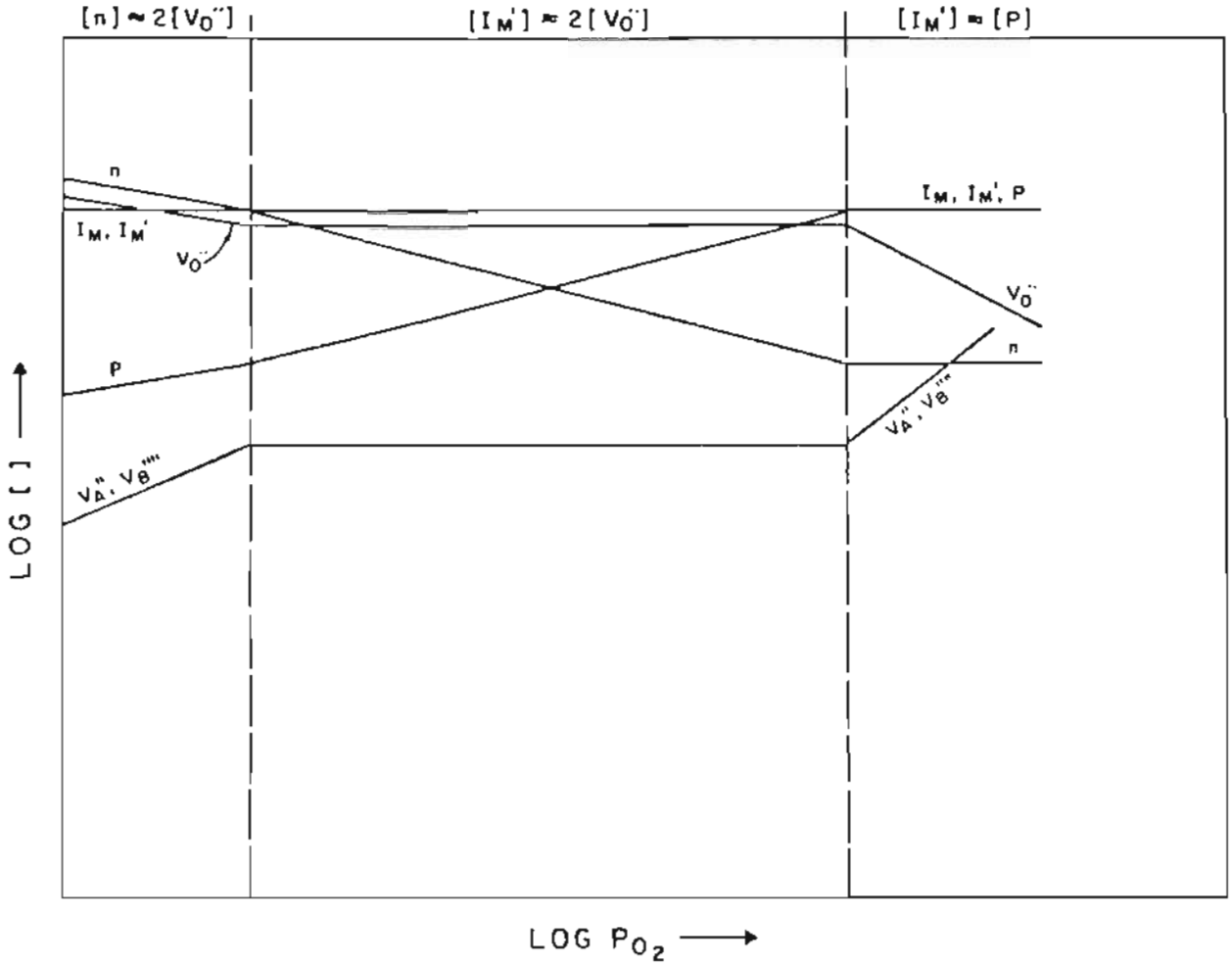

Figure 13. CALCULATED CONCENTRATIONS OF CHARGED DEFECTS AS A FUNCTION OF P_{O_2} FOR ACCEPTOR-DOPED ABO_3.

the conductivity changes sign. This is actually observed in the present investigation for deliberately acceptor doped and undoped $SrTiO_3$ (due to the presence of accidental acceptor impurities).

If the foreign atom is a donor, we have the possibilities for the sequence of the charge neutrality conditions such as:

$$[n] \cong [V_O^{\cdot}],\ [n] \cong 2[V_O^{\cdot\cdot}],\ [n] \cong [I_m^{\circ}]$$

$$[I_m^{\circ}] \cong 2[V_A^{''}] + 4[V_B^{''''}],$$

$$[p] \cong 2[V_A^{''}] + 4[V_B^{''''}],$$

$$[p] \cong [V_A^{'}] + 3[V_B^{'''}], \tag{68}$$

$$[n] \cong [V_O^{\cdot}],\ [n] \cong 2[V_O^{\cdot\cdot}],\ [n] \cong [p],$$

$$[p] \cong 2[V_A^{''}] + 4[V_B^{''''}],$$

$$[p] \cong [V_A^{'}] + 3[V_B^{'''}]$$

The calculated values of the defect concentration as a function of P_{O_2} are shown in Table V.

For large donor concentrations we may expect a region in which the electron concentration is independent of P_{O_2}, (see Figure 14). In the donor doped ABO_3, the p to n intersection point is moved to higher P_{O_2} value and within the experimental range one may not observe the p-type conductivity because the n to p transition will occur at $P_{O_2} >> 1$ atm. A flat region (at low P_{O_2} range) where the conductivity is independent of P_{O_2} is observed in the present work for the lanthanum doped $SrTiO_3$.

Table V.

P_{O_2} DEPENDENCE OF THE DEFECT CONCENTRATIONS IN THE DONOR-DOPED ABO_3 [see Fig. 17]

Defect	$[n]=2[V_O^{\cdot\cdot}]$	$[n]=[I_m^{\cdot}]$	$[I_m^{\cdot}]=2[V_A^{\prime\prime}]+4[V_B^{\prime\prime\prime\prime}]$
$[n]$	-1/6	0	1/4
$[p]$	1/6	0	-1/4
$[V_O^{\cdot\cdot}]$	-1/6	-1/2	0
$[V_A^{\prime\prime}]=[V_B^{\prime\prime\prime\prime}]$	5/12	3/4	0

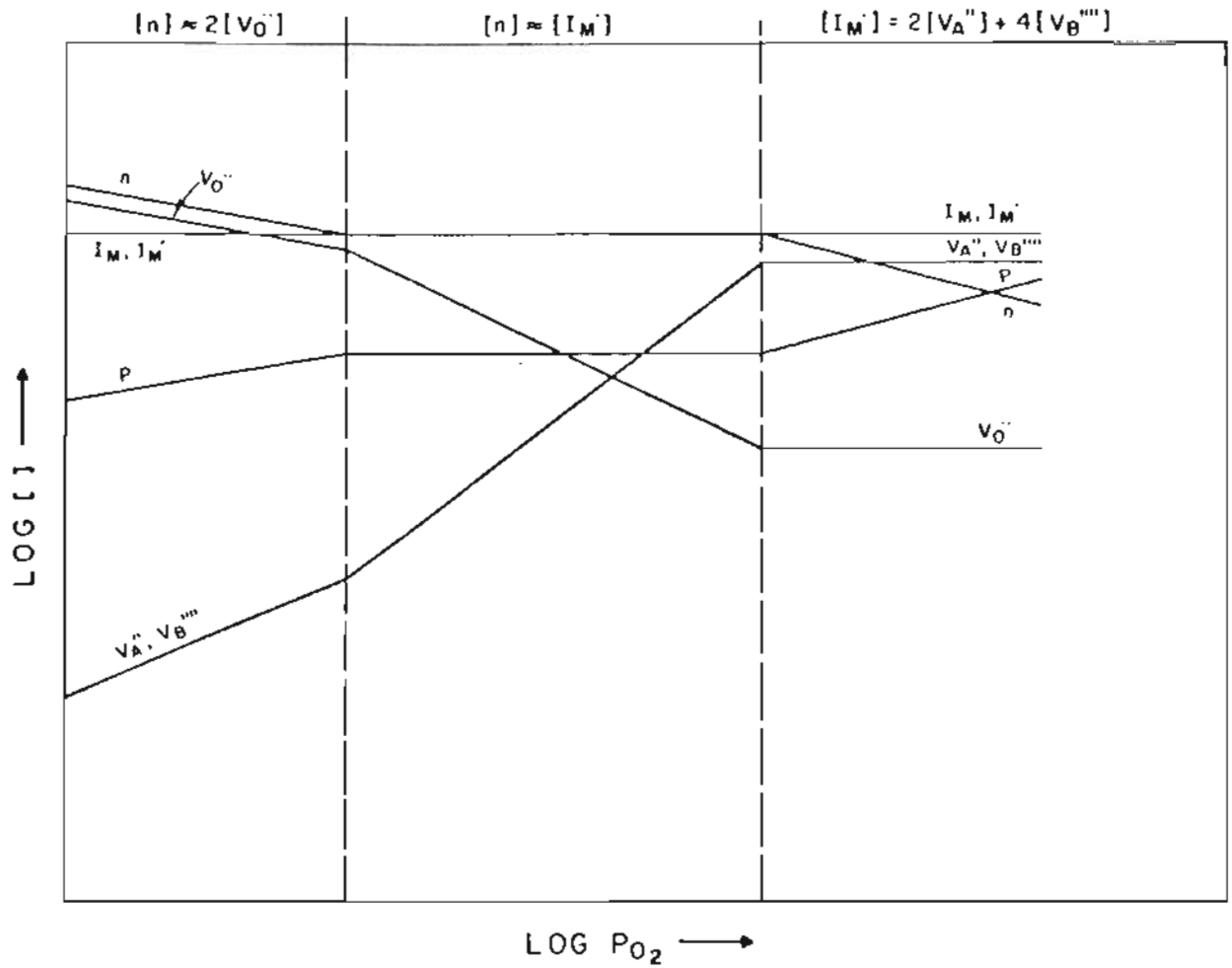

Figure 14. CALCULATED CONCENTRATIONS OF CHARGED DEFECTS AS A FUNCTION OF P_{O_2} FOR DONOR-DOPED ABO_3.

Upon increasing the P_{O_2}, the conductivity becomes $\propto$ -1/4th power of P_{O_2} as predicted from Figure 14.

1.8 Disorder in a Ternary Compound ABO_3 with Non-Ideal Cation-Cation Ratio (A/B $\neq$1)[18,19]

The assumption of the cation-cation ratio as constant in order to thermodynamically define the ternary compound ABO_3 is usually not a completely adequate thermodynamic characterization over a range of temperature, because the solubility of the binary constituent in the ternary compound will be a function of temperature. Thus, the composition of ABO_3, having a fixed A/B ratio, will correspond to that obtained by equilibration with a different a_{AO} at each temperature.

It has not been adequately appreciated that a fixed cation-cation ratio does not define the activities of the binary constituents, even at constant temperature, when the non-metal activity is varied over a significant range. Thus, measurements of defect concentrations, electrical conductivity, or self-diffusion constants as a function of oxygen pressure at constant temperature and cation composition are equivalent to making the measurements with the ternary oxide in equilibrium with a different activity of binary constituent at each oxygen pressure. The effect can be very large for easily achievable experimental conditions, and can even drive the system to a phase boundary with subsequent separation of a second solid phase.

The nonstoichiometric compositions ($A/B \neq 1$) must result in the presence of structural defects. It will be assumed here that V_A'' and $V_O^{\cdot\cdot}$ are the preferred defects for the incorporation of excess BO_2 which corresponds to the large cation to small cation ratio (A/B) less than unity. The alternative choices of B_i^{+4} and O_i^{-2} or B_A^{+2} and O_i^{-2} being less probable in the close packed structures like in $BaTiO_3$, $CaTiO_3$, and $SrTiO_3$. The defects V_A'' and $V_O^{\cdot\cdot}$ may be associated into neutral vacancy pairs or remain as charged defects. Both the extreme cases of defect association and negligible defect association were treated by Smyth[18,19] and Eror and Smyth.[20]

The variation of defect concentrations as a function of oxygen partial pressure for the cases of negligible and extensive defect association are shown in Figures 15 and 16 respectively. In Figures 15 and 16, $P_{O_2}^{\circ}$ represent the oxygen partial pressure for the precise oxygen stoichiometry, i.e., the oxygen content exactly satisfies the ideal valence requirements of the cations present.

The plots shown in Figures 15 and 16 are based on the ideally pure material; but, such materials do not exist in reality. In oxides in particular, the concentrations of intrinsic defects are generally low compared with presently achievable impurity levels. The defect chemistry is dominated by these impurities and their charge compensating defects over some range of conditions centered on precise stoichiometry, as can be seen later in the results and discussion part of the present work in $SrTiO_3$. Similar behavior has been reported in $BaTiO_3$.[20,22]

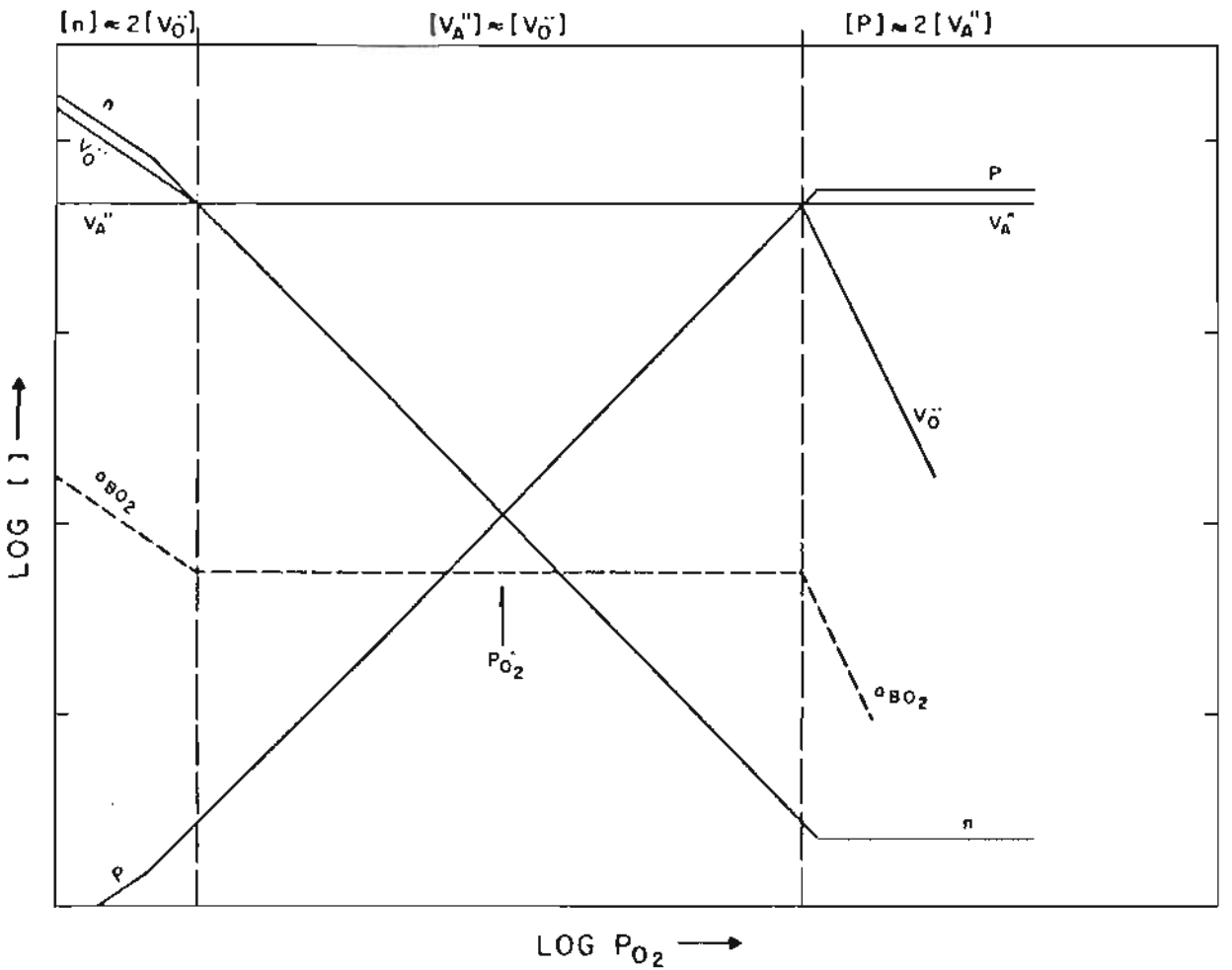

Figure 15. IDEALIZED DEFECT DIAGRAM FOR BO_2-RICH ABO_3 WITH ARBITRARY UNITS FOR a_{BO_2} [NEGLIGIBLE DEFECT ASSOCIATION].

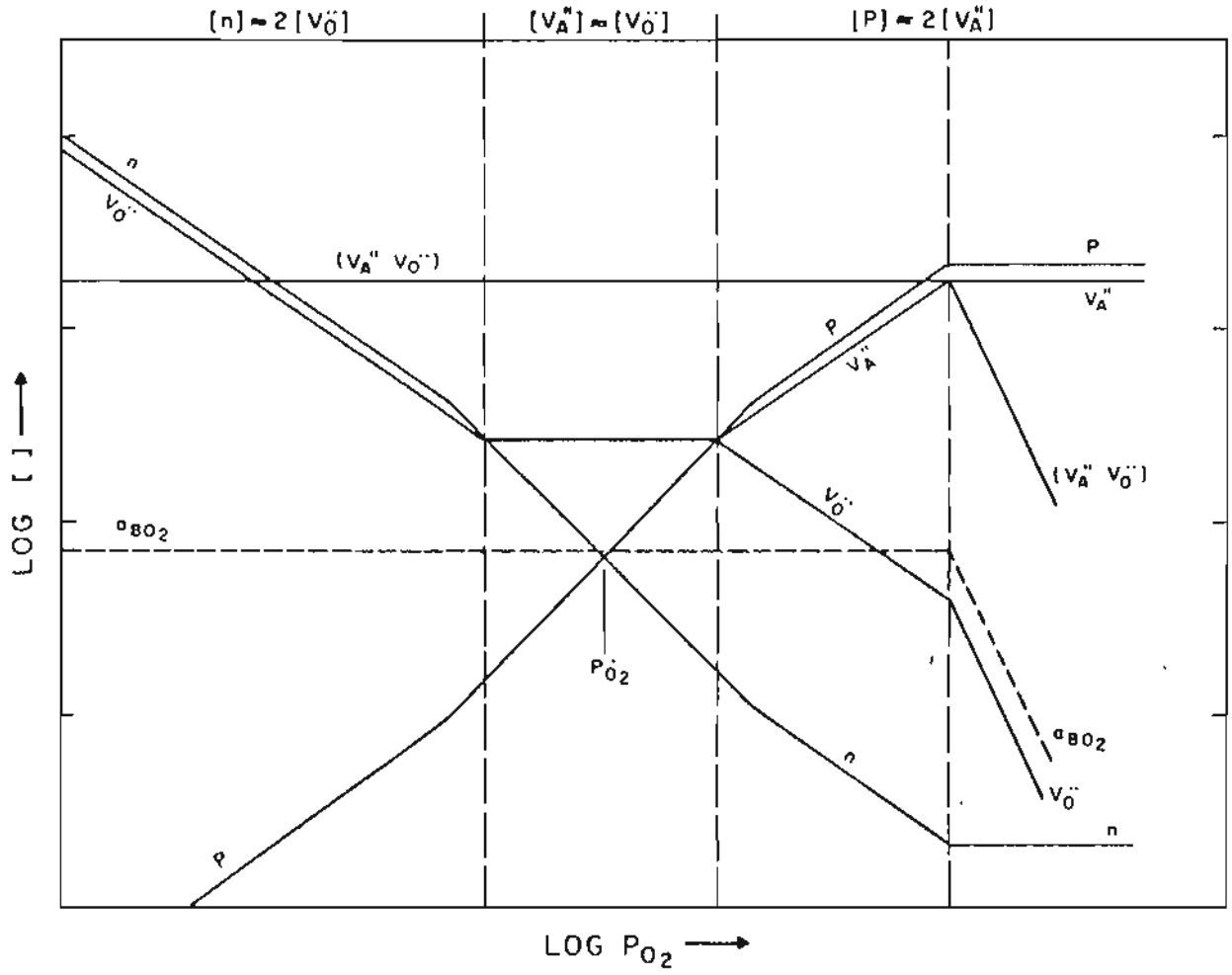

Figure 16. IDEALIZED DEFECT DIAGRAM FOR BO_2-RICH ABO_3 WITH EXTENSIVE DEFECT ASSOCIATION.

2. REVIEW OF RELATED WORK

2.1 Solubility of Lanthanum in Strontium Titanate

The existence of a perovskite (ABO_3) phase of composition $Sr_{1-1.5x}La_xTiO_3$ in the ternary system $SrO-TiO_2-La_2O_3$ has been reported by Tien and Hummel.[24] They have observed ordering phenomena at compositions containing more than 70 mole % $La_{2/3}TiO_3$ in $SrTiO_3$. These had been cooled slowly from 1400°C to room temperature. In all their samples the large cation to small cation ratio was less than unity. Bouwma et al[25] reported that the sample of composition $La_{.35}Sr_{.65}TiO_3$ and large cation to small cation ratio unity consisted of two or more phases, one of which was a perovskite phase. They concluded that this composition lies outside the perovskite homogeneity range. Tofield and Scott[26] reported that they were not able to obtain single phase materials of composition $Sr_{0.8}La_{0.2}TiO_{3.0-3.10}$. After firing in oxygen at 1500°C, reduced in hydrogen at 1100°C and reoxidation in air at 800°C, La_2O_3 lines were always present in their compound. The reduced and oxidized forms had identical lattice parameters (3.9084 Å and 3.9080 Å respectively). From this they indicated that lanthanum is only slightly soluble in $SrTiO_3$. In the structural analog $BaTiO_3$, Eror and Smyth[27] have reported that up to 20 at.% barium may be substituted by lanthanum to retain a single phase fully oxidized material. They did not observe the presence of any second phase, by either optical or by x-ray diffraction studies.

It is possible to consider strontium titanate in which lanthanum has been substituted at part of the A-sites as a mixed-crystal series $SrTiO_3$-$La_{2/3}\square_{1/3}TiO_3$, where $\square$ represents the vacancy on lanthanum site. Although pure $La_{2/3}\square_{1/3}TiO_3$ cannot be prepared, small amounts of $SrTiO_3$ suffice for the stabilization of this phase.[28] Similar relationships are found in lanthana-substituted lead titanate,[29] in which perovskite phases of the composition $Pb_{1-1.5x}La_xTiO_3$ can be produced.

2.2 Self-Compensation in Lanthanum Doped Strontium Titanate

Tofield and Scott[26] reported that the lanthanum doped $SrTiO_3$ has no significant range of nonstoichiometry. In the similar system, lanthanum doped $BaTiO_3$, Eror and Smyth[27] reported the observation of self-compensation behavior for up to 20 at.% of lanthanum. They have shown that the reversible change of oxygen content, between specified states of oxidation and reduction, is proportional to the dopant concentration. This range of reversible weight change in oxygen stoichiometry is up to more than an order of magnitude larger than the oxygen nonstoichiometry of the undoped $BaTiO_3$.

The disorder created by La^{+3} as a donor dopant in $BaTiO_3$[27] should lend itself to description by Verwey's controlled valency model.[30] By this model, there would be compensation for the La^{+3} on Ba^{+2} sites by the creation of equal numbers of Ti^{+3} ions. The Ti^{+3} ions are then responsible for the increase in electrical conductivity. In this case the donor-dopant dominates the positive side of the electroneutrality equation

and as a consequence the negative defect concentration would be independent of equilibrium oxygen activity. This compensation mechanism has also been referred to as controlled electronic imperfection.[4] Similarly, the donor-dopant may be compensated by the formation of charged point defects that would also be independent of equilibrium oxygen activity. This compensation mechanism has been referred to as controlled atomic imperfection,[4] self-compensation,[27,31-36] and stoichiometric compensation.[27] The controlled valency model is appropriate only for dopant concentrations of a few tenths percent.

2.3 Electrical Conductivity in Undoped and Impurity Added $SrTiO_3$

The electrical transport properties of semiconducting n-type $SrTiO_3$ were first investigated by Frederikse et al.,[37] who found a band-type conduction process with an electron effective mass much greater than the free-electron mass and low-temperature mobilities greater than 1000 cm^2/Volt.sec. A theoretical examination of the electronic energy bands of strontium titanate has been carried out by Kahn and Leyendecker.[38] Their calculations led to filled valence bands derived primarily from oxygen 2p orbitals, and empty conduction bands derived predominantly from titanium 3d orbitals. From the optical transmission studies on single crystal strontium titanate which was heated in vacuum, Gandy[39] determined an energy band of 3.15 ev. The oxygen self-diffusion has been studied by Paladino et al.[40] in single crystal $SrTiO_3$. Walters and Grace[41] investigated the diffusion of point defects in $SrTiO_3$. Paladino[42] studied the

oxidation kinetics of single crystal $SrTiO_3$. On the basis of the oxygen self-diffusion and oxidation measurements, Paladino et al[40,42] concluded that an oxygen vacancy defect model was applicable to $SrTiO_3$ at elevated temperatures.

Walters and Grace[43] examined the electrical conductivity and Seebeck coefficient of $SrTiO_3$ in water-hydrogen atmospheres for a narrow range of oxygen partial pressure. They also concluded that an oxygen vacancy model was applicable to their results. Yamada and Miller[44] have determined the carrier concentration by Hall effect measurements for single-crystal $SrTiO_3$ quenched from equilibrium with various oxygen partial pressures. All of the reported studies on $SrTiO_3$ indicate that there is an extensive range at low oxygen partial pressures (P_{O_2}) where the conductivity increases with decreasing P_{O_2}, characteristic of n-type conduction related to oxygen deficiency. The structural analog $BaTiO_3$ has been studied in much detail both in the polycrystalline[21,22,45-48] and single crystal[20] states. These studies indicate that in the P_{O_2} range near 1 atm., the conductivity increases with increasing P_{O_2}, characteristic of P-type conduction, related to a stoichiometric excess of oxygen. But $SrTiO_3$ has not been studied in the past while in equilibrium with P_{O_2} near 1 atm., and no equilibrium behavior characteristic of P-type conduction has been reported.

The defect structure of $SrTiO_3$ when the Sr to Ti ratio is different from 1:1 is not known to this date. Such deviations were found to be accommodated by the formation of neutral vacancy pairs ($V''_{Ba}\ V^{\cdot\cdot}_{o}$) in $BaTiO_3$.[20,22]

Strontium titanate can be converted into a good n-type semiconducting material at room temperature either by reduction or by doping with donors. Frederikse et al,[37] investigated the electrical conductivity and the Hall and Seebeck coefficients of niobium doped (0.05 and 0.005 wt. %) single crystal $SrTiO_3$ over the temperature range 4.2-300 K. Tufte and Chapman[49] used niobium doped $SrTiO_3$ and measured the Hall mobility over the temperature range from 1.6 to 550 K. They concluded that niobium donor centers remain fully ionized down to 1.6 K. The only high temperature study on donor-doped $SrTiO_3$ is that of Frederikse and Hostler[50] who reported the Hall mobility of niobium and lanthanum doped single crystal $SrTiO_3$ at 1000 K in air. No data on the conductivity of donor doped $SrTiO_3$ at elevated temperatures and in equilibrium with different oxygen partial pressures has been found in the literature.

Electrical conductivity of acceptor-doped $SrTiO_3$ has not been studied in the past. We have noted high temperature electrical conductivity as reported for Al and Ga doped $BaTiO_3$.[22,51] For large amounts of acceptor doped $BaTiO_3$, the conductivity varied as -1/4th power of oxygen partial pressure in the n-type region.

2.4 Raman Spectra of Strontium Titanate

The lattice dynamics of the perovskite-type ferroelectrics have received considerable attention in the past two decades.[52,53] The use of the Raman effect to study the lattice dynamics of crystals has been suggested[54] and carried out[55,56] by several authors. In particular, the

Raman spectrum of $SrTiO_3$ has been recorded in some detail by earlier investigators.[55,57-60] Some of them have[55] interpreted the observed spectrum as first-order, even though first-order scattering is forbidden in the cubic perovskite phase according to the selection rules. In the case of perovskite structures, the spectra are quite complex and the value of Raman studies has been limited because of the difficulty in reliably interpreting the spectra-Neutron diffraction studies of $SrTiO_3$ have provided frequency-vs.-wave vector dispersion curves for some of the vibrational modes.[53,61] The neutron diffraction studies also indicated that near the Brillouin zone center the lowest-energy transverse optic mode $\omega_1(0)$ [soft mode] decreases in energy as the temperature is reduced. Cowley[53] observed the frequency of this soft optical mode in the temperature range between 90K and 440K with neutron scattering, and found that the temperature dependence of the $\omega_1(0)$ is described by $\omega_1(0) = K(T-T_0)^{1/2}$ with $T_0 = 32 \pm 5K$.

The lattice dynamics of $SrTiO_3$ have also been studied by infrared techniques. Last[62] has made an approximate calculation of the force constants in $SrTiO_3$ from his infrared measurements. From these force constants he calculated some of the elastic constants. He fits his two experimentally determined frequencies to get the values of force constants from which he estimates the compressibility. Both Barker and Tinkham,[63] as well as Spitzer et al,[64] measured the energy of three active TO modes and observed that the energy of the ferroelectric soft mode decreased as the temperature was reduced. Accurate energies for the polar TO modes[65] as well as polar LO modes[66] at the zone center are obtained by extended

analysis of the infrared data. The upper curves having non-zero frequencies in the energy vs. wave vector dispersion plots are referred to as the optical branch phonons, since they represent frequencies in the optical (infrared) spectral region. These optical branch phonons are again classified as transverse (TO) modes and longitudinal (LO) modes.

$SrTiO_3$ is known to have the ideal cubic structure of the perovskite family of crystals[67,68] (Fig. 17). In fact among the titanates, strontium titanate satisfies well the criterion for stability put forward by Goldschmidt based on the empirical rules derived by him.[69] Since $SrTiO_3$ is known to exist only in the cubic form at room temperature where every atom in the structure lies at a center of inversion, it is not expected to exhibit any first-order Raman spectrum and only a second-order spectrum is hoped for. The dielectric constant is roughly 300 at room temperature and increases rapidly as the temperature is reduced.[70,71] The Curie-Weiss law is obeyed down to about 50 K with an extrapolated Curie temperature of 38 K. The static dielectric constant shows a deviation from the Curie-Weiss law below 50 K.

Both room temperature and low temperature acoustic properties of $SrTiO_3$ have been studied extensively.[72,74] Acoustic properties of $SrTiO_3$ at room temperature are in accord with its cubic symmetry. As the temperature decreases down to 110 K, the ultrasonic attenuation abruptly increases and the elastic constants are greatly altered. This behavior indicates that a phase transition takes place at 110 K. Further evidence for a phase transition at about 110 K was obtained from electron paramagnetic resonance [EPR] studies of $SrTiO_3$ containing small amounts of

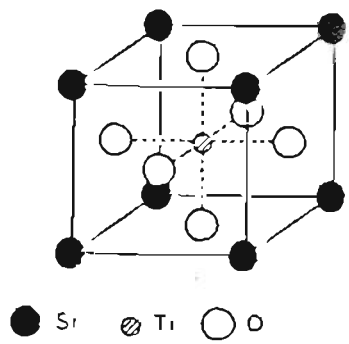

Figure 17. STRUCTURE OF CUBIC $SrTiO_3$.

paramagnetic ions.[75,76] Lytle,[77] using x-ray diffraction methods, observed phase transitions at 65 K and 35 K in addition to the cubic-tetragonal transition at 110 K.

2.5 Ruddlesden-Popper [$nSrTiO_3 \cdot SrO$] Phases

When the strontium content of $SrTiO_3$ is increased it forms a series of compounds called Ruddlesden-Popper phases. Sr_2TiO_4, $Sr_3Ti_2O_7$, and $Sr_4Ti_3O_{10}$ are examples of the Ruddlesden-Popper type of superstructures.[81-83] Figure 18 shows the structures of these three compounds. In Sr_2TiO_4, perovskite $SrTiO_3$ layers are interleaved with SrO layers, forming a tetragonal, body centered unit cell. In $Sr_3Ti_2O_7$ and $Sr_4Ti_3O_{10}$, double and triple perovskite blocks of $SrTiO_3$ are interleaved with SrO layers respectively.[78,79] For these three compounds the space group is determined to be D_{4h}^{17} [I4/mmm] with two formula units in a crystallographic unit cell. The a-axis is ≈3.90 Å for all these compounds, while the c-axis increases from 13.71 to 20.3 to 28.1 Å as the number of perovskite blocks increases from one to two to three, respectively. The first two compounds were prepared by Ruddlesden and Popper.[78,79] They also tried to prepare $Sr_4Ti_3O_{10}$ but it was found associated with $SrTiO_3$ and $Sr_3Ti_2O_7$. The proportion of $Sr_4Ti_3O_{10}$ depended on the firing schedule. This compound was prepared in pure form for the first time by MacCarthy et al.[80] by firing appropriate amounts of TiO_2 and SrO over a week at 1475°C, with several intermediate regrindings.

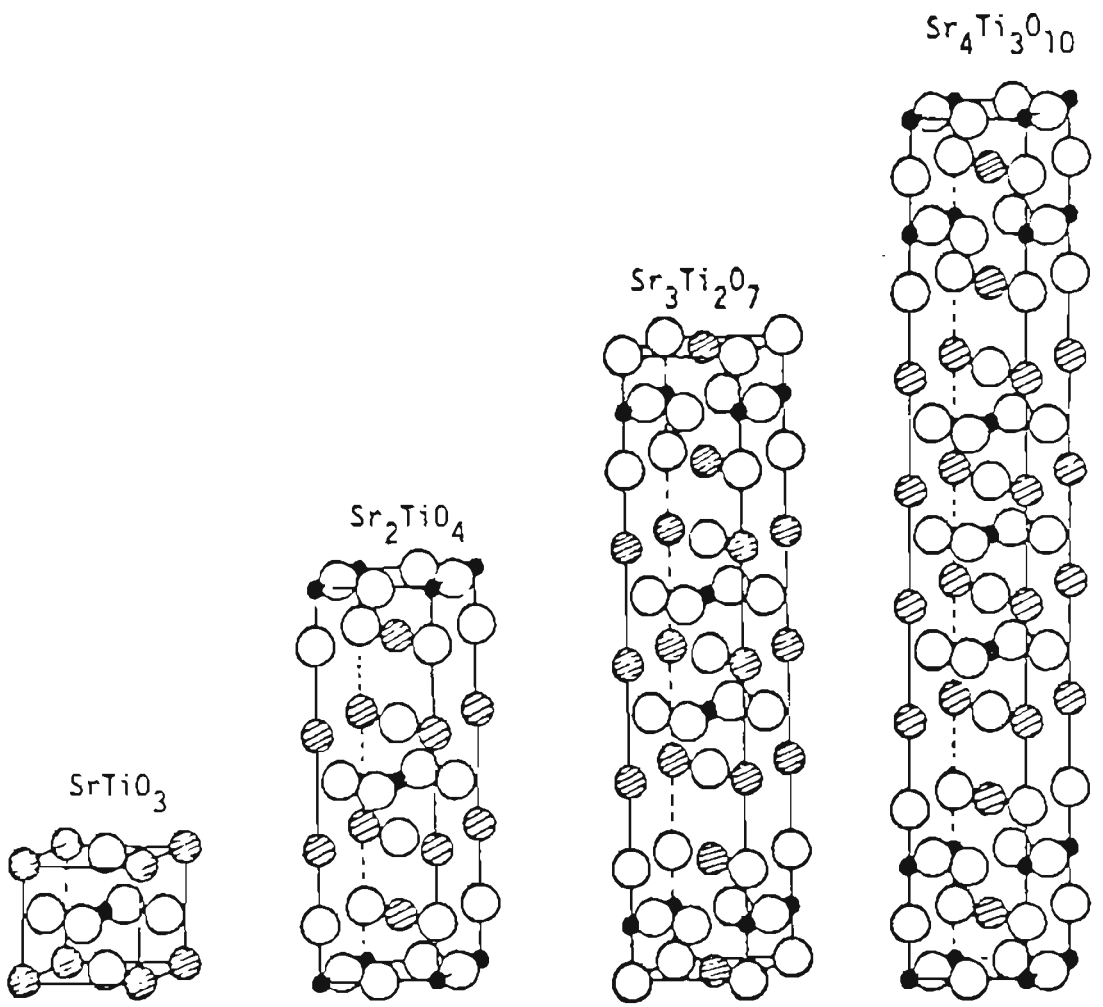

Figure 18. STRUCTURES OF $SrTiO_3$, Sr_2TiO_4, $Sr_3Ti_2O_7$, and $Sr_4Ti_3O_{10}$.

No detailed investigation regarding the vibrational spectra of these compounds have been reported. However, we note the results of the factor group analysis for these three compounds given by White and Kermidas.[81] The observed Raman spectra were not discussed in terms of the results obtained from factor group analysis for these compounds. The same authors proposed that coordination of titanium is octahedral. Infrared absorption characteristics for Sr_2TiO_4 were examined by Tarte.[82] He also concluded that oxygen is coordinated around titanium octahedrally. No such vibrational spectra were investigated or factor group analysis made for the compounds in the series $nSrTiO_3 \cdot SrO$ with $n>3$.

3. OBJECTIVES

From the discussion of imperfections in oxides it is evident that disorder in the systems of interest [$SrTiO_3$, and donor-and acceptor-doped $SrTiO_3$] may be determined by measuring the electrical conductivity as a function of oxygen partial pressure and temperature.

The results of Tofield and Scott[26] indicate that lanthanum is soluble only in very small amounts in $SrTiO_3$. Based on this they suggested that there is no range of nonstoichiometry in the lanthanum-doped $SrTiO_3$. First we will try to establish the solubility limit of lanthanum in $SrTiO_3$ by employing a special sample preparation technique, namely the "liquid mix technique".[27,83] In order to see how the donor dopants are compensated in $SrTiO_3$, thermogravimetric measurements will be performed by equilibrating the sintered pellets of the lanthanum doped $SrTiO_3$ at a fixed high temperature and oxygen partial pressure, and by quenching and weighing in a conventional microbalance. By the gravimetric measurements we can find the agreement between the calculated amount of oxygen necessary to compensate the donor-dopant and the measured reversible oxygen weight change between the oxidized state at one atmosphere oxygen and the reduced state established by a CO/CO_2 gas mixture.

Electrical conductivity measurements will be carried out in lanthanum-doped samples as a function of oxygen partial pressure and temperature, to distinguish the region of ionic and electronic compensations. Such measurements are planned for the undoped and acceptor doped $SrTiO_3$ in order to characterize the defect models. It is noted in Chapter I that

in $BaTiO_3$, any deviation from the ideal Ba/Ti ratio is accomplished by the formation of neutral vacancy pairs (V''_{Ba} $V^{\cdot\cdot}_{O}$).[20] In this work, we will be verifying the above result in $SrTiO_3$ by measuring high temperature electrical conductivity.

For $SrTiO_3$, there are presently two schools of thought that assign the Raman spectrum either to first-order or to second-order. Observation of Raman spectra at various temperatures will help to resolve this controversy. The low temperature spectrum of $SrTiO_3$ will permit the observation of the additional first-order modes allowed in the tetragonal phase, since $SrTiO_3$ undergoes a cubic to tetragonal phase transition around 110 K. Raman spectral measurements as a function of temperature are planned for $SrTiO_3$.

The existence of ordered members of the series $nSrTiO_3 \cdot SrO$ (Ruddlesden-Popper phases) will be studied for different values of n by preparing the samples by the liquid mix technique. These samples will be studied by X-ray powder diffraction and Raman spectroscopy techniques. A detailed factor-group analysis is planned for the Ruddlesden-Popper phases and the observed Raman spectra will be interpreted on the basis of the factor-group analysis results.

4. EXPERIMENTAL PROCEDURE

4.1 Sample Preparation

The samples used in this investigation were prepared by a "liquid mix technique".[27,83,84] It is important to prepare thermodynamically-defined samples so that any measurements made on them will be meaningful. In a single phase binary oxide the compound is unambiguously defined if the activity of one of the components, oxygen partial pressure, is known and the temperature is sufficiently high to establish thermodynamic equilibrium with the oxygen-containing atmosphere. For oxides with more than two components, additional variables must be determined in order to unambiguously define the system. For a ternary oxide, two independent variables in addition to temperature and total pressure must be taken into account. In addition to the oxygen activity one could fix the activity of one of the cations or the ratio of the two cations. If the additional variable is not fixed, the thermodynamic state of the ternary oxide is not defined, and the measurements of any disorder phenomena are generally meaningless.[85]

When the cations are not volatile one may equilibrate the ternary compound with an excess of either cation at the two respective phase boundaries. This technique only allows the study of the edges of the single-phase region and limits the experimental techniques to those that are not restricted by the existence of a two-phase mixture. A technique has been

established[27,83,84] by which it is possible to know the non-volatile cationic stoichiometries of the major and minor constituents to within a few parts per million precision (0.001%) and thereby thermodynamically define the system in question to this precision.

This preparation technique is based upon having the individual cations complexed in separate weak organic acid solutions or available in salts that are soluble in the weak organic acid solutions. The individual solutions or soluble salts are gravimetrically analyzed for the respective cation concentration to a precision of better than ten parts per million. In this way it is possible to precisely control all of the cation concentrations and to mix the ions on an atomic scale in the liquid state. There is no precipitation in the mixed solutions, as they are evaporated to the rigid polymeric state in the form of a uniformly colored transparent glass. The glass retains homogeneity on an atomic scale, and may be calcined at a relatively low temperature (of only a few hundred degrees Celsius) to the homogeneous single phase oxide of precise stoichiometry and particle size of a few hundred angstroms.

This technique of liquid mix is quite dintinct from processes involving precipitation from precursors.[86,87] Pyrolysis of these precipitates is a distinct improvement over solid state reaction of the simple oxides or salts of the various cations at high temperatures; however, the precipitation from a precursor suffers from a restriction imposed by stoichiometric requirements of the complex salt with several cations and lack of homogeneity during the precipitation process.[84]

By using the technique of "liquid mix" one may prepare multicomponent oxides with as high a purity as the starting materials (no subsequent milling is required), homogeneity on the atomic scale, and with a very small particle size of a few hundred angstroms.

The requirements for the "liquid mix technique" to be successful are that the particular cation solutions be stable with respect to time at room temperature and stable when mixed together and heated near the boiling point of the solvent. Solutions of cations complexed in an ethylene glycol-citric acid solvent have been found to satisfy these requirements. They do not precipitate or disproportionate either on storage or when evaporated to the state of a rigid polymeric glass.

Required amounts of strontium carbonate (Johnson-Matthey Corp., Spec. Pure) lanthanum carbonate (Rare-Earth Division, Spec. Pure) and tetra isopropyl titanate solution (Dupont Co., Tyzor) according to the general formula $La_xSr_{1-x}TiO_3$ were dissolved in an ethylene glycol-citric acid solution. The rigid transparent polymeric glassy samples obtained by slow evaporation of the solution were then calcined at 1350°C in air for a period of 8 to 12 hours. Strontium titanate with different Sr/Ti ratios were prepared by the same technique using strontium carbonate and tetra isopropyl titanate solution. Ferric nitrate and aluminum nitrate dissolved in ethylene glycol-citric acid complex formed the source for acceptor dopings.

4.2 X-ray Powder Diffraction

X-ray diffraction analysis of the samples were performed using the Debye-Scherrer powder technique. Samples were ground and loaded into the tip of a 0.2 mm diameter glass needle and aligned in a Siemens Debye-Scherrer powder camera having a diameter of 57.3 mm. The radiation used was a nickel filtered CuK_{α}. A lighted film measuring device was used to measure the linear diffraction length of the reflections, which were recorded to 0.005 mm. Front reflections were used to identify the phases and both front and back reflections were used to determine lattice parameters.

4.3 Thermogravimetric Measurements

For gravimetric measurements, the pure and lanthanum doped strontium titanate powders were first pressed into small pellets of weight ≈150 mg and sintered at 1350°C for about 12 hours in air. These sintered pellets were suspended in the furnace by means of a basket made with platinum mesh. Gravimetric measurements were carried out at 1050°C. The samples were equilibrated in oxygen or carbon dioxide/carbon monoxide mixtures for the oxidized and reduced states, respectively, and quenched in the ambient gas by raising the platinum basket rapidly to a cooler part of the furnace-reaction tube assembly. The CO/CO_2 mixture was adjusted to

provide oxygen partial pressure of 10^{-15} atm. at the equilibration temperature. All the gases were metered and cleaned as explained in the following section.

All gravimetric measurements were made at room temperature on at least duplicate samples on a Cahn Model 4100 microbalance. Each sample was subjected to at least six cycles of oxidation and reduction and the average value was taken as the reversible weight change. All the oxidized samples were bright yellow in color whereas the reduced samples were dark and semiconducting.

4.4 Gas Preparation

The oxygen partial pressure surrounding the sample was controlled by flowing metered mixtures of gases past the sample. For thermogravimetric measurements, the gases employed were oxygen and carbon dioxide-carbon monoxide mixtures. The following gases were used to establish desired oxygen partial pressures in the electrical conductivity measurements: argon, oxygen, carbon dioxide, carbon monoxide, hydrogen and tank gases of various argon-oxygen mixtures with analysis for oxygen. The argon was passed successively through tubes containing copper turnings at 450°C, magnesium perchlorate, ascarite and magnesium perchlorate. The copper turnings at 450°C were used to remove oxygen, since copper reacts with oxygen according to the reaction,

$$2Cu_{(s)} + 1/2\ O_2\ (g) \rightleftharpoons Cu_2O_{(s)}$$

From the available thermodynamic data, the equilibrium oxygen partial pressure for the above reaction can be estimated. At 450°C, the P_{O_2} is 2.1×10^{-16} atm. and at 600°C, it is 7.8×10^{-13} atm. The removal of oxygen from argon is more effective as the temperature of copper turnings are lowered. Kinetics becomes a problem as the temperature is decreased and a balance has to be reached between the thermodynamic and kinetic problems. An optimum temperature of 450°C is used in this work. The magnesium perchlorate removed moisture and ascarite was used to remove carbon dioxide. The oxygen and argon-oxygen mixtures were passed through successive tubes containing magnesium perchlorate, ascarite and magnesium perchlorate. The carbon dioxide was passed through tubes containing drierite, copper turnings at 450°C and drierite. The drierite was employed to remove moisture. Carbon monoxide was passed through tubes containing magnesium perchlorate, ascarite and magnesium perchlorate. Hydrogen was passed through drierite, copper turnings at 450°C and silica gel. Silica gel removed moisture from the hydrogen gas. A schematic diagram of the all glass gas-cleaning and metering train is shown in Figure 19.

All gases were metered with conventional manometric flow meters using capillary constructions and di-butyl phthalate in the two arms of the manometer as well as the gas blow-off column. Adjustment of the level of the fluid in the gas blow-off column determined the pressure drop across the capillary which was read from the manometer. Calibration of the flow rates of the various capillaries as a function of pressure drop was performed by measuring the displacement of a bubble interface in a

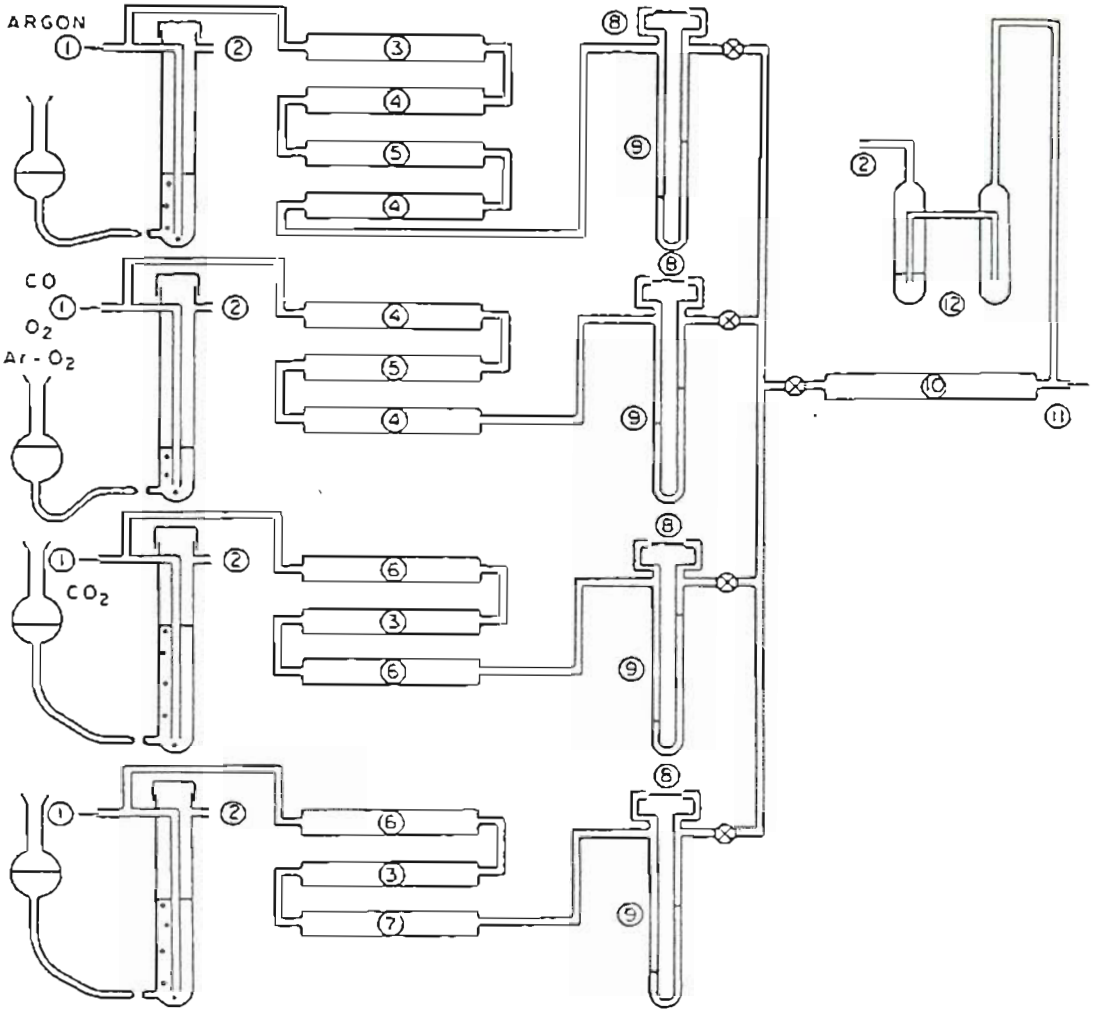

Figure 19. SCHEMATIC DIAGRAM OF THE GAS CLEANING AND METERING TRAIN.

graduated burrette. The rate of flow of a gas through a capillary is dependent upon its viscosity.

After the gases had been metered, they are passed through a mixing chamber of glass beads to insure a completely uniform mixing before entering the furnace. The gases entered at the bottom of the vertical-reaction tube assembly and exited at the top through a stop-cock and finally exited through a di-butyl phthalate bubbler. The furnace reaction tube assembly consisted of a mullite tube to which were sealed pyrex standard taper joints.

4.5 Establishment of Low oxygen Partial Pressures

Low oxygen partial pressures may be obtained from CO_2/CO and/or CO_2/H_2 gas mixtures. The oxygen partial pressure has been calculated according to the available data of standard free energy for the formation of CO, CO_2 and H_2O. The reactions involved in obtaining the oxygen partial pressures are:

$$CO_2 \rightleftharpoons CO + 1/2\ O_2 \tag{69}$$

and

$$CO_2 + H_2 \rightleftharpoons CO + H_2O \tag{70}$$

4.5.1 CO_2-CO Mixtures.

a) Physico-Chemical Considerations:

If n_1 mole fractions of carbon dioxide are mixed with n_2 mole fractions of carbon monoxide, and subsequently a fraction "a" of the carbon dioxide molecules dissociates to form free oxygen and carbon monoxide according to reaction (69)

$$CO_2 \rightleftharpoons CO + 1/2\ O_2 \tag{69}$$

the mole fraction of carbon dioxide left is $n_1(1-a)$, the mole fraction of oxygen formed is $1/2\ an_1$, and the mole fraction of carbon monoxide present is $n_2 + an_1$. Hence, the total number of fractions in the gas mixture is: $n_t = n_1(1 + a/2) + n_2$. For a total pressure of one atmosphere the partial pressures of the three chemical species are:

$$P_{CO_2} = 2n_1(1-a)/[n_1(2+a) + 2n_2]$$

$$P_{CO} = 2(an_1 + n_2)/[n_1(2+a) + 2n_2]$$

$$P_{O_2} = an_1/[n_1(2+a) + 2n_2]$$

or in terms of the mixing ratio $R_m = n_2/n_1$ for CO/CO_2 mixtures:

$$P_{CO_2} = 2(1-a)/[2 + a + 2R_m] \tag{71}$$

$$P_{CO} = 2(a + R_m)/[2 + a + 2R_m] \tag{72}$$

$$P_{O_2} = a/[2 + a + R_m] \tag{73}$$

At equilibrium the partial pressures of carbon dioxide, carbon monoxide, and oxygen are related through the equilibrium constant:

$$K_{69} = P_{CO}\, P_{O_2}^{1/2}/P_{CO_2} \tag{74}$$

From equations (71) and (72), "a" may be eliminated and expressed in terms of K_{69} and the oxygen partial pressure:

$$P_{CO_2}/P_{CO} = (1-a)/(a + R_m) = P_{O_2}^{1/2}/K_{69}$$

$$a = [K_{69} - R_m P_{O_2}^{1/2}]/[K_{69} + P_{O_2}^{1/2}] \tag{75}$$

One may now substitute "a" into equation (73) and obtain a relationship between the mixing ratio, R_m, the equilibrium constant, K_{69}, and the oxygen partial pressure, P_{O_2}.

$$R_m = [K_{69}-3K_{69}P_{O_2}-2P_{O_2}^{3/2}]/[2K_{69}P_{O_2}+P_{O_2}+P_{O_2}^{3/2}+P_{O_2}^{1/2}] \tag{76}$$

From this equation one may compute what mixing ratio of carbon monoxide to carbon dioxide is required to produce a given oxygen partial pressure at a given temperature. Alternately one may compute the volume percent of carbon dioxide from R_m:

$$\text{vol. \% } CO_2 = 100/(1 + R_m) \text{ \%} \tag{77}$$

The control of the oxygen partial pressure with the aid of reaction (69) is no longer possible if the oxygen pressure is equal to or falls below the equilibrium oxygen pressure of the reaction:

$$CO \rightleftharpoons C + O_2 \tag{78}$$

If this is the case, carbon precipitation will occur. The equilibrium oxygen partial pressure for reaction (78), $\bar{P}_{O_2}$, may be computed from the equilibrium constant of reaction (78), and the existing partial pressure of carbon dioxide.

$$K_{78} = \bar{P}_{O_2}/P_{CO_2}$$

$$P_{O_2} = K_{78}P_{CO_2} \tag{79}$$

Hence, the deposition of carbon will occur if:

$$P_{O_2} \leqslant \bar{P}_{O_2}$$

The equilibrium constant K_{78} may be evaluated from the data for the free energy of formation of carbon dioxide in the JANAF (88) tables: the partial pressure of carbon dioxide may be determined from equation (71) after an evaluation of "a" from equation (75).

b) Computations:

The change in free energy for reaction (69), ΔG_1° was computed as a function of temperature from the free energy of formation data for CO and CO_2 in the JANAF (88) tables. From the free energy change of a reaction the equilibrium constant for that reaction may be computed as follows:

$$K_{69} = \exp\ [\Delta G_1^\circ/RT] \tag{80}$$

The dependence of K_{69} on temperature is given in Figure 20. The free energy charge, ΔG_2°, for reaction (78) was computed in the same way from JANAF (88) tables. From ΔG_2° the equilibrium constant for reaction (78) may be determined according to equation (80).

For a given temperature, K_{69} and K_{78} were evaluated. The mixing ratio, R_m, required to produce the desired oxygen partial pressure was then computed from equation (76) and the volume percent of carbon dioxide in the initial gas mixture from equation (77). Subsequently $\overline{P}_{O_2}$ was determined from equation (79), after having evaluated P_{CO_2} by computing "a" from equation (75) and substituting the value into equation (71). It was then tested whether the desired oxygen partial pressure was equal to or smaller than $\overline{P}_{O_2}$. If the test was positive, i.e., $P_{O_2} \leq \overline{P}_{O_2}$ then the precipitation of carbon would occur from the gas mixture and hence oxygen partial pressures equal to or less than that P_{O_2} cannot be established at the temperature of consideration using CO_2/CO mixtures.

Figure 21 shows schematically the volume percent isopleths summarizing P_{O_2} - T calculations based on JANAF-based data for $CO-CO_2$ mixtures. The carbon deposition as elucidated before, is indicated by shading in the graph.

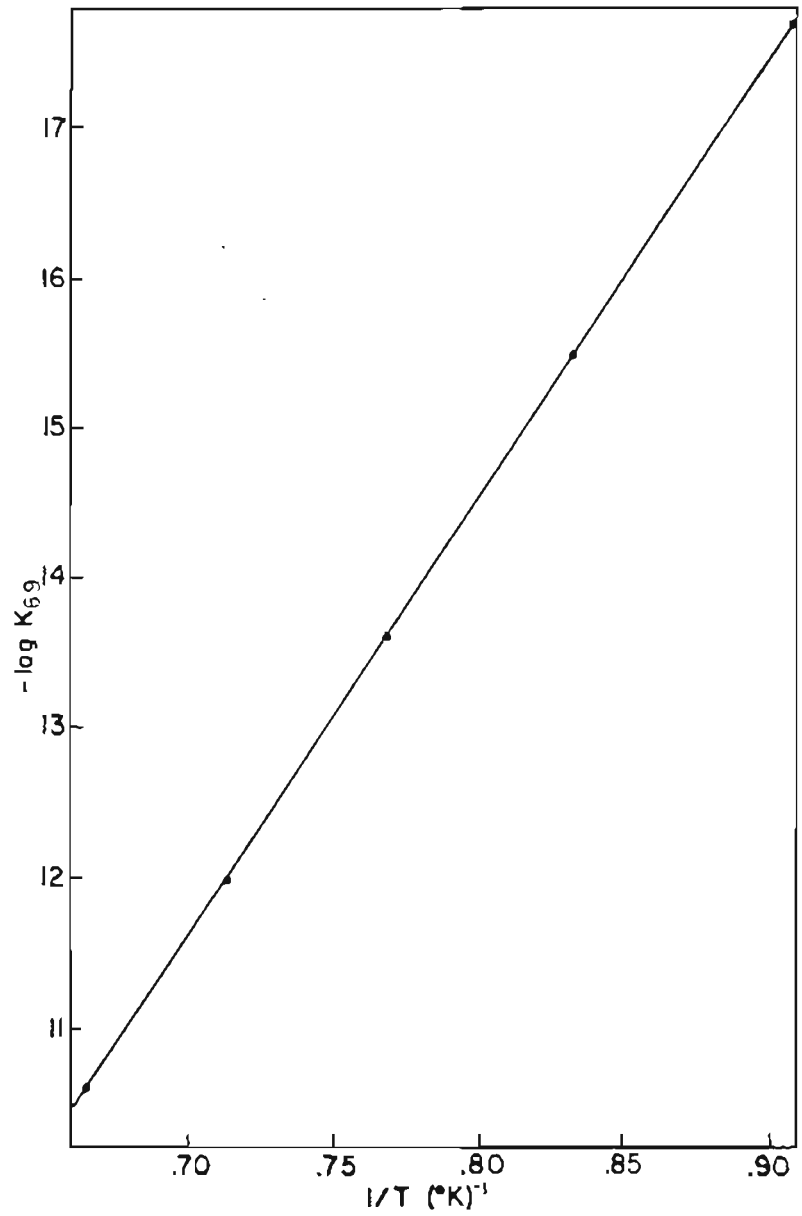

Figure 20. THE DEPENDENCE OF THE EQUILIBRIUM CONSTANT, K_{69}, FOR THE REACTION $CO_2 \rightleftharpoons CO + 1/2\ O_2$.

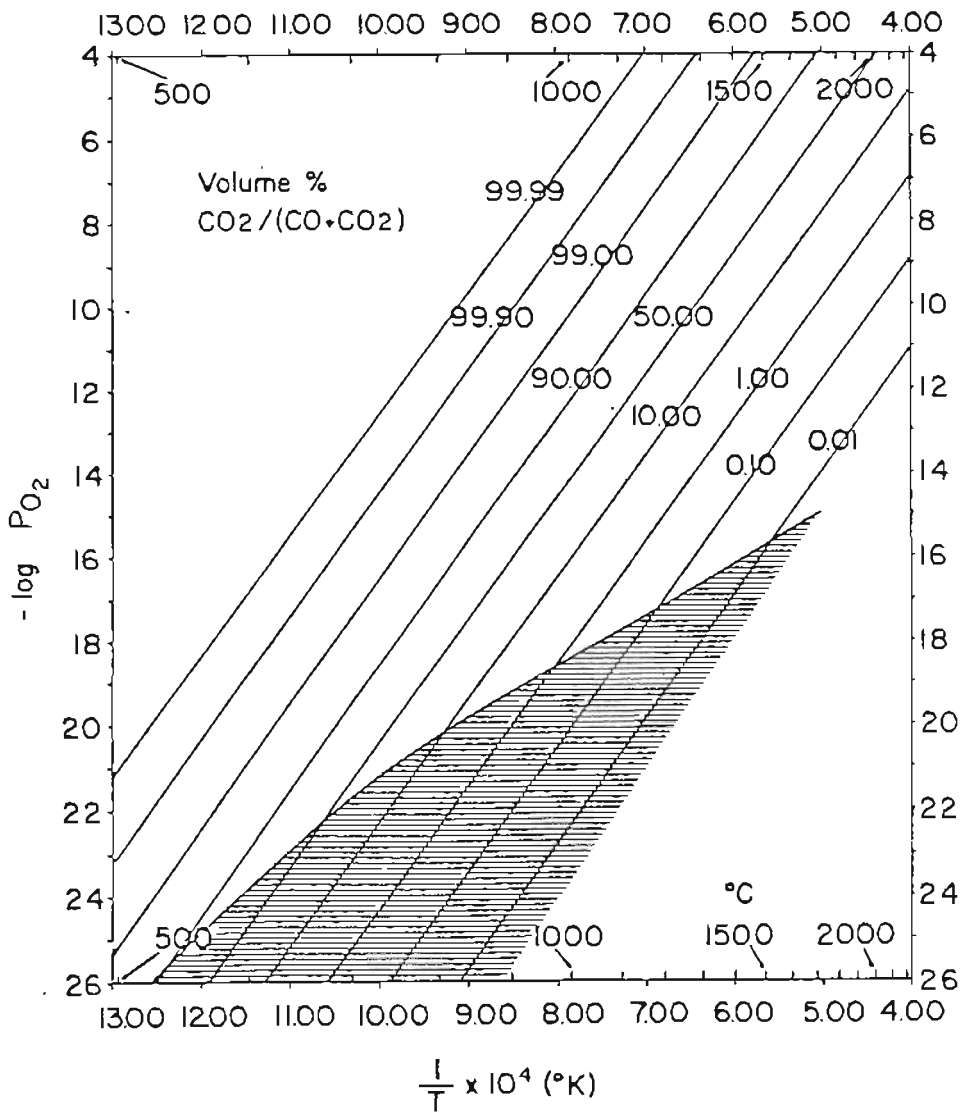

Figure 21. VOLUME PERCENT ISOPLETHS SUMMARIZING P_{O_2}-T CALCULATIONS BASED ON JANAF DATA FOR CO_2-CO MIXTURES. SHADED AREA IS PROHIBITED BY THE PRECIPITATION OF CARBON AS EXPLAINED IN THE TEXT.

4.5.2 H_2-CO_2 Mixtures.

a) Chemical Considerations:

Let n_1 fractions of carbon dioxide be mixed with n_2 mole fractions of hydrogen, and subsequently let carbon dioxide dissociate to form carbon monoxide and oxygen according to reaction (69), and let hydrogen react with oxygen to form water,

$$H_2 + 1/2\ O_2 \rightleftharpoons H_2O \tag{81}$$

If a fraction "a" of each mole of carbon dioxide dissociates to form oxygen, and the fraction "b" of each mole of hydrogen reacts to form water, then the mole fraction of carbon dioxide left will be n_1 (1-a), the mole fraction of carbon monoxide formed is $n_1 a$, the number of mole fraction of hydrogen left is n_2 (1-b), and the number of mole fractions of oxygen present is 1/2 (n_1 a - n_2 b). The total number of mole fractions present are:

$$n_t = n_1\ (1 + a/2) + n_2\ (1 - b/2)$$

For a total pressure of one atmosphere and with the mixing ratio defined for the H_2/CO_2 mixtures as $R_m = n_2/n_1$, the partial pressures of the five components present may be expressed as follows:

$$P_{CO_2} = 2\ (1-a)\ /\ [2 + a + R_m(2-b)] \tag{82}$$

$$P_{CO} = 2a\ /\ [2 + a + R_m(2-b)] \tag{83}$$

$$P_{H_2} = 2R_m (1-b) / [2 + a + R_m(2-b)] \quad (84)$$

$$P_{H_2O} = 2R_m b / [2 + a + R_m(2-b)] \quad (85)$$

$$P_{O_2} = (a-bR_m) / [2 + a + R_m(2-b)] \quad (86)$$

from which "a" may be expressed with the aid of equations (82) and (83) and the equilibrium constant K_{69} (equation 74)

$$P_{CO_2}/P_{CO} = (1-a)/a = P_{O_2}^{1/2}/K_{69}$$
$$a = K_{69}/ [K_{69} + P_{O_2}^{1/2}] \quad (87)$$

and from which "b" may be expressed with the aid of equations (84) and (85) and the equilibrium constant K_{88} from the following:

$$H_2O \rightleftharpoons H_2 + 1/2\ O_2 \quad (88)$$

$$K_{88} = P_{H_2} \cdot P_{O_2}^{1/2} / P_{H_2O} \quad (89)$$

$$P_{H_2O}/P_{H_2} = b / (1-b) = P_{O_2}^{1/2}/K_{88} \quad (90)$$

$$b = P_{O_2}^{1/2} / [K_{88} + P_{O_2}^{1/2}] \quad (91)$$

Hence, for any given temperature (which determines the values of K_{69} and K_{88}) and any desired oxygen partial pressures, the fractions "a" and "b" may be computed from equations (87) and (91).

We may now express R_m in terms of "a", "b", and P_{O_2} with the aid of equation (86):

$$R_m = [a\ (1-P_{O_2}) - 2P_{O_2}] \ /\ [b\ (1-P_{O_2}) + 2\ P_{O_2}] \qquad (92)$$

Hence, if we wish to determine the mixing ratio of hydrogen to carbon dioxide which is required to produce a desired oxygen partial pressure, we evaluate "a" and "b" from equation (87) and (91) at that temperature and use equation (92) to compute the necessary mixing ratio to produce the desired oxygen partial pressure.

In this system, the control of the oxygen partial pressure through variation of the mixing ratio H_2/CO_2 is also no longer possible if the oxygen partial pressure is equal to or falls below that of the equilibrium oxygen pressure for reaction (78), thereby causing carbon precipitation. Again the condition for carbon precipitation is:

$$P_{O_2} \leqslant \bar{P}_{O_2}$$

The value of $\bar{P}_{O_2}$ can be computed from the equilibrium constant K_{78} and the partial pressure of carbon dioxide. The latter may be determined from equation (82), since "a", "b", and R_m are known.

As indicated by French,[89] the mixing of hydrogen and carbon dioxide could also involve the formation of methane according to:

$$CO + 3H_2 \rightleftharpoons CH_4 + H_2O \tag{93}$$

or

$$2CO + 3H_2 \rightleftharpoons CH_4 + CO_2 \tag{94}$$

Both reactions (93) and (94) have negative values of ΔG° below about 900 K. Since methane can react with oxygen according to:

$$CH_4 + 2O_2 \rightleftharpoons CO_2 + 2H_2O \tag{95}$$

to form water and carbon dioxide, the presence of methane could influence the calculated oxygen partial pressure.

The equilibrium partial pressure of methane for reaction (93) is given by:

$$\overline{P}_{CH_4} = K_{93}\, P_{CO}\, P_{H_2}{}^3/P_{H_2O} \tag{96}$$

for reaction (94) by:

$$\overline{\overline{P}}_{CH_4} = K_{94}\, P^2_{CO}\, P_{H_2}{}^3/P_{CO_2} \tag{97}$$

and for the reaction (95) by:

$$P_{CH_4} = P^2_{H_2O}\, P_{CO_2}/K_{95}\, P^2_{O_2} \tag{98}$$

K_{93}, K_{94}, and K_{95} are the equilibrium constants for reactions (93), (94), and (95). Oxygen will be consumed by reaction (95) as soon as the partial pressure P_{CH_4} or $\overline{\overline{P}}_{CH_4}$ is in excess of P_{CH_4}, i.e., when

$\overline{P}_{CH_4} \geqslant P_{CH_4}$ or $\overline{\overline{P}}_{CH_4} \geqslant P_{CH_4}$

b) Computations:

For a given temperature, the six equilibrium constants were calculated from ΔG_1° through ΔG_6° with the aid of equation (80), and "a" and "b" were determined from equations (87) and (91). R_m was computed from (92), and with the aid of "a", "b", and R_m, the partial pressures of carbon dioxide, of carbon monoxide, of hydrogen, and of water were evaluated from equations (82) through (85). Subsequently, using these determined values for P_{CO_2}, P_{CO}, P_{H_2}, P_{H_2O} and the given value of P_{O_2} as well as the equilibrium constants, evaluation of the values of $\overline{P}_{O_2}$, $\overline{P}_{CH_4}$, $\overline{\overline{P}}_{CH_4}$, and P_{CH_4} were performed from equations (79), (96), (97) and (98). Control of the oxygen partial pressure through variation of the mixing ratio H_2/CO_2 is no longer possible when any one of the inequalities

$P_{O_2} \leqslant \overline{P}_{O_2}$

$\overline{P}_{CH_4} \geqslant P_{CH_4}$

$\overline{\overline{P}}_{CH_4} \geqslant P_{CH_4}$

was fulfilled.

Figure 22 shows the volume percent isopleths summarizing P_{O_2}-T calculations based on JANAF (88) data for H_2/CO_2 mixtures.

The region prohibited by the precipitation of carbon or the formation of methane is shown by shading in the Figure 25. In all cases it was assumed that the gases behaved ideally, that is, their respective partial pressures were equal to their volume fractions in the flowing gas stream.

4.6 Temperature Control

Each furnace employed in this investigation consisted of a winding of either Kanthal or platinum-40% Rhodium around an alumina tube around which was an insulating material which in turn was contained within a metal sleeve (Figure 23). The platinum-40% Rhodium wound furnace was used in the thermogravimetric measurements and the Kanthal wound furnace was used for the electrical conductivity measurements. In both cases the furnace winding was continuous so as to provide evenly spaced taps from the winding to the exterior of the furnace. These taps could then be shunted to adjust the temperature gradient within the furnace.

The temperature was measured with a platinum-platinum 10% Rhodium thermocouple. The hot zone of the furnace varied by ±1°C during an on-off cycle of the furnace controller. It was found that the temperature in the center of the hot zone within the furnace reaction tube was uniform in cross-section and did not change when the gases were flowing. The temperatures reported should, therefore, be accurate to ±1°C.

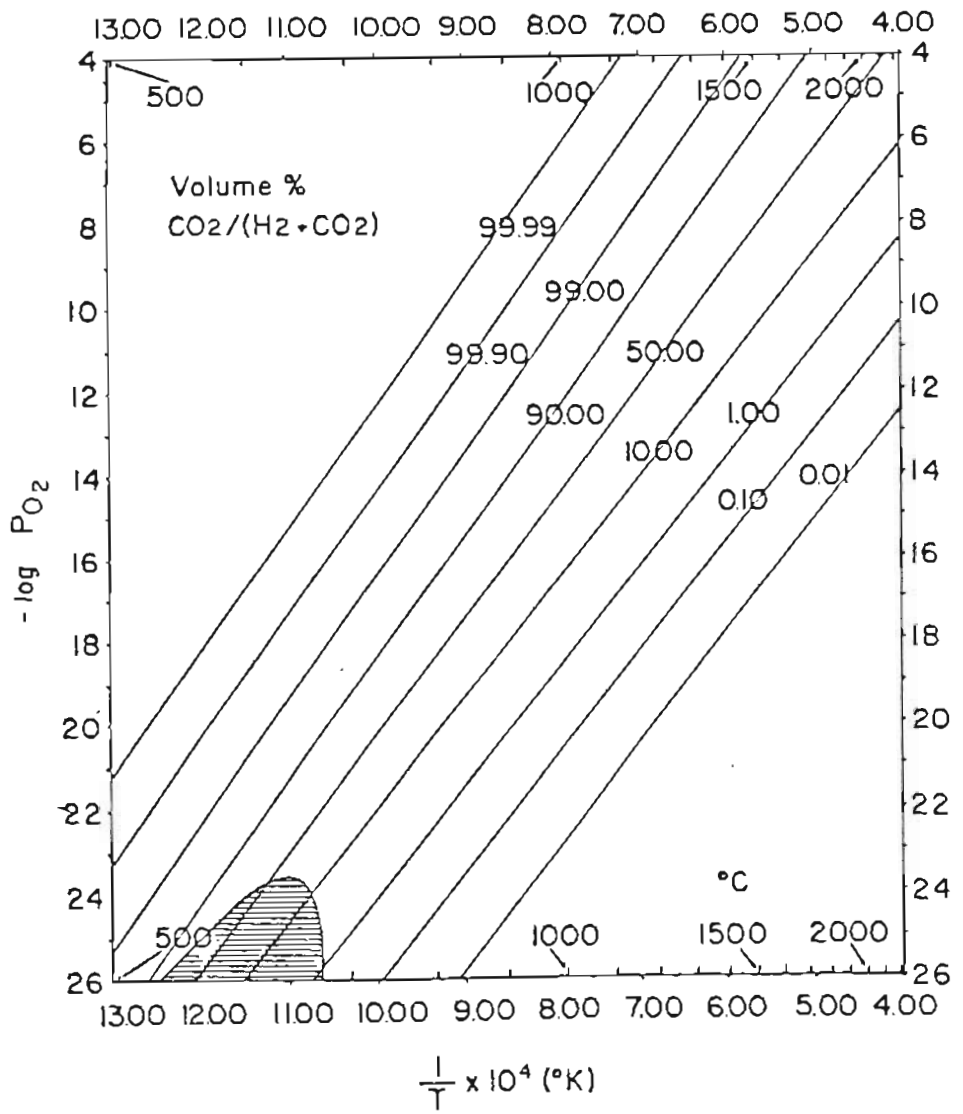

Figure 22. VOLUME PERCENT ISOPLETHS SUMMARIZING P_{O_2}-T CALCULATIONS BASED ON JANAF DATA FOR CO_2-H_2 MIXTURES. THE SHADED AREA IS PROHIBITED BY THE PRECIPITATION OF CARBON OR THE FORMATION OF METHANE AS EXPLAINED IN THE TEXT.

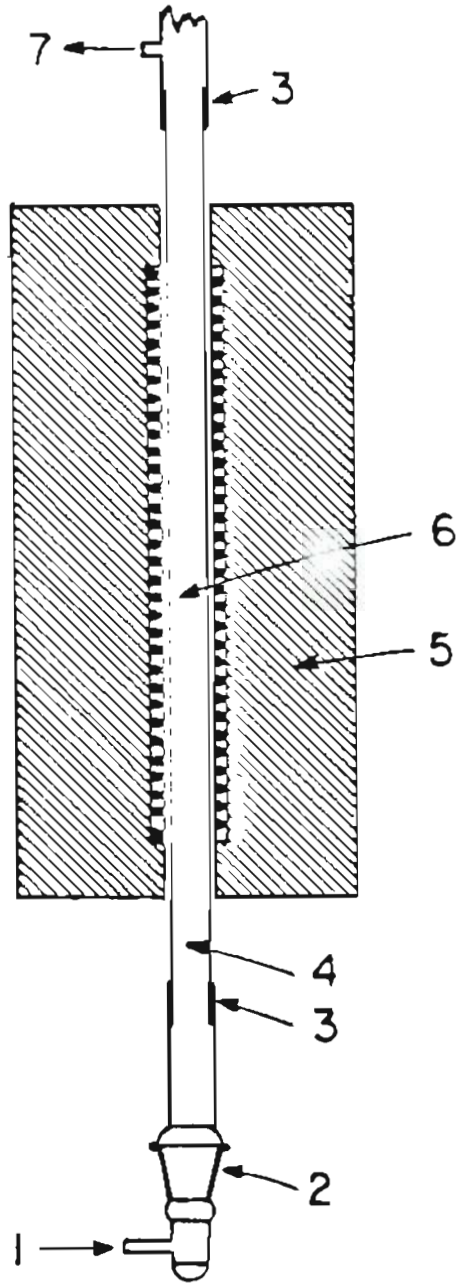

Figure 23. FURNACE REACTION TUBE ASSEMBLY. 1) GAS INLET, 2) STANDARD PYREX TAPER JOINT, 3) PYREX-MULLITE SEAL, 4) MULLITE TUBE, 5) FURNACE, 6) HOT ZONE, AND 7) GAS OUTLET.

4.7 Electrical Conductivity Measurements

The powder samples prepared by the liquid mix technique were pressed under a load of 40,000 psi to either a thin rectangular slab (21 x 6 x 0.5 mm) or a circular disc of 1.25 cm diameter, and sintered in air at 1350°C for about 12 hours. Conductivity specimens were cut from this sintered slab/disc using an airbrasive (S. S. White Industrial airbrasive unit model-F) unit. Each specimen was wrapped with four 0.25 mm platinum wires for electrical contacts. Small notches were cut in the edges of the sample to aid in holding the platinum wires in place. The spacings of the two inner-most wires were measured, and the cross-section area to length ratio (a/ℓ) was calculated.

A conventional four-probe direct current technique was employed for all electrical conductivity measurements. The four platinum wires were insulated from one another by recrystallized high purity alumina insulators. A standard taper pyrex joint to which capillary tubes had been sealed was mounted on top of the furnace reaction tube assembly. The platinum wires exited through the capillary tubes, and were sealed vacuum tight into the tubes.

The conductivity was measured as a function of oxygen partial pressure in the temperature range 800-1050°C. The conductivity was determined by measuring the voltage across the potential probes (two inner-most wires) using a high impedance ($> 10^{10}$ ohm) digital voltmeter (Keithley 191 Digital Multimeter) and the calculated (a/ℓ) value for the sample. The current was supplied between the two outer leads by a constant current

source (Keithley 225 Current Source). The voltage was measured with the current in both forward and reverse directions, and the conductivity was calculated from the average values. All the measurements were taken when the sample was in complete thermodynamic and thermal equilibrium with the surrounding gas environment at a given temperature. Current was varied from 5 to 500μA and no significant change in conductivity was observed. There were no problems with short circuit paths through a sample holder since the platinum lead wires were also the specimen support.

4.8 Raman Spectral Measurements

The powder samples were placed in capillary tubes and supported by a sample holder for the back scattering geometry. A schematic diagram of the computer controlled laser Raman Spectrophotometer is shown in Figure 24. Radiation (4880Å) from a Coherent Radiation Laboratory Model-52 argon-ion laser served as the excitation wavelength and the scattered light was analyzed by a Jarrell-Ash 25-300 Raman Spectrophotometer equipped with an ITT FW-130 (S-20) or an RCA C31034 (Ga-As) photomultiplier, and a Hamner or ORTEC amplifier/discriminator. Photon counting was performed by the computer. The laser beam was focussed to < 1mm spot size on the capillary tube by a lens system, and the Raman scattered radiation was collected by an f 1.2 objective lens and focussed into the manochromator. An interactive graphics terminal (Tektronix, Inc., 4010-1) facilitated spectral analysis, such as rapid and accurate determination

of peak positions. The laser source provided well focussed, intense, monochromatic light. The improved electronic system of the Raman Spectrophotometer used in this work also permitted rapid corrections for spectral background near the laser line. Excellent stray light rejection of the manochromator and ghost-free gratings allowed the spectra to be examined quite close to the wavelength of the excitation source. Most of the spectra were obtained with a scan rate of 4 cm^{-1}/sec, and a spectral slit width of 2 cm^{-1}. Some of the spectra were run with a lower scan rate (1 cm^{-1}/sec) in order to show greater detail near the excitation line. Each sample was scanned as many as ten times and the summed spectra were recorded.

The Raman spectra above room temperature were obtained by using preheated nitrogen gas that was caused to flow through a transfer tube and around the sample. The temperature was maintained by monitoring the output of a calibrated chromel-alumel thermocouple which was attached in the gas stream close to the sample. The fine adjustment of the gas flow system controlled the temperature of the sample environment to ± 1k for the duration of the experiment. This arrangement was repeated from room temperature down to liquid nitrogen temperature with the same precision by controlling the flow of gas exchanging in a coil immersed in liquid nitrogen.

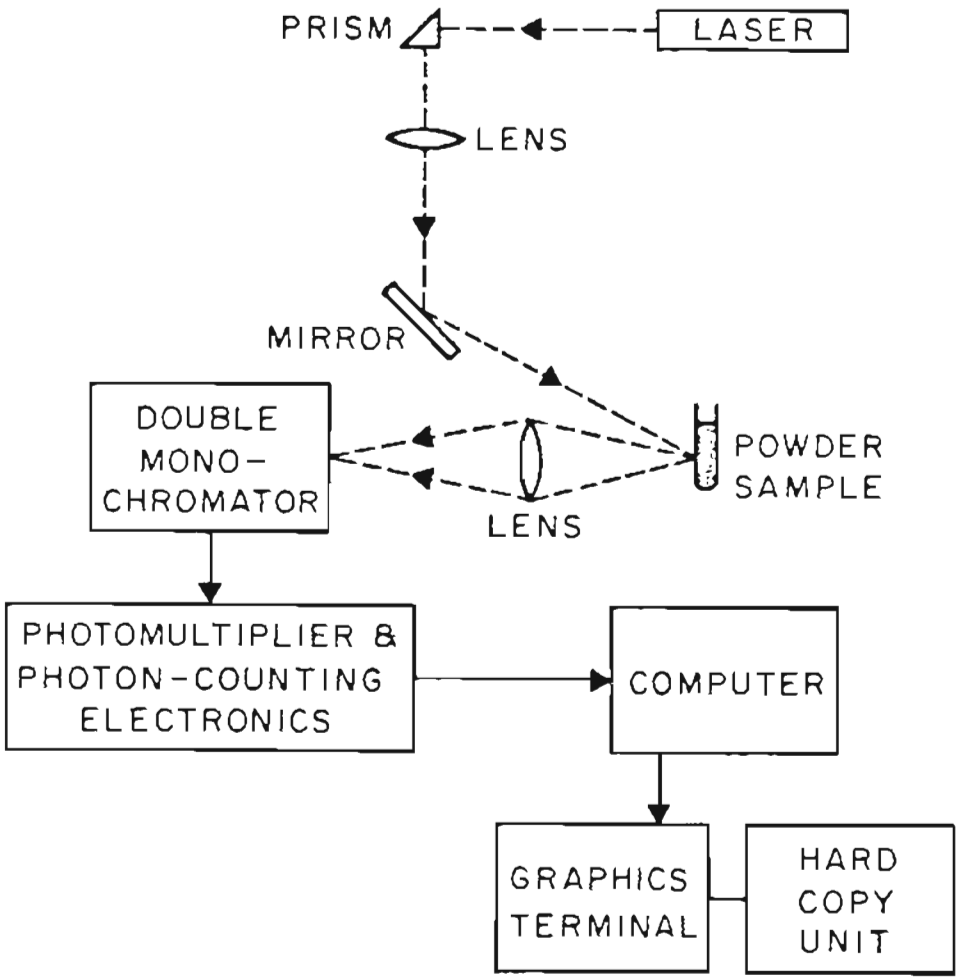

Figure 24. SCHEMATIC DIAGRAM OF THE COMPUTER-CONTROLLED LASER RAMAN SPECTROPHOTOMETER.

5. EXPERIMENTAL RESULTS AND DISCUSSION

5.1 Solubility of lanthanum in strontium titanate

Both the microscopic and the X-ray diffraction examination of the specimen of the composition $La_xSr_{1-x}TiO_3$ showed that an extensive region occurs in the system $SrO-TiO_2-La_2O_3$ in which the perovskite structure exists as a single phase. Single-phase cubic perovskite type solid solutions were obtained for all compositions containing up to 40 at.% of lanthanum (for samples heated at 1350°C in air). The lattice parameter decreased, as expected, with increasing lanthanum content as shown in Figure 28. There were no extraneous lines in the X-ray diffraction patterns for compositions up to 40 at.% lanthanum. The plot of a_o vs x (Figure 25) indicates a Vegard's law dependence within experimental error. The lattice parameters were obtained by the extrapolation method developed by Nelson and Riley.[90]

When the lanthanum exceeds 40 at.%, extra lines appeared in the X-ray diffraction pattern. These new reflections were all assignable to the phase $La_2Ti_2O_7$ described by MacChesney and Sauer.[91] The intensity of these new reflections of the $La_2Ti_2O_7$ phase increased as the lanthanum content was increased beyond 40 at.%. No evidence was found for the existence of the multiple-cell perovskite structure reported by Tien and Hummel.[24] They have shown that for the 80 mole % $La_{2/3}\square_{1/3}TiO_3$ composition in $SrTiO_3$, the observed d-spacings fit reasonably well with calculated d-spacings using the double-cell edge structure. There was no evidence

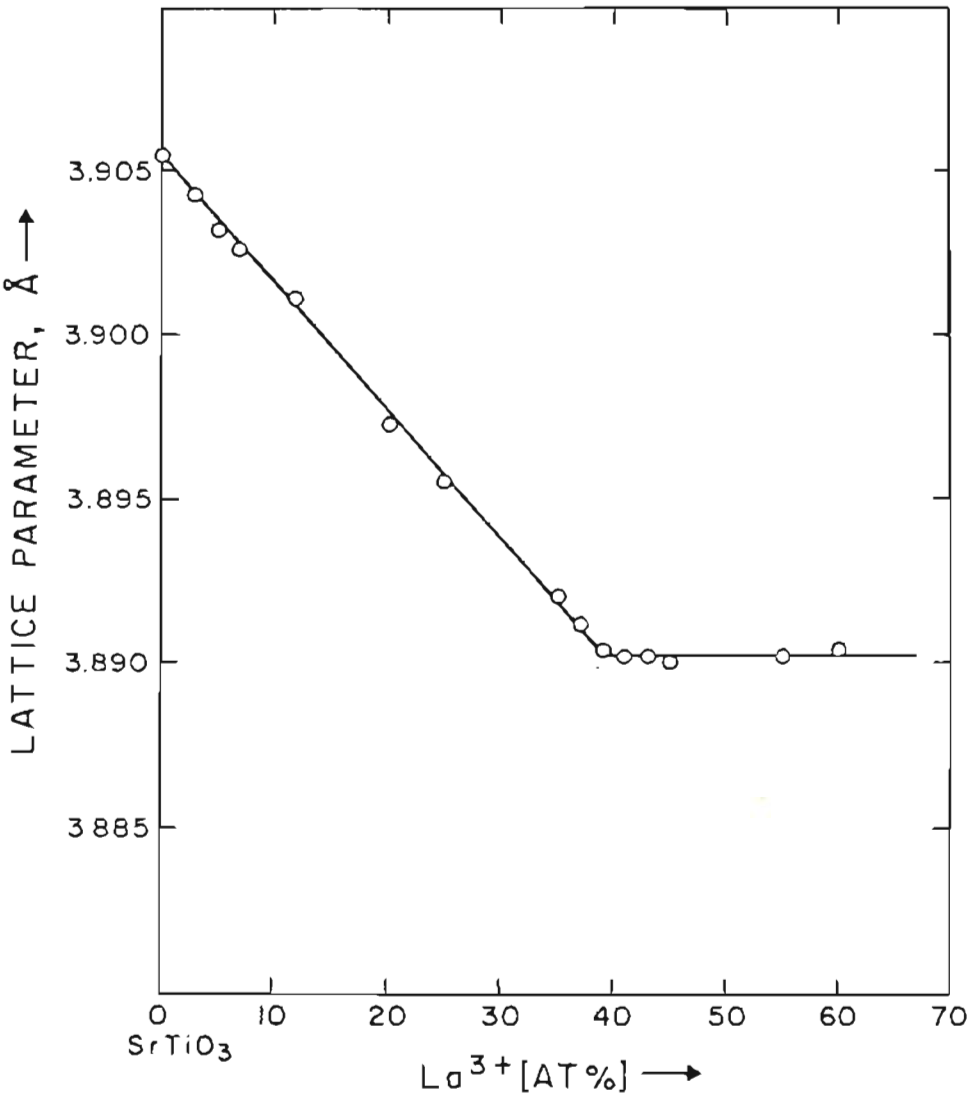

Figure 25. LATTICE PARAMETERS OF SOLID SOLUTIONS IN LANTHANUM DOPED STRONTIUM TITANATE.

of the presence of any second phase in the composition 80 mole % $La_{2/3}\square_{1/3}TiO_3$ in $SrTiO_3$. However, we report that when the large cation to small cation ratio is unity the compound $La_xSr_{1-x}TiO_3$ with x = 55 at.% contains substantial amounts of $La_2Ti_2O_7$ phase as can be seen from the photomicrograph shown in Figure 26(g).

From Figure 26 it is evident that the second phase is in the form of long needles. The precipitation of needle shaped second phase has been reported in the system Pbo-TiO_2-La_2O_3,[28] and in niobium-doped TiO_2.[27,92] X-ray energy dispersive analysis of the needle-shaped second phase indicates that this phase is enriched with titanium and lanthanum, while its strontium content is very much diminished in comparison with the principal perovskite phase.

From these results and from Tien and Hummel's[24] work it can be concluded that the shape of the homogeneity range (Figure 27) is analogous to that found for the perovskite phase in the system Pbo-TiO_2-La_2O_3 which has been extensively studied.[28,93] Therefore, these results indicate that Tofield and Scott's[26] conclusion as to the absence of a significant range of solubility for lanthanum in strontium titanate is incorrect.

5.2 Thermogravimetric Measurements

Gravimetric measurements on "pure" $SrTiO_3$ and on samples doped with up to 20 at.% La^{+3} substituted for Sr^{+2} have shown that reversible change of oxygen content, between specified states of high and low oxygen activity, is proportional to the dopant concentration. If it is assumed that

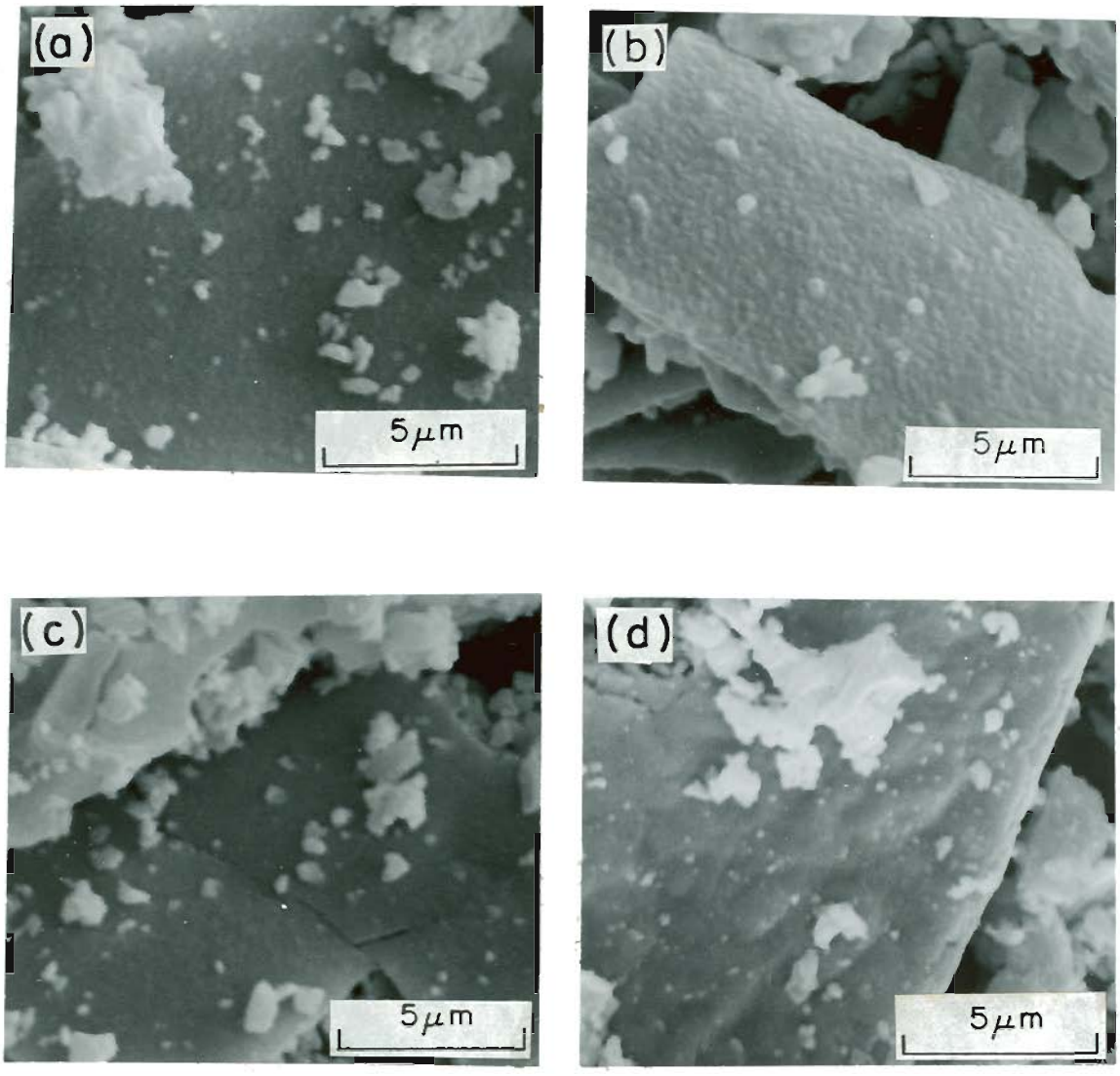

Figure 26. PHOTOMICROGRAPHS OF STRONTIUM TITANATE POWDERS HEATED AT 1350°C IN AIR. THE LANTHANUM LEVELS (AT.%) WERE: a) 0 b) 25 c) 35 d) 39.

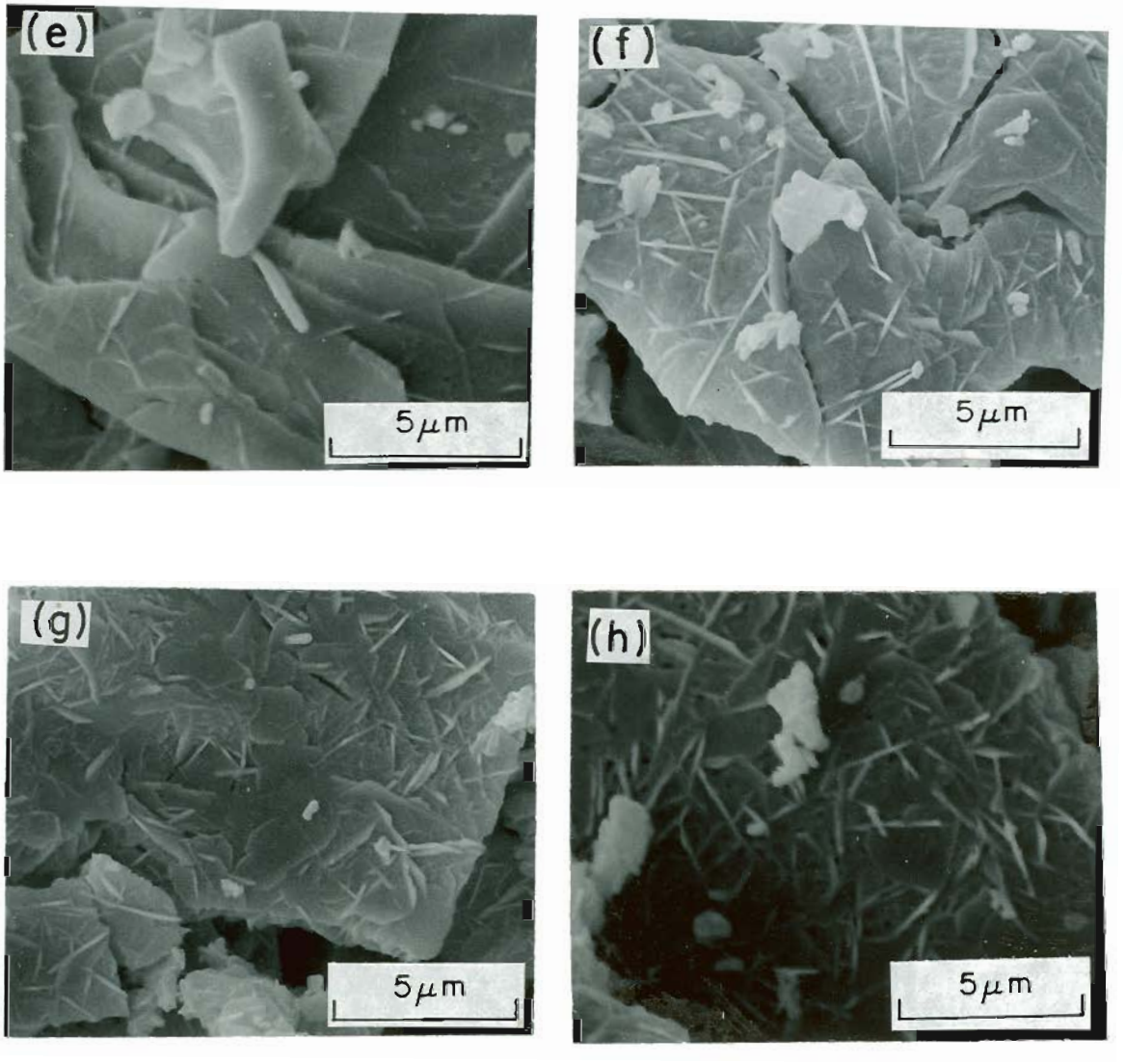

Figure 26. (cont.) PHOTOMICROGRAPHS OF STRONTIUM TITANATE POWDERS HEATED AT 1350°C IN AIR. THE LANTHANUM LEVELS (AT.%) WERE:

e) 43 f) 45 g) 55 h) 60.

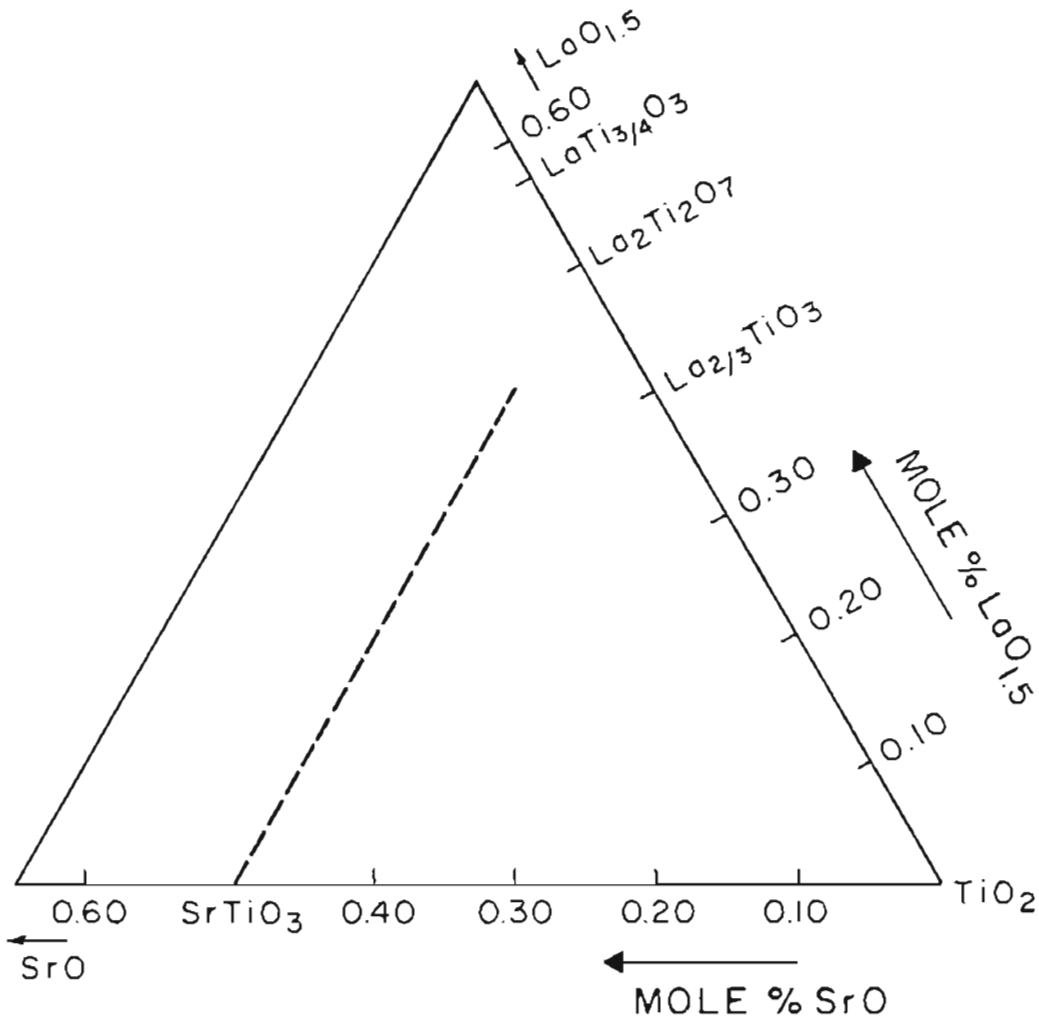

Figure 27. SCHEMATIC PHASE DIAGRAM OF THE SYSTEM SrO-TiO_2-La_2O_3 (APPLICABLE TO SPECIMENS HEATED AT 1350°C IN AIR).

each added oxygen will neutralize two La^{+3} dopant ions, there is a correlation of 95% or better between the measured increase in weight upon oxidation of a sample that had been equilibrated in an atmosphere of low oxygen activity and the calculated amount of oxygen required to neutralize the dopant.

The driving force for additional uptake of oxygen is the compensation of the electronic disorder introduced by the donor-dopant. Such charge compensation has been described for the case of doped elemental semiconductors[94] where the solid solubility of impurities is found to be proportional to the concentration of electronic disorder. The increase in energy that is required to introduce an ion into the host lattice is more than compensated by the decrease in electronic disorder. The amount of energy gained by the compensation of the electronic disorder is determined by its ionization energy and may be of the order of an electron-volt.

It is possible to increase the amount of electronic disorder created by a given donor-dopant concentration by substituting a +4 valent dopant of the appropriate ionic size for Sr^{+2} or a +6 valent dopant for Ti^{+4}. Such dopants would require twice as much reversible oxygen weight change for electronic compensation as would an equal atomic concentration of La^{+3} on Sr^{+2} site or Ta^{+5} on Ti^{+4} site. Self-compensation of $BaTiO_3$ with up to 1 at.% Th^{+4} substituted for Ba^{+2} or up to 2 at.% Mn^{+6} substituted for Ti^{+4} has been measured by Eror and Smyth,[27] and found to agree with the assumption that each added oxygen ion will neutralize one donor-dopant

ion. Their results establish that Mn^{+6} substitutes for Ti^{+4} in $BaTiO_3$ when equilibrated with an atmosphere of high oxygen activity and that Th^{+4} does substitute for Ba^{+2}.

La^{+3} was chosen as a dopant in order to understand the mechanism by which the "self-compensation" by oxygen occurs because we found its extensive range of solid solution (up to 40 at.%).[112] As can be seen in Figure 28 there is an excellent agreement between the calculated amount of oxygen necessary to compensate the La^{+3} dopant and the measured reversible oxygen weight-change between the oxidized state at one atmosphere oxygen and the reduced state of equilibration in CO/CO_2 mixture. The maximum oxygen non-stoichiometry of "pure" $SrTiO_3$ was found to be 0.04 at.% at 1050°C (corresponds to $SrTiO_{2.9988}$ taking $SrTiO_3$ as the true composition at 1 atm. oxygen pressure) when the reduction was carried out under an oxygen partial pressure of 10^{-15} atm. This value increased to 0.15 at.% ($SrTiO_{2.9955}$) when the reduction was carried out in hydrogen. For the 10 at.% La^{+3} concentration the measured reversible weight change amounts to a 40-fold increase in oxygen non-stoichiometry compared with that of the undoped $SrTiO_3$. For a La^{+3} concentration of 20 at.%, the oxidation kinetics became extremely slow so that good quantitative results were difficult to obtain. However, there is self-compensation at this concentration also with at least an 85% correlation with the predicted weight change.[95]

For a similar situation in $BaTiO_3$ with higher concentration of donor-dopants, the theories that have been offered ranged from the creation of compensating barium vacancies[96-98] to a change of cation site occupied by

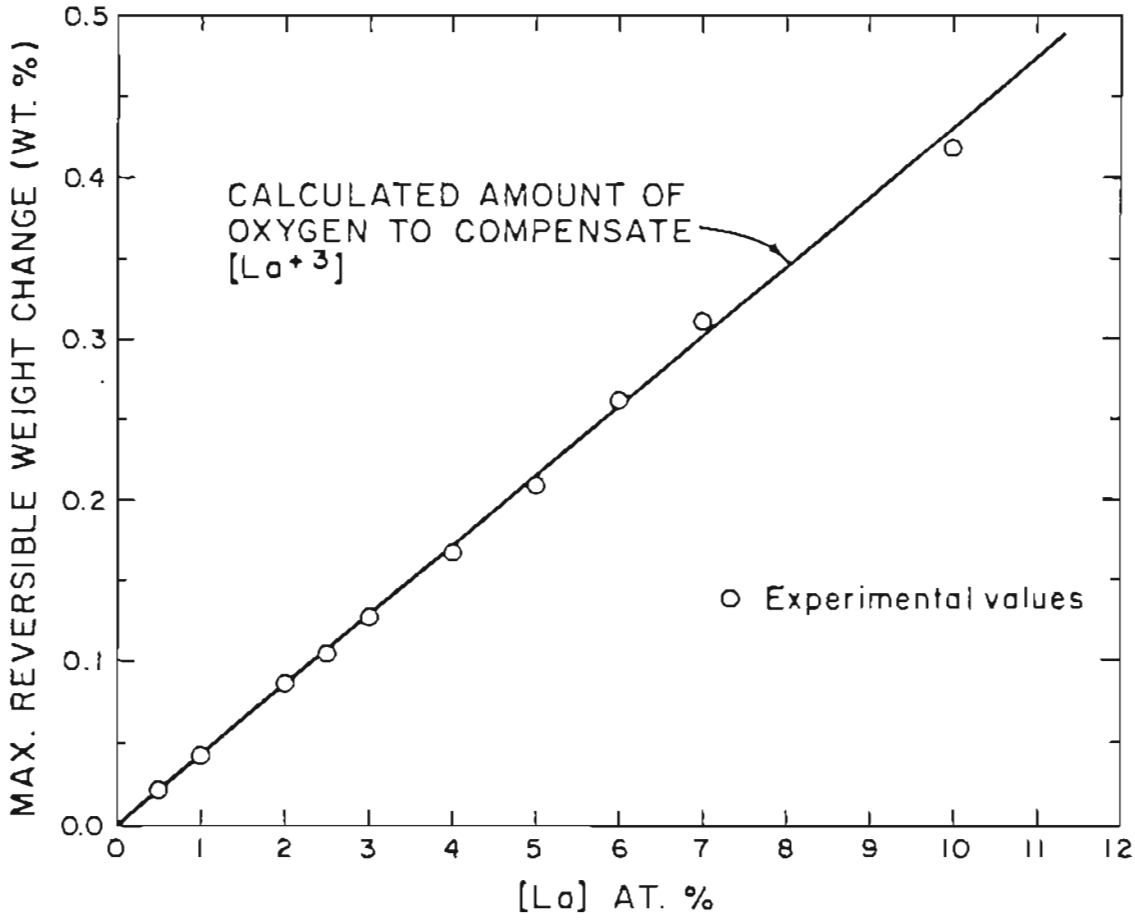

Figure 28. MAXIMUM REVERSIBLE WEIGHT CHANGE OBSERVED FOR $SrTiO_3$, BETWEEN OXYGEN PARTIAL PRESSURES ESTABLISHED BY CO/CO_2 MIXTURE, OR OXYGEN, AS A FUNCTION OF La^{+3} DOPANT CONCENTRATION (1050°C).

the donor-dopant.[99] In considering these theories for the donor doped $SrTiO_3$, it must be kept in mind that $SrTiO_3$ is a ternary compound and that the Sr/Ti ratio is fixed. For the case of the creation of the strontium vacancies at higher donor-dopant concentrations there should be an irreversible loss of strontium or precipitation of a strontium-rich phase. For the case of different site occupancy it would be possible to have compensation if some of the donor-dopant substituted for Sr^{+2} were to shift to Ti^{+4} sites and vice versa. For the case of a +3 valent dopant substituted for Sr^{+2} only 1/6 of the dopant would have to shift from +2 to +4 valent sites for complete compensation to occur. The factor 1/6 arises from the fact that the +3 valent dopant removes itself as a donor when it shifts site, becomes an acceptor on a Ti^{+4} site, and results in two strontium vacancies which may become doubly ionized (one vacancy from the site it left behind and another since it now occupies and, therefore, creates a new Ti site). For the case of +5 ion donor-dopant substituted for Ti^{+4} shifting to Sr^{+2} sites, 1/6 of the dopant would have to occupy Sr^{+2} sites for complete compensation to occur. From a crystal chemistry point of view, some of these schemes involve some very unlikely site assignments and would require significant concentrations of titanium vacancies which are structurally unsound for the perovskite structure.

The observation that highly donor-doped $SrTiO_3$ is self-compensated is unequivocally explained by the measured reversible change in oxygen stoichiometry, the question of how the extra oxygen is accommodated remains to be answered. The observation of "self-compensation" phenomena

at a La^{+3} concentration as high as 20 at.% eliminates the following possibilities:

a. Additional oxygen uptake at grain boundaries;

b. A discrete second phase that is stable only in the fully oxidized state (no second phase observed optically, by x-ray diffraction or by Raman laser spectroscopy which is a more sensitive technique than the first two);

c. Irreversible loss of Sr resulting in both V_{Sr} and V_o in the reduced state (none observed);

d. Interstitial oxygen (presence of interstitials looks unrealistic in this well-filled structure--also no significant lattice parameter change between the oxidized and reduced states is observed as can be seen in Figure 29).

Even though the La^{+3} deficit compounds like $La_{2/3}TiO_3$,[100] and $La_{(2/3 + x)}TiO_3$,[101] $0 < x < 1/3$, would be a possible compensating mechanism, since (Sr + La)/Ti ratio is unity, a second Sr rich phase would have to be exsolved to provide the Sr site vacancies required for compensation.

The observation of "self-compensation" could be explained by the following ways:

a. The addition of oxygen on oxygen sites creating both strontium and titanium vacancies (although the latter is unlikely structurally)

$$La^{\bullet}_{Sr} + Ti'_{Ti} + 1/4\ O_2 \rightleftharpoons 1/2\ O_o + 1/6V''_{Sr} + 1/6V''''_{Ti} + La^{\bullet}_{Sr} + Ti_{Ti}$$

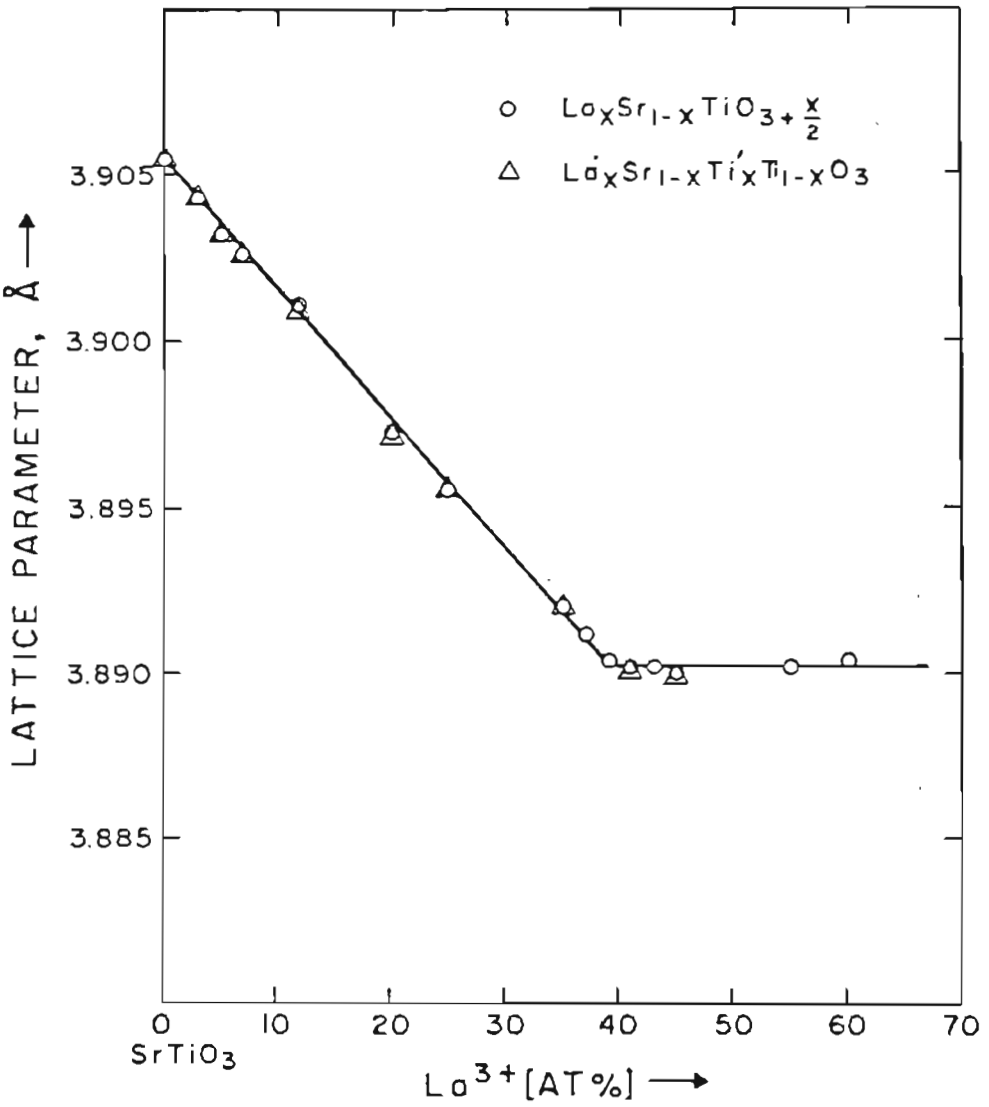

Figure 29. LATTICE PARAMETERS OF SOLID SOLUTIONS IN LANTHANUM DOPED STRONTIUM TITANATE.

The presence of B-site vacancies in perovskites has only been reported for lanthana substituted $PbTiO_3$ by Hennings and Resenstein,[102] and for lanthanum manganite by Tofield and Scott.[26] These conclusions were not based on convincing experimental results.

b. A shift in the cation site occupied by the donor-dopant when the samples are oxidized,

$$La_{Sr}^{\cdot} + Ti_{Ti}' + 1/4\ O_2 \rightleftharpoons 1/2\ O_o + 1/6\ La_{Ti}' + 1/3\ V_{Sr}'' + 5/6\ La_{Sr}^{\cdot} + Ti_{Ti}$$

Kwestroo and Paping[103] found evidence that Ca^{+2} ions can be incorporated at titanium sites in the perovskite phase in the system $BaO-CaO-TiO_2$. From the luminescence measurement on Sm substituted $BaTiO_3$ Murakami et al.[104] concluded that Sm^{+3} ions were present at Ti sites as well as at Ba sites. But neither paper proves that a significant number of such large ions (Ca, Sm) enters Ti sites. Takeda and Watanabe[105] have reported evidence of La^{+3} on Ti^{+4} sites. They obtained an EPR signal characteristic of an F-center equivalent to the acceptor, La_{Ti}'. This signal was present only for the case of a Ba/Ti ratio of 1.02 plus an additional 1.0 at.% La (Ba/Ti ratios of 1.01 and 1.03 had little or no signal). In the present investigation, the large cations to small cation ratio is maintained at unity with a variation of 15-25 ppm. So, from the results of

Takeda and Watanabe's[105] work and the cation ratios used in this experiment, one can assume that La^{+3} ions mainly occupy the Sr^{+2} sites. Also, by careful structure factor analysis Hennings and Rosenstein eliminated the possibility of La^{+3} ions occupying the titanium sites in lanthanum modified lead titanate. Further, the possibility of a change in cation site occupied by the donor-dopant can be discounted because of the unlikely possibility of the creation of titanium vacancies in the perovskite structure that are required to compensate donor-dopants substituted for Ti^{+4}. Careful x-ray diffraction intensity measurements should be performed before completely discarding this possibility as well as the possibility of the addition of oxygen on oxygen sites creating both strontium and titanium vacancies.

c. A reversible change from a classic, randomly distributed, point defect model in the reduced state to a compensated structure with ordered defects in the oxidized state.

$$\tfrac{1}{2}\ Sr_{Sr} + La_{Sr}^{\cdot} + Ti_{Ti}^{\prime} + \tfrac{1}{4}\ O_2 \rightleftharpoons \tfrac{1}{2}\ (SrO) + \tfrac{1}{2}\ V_{Sr}^{''} + La_{Sr}^{\cdot} + Ti_{Ti}$$

For a La^{+3} concentration of 20 at.% it will be,

$$La_{0.2}^{+3}\ Sr_{0.8}^{+2}\ Ti^{+4}\ O_{3.10}^{=} = [La_{0.2}Sr_{0.7}\square_{0.1}]\ TiO_3 + 0.1\ (SrO)$$

where $\square$ represents the vacancy on A site.

The existence of a perovskite phase of composition $Sr_{1-1.5x}La_xTiO_3$ has been reported by Tien and Hummel.[24] (SrO) does not represent a separate phase but a structural accommodation in an ordered fashion, perhaps in the way that Ruddlesden-Popper phases,[78,79] i.e., $nSrTiO_3 \cdot SrO$ are formed by ordered layers of SrO between perovskite type $SrTiO_3$ layers of various thickness. Figure 30 shows the $Sr_3Ti_2O_7$ structure where double $SrTiO_3$ perovskite layers are interleaved with SrO layers. By this type of proposed model, the compensation of donor-doped $SrTiO_3$ is by the strontium vacancy model, but since we have a ternary oxide the additional strontium that results from the strontium vacancies combines with oxygen, accounting for the gravimetric observations, to form (SrO) which is built into the lattice in a reasonably ordered fashion. It should be noted that the perovskite layers may still contain a random distribution of dopant ions and strontium vacancies even in the fully compensated oxidized state. The inter-layer ordering might not be detected by conventional x-ray powder pattern techniques, because only one (SrO) layer would be required for each ten perovskite $SrTiO_3$ layers for the case of 20 at.% La^{+3} substitution for Sr^{+2}.

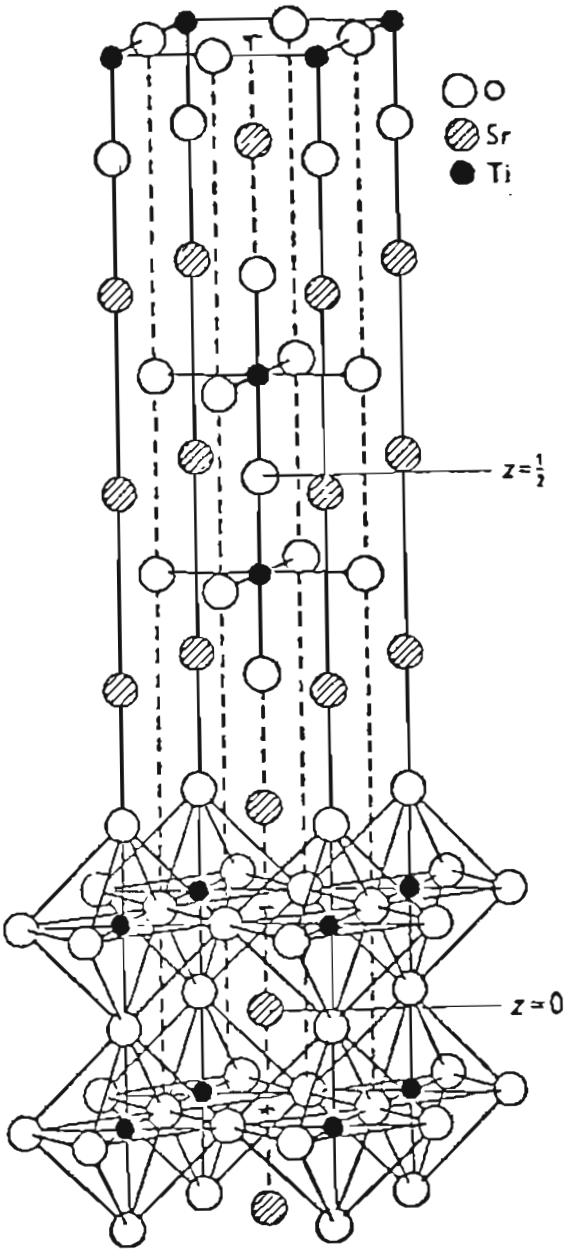

Figure 30. THE STRUCTURE OF $Sr_3Ti_2O_7$.

5.3 Electrical Conductivity in Strontium Titanate

The electrical conductivity of polycrystalline $SrTiO_3$ in the temperature range 800-1050°C and in equilibrium with oxygen partial pressures between 10^0 to 10^{-22} atm. is shown in Figure 31. The conductivity changes from p- to n-type as the oxygen partial pressure is decreased for the temperature range used. The data were found to be proportional to the -1/6th power of the oxygen partial pressure for the oxygen pressure range 10^{-15} - 10^{-22} atm., proportional to $P_{O_2}^{-1/4}$ for the oxygen pressure range 10^{-8} - 10^{-15} atm., and porportional to $P_{O_2}^{+1/4}$ for the oxygen pressure range 10^0 - 10^{-3} atm. These three regions are treated separately in the following text.

Region I: [$P_{O_2} = 10^{-22} - 10^{-15}$ atm.]

The log σ vs log P_{O_2} data [Figure 32] are linear for as many as seven decades of oxygen partial pressures for a given temperature. This extensive region of linearity affords the opportunity to determine the defect model responsible for the n-type electrical conductivity in this region. A slope of approximately -1/6 is found for the log σ vs log P_{O_2} data. This slope is similar to that found for $BaTiO_3$[20,22,47,48] and $CaTiO_3$[106] as well as the results of Walters and Grace[43] for single-crystal $SrTiO_3$ in the narrow P_{O_2} range [10^{-21} - 10^{-19} atm.]. Yamada and Miller[44] have determined the carrier concentration by Hall effect measurements for single-crystal $SrTiO_3$ quenched from equilibrium with various oxygen partial pressures, and they found a similar relationship between the electron

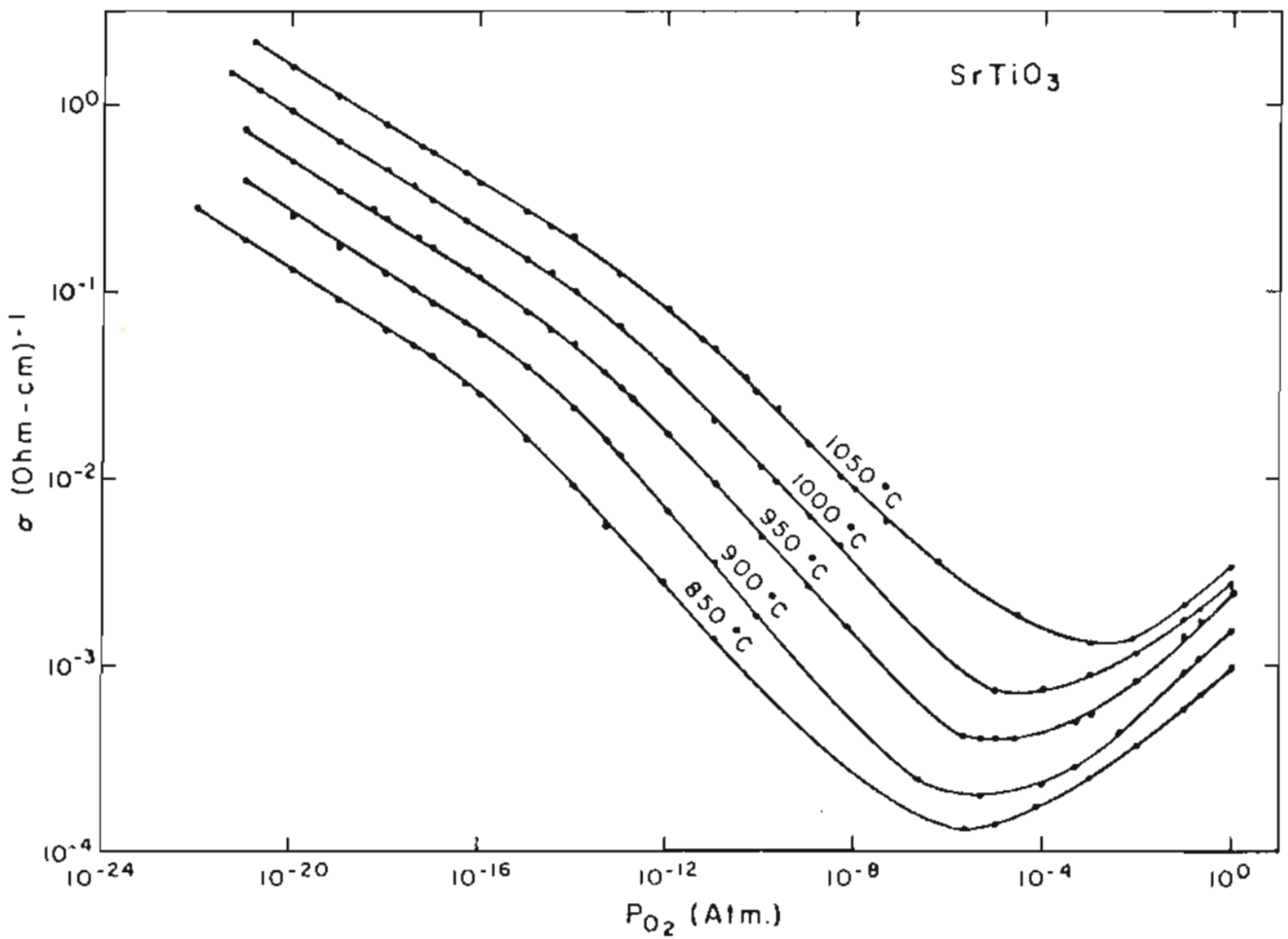

Figure 31. THE ELECTRICAL CONDUCTIVITY OF POLYCRYSTALLINE $SrTiO_3$

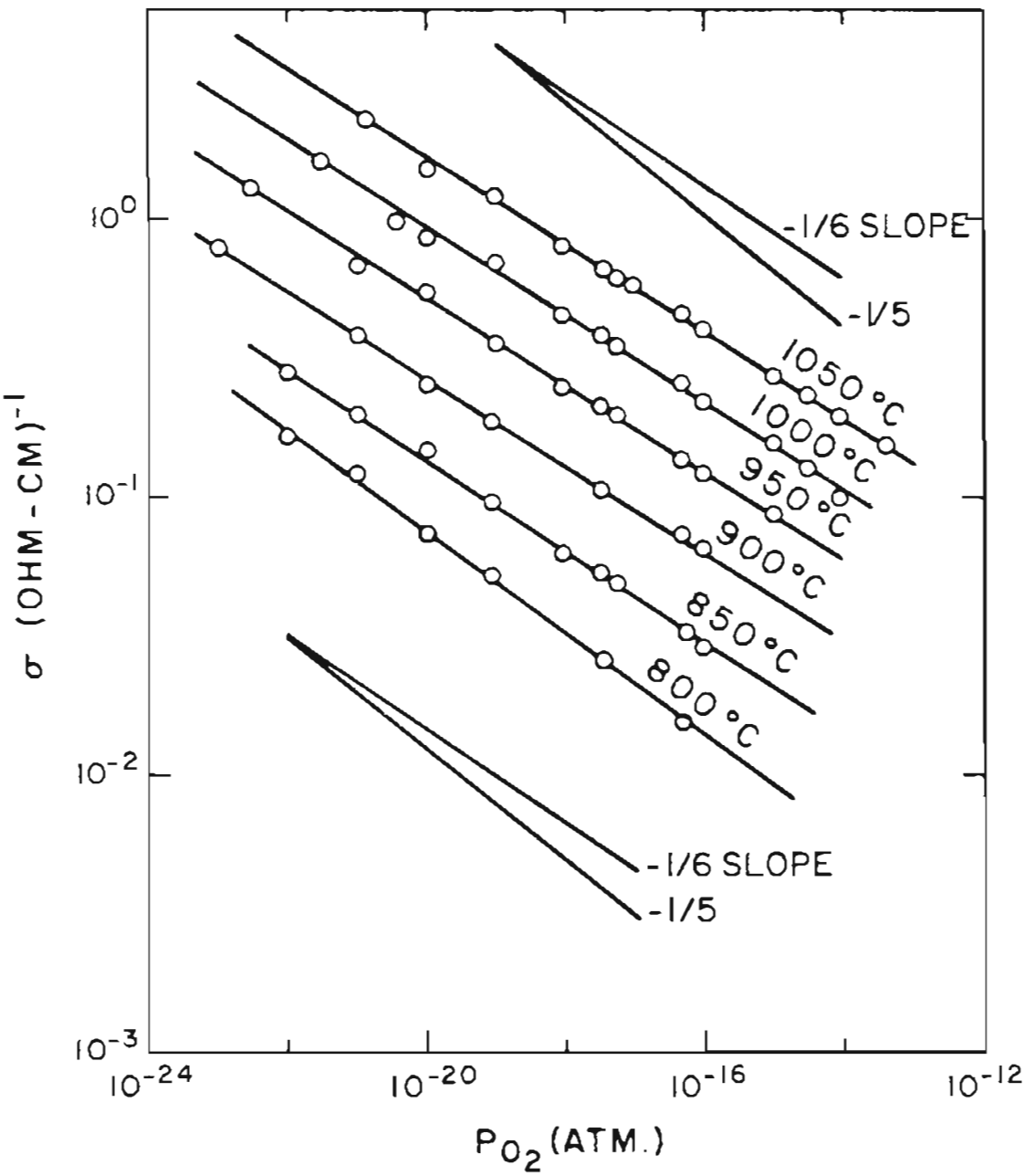

Figure 32. THE CONDUCTIVITY OF POLYCRYSTALLINE $SrTiO_3$ AS A FUNCTION OF OXYGEN PARTIAL PRESSURE AT CONSTANT TEMPERATURE, FROM 10^{-22} TO 10^{-15} ATM.

concentration and the equilibrium partial pressure. These same authors have shown that the oxygen vacancies formed upon reduction can be quenched in upon cooling to ambient and they remain doubly ionized to very low temperatures.

The variation of the electrical conductivity with the oxygen partial pressure is calculated in terms of the oxygen vacancy defect model. The basis for the calculation is the reaction that represents the formation of a doubly ionized oxygen vacancy $[V_o^{\cdot\cdot}]$ and two electrons available for conduction by the removal of an oxygen from a normal lattice site into the gas phase. The reaction is

$$O_o \rightleftharpoons 1/2\ O_2 + V_o^{\cdot\cdot} + 2\ e' \tag{99}$$

The equilibrium constant for the reaction (99) is

$$K_{99} = [V_o^{\cdot\cdot}]\ [n]^2\ P_{O_2}{}^{1/2} = \exp\left(\frac{-\Delta G_f}{RT}\right) \tag{100}$$

where $[n] \equiv e'$. It is assumed that the defects exist in a dilute solution and do not interact. The Gibbs standard free energy change for reaction (99) is represented by ΔG_f. With two electrons resulting from each oxygen vacancy it follows that

$$[n] = 2\ [V_O^{\cdot\cdot}] \tag{101}$$

Expressing the free energy change in terms of the enthalpy change, ΔH_f, and entropy change ΔS_f and substituting equation (101) into equation (100) the result for the electron concentration is

$$[n] = 2^{1/3} P_{O_2}^{-1/6} \exp\left[\frac{\Delta S_f}{3R}\right] \exp\left[\frac{-\Delta H_f}{3RT}\right] \quad (102)$$

The electrical conductivity, σ, for the case where the sole charge carriers are electrons in the conduction band is

$$\sigma = ne\mu \quad (103)$$

where e is the electronic charge, and μ is the mobility of the conduction electrons. When Equation (102) is substituted into Equation (103) the electrical conductivity becomes

$$\sigma = 2^{1/3} P_{O_2}^{-1/6} e \mu \exp\left[\frac{\Delta S_f}{3R}\right] \exp\left[\frac{-\Delta H_f}{3RT}\right] \quad (104)$$

At constant temperature, assuming that mobility is independent of the change in concentration of oxygen vacancies, a plot of the logarithm of the electrical conductivity vs. the logarithm of the P_{O_2} should result in a straight line with a slope of -1/6. The data in Figure 32 and Table VI are in good agreement with the predicted -1/6 dependence.

An indication of the magnitude of ΔH_f, the enthalpy of the oxygen extraction reaction, is typically obtained from Arrhenius plots of the conductivity, as deduced from Equation (104). This procedure neglects contributions from the temperature dependences of the carrier mobility or density of states. The value of ΔH_f calculated from the slope of the Arrhenius plots in Figure 33 are listed in Table VII. An average value of 4.85 ev [111.8 kcal/mole] is estimated for ΔH_f. Walters and Grace[43] obtained a value of 6.3 ev. Yamada and Miller[44] determined a value for

Table VI.

P_{O_2} DEPENDENCE OF CONDUCTIVITY IN THE REGION 10^{-22} - 10^{-15} ATM. FOR $SrTiO_3$

T (°C)	m for $\sigma_n \propto P_{O_2}^{-1/m}$
800	5.5
850	6.06
900	6.3
950	6.3
1000	6.3
1050	6.3

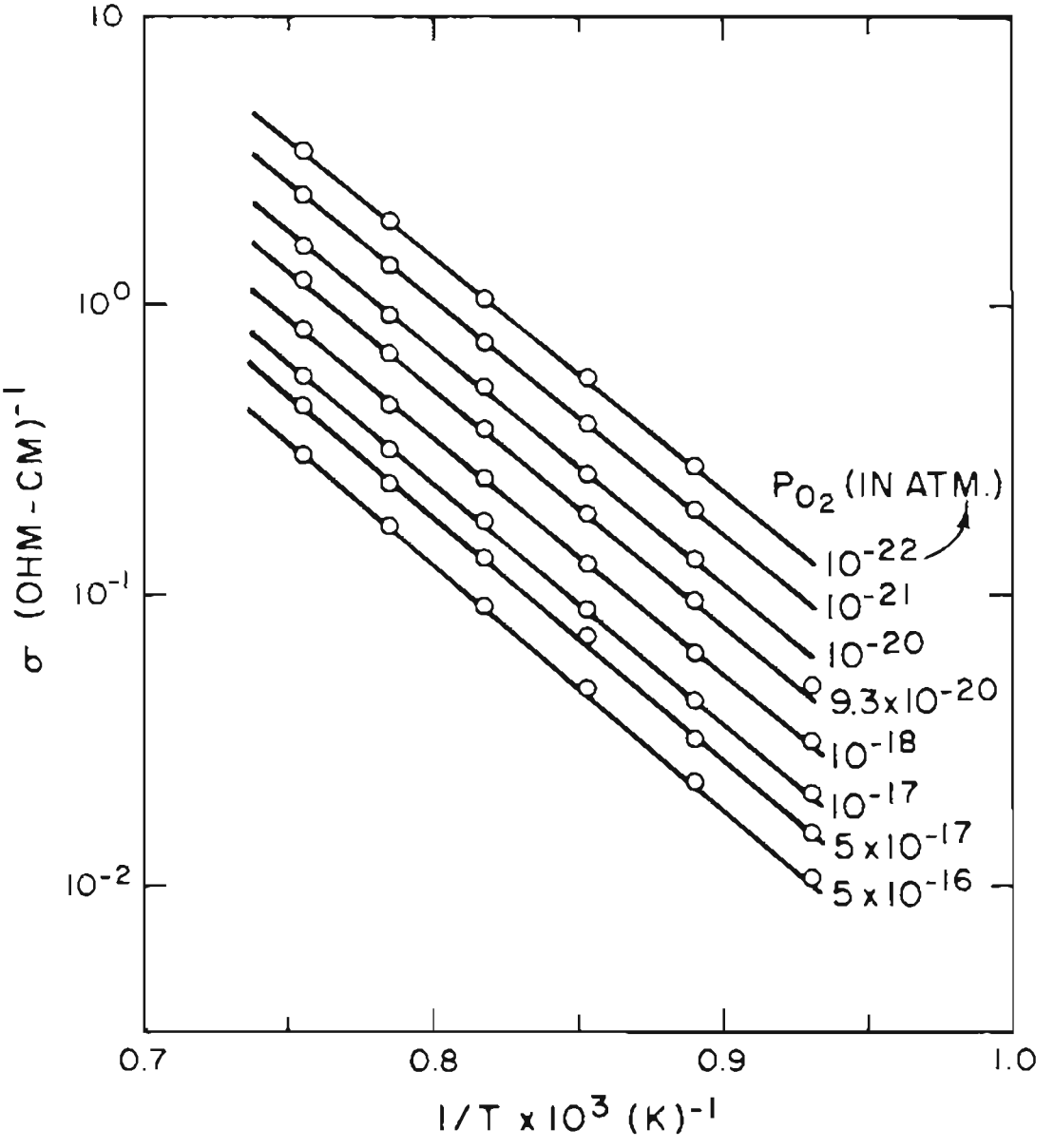

Figure 33. TEMPERATURE DEPENDENCE OF CONDUCTIVITY OF POLYCRYSTALLINE $SrTiO_3$ IN THE N-TYPE, OXYGEN-DEFICIENT REGION.

Table VII.

ACTIVATION ENTHALPIES FOR CONDUCTION IN THE REGION 10^{-22} - 10^{-15} ATM. FOR $SrTiO_3$

P_{O_2} (atm)	Activation enthalpies [Kcal/mole]
10^{-22}	110.61
10^{-21}	109.72
10^{-20}	110.67
9.3×10^{-20}	111.17
10^{-18}	110.98
10^{-17}	112.68
5×10^{-17}	114.67
5×10^{-16}	113.88

ΔH_f of 5.76 ± .2 ev for $SrTiO_3$. This was based on a direct measurement of n by the Hall effect on reduced single crystals.

The temperature dependence of mobility of electrons in $SrTiO_3$ is not known for the temperature range covered in the present study. Frederikse et al.[37] found a band-type conduction process in $SrTiO_3$. This implies that electron mobility varies proportional to $T^{-3/2}$ and the equilibrium constant K_{99} in Equation (100) should thus contain N_c^2, the square of the density of states near the conduction band edge. For $\mu_n \propto T^{-3/2}$ and $N_c \propto T^{3/2}$ there is an additive correction to ΔH_f of 3/2RT-RT or about 0.11 ev. Seuter[49] has determined the mobility of electrons in $BaTiO_3$ in the temperature range 800-1000°C by a combination of the Hall effect and conductivity. He describes the temperature dependence as T^{-1}. If $\mu \propto T^{-1}$, then the corrections for ΔH_f cancel.

Region II: [$P_{O_2} = 10^{-8} - 10^{-15}$ atm.]

A slope of approximately -1/4 is found for the log σ vs. log P_{O_2} data [see Figure 34]. Daniels and Hardtl[107] reported from their log σ vs. log P_{O_2} plot, a slope of -1/4 between 700 and 900°C and -1/5 at 1200°C for $BaTiO_3$ in the P_{O_2} range, $10^{-18} - 10^{-8}$ atm. They attributed the -1/4 slope to singly ionized oxygen vacancies as the cause of conductance and -1/5 value to the more frequent occurrence of doubly ionized oxygen vacancies. However, for $SrTiO_3$, it has been shown by earlier investigators,[41,44] that the oxygen vacancies in the quenched samples remain doubly ionized down to liquid nitrogen temperature. The observed slope of -1/4

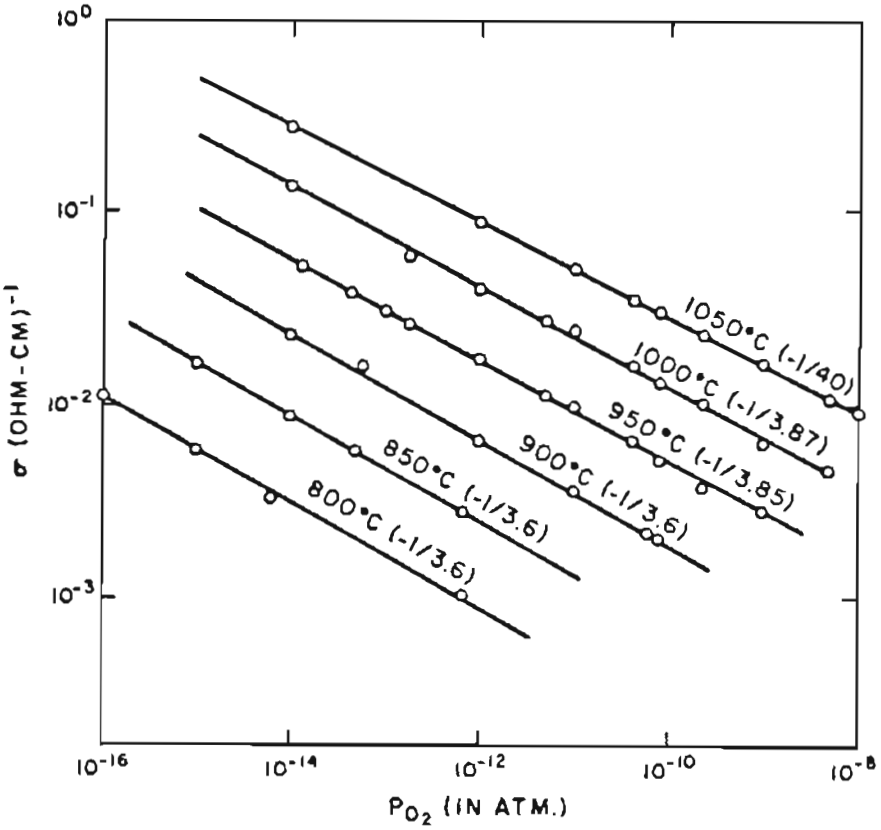

Figure 34. THE CONDUCTIVITY OF POLYCRYSTALLINE $SrTiO_3$ AS A FUNCTION OF OXYGEN PARTIAL PRESSURE AT CONSTANT TEMPERATURE, FROM 10^{-15} TO 10^{-8} ATM.

in this region must, therefore, be due to the presence of an unknown, negatively charged impurity, i.e., an acceptor impurity such as Al, Fe, or Cr on Ti sites. For the case of undoped $BaTiO_3$ prepared by the same technique as the one used here, Chan and Smyth[22] report a net acceptor impurities about 130 ppm (atomic). They proposed that all undoped material [$BaTiO_3$] studied to date had a net excess of acceptor impurities, and attributed this to the fact that potential acceptor elements are naturally much more abundant than potential donor-elements. Seuter[48] was able to observe an extensive range of $P_{O_2}^{-1/4}$ dependence for conductivity in the oxygen-deficient region below the p-n transition in the $BaTiO_3$ presumably because of greater acceptor impurity content of his samples. We believe that our samples also contain some unknown acceptor impurities which are singly ionized. Thus, the condition of charge neutrality in this region can be

$$2\,[V_O^{\cdot\cdot}] \simeq [A'] \tag{105}$$

With this neutrality condition and Equations (99), (100), (102), (103), and (104), the conductivity varies with oxygen partial pressure as shown in Equation (106) below.

$$\sigma = P_{O_2}^{-1/4}\, e\mu \exp\left[\frac{\Delta S_f}{2R}\right] \exp\left[\frac{-\Delta H_f}{2RT}\right] \tag{106}$$

The slopes of the lines drawn in Figure 37 are well in agreement with the predicted value of -1/4 by the above impurity model. The activation enthalpies of conduction derived from the Arrhenius slopes are shown in

Table VIII. An average value of 4.56 ev [105.2 Kcal/mole] is estimated for this region.

Transition Region:

Becker and Frederikse[108] showed that the band-gap energy (extrapolated to zero temperature) of a semiconductor which exhibit a p to n transition may be determined from the Arrhenius plots of the conductivity minima. The log σ_{min} vs. 1/T data in Figure 35 indicate a value E_g° = 3.36 ev [77.54 Kcal/mole] as the band-gap for the polycrystalline $SrTiO_3$ extrapolated to 0°K. This is in good agreement with the range of values 3.2 - 3.4 ev reported from optical absorption data[109-111] on single crystal $SrTiO_3$. Assuming band-conduction for both electrons and holes, the full expression for the Arrhenius plot is

$$\frac{\partial \ell n\ \sigma_{min}}{\partial (RT)^{-1}} = \frac{\partial}{\partial (RT)^{-1}} \left[\frac{\ell n\ \mu_n \mu_p}{2} + \ell n\ N_c\ N_v \right] - \frac{E_g^\circ}{2} \qquad (107)$$

Assuming that the temperature dependence of the mobilities are $\propto T^{-3/2}$ for electrons and holes, and if both N_c and N_v, (the densities of states near the band edges) are proportional to $T^{+3/2}$, mobility and density of states terms cancel each other, and the Arrhenius slope is directly proportional to E_g°.

Region III: [$P_{O_2} > 10^{-3}$ atm]

The conductivity in this region increases with increasing oxygen partial pressure [see Figure 36], indicative of p-type, or oxygen-excess,

Table VIII.

ACTIVATION ENTHALPIES FOR CONDUCTION IN THE REGION 10^{-15} - 10^{-8} ATM. FOR $SrTiO_3$

P_{O_2} (atm)	Activation Enthalpies [Kcal/mole]
10^{-15}	100.70
10^{-14}	100.62
10^{-13}	102.42
10^{-12}	104.02
10^{-11}	103.71
10^{-10}	112.34
10^{-9}	112.66

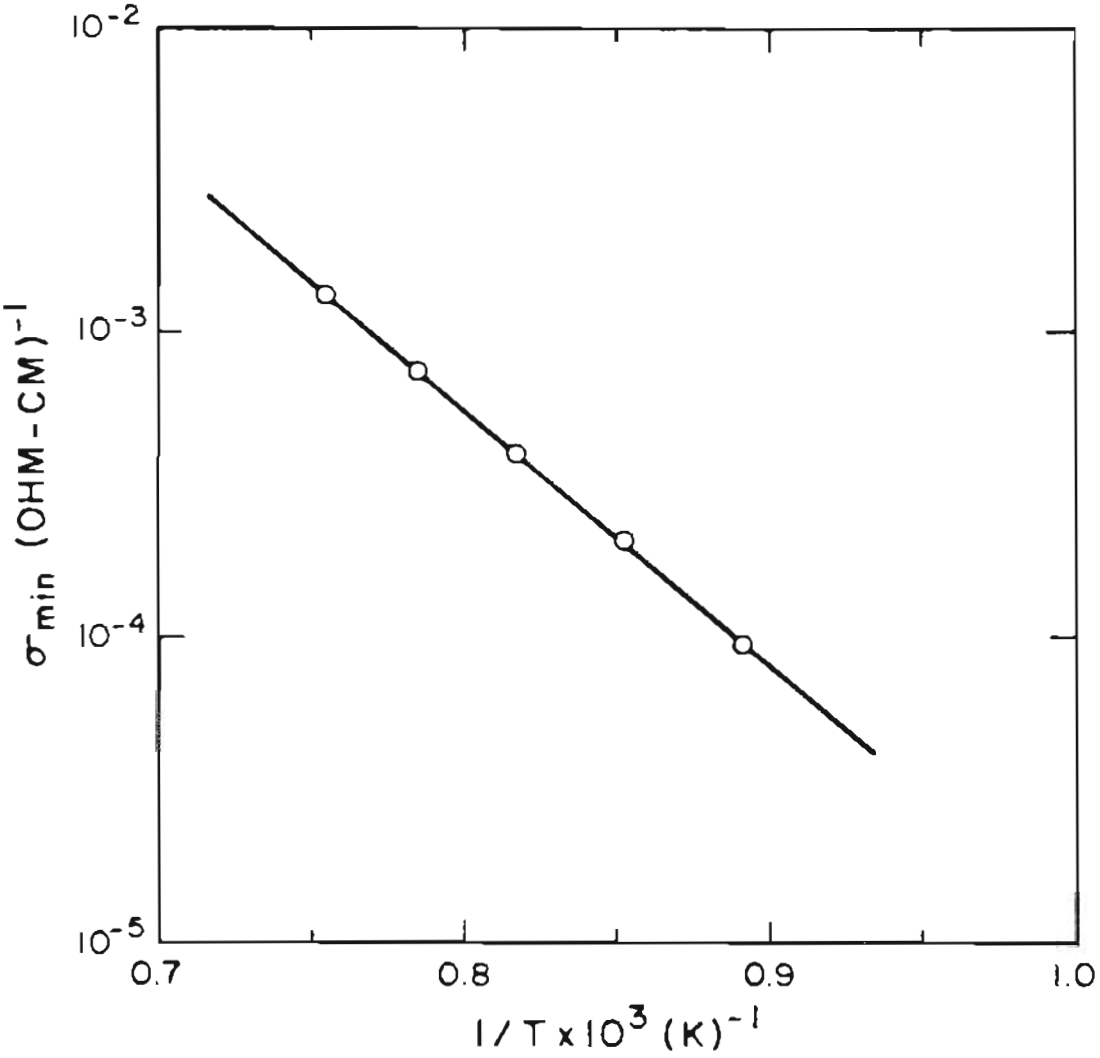

Figure 35. TEMPERATURE DEPENDENCE OF THE CONDUCTIVITY MINIMA OF POLYCRYSTALLINE $SrTiO_3$.

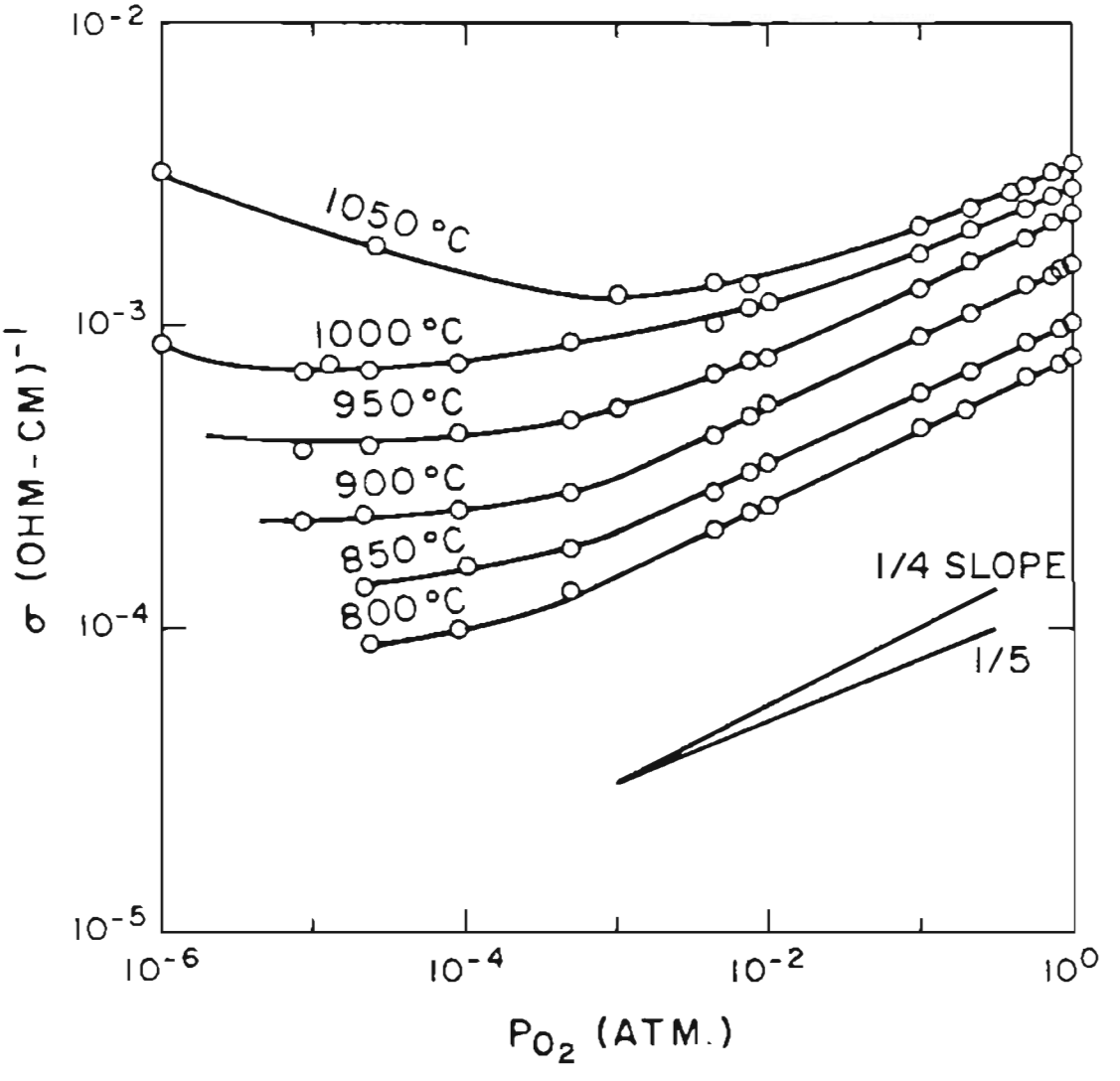

Figure 36. THE CONDUCTIVITY OF POLYCRYSTALLINE $SrTiO_3$ AS A FUNCTION OF OXYGEN PARTIAL PRESSURE AT CONSTANT TEMPERATURE, FROM 10^{-6} TO 10^{0} ATM.

conductivity. The region of linearity in the p-type region increases in width with decreasing temperature as the p-n transition moves to lower P_{O_2}. The slopes of the pressure dependence given in Table IX indicate that the values are tending toward 1/4 with decreasing temperature where the range of linearity is greatest. Measurements of the electrical conductivity under fixed oxygen pressure as a function of temperature result in a nearly constant value for the slopes of log σ vs. 1/T for various oxygen partial pressures in this region [Figure 37]. The activation enthalpies of conduction, ΔH_p, derived from the slopes are given in Table X. A value of about 1.59 ev [36.7 Kcal/mole] appears to be typical.

It is apparent that a stoichiometric excess of oxygen can be incorporated into $SrTiO_3$ by a remarkably favorable process without the need of creating a crystallographic excess. The oxygen is incorporated into the impurity-related oxygen vacancies where the reaction is,

$$[V_o^{\cdot\cdot}] + 1/2\ O_2 \rightleftharpoons O_o + 2\ h^{\cdot} \qquad (108)$$

The charge neutrality condition near the stoichiometric region is

$$[A'] \approx 2\ [V_o^{\cdot\cdot}] \qquad (105)$$

The chemical mass action expression for Equation (108) combined with Equation (105) gives

$$\sigma \propto P_{O_2}^{+1/4} \qquad (109)$$

as observed, as long as only a minor fraction of the impurity-related $V_o^{\cdot\cdot}$

Table IX.

P_{O_2} DEPENDENCE OF CONDUCTIVITY FOR THE p-TYPE REGION

T (°C)	m for $\sigma_p \propto P_{O_2}^{1/m}$
800	4.08
850	4.3
900	4.2
950	4.2
1000	4.6
1050	4.6

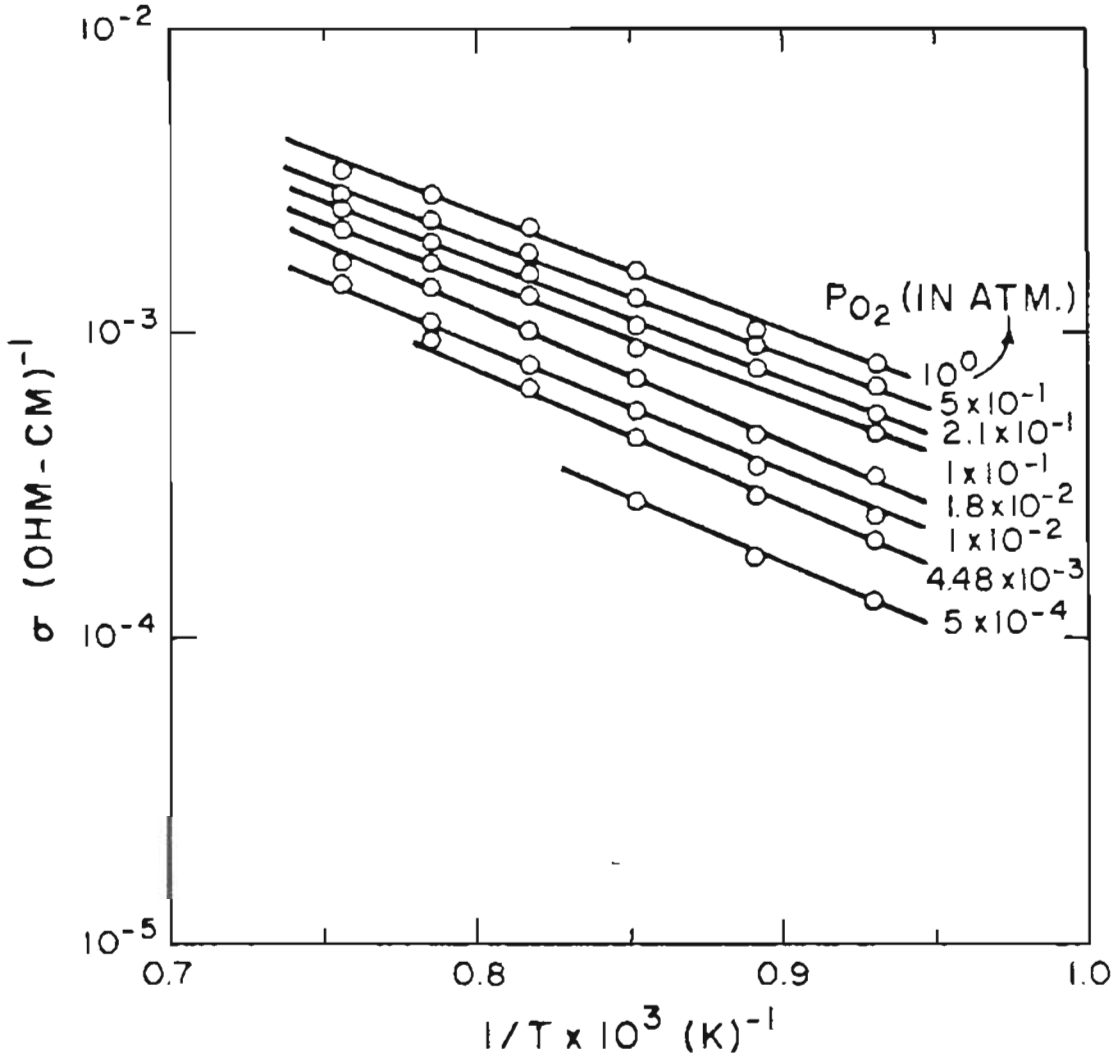

Figure 37. TEMPERATURE DEPENDENCE OF CONDUCTIVITY OF POLYCRYSTALLINE $SrTiO_3$ IN THE p-TYPE REGION.

Table X.

ACTIVATION ENTHALPIES FOR CONDUCTION IN THE p-TYPE REGION

P_{O_2} (atm)	Activation enthalpies [Kcal/mole]
10^{0}	34.72
5×10^{-1}	34.32
2.1×10^{-1}	35.10
10^{-1}	34.60
1.8×10^{-2}	39.20
1×10^{-2}	37.30
4.48×10^{-3}	39.80
5×10^{-4}	38.52

is filled. If a significant proportion of the $V_o^{\cdot\cdot}$ has been filled then both h and $V_o^{\cdot\cdot}$ become dependent on P_{O_2}. The trend toward shallower slopes at higher temperatures represents an intrusion of the transition region leading to the conductivity minima which are moving toward higher P_{O_2} with increasing temperature. The ready availability of oxygen vacancies explains the unusual ease with which the material accepts a stoichiometric excess of oxygen.

Earlier investigators[20-22] have invoked the presence of an unknown acceptor impurities in order to explain their very similar experimental results in $BaTiO_3$ in the P_{O_2} range under consideration. The estimated acceptor impurity in our sample is approximately 170 ppm. These impurities and their charge compensating partner, $V_o^{\cdot\cdot}$, dominate the charge neutrality condition in a wide range of P_{O_2} ($>10^{-15}$ atm). The only region where impurity-insensitive behavior is observed is in the range of lowest P_{O_2} and highest temperature where the conductivity varies as $P_{O_2}^{-1/6}$ and the $V_o^{\cdot\cdot}$ generated by Equation (99) exceed those due to the acceptor impurity.

When the conductivities obtained from this work are compared with the reported data of Walters and Grace[43] in the narrow range of P_{O_2} used by them, the two values are well within the range 0.03 $ohm^{-1}cm^{-1}$. This agreement between the polycrystalline sample used in this investigation and the single crystal used by Walters and Grace[43] indicates that grain boundaries have no significant effect on electronic transport in this range of experimental conditions.

5.4 Electrical Conductivity in Strontium Titanate with Non-Ideal Cation-Cation Ratio

The electrical conductivity of polycrystalline strontium titanate with Sr/Ti = 0.996 and 0.99 in the temperature range 850-1050°C and in equilibrium with oxygen partial pressures between 10^{0} to 10^{-22} atm. is shown in Figures 38 and 39 respectively. In both cases the conductivity changes from p- to n-type as the oxygen partial pressure is decreased. Three regions are observed as the P_{O_2} value is decreased at any given temperature (Figures 38 and 39). Figures 40-44 show the conductivity of $SrTiO_3$, $Sr_{.996}TiO_3$, and $Sr_{.99}TiO_3$ at five different temperatures.

The log σ vs log P_{O_2} data are linear with a slope ranging from (-1/5.8) to (-1/6.4) as the temperature is increased in the P_{O_2} region 10^{-21} - 10^{-16} atm. (see Table XII) for $Sr_{.996}TiO_3$. In the same P_{O_2} region, the slopes vary (-1/5.3) to (-1/5.7) for $Sr_{.99}TiO_3$ as can be seen from Table XIII. As P_{O_2} is increased further, the P_{O_2} dependence of conductivity changes for both the samples as observed in $SrTiO_3$. The new values of slopes of log σ vs log P_{O_2} plots are (-1/4.4) to (-1/4.6) for both $Sr_{.996}TiO_3$ and $Sr_{.99}TiO_3$ in the P_{O_2} region 10^{-15} - 10^{-8} atm. These data are shown in Tables XIV and XV, respectively.

The region of linearity in the p-type region increases in width with decreasing temperature as the p-n transition moves to lower P_{O_2} in both the samples with Sr/Ti < 1. The oxygen pressure range in which the p-type behavior observed in the samples with non-ideal cationic ratio is nearly

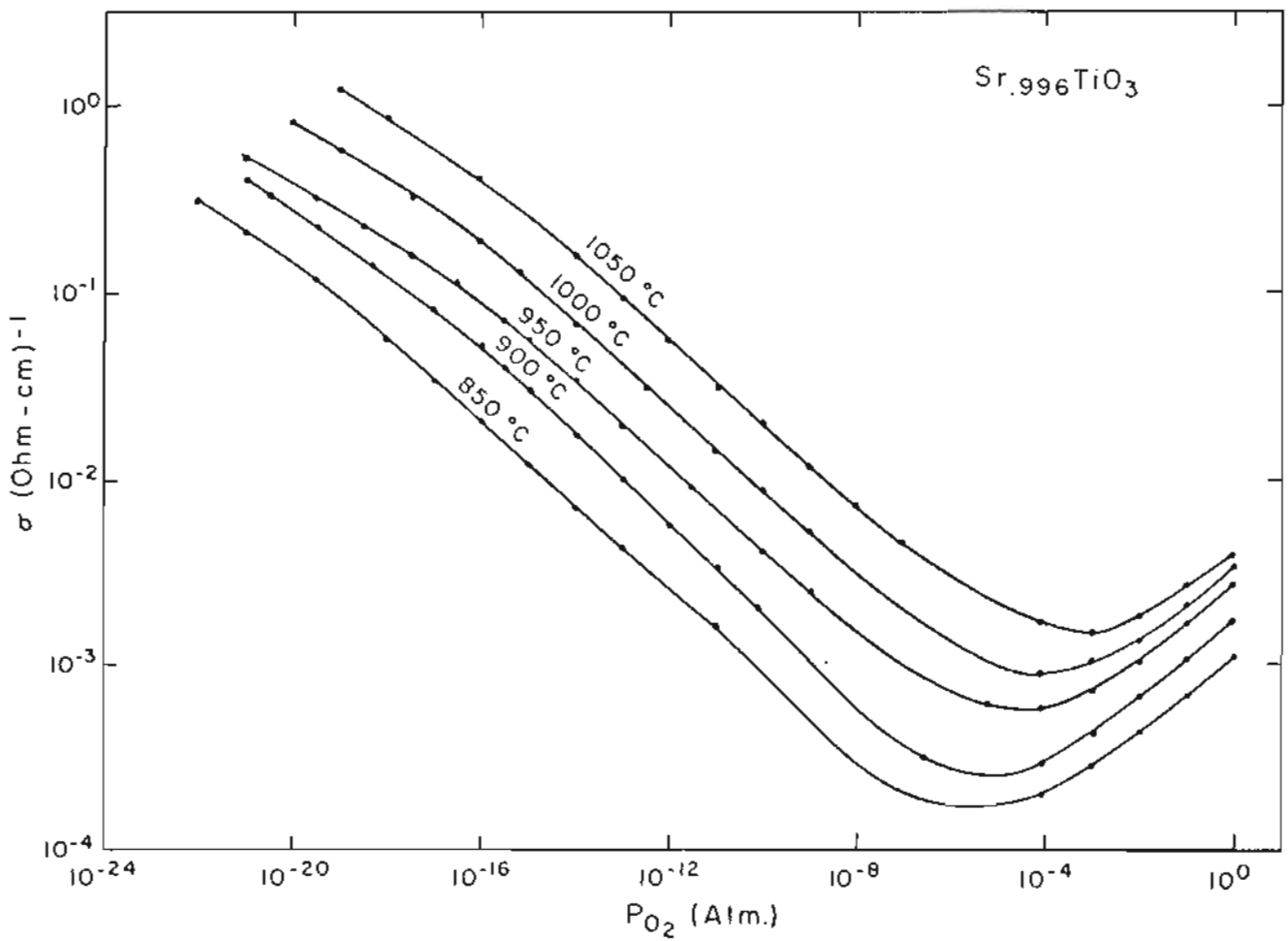

Figure 38. THE ELECTRICAL CONDUCTIVITY OF $Sr_{.996}TiO_3$.

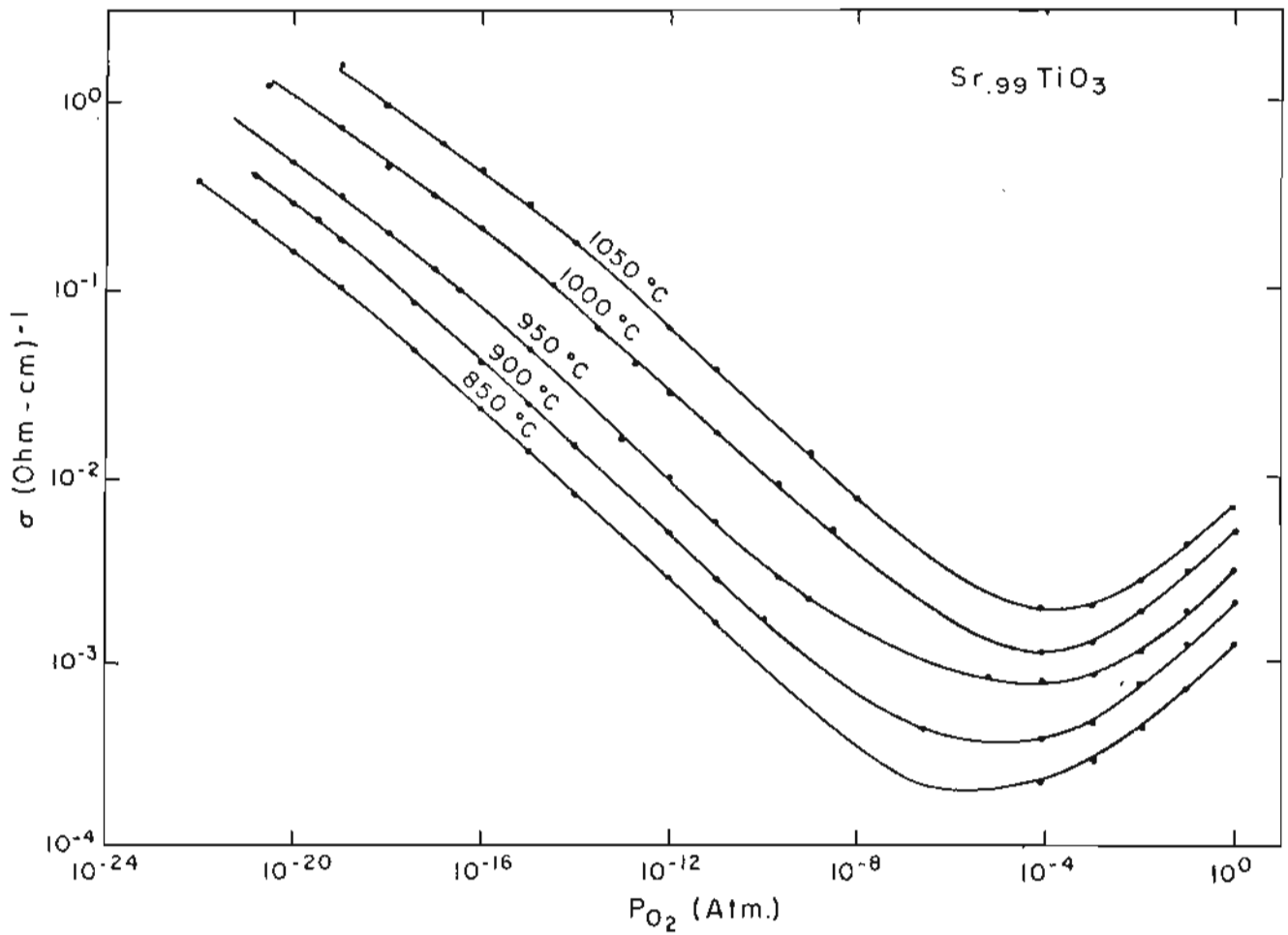

Figure 39. THE ELECTRICAL CONDUCTIVITY OF $Sr_{.99}TiO_3$.

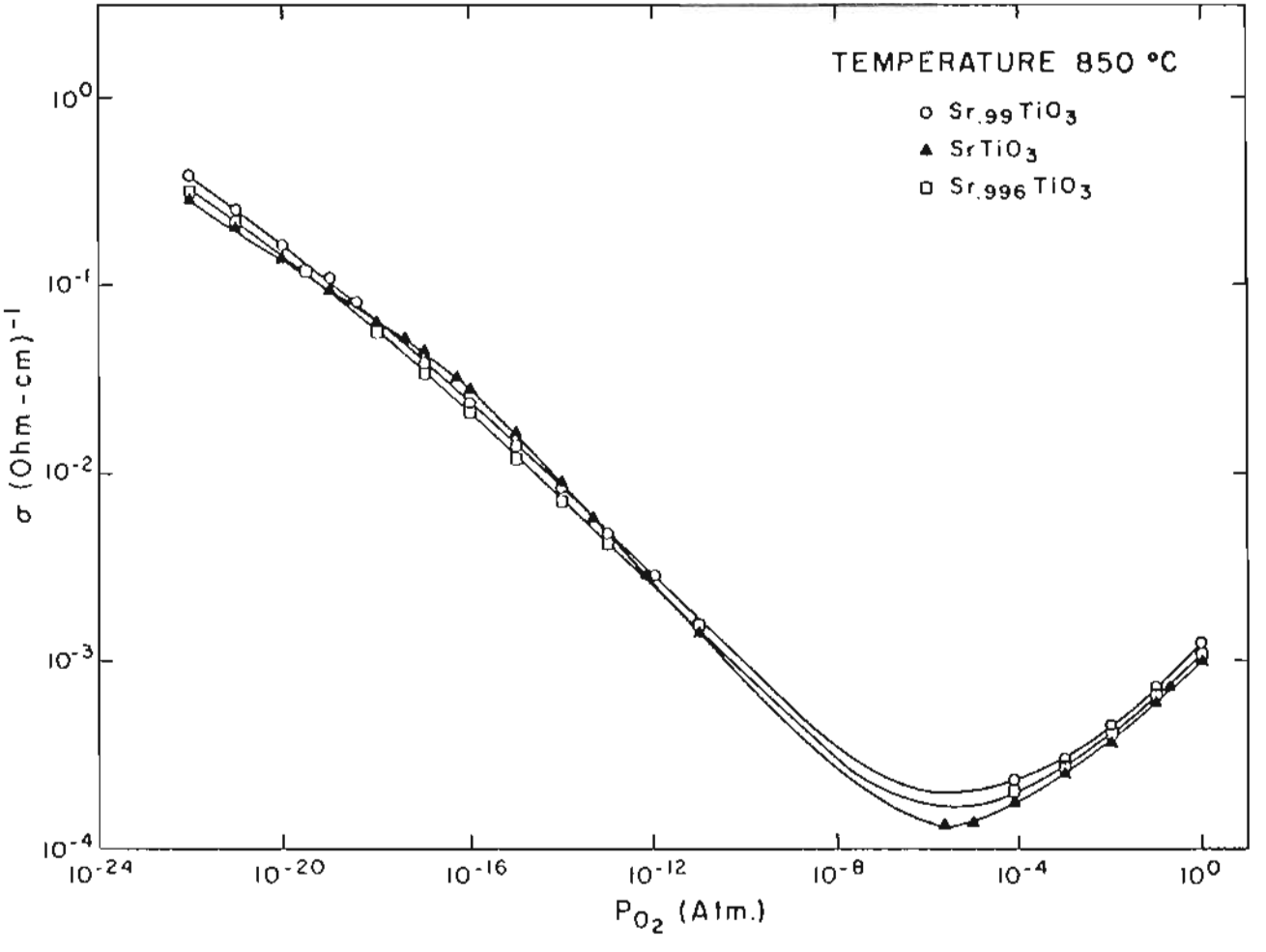

Figure 40. ELECTRICAL CONDUCTIVITY IN $SrTiO_3$, $Sr_{.996}TiO_3$, and $Sr_{.99}TiO_3$ AT 850°C.

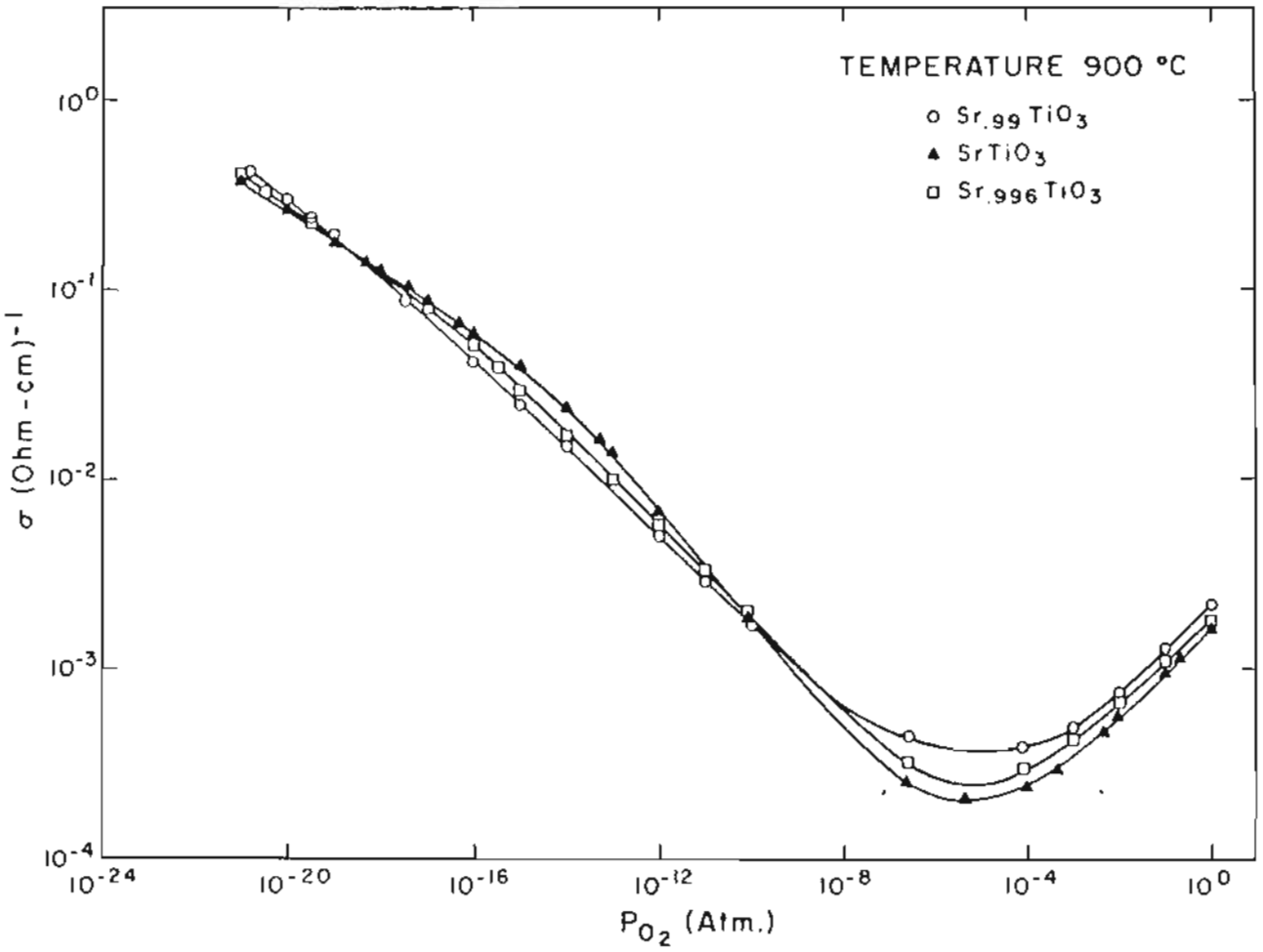

Figure 41. ELECTRICAL CONDUCTIVITY IN $SrTiO_3$, $Sr_{.996}TiO_3$, and $Sr_{.99}TiO_3$ AT 900°C.

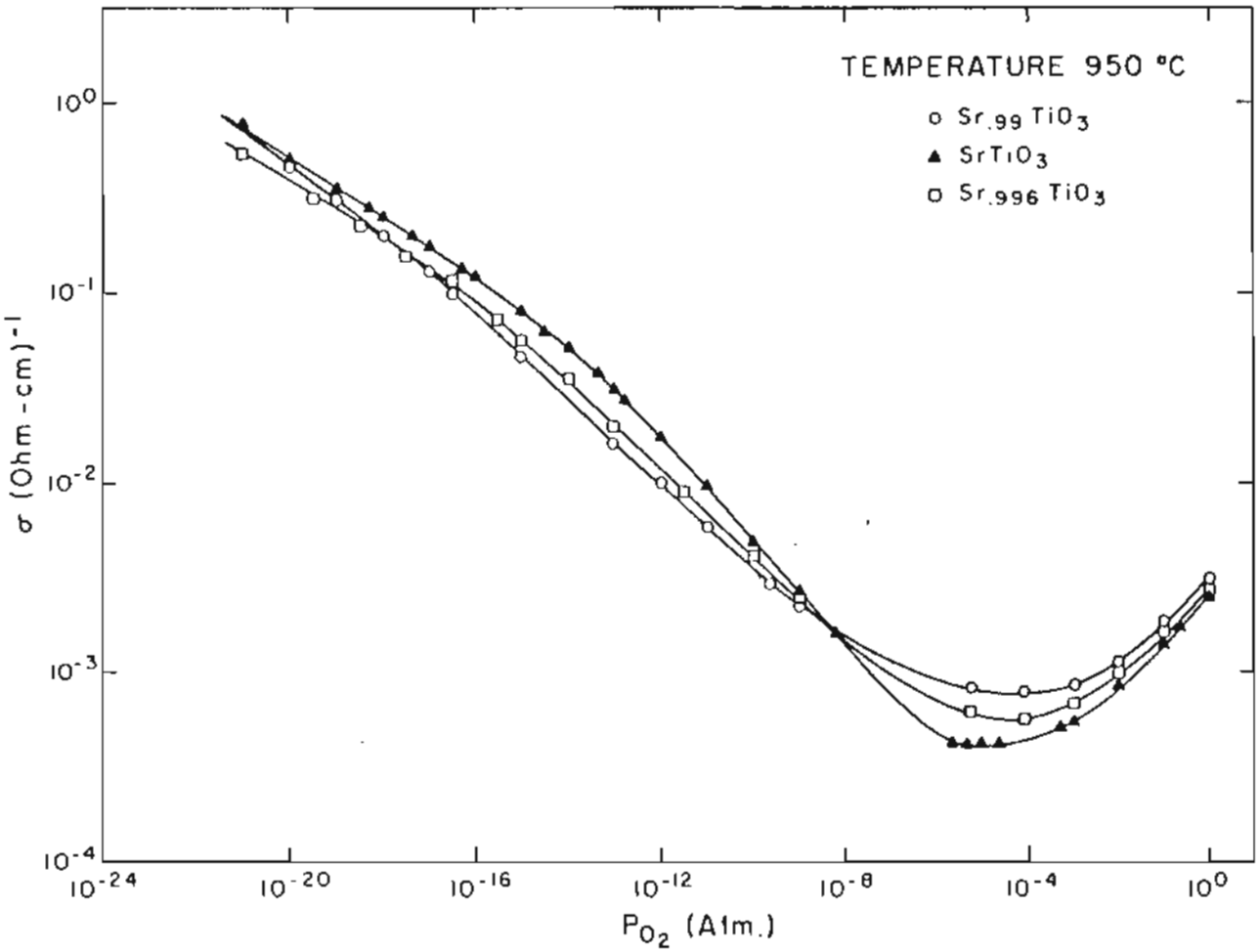

Figure 42. ELECTRICAL CONDUCTIVITY IN $SrTiO_3$, $Sr_{.996}TiO_3$, and $Sr_{.99}TiO_3$ AT 950°C.

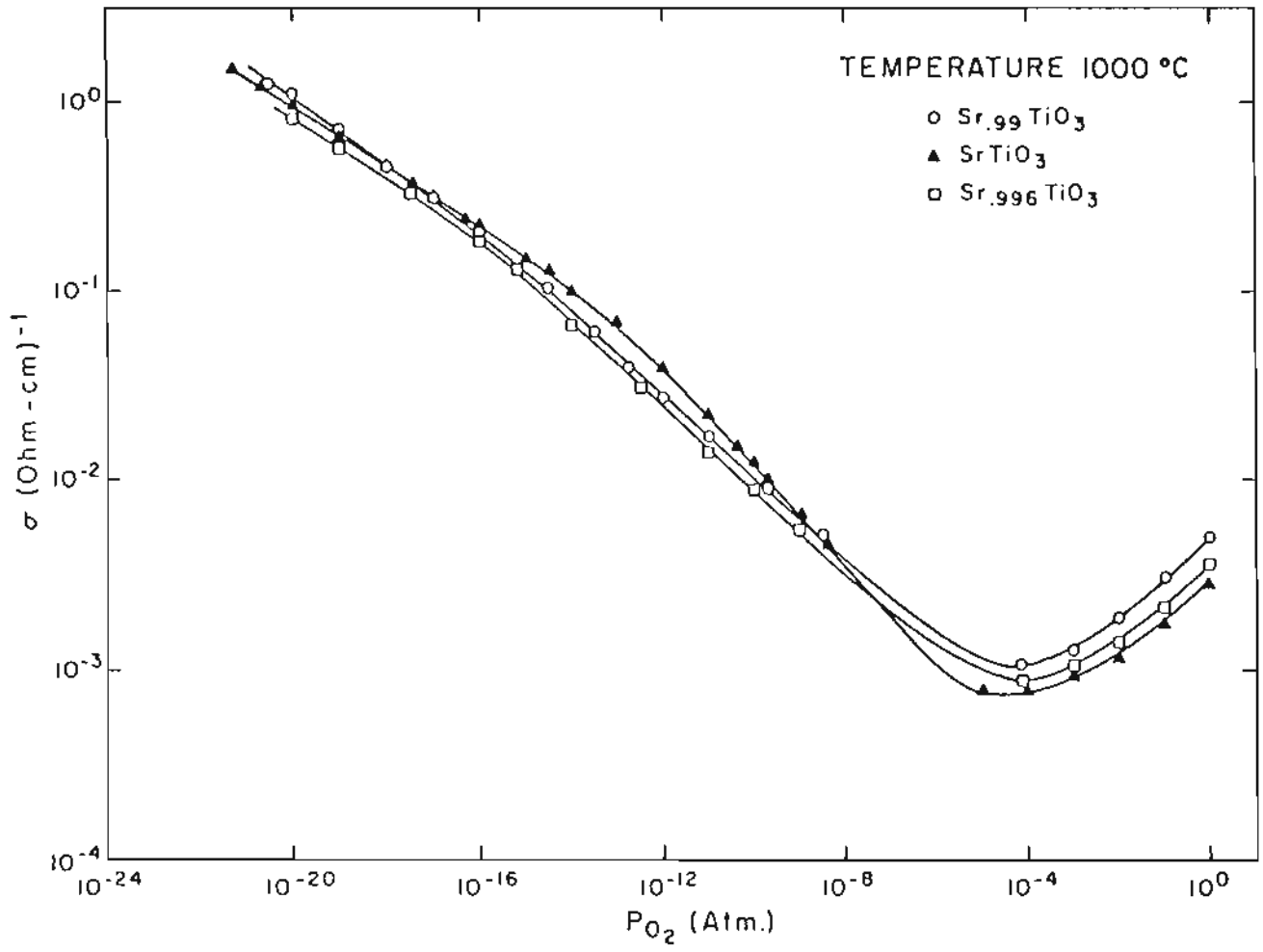

Figure 43. ELECTRICAL CONDUCTIVITY IN $SrTiO_3$, $Sr_{.996}TiO_3$, and $Sr_{.99}TiO_3$ AT 1000°C.

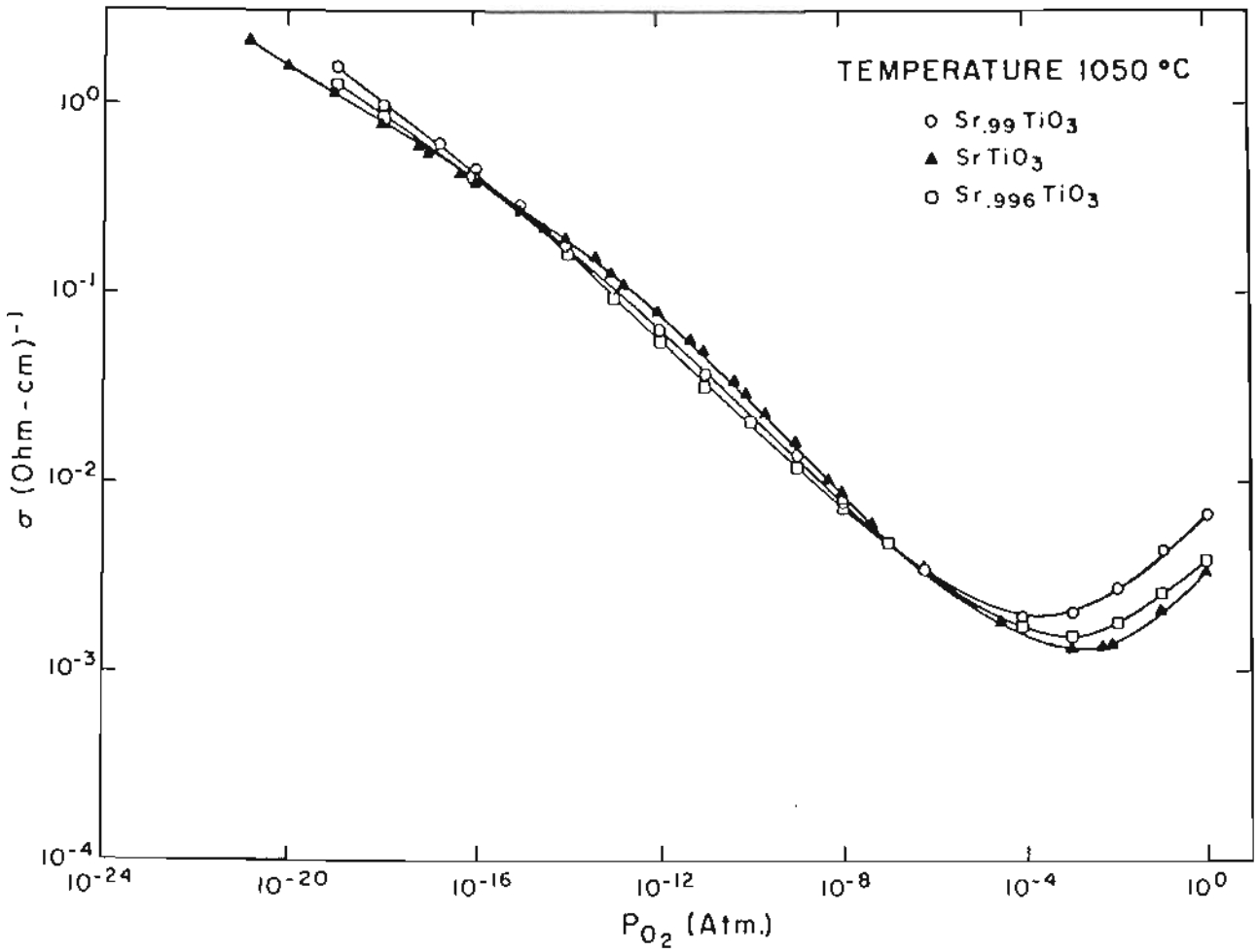

Figure 44. ELECTRICAL CONDUCTIVITY IN $SrTiO_3$, $Sr_{.996}TiO_3$, and $Sr_{.99}TiO_3$ AT 1050°C.

Table XI.

P_{O_2} DEPENDENCE OF CONDUCTIVITY IN $Sr_{.996}TiO_3$ IN THE REGION 10^{-21} - 10^{-16} ATM.

T (°C)	m for $\sigma_n \propto P_{O_2}^{-1/m}$
850	6.04
900	5.8
950	6.4
1000	6.15
1050	6.15

Table XII.

P_{O_2} DEPENDENCE OF CONDUCTIVITY IN $Sr_{.99}TiO_3$ IN THE REGION 10^{-21} - 10^{-16} ATM.

T (°C)	m for $\sigma_n \propto P_{O_2}^{-1/m}$
850	5.3
900	5.5
950	5.5
1000	5.5
1050	5.7

Table XIII.

P_{O_2} DEPENDENCE OF CONDUCTIVITY IN $Sr_{.996}TiO_3$ IN THE REGION 10^{-15} - 10^{-8} ATM.

T (°C)	m for $\sigma_n \propto P_{O_2}^{-1/m}$
850	4.4
900	4.2
950	4.4
1000	4.5
1050	4.6

Table XIV.

P_{O_2} DEPENDENCE OF CONDUCTIVITY IN $Sr_{.99}TiO_3$ IN THE REGION 10^{-15} - 10^{-8} ATM.

T (°C)	m for $\sigma_n \propto P_{O_2}^{-1/m}$
850	4.4
900	4.4
950	4.4
1000	4.6
1050	4.4

Table XV.

P_{O_2} DEPENDENCE OF CONDUCTIVITY IN $Sr_{.996}TiO_3$ IN THE p-TYPE REGION

T (°C)	m for $\sigma_p \propto P_{O_2}^{1/m}$
850	4.5
900	4.4
950	4.4
1000	4.4
1050	4.8

the same as observed in $SrTiO_3$. The P_{O_2} dependence of conductivity in both the samples are given in Tables XVI and XVII.

REGION I: ($P_{O_2} < 10^{-16}$ atm.)

Deviation from ideal Sr/Ti ratio must be accommodated by point defects. A number of mechanisms can be envisioned for the incorporation of excess TiO_2 into $SrTiO_3$ of ideal composition so as to make Sr/Ti ratio less than unity. The mechanisms include:

$$TiO_2 \rightleftharpoons Ti_i^{+4} + 2O_i^{-2} \tag{110}$$

$$TiO_2 \rightleftharpoons Ti_i^{+4} + O_2 + 4e' \tag{111}$$

$$TiO_2 \rightleftharpoons Ti_{Sr}^{+2} + Ti_{Ti} + 3O_o + O_i^{-2} \tag{112}$$

$$2TiO_2 \rightleftharpoons Ti_{Sr}^{+2} + Ti_{Ti} + 3O_o + 2e' + 1/2\ O_2 \tag{113}$$

$$TiO_2 \rightleftharpoons Ti_{Ti} + 2O_o + V_{Sr}'' + V_o^{\cdot\cdot} \tag{114}$$

$$TiO_2 + 1/2\ O_2 \rightleftharpoons Ti_{Ti} + 3O_o + V_{Sr}'' + 2h^{\cdot} \tag{115}$$

Equations (111), (113), and (115), which generate electronic defects, can be excluded because of the observed lack of the Sr/Ti ratio on the electronic conductivity. Both Ti_i^{+4} and O_i^{-2} are unfavorable defects in the close-packed perovskite structure, so Equation (114), involving the formation of V_{Sr}'' and $V_o^{\cdot\cdot}$, is the most probable choice. This is in accord with our electrical conductivity measurements in $SrTiO_3$ which showed that

Table XVI.

P_{O_2} DEPENDENCE OF CONDUCTIVITY IN $Sr_{.99}TiO_3$ IN THE p-TYPE REGION

T (°C)	m for $\sigma_p \propto P_{O_2}^{1/m}$
850	4.4
900	4.3
950	4.4
1000	4.8
1050	4.8

Table XVII.

ACTIVATION ENTHALPIES FOR CONDUCTION IN $Sr_{.996}TiO_3$ IN THE REGION 10^{-21} - 10^{-16} ATM.

P_{O_2} (atm.)	Activation Enthalpies [Kcal/mole]
10^{-21}	109.75
10^{-20}	109.75
10^{-19}	109.75
10^{-18}	115.24
10^{-17}	115.24
10^{-16}	116.60

$V_o^{\cdot\cdot}$ is the preferred defect for oxygen deficiency in $SrTiO_3$, and they appear to be the dominant ionic defect in the closely related $BaTiO_3$[20, 21,47] in the oxygen-deficient region.

The assignment of double effective charges to both kinds of vacancies implies that both donor levels associated with oxygen vacancies lie above both acceptor levels associated with strontium vacancies. This is supported by evidence that the oxygen vacancies in the similar compound $BaTiO_3$ are either substantially,[21] or entirely,[20] doubly ionized at temperatures of 800°C and above, and that the oxygen vacancy levels in $SrTiO_3$ are extremely close to the conduction band.[37]

The equilibrium incorporation reaction, Equation (114), can be characterized by a mass-action expression

$$[V''_{Sr}]\,[V_o^{\cdot\cdot}] = K_{114}\, a_{TiO_2} \tag{116}$$

where a_{TiO_2} is the equilibrium activity of TiO_2.

When oxygen deficiency is also incorporated into such a system by reducing the oxygen activity in equilibrium with the SrO-deficient $SrTiO_3$, we should consider

$$O_o \rightleftharpoons 1/2\ O_2 + V_o^{\cdot\cdot} + 2e' \tag{117}$$
$$(= \text{Eq. } 99)$$

and

$$[V_o^{\cdot\cdot}]\,[n]^2 = K_{117}\, P_{O_2}^{-1/2} \tag{118}$$

It is clear that a substantial built-in SrO deficiency will initially exceed the disorder from the oxygen loss described in Equation (117). For

this case the electrical neutrality condition will read,

$$[V''_{Sr}] = [V_o^{\cdot\cdot}] = K_{208}^{1/2}\ a_{TiO_2}^{1/2} \tag{119}$$

From equations (118) and (119) we can then obtain

$$[n] = \left[\frac{K_{211}^{1/2}}{K_{208}^{1/4}\ a_{TiO_2}^{1/4}}\right] P_{O_2}{}^{-1/4} \tag{120}$$

The data in Figures 38 and 39 and Tables XI and XII indicate that at low P_{O_2} region, the slope is $\approx(-1/6)$ for (Sr/Ti) = 0.996 and 0.99. This is similar to the slope found in strontium titanate with ideal cationic ratio (see Table VI). This indicates that at low P_{O_2} the electrical neutrality condition should be

$$[n] \simeq 2[V_o^{\cdot\cdot}] \tag{121}$$

to give

$$[n] \approx (2K_{117})^{1/3}\ P_{O_2}{}^{-1/6} \approx K_{122}\ P_{O_2}{}^{-1/6}\ \exp\left\{\frac{-\Delta H_n}{3RT}\right\} \tag{122}$$

where ΔH_n is the enthalpy of reaction for Equation (117). For Equation (121) to hold, the oxygen deficiency must greatly exceed the built-in SrO deficiency.

Our thermogravimetric work indicates a maximum value of about 4.5×10^{-3} for x in $SrTiO_{3-x}$ when reduction was carried out in hydrogen (corresponds to the most extreme conditions used in this study) at 1050°C and

a value of about 1.2×10^{-3} is obtained when the reduction was carried out at an oxygen partial pressure value of 10^{-15} atm. For Equation (121) to be a valid expression for the dominant charged defects, no other charged defect can be present in excess of about 4×10^{-4} per cation site (400 ppm atomic). But for the samples under consideration the SrO deficiency amounts to 4000-10000 ppm (Sr/Ti = 0.996 and 0.99). Our experimental results give a slope $\approx -1/6$ for the oxygen pressure dependence in the lower P_{O_2} range and the absolute values are very close to the values obtained in strontium titanate with ideal cationic ratio (Figures 40-44). This could be possible only when the defects related to the SrO deficiency are associated into neutral complexes, such as vacancy pairs, to such an extent that the residual, isolated, charged defects from this source do not affect the condition of charge neutrality, Equation (121), and thus have no influence on the oxygen-deficient defect chemistry. This association can be represented as

$$V''_{Sr} + V^{\cdot\cdot}_{O} \rightleftharpoons (V''_{Sr}\ V^{\cdot\cdot}_{O}) \tag{123}$$

where the parentheses indicate that the enclosed species are electrostatically bound to adjacent lattice sites.

The mass-action expression for Equation (123) gives

$$\frac{\left[(V''_{Sr}\ V^{\cdot\cdot}_{O})\right]}{[V''_{Sr}]\ [V^{\cdot\cdot}_{O}]} = K_a(T) = K'_a \exp\left(\frac{-\Delta H_a}{RT}\right) \tag{124}$$

where ΔH_a, the enthalpy of association, is a negative number for this

exothermic process. From Equation (124) one can estimate the value of ΔH_a necessary to keep the concentration of the dissociated vacancies below, say, 10 ppm level for the experimental temperature range. Kröger[113] has reviewed published parameters for defect association and showed that the entire pre-exponential term in the association relationships such as Equation (124), i.e., the entropy factor, is generally close to unity. At the expense of introducing a considerable uncertainty, we shall assume that to be the case. With this assumption Equation (124) reduces to $\Delta H_a = -18.4$ RT for Sr/Ti = .99 with $[V''_{Sr}] = [V_o^{\cdot\cdot}] = 10$ ppm. The calculated values of $-\Delta H_a$ then range from 2.1 ev at 1050°C to 1.78 ev at 850°C for the sample with Sr/Ti = 0.99. Of course, the presence of oxygen vacancies related to the accidental acceptor impurities in the sample will suppress the dissociation to some extent. For the case of Sr/Ti = 0.99, $[V_o^{\cdot\cdot}] = 100$ ppm would reduce the absolute value of the calculated values of ΔH_a by about 15%. Moreover, the values will be even smaller if the entropy term favors the dissociation, which is not unlikely. An association enthalpy of ≈2 ev would be adequate to provide the association to be sufficiently advanced in the experimental temperature range used in this investigation. This value is not an unrealistic magnitude for doubly charged defects such as V''_{Sr} and $V_o^{\cdot\cdot}$ on adjacent lattice sites, when it is recalled that the association enthalpies for divalent impurity cations and cation vacancies in alkali halides, e.g., $[Sr^{\cdot}_{Na}\ V'_{Na}]$ in NaCl is about -0.5 ev,[114,115] and there is enough evidence to suggest that ΔH_a for cation and anion vacancies in these crystals, e.g., $(V'_{Na}\ V^{\cdot}_{Cl})$ in NaCl, is about -1 ev.[114,115] The latter value is

larger than the former because these defects involve adjacent lattice sites and is thus the closer analog of the (V''_{Sr}, $V_O^{\cdot\cdot}$) complex discussed here. Even when only one of the defects is doubly charged, the degree of association can be significant to quite high temperatures. It has been proposed that defect pairs of the type $(M'_{Ni}\ V''_{Ni})'$ make significant contributions to the diffusion of Al^{+3} and Cr^{+3} in NiO up to nearly 1800°C.[116,117]

The region of very low P_{O_2}, where $n \propto P_{O_2}^{-1/6}$ has been observed for samples with Sr/Ti = 0.996 and 0.99 (see Figures 38 and 39). Samples prepared with Sr/Ti = 1, 0.996, 0.99 all behaved very similarly. There is no significant increase in conductivity between the samples with Sr/Ti = 0.99 and 0.996. From the known levels of oxygen deficiency, and the known levels of SrO deficiency, this condition of $\sigma \propto P_{O_2}^{-1/6}$ could not be achieved without substantial association of the SrO-deficient defects. Otherwise, reaction (117) could not become the dominant source of $[V_O^{\cdot\cdot}]$ at low pressures and the relationship $\sigma \propto P_{O_2}^{-1/6}$ would not be observed. The region of low P_{O_2}, where $\sigma \propto P_{O_2}^{-1/6}$ has also been observed in studies of $BaTiO_3$ with high deficient in BaO.[20-22]

An indication of the magnitude of ΔH_n, the enthalpy of the oxygen extraction reaction, is typically obtained from Arrhenius plots of the conductivity, as deduced from Equation (122). This procedure neglects the contributions from the temperature dependence of the carrier mobility or density of states. Arrhenius plots for the oxygen partial pressure region $<10^{-16}$ atm. are shown in Figures 45 and 46 for the samples with Sr/Ti = 0.996 and 0.99, respectively, and the calculated values of ΔH_n are

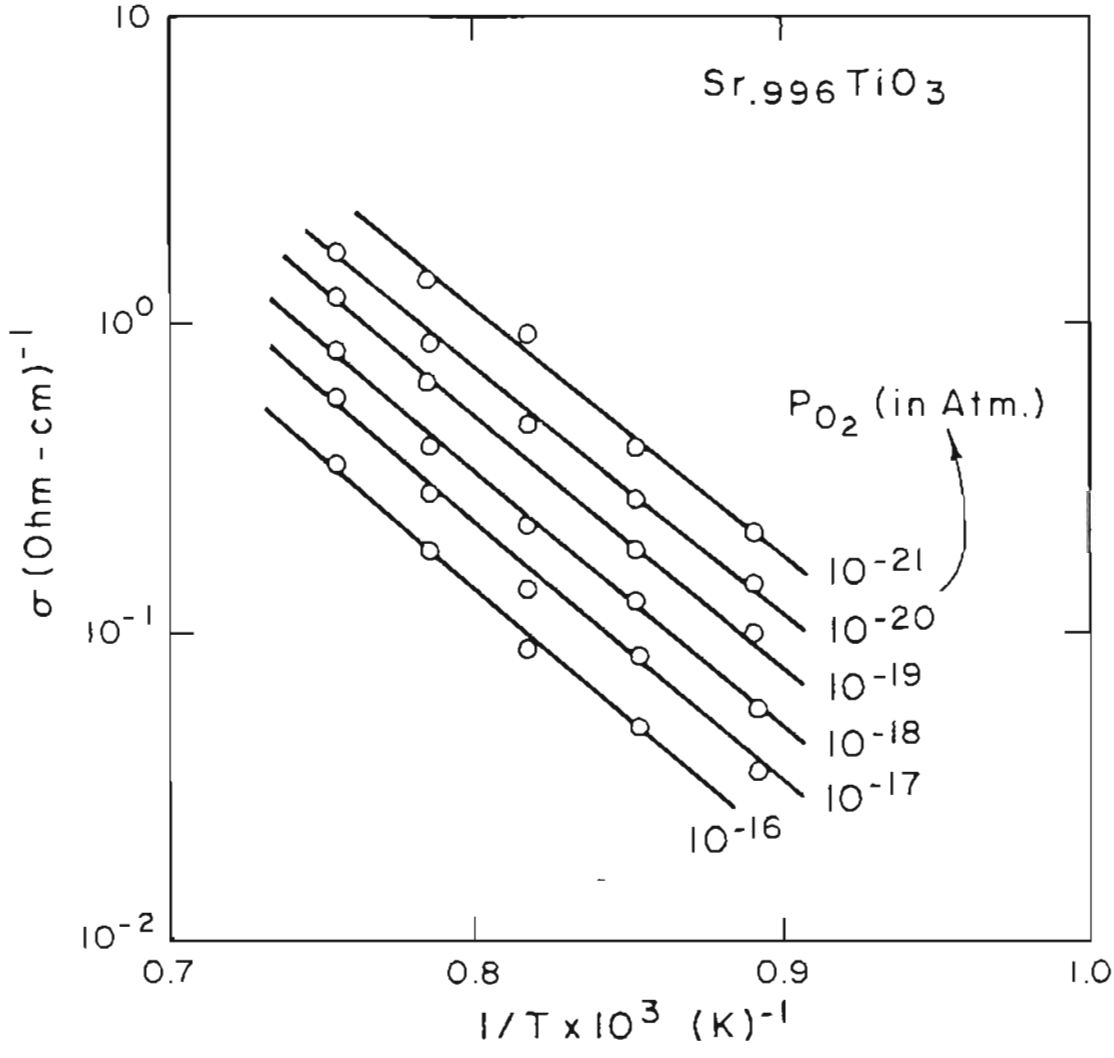

Figure 45. TEMPERATURE DEPENDENCE OF CONDUCTIVITY IN $Sr_{.996}TiO_3$ IN THE n-TYPE, OXYGEN-DEFICIENT REGION.

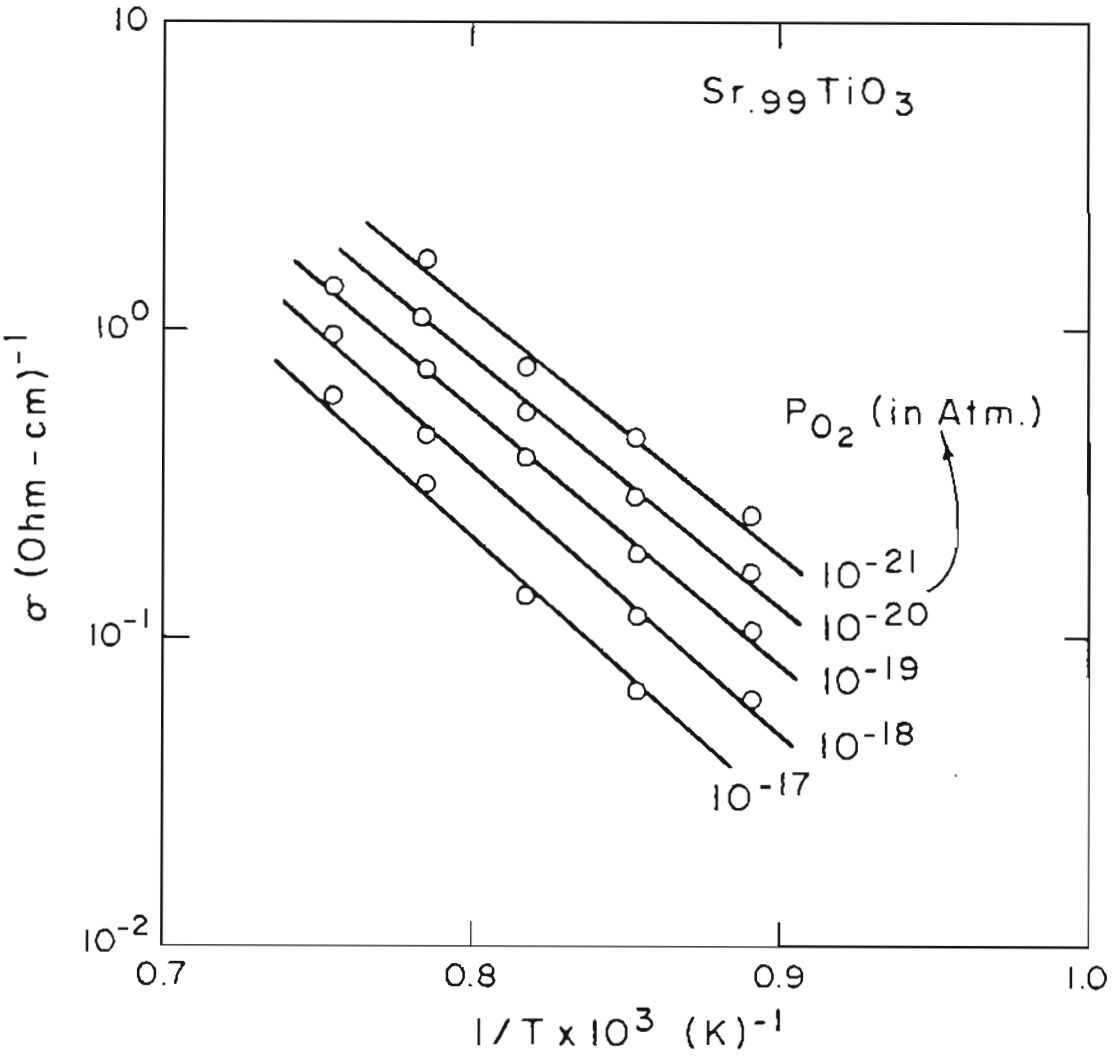

Figure 46. TEMPERATURE DEPENDENCE OF CONDUCTIVITY OF $Sr_{.99}TiO_3$ IN THE n-TYPE, OXYGEN-DEFICIENT REGION.

listed in Tables XVII and XVIII. Average values of 4.89 ev (112.72 Kcal/mole) and 4.98 ev (114.96 Kcal/mole) are obtained for the samples with cation-cation ratio equal to 0.996 and 0.99, respectively. An average value of 4.85 ev (111.8 Kcal/mole) is reported in Section (5.3) for the same P_{O_2} region in $SrTiO_3$ with ideal cationic ratio.

Region II. ($P_{O_2} = 10^{-15} - 10^{-8}$ atm.)

A slope of approximately (-1/4.4) is found for the log σ vs log P_{O_2} data (see Tables XIII and XIV). A slope of $\approx$-1/4 was observed in sample with ideal cationic ratio and was attributed due to the presence of an unknown negatively charged impurity, i.e., an acceptor such as Al, Fe, Mg, or Cr on Ti sites (see Section 5.3). The presence of small quantities of the acceptor impurities are responsible for the observed P_{O_2} dependence in the present samples too. The charge neutrality condition in this region is

$$2[V_O^{\cdot\cdot}] \simeq [A'] \qquad (105)$$

It was shown in Chapter I, that in a ternary compound ABO_3 with A/B <1, for the case of negligible defect association, there exists a region where the electronic conductivity varies as -1/4th power of oxygen partial pressure in certain P_{O_2} region (see Figure 15). If that were true, then as the Sr/Ti ratio is changed, there should be a considerable change in the observed conductivity values. But on the contrary the observed values are close to each other (Figures 40-44) for samples with Sr/Ti = 1, 0.996,

Table XVIII.

ACTIVATION ENTHALPIES FOR CONDUCTION IN $Sr_{.99}TiO_3$ IN THE REGION 10^{-21} - 10^{-16} ATM.

P_{O_2} (atm.)	Activation Enthalpies [Kcal/mole]
10^{-21}	109.75
10^{-20}	109.75
10^{-19}	112.49
10^{-18}	120.73
10^{-17}	122.10

and 0.99. This again suggests that defects related to the deviation from the ideal cationic ratio are associated into neutral complexes ($V''_{Sr}\ V^{\cdot\cdot}_{o}$).

The activation enthalpies for conduction in this region derived from Arrhenius plots (Figures 47 and 48) are shown in Tables XIX and XX. Average values of 4.04 ev (93.06 Kcal/mole) and 4.45 ev (102.51 Kcal/mole) are estimated for the samples with 0.4 and 1.0 mole % SrO deficiency respectively.

Region III. ($P_{O_2} > 10^{-4}$ atm.)

The conductivity in this region increases with oxygen partial pressure (see Figures 38 and 39), indicative of p-type, or oxygen excess conductivity. The slopes of log σ vs log P_{O_2} plots for both the samples with non-ideal Sr/Ti ratios are given in Tables XV and XVI. The slopes are in the range (1/4.4) - (1/4.8). The region of linearity increases in width with decreasing temperature as the p-n transition moves to lower P_{O_2}. In the same P_{O_2} region a slope of ≈1/4 was observed in $SrTiO_3$ (see Section 5.3) in the lower temperature ranges. In all the samples, the slopes decreased to ≈(1/4.6) - (1/4.8) as the temperature was increased to 1000°C and above.

The activation enthalpies of conduction, ΔH_p, derived from Arrhenius slopes, Figure 49 and 50, are given in Tables XXI and XXII. A value of 1.73 ev (39.9 Kcal/mole) and 2.32 ev (53.5 Kcal/mole) are typical for the samples with Sr/Ti = 0.996 and 0.99, respectively.

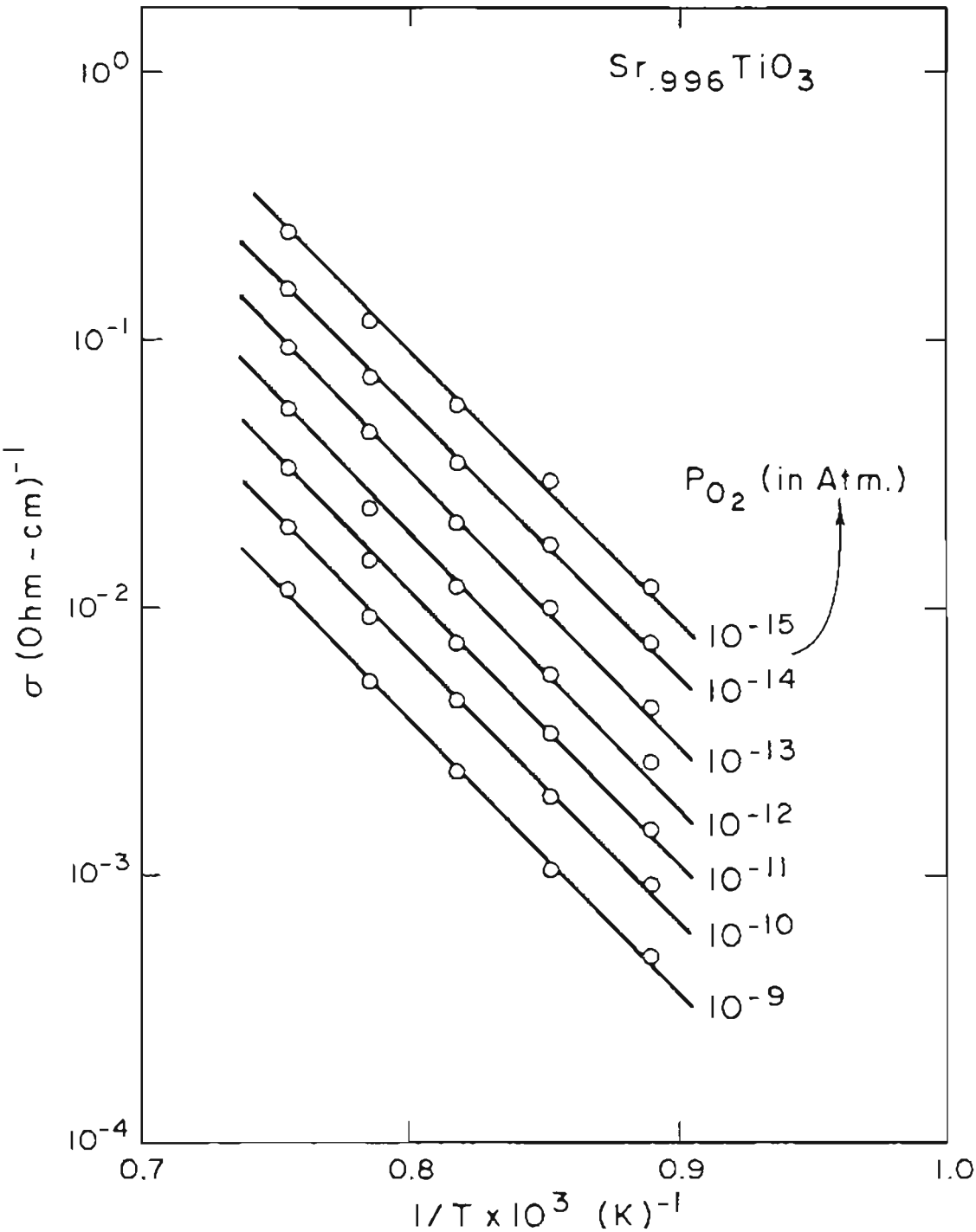

Figure 47. ARRHENIUS PLOTS FOR $Sr_{.996}TiO_3$ IN THE P_{O_2} REGION 10^{-15} - 10^{-9} ATM.

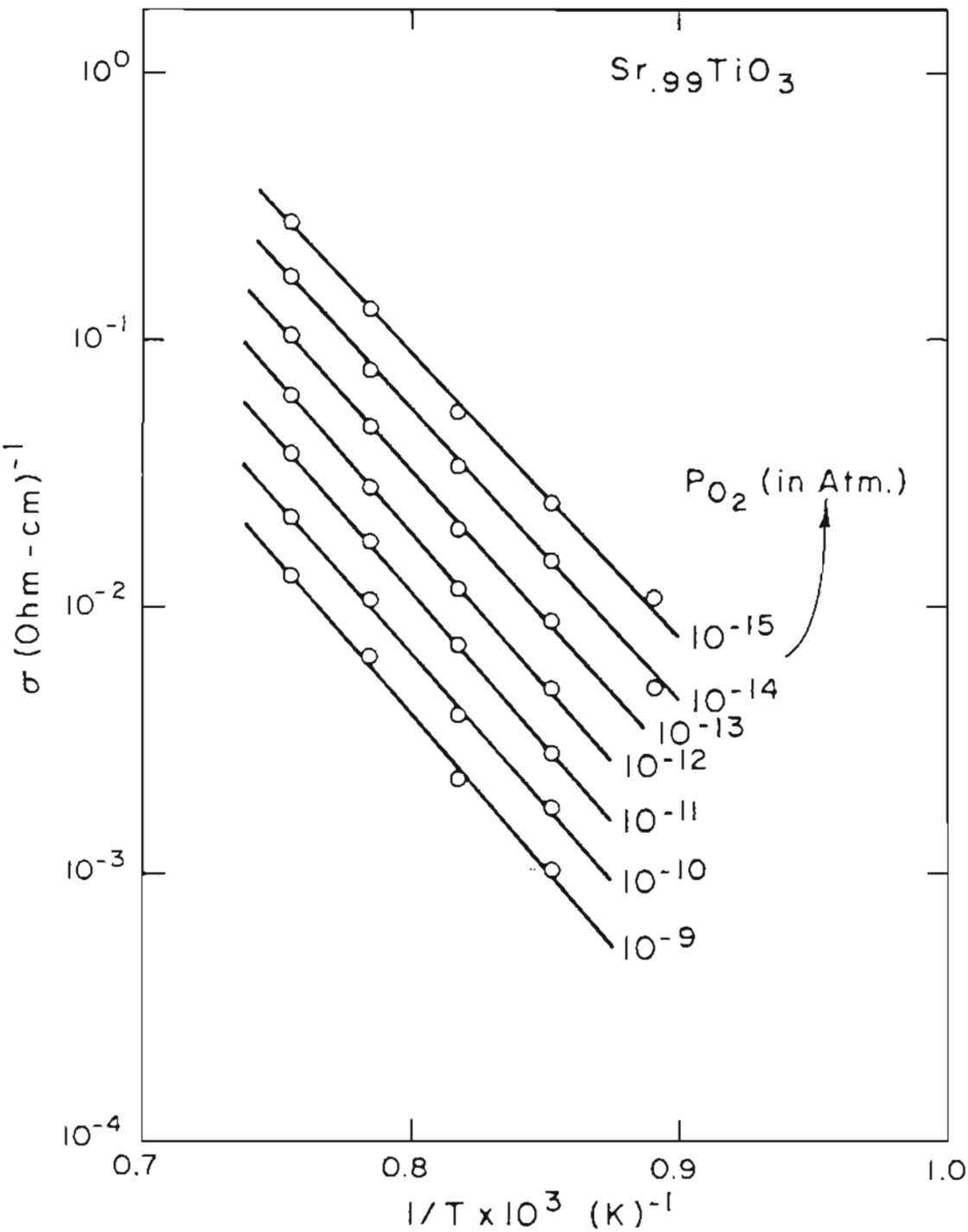

Figure 48. ARRHENIUS PLOTS FOR $Sr_{.99}TiO_3$ IN THE P_{O_2} REGION 10^{-15} - 10^{-9} ATM.

Table XIX.

ACTIVATION ENTHALPIES FOR CONDUCTION IN $Sr_{.996}TiO_3$ IN THE REGION 10^{-15} - 10^{-8} ATM.

P_{O_2} (atm.)	Activation Enthalpies [Kcal/mole]
10^{-15}	92.74
10^{-14}	90.54
10^{-13}	94.20
10^{-12}	94.20
10^{-11}	93.56
10^{-10}	92.37
10^{-9}	93.84

Table XX.

ACTIVATION ENTHALPIES FOR CONDUCTION IN $Sr_{.99}TiO_3$ IN THE REGION 10^{-15} - 10^{-8} ATM.

P_{O_2} (atm.)	Activation Enthalpies [Kcal/mole]
10^{-15}	97.85
10^{-14}	99.69
10^{-13}	101.52
10^{-12}	104.26
10^{-11}	104.72
10^{-10}	103.92
10^{-9}	105.63

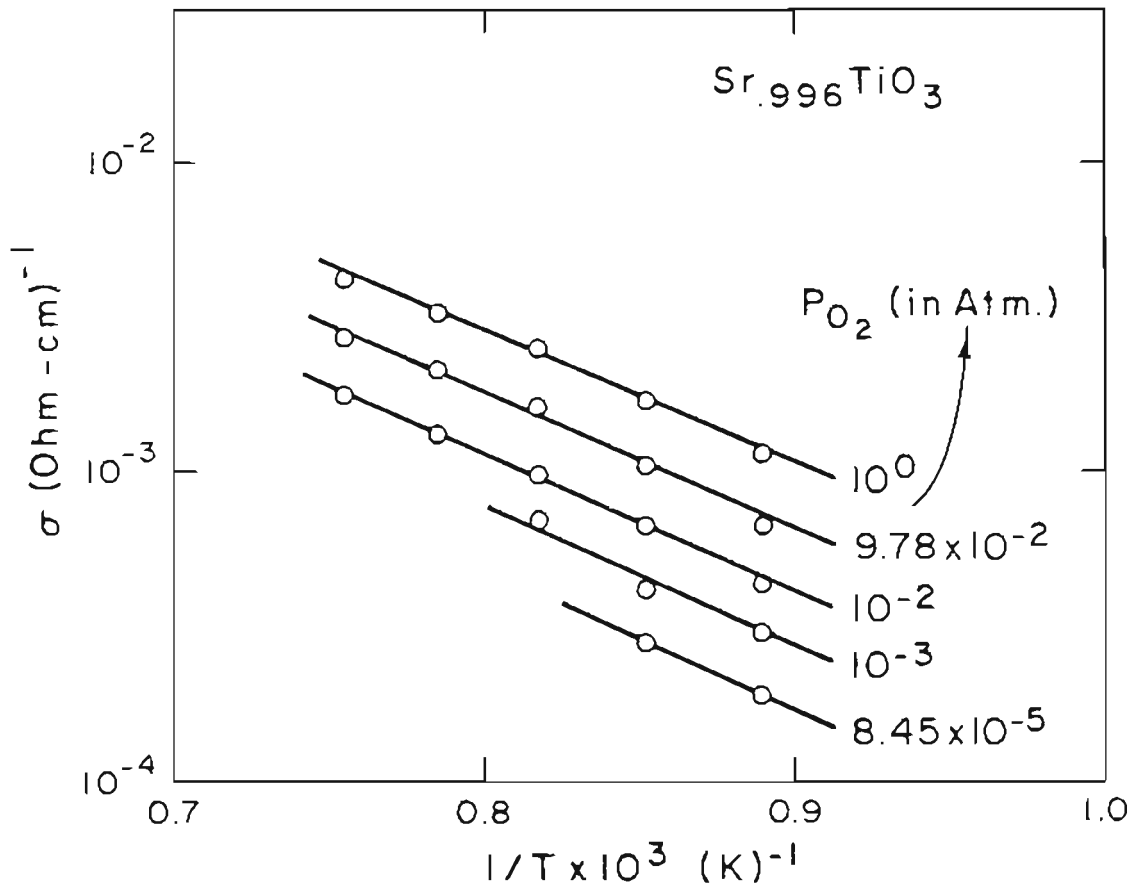

Figure 49. TEMPERATURE DEPENDENCE OF CONDUCTIVITY IN $Sr_{.996}TiO_3$ IN THE p-TYPE REGION.

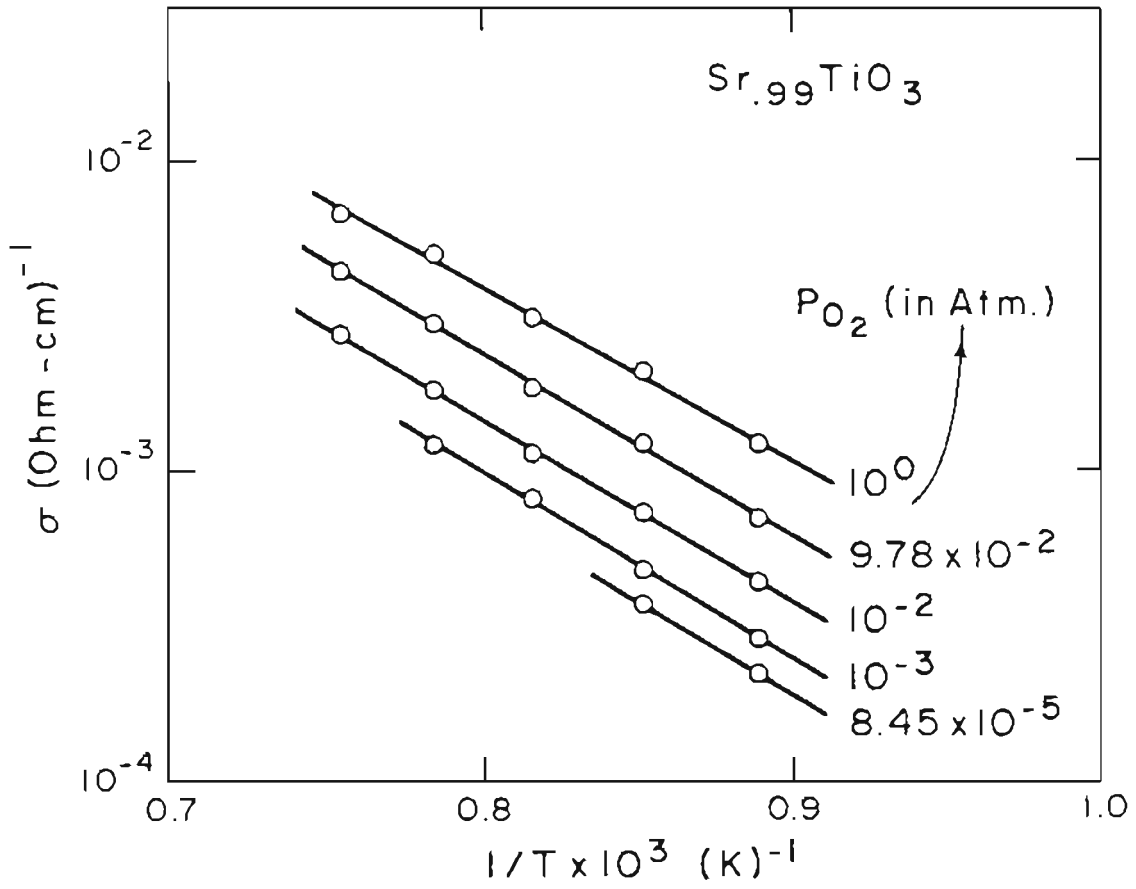

Figure 50. TEMPERATURE DEPENDENCE OF CONDUCTIVITY IN $Sr_{.99}TiO_3$ IN THE p-TYPE REGION.

Table XXI.

ACTIVATION ENTHALPIES FOR CONDUCTION IN $Sr_{.996}TiO_3$ IN THE p-TYPE REGION

P_{O_2} (atm.)	Activation Enthalpies [Kcal/mole]
10^{0}	38.96
9.78×10^{-2}	39.51
10^{-2}	40.24
10^{-3}	39.63
8.45×10^{-5}	41.16

Table XXII.

ACTIVATION ENTHALPIES FOR CONDUCTION IN $Sr_{.99}TiO_3$ IN THE p-TYPE REGION

P_{O_2} (atm.)	Activation Enthalpies [Kcal/mole]
10^{0}	50.85
9.78×10^{-2}	53.41
10^{-2}	53.96
10^{-3}	54.87
8.45×10^{-5}	54.42

It is apparent that a stoichiometric excess of oxygen can be incorporated into $SrTiO_3$ by a remarkably favorable process. In contrast to this low value, enthalpies of oxygen addition for a large number of rare earth and alkaline earth oxides are of the order of 3-6 ev.[118] The SrO deficiency makes available systematic oxygen vacancies which might accommodate a stoichiometric excess of oxygen without the need of creating a crystallographic excess.

$$(V''_{Sr}\ V^{\cdot\cdot}_{O}) + 1/2\ O_2 \rightleftharpoons O_O + V'_{Sr} + h^{\cdot} \tag{125}$$

$$\frac{[V'_{Sr}]\ [p]}{[(V''_{Sr}\ V^{\cdot\cdot}_{O})]} = K_{125}\ P_{O_2}{}^{1/2}$$

$$= K'_{125}\ P_{O_2}{}^{1/2}\ \exp\left\{\frac{-\Delta H_p}{RT}\right\} \tag{126}$$

$[(V''_{Sr}\ V^{\cdot\cdot}_{O})]$ can be taken as constant in Equation (126) for a given composition. The unassociated strontium vacancies that results when the oxygen vacancy in the neutral strontium vacancy-oxygen vacancy complex is filled must be singly ionized in order to lead to the +1/4 oxygen partial pressure dependence of the electrical conductivity data when Equation (126) is combined with the corresponding charge neutrality condition

$$[V'_{Sr}] \simeq [p] \tag{127}$$

The combination of equations (126) and (127), however, indicates that [p] and, therefore, the conductivity in this region should be proportional to $[V''_{Sr}\ V^{\cdot\cdot}_{O}]^{1/2}$. No such variation in the conductivity has been noted (see

Figures 40-44). Only in Figure 44, which is at 1050°C, is there a slight increase in conductivity in the p-type region for $Sr_{.99}TiO_3$ as compared with $Sr_{.996}TiO_3$ and $SrTiO_3$. This may be due to filling of a few unassociated oxygen vacancies that could be present at 1050°C and above.

One other source of oxygen vacancies is possible. Those necessary to compensate for a net excess of the acceptor impurity present in the samples. The oxygen is incorporated into the impurity-related oxygen vacancies. The reaction is the same as seen for the case of $SrTiO_3$ with Sr/Ti = 1. That reaction is,

$$[V_O^{\cdot\cdot}] + 1/2\ O_2 \rightleftharpoons O_O + 2h^{\cdot} \tag{108}$$

The charge neutrality condition in the near stoichiometric region is

$$2[V_O^{\cdot\cdot}] = [A'] \tag{105}$$

where A' is the singly ionized acceptor impurity such as Al'_{Ti}. From the mass-action expression for reaction (108) and the charge neutrality condition (105) we obtain

$$[p] = \left\{\frac{K'_{108}\ [A']}{2}\right\}^{1/2} P_{O_2}{}^{1/4} \exp\left\{\frac{-\Delta H_A}{2RT}\right\} \tag{128}$$

as long as an insignificant fraction of the impurity-related oxygen vacancies have been filled. This model fits the observed pressure dependence in this region. The ready availability of unassociated oxygen vacancies in this model explains the low enthalpy of oxygen incorporation.

The conductivity data obtained in samples with Sr/Ti < 1 suggest that the deviation from the ideal cation/cation ratio in this material is accommodated by the formation of neutral vacancy pairs (V''_{Sr}, $V_O^{\cdot\cdot}$). This is in agreement with the behavior found in $BaTiO_3$ by earlier investigators.[20,22]

5.5 Electrical Conductivity in Donor-Doped $SrTiO_3$

Electrical conductivity of polycrystalline $SrTiO_3$ doped with 0.1 - 2.0 at.% lanthanum was determined for the oxygen partial pressure range of 10^0 to 10^{-22} atm. and temperature range of 850-1050°C. Figures 51-55 show the dependence of electrical conductivity of lanthanum doped $SrTiO_3$ specimens on the oxygen partial pressure at temperatures from 850-1050°C. From the general shape of the curves two regions of the partial pressure can be clearly distinguished. In one region, the conductivity is almost independent of oxygen partial pressure (plateau region for higher lanthanum content samples) and in the other region, the conductivity decreases for all compositions as the oxygen partial pressure increases, characteristic of n-type conduction.

The compensation of extra charge in the case of a substitutional incorporation of lanthanum within the strontium sublattice in the perovskite $SrTiO_3$ may occur via an electronic or a lattice defect, according to the temperature and the oxygen partial pressure. For a moderately low oxygen partial pressure, a charge compensation by an extra electron is expected according to

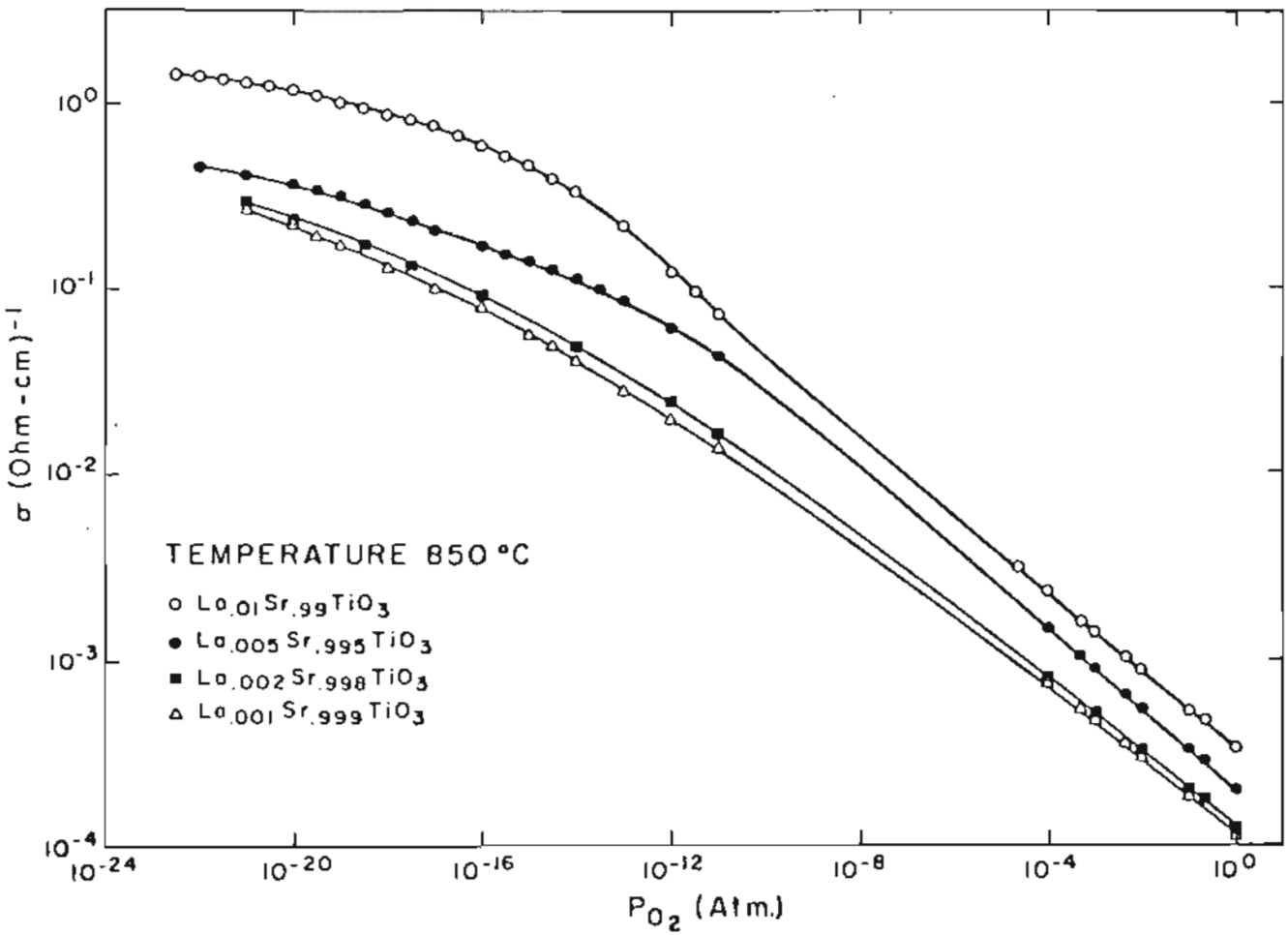

Figure 51. THE CONDUCTIVITY OF LANTHANUM DOPED $SrTiO_3$ AS A FUNCTION OF OXYGEN PARTIAL PRESSURE AT CONSTANT TEMPERATURE.

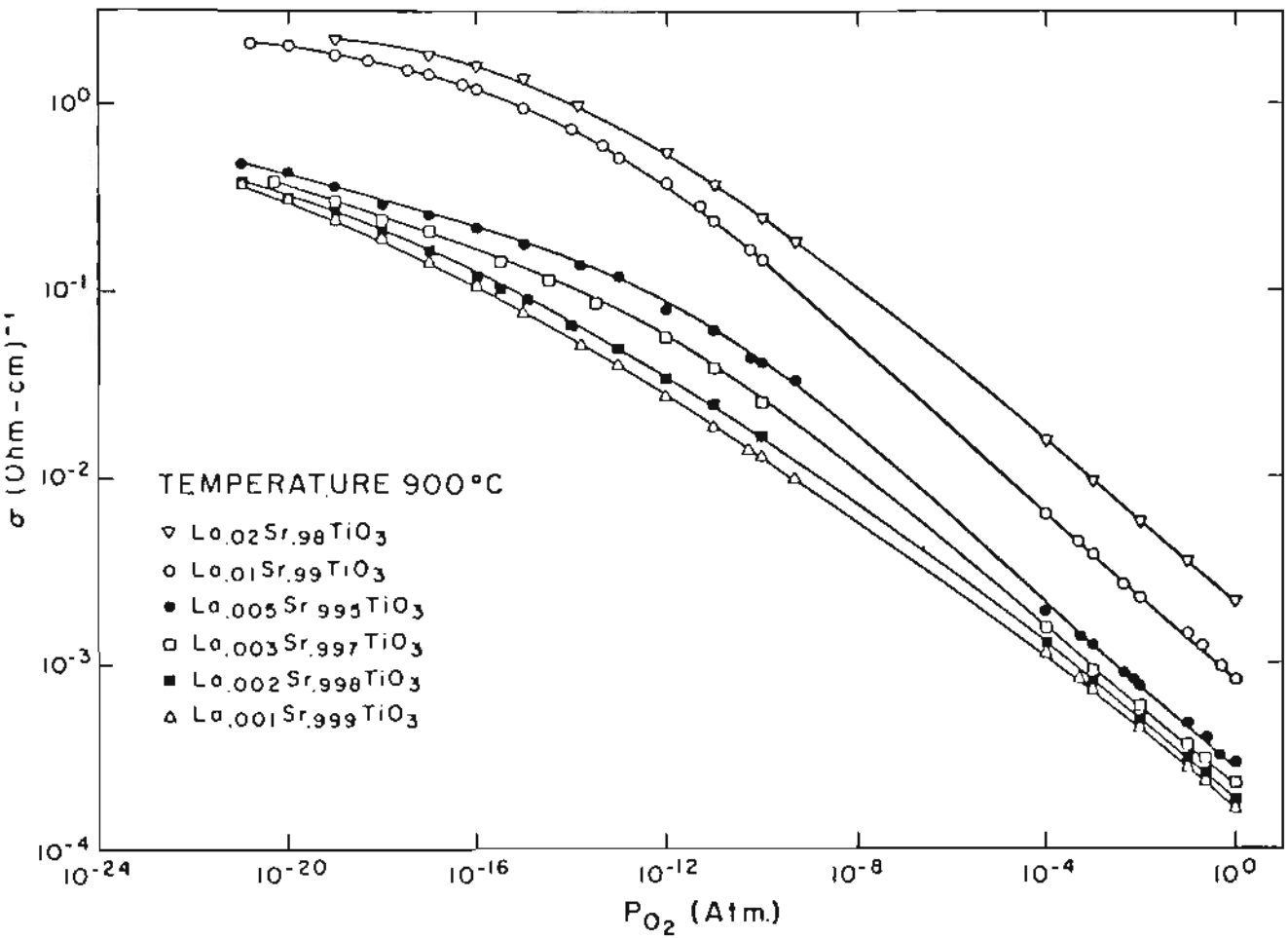

Figure 52. THE CONDUCTIVITY OF LANTHANUM DOPED $SrTiO_3$ AS A FUNCTION OF OXYGEN PARTIAL PRESSURE AT CONSTANT TEMPERATURE.

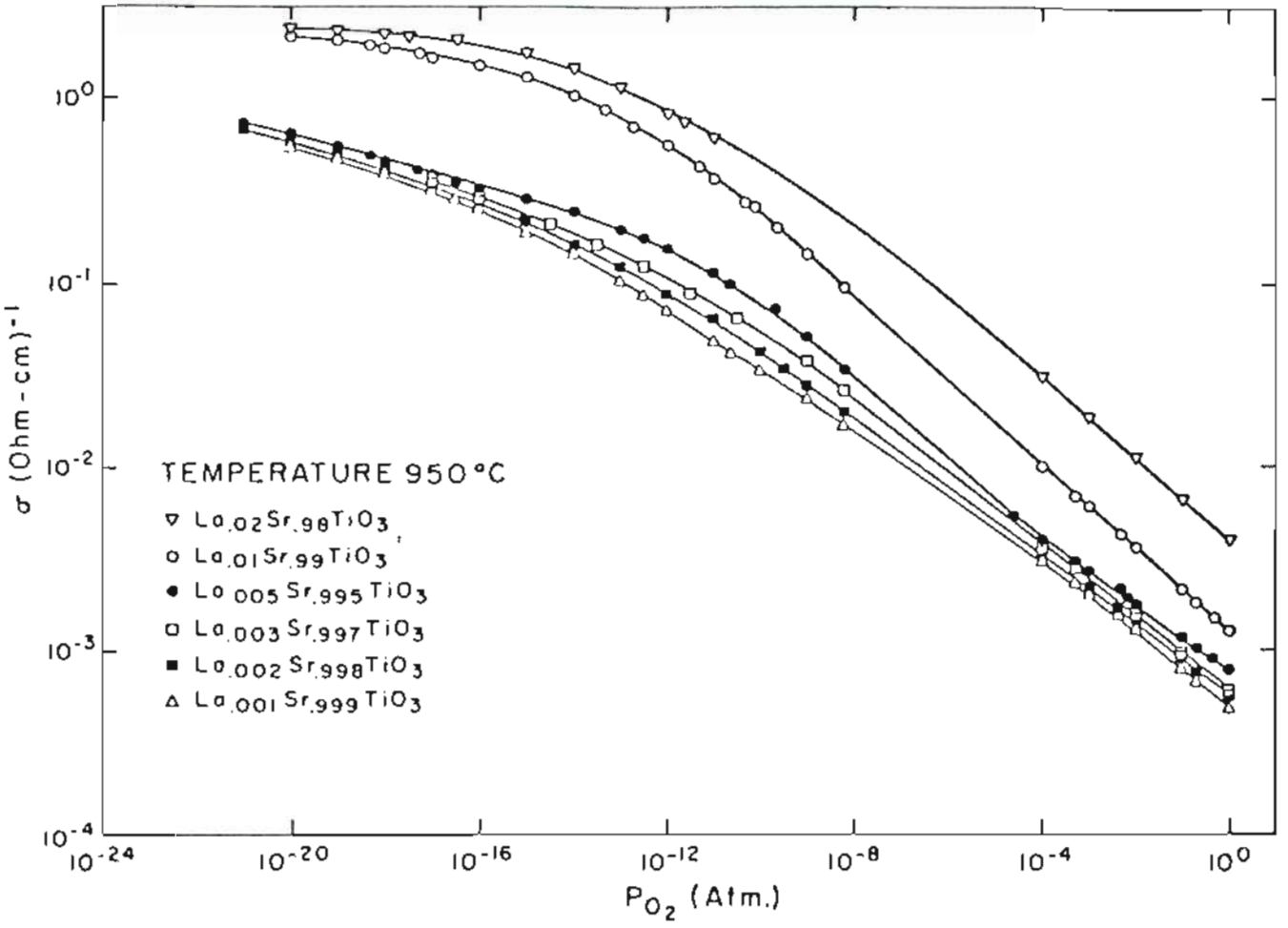

Figure 53. THE CONDUCTIVITY OF LANTHANUM DOPED $SrTiO_3$ AS A FUNCTION OF OXYGEN PARTIAL PRESSURE AT CONSTANT TEMPERATURE.

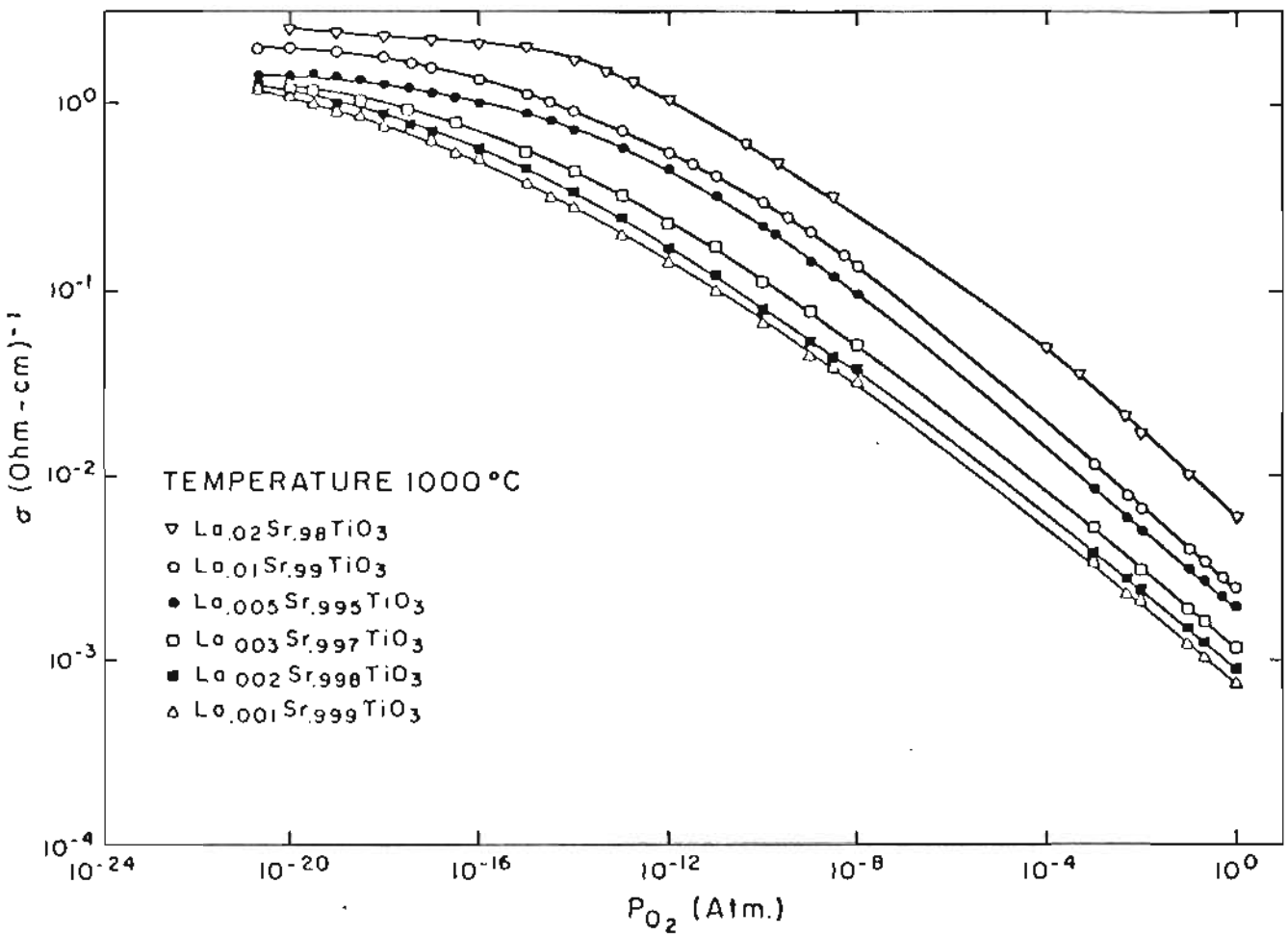

Figure 54. THE CONDUCTIVITY OF LANTHANUM DOPED $SrTiO_3$ AS A FUNCTION OF OXYGEN PARTIAL PRESSURE AT CONSTANT TEMPERATURE.

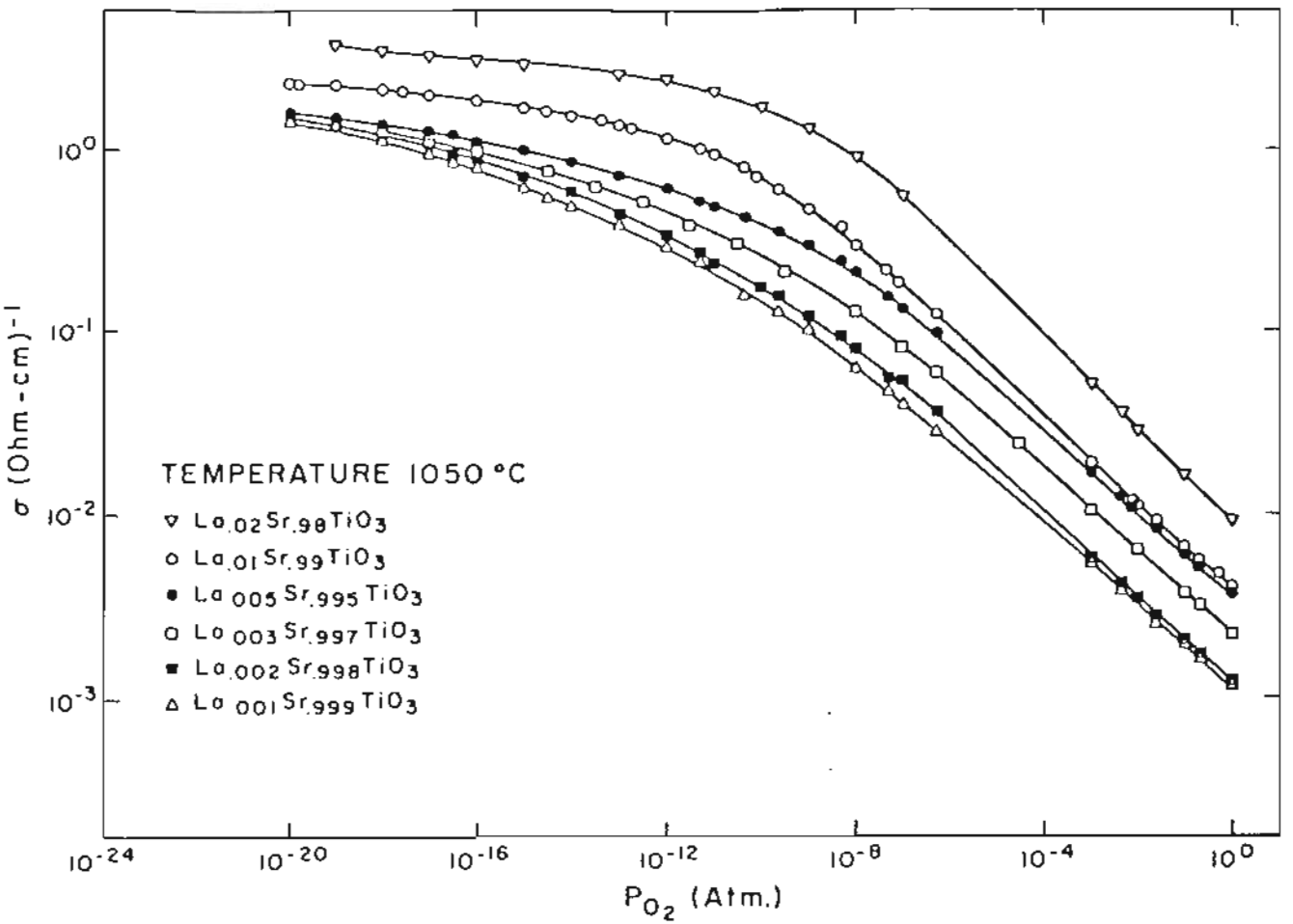

Figure 55. THE CONDUCTIVITY OF LANTHANUM DOPED $SrTiO_3$ AS A FUNCTION OF OXYGEN PARTIAL PRESSURE AT CONSTANT TEMPERATURE.

$$La_2O_3 \rightarrow 2\ La_{Sr}^{\cdot} + 2e' + 2O_o + 1/2\ O_2 \qquad (129)$$

In the case of a complete exhaustion of the lanthanum donor levels, the carrier concentration will depend linearly on lanthanum content in $La_x^{+3}\ Sr_{1-x}^{+2}\ Ti_x^{+3}\ Ti_{1-x}^{+4}\ O_3^{-2}$, at least for the amounts of lanthanum used in this investigation. The electrical neutrality condition under this condition will become:

$$[n] \simeq [La^{\cdot}] = \text{constant} \qquad (130)$$

Lanthanum substitution for strontium is compensated by the creation of equal numbers of Ti^{+3} ions and the negative defect concentration is independent of equilibrium oxygen activity. This compensation mechanism has been referred to as controlled electronic imperfection or electronic compensation.[113] As the lanthanum content increases the amount of Ti^{+3} should also increase. This should result in an increase in the conductivity.

From Figures 51-55 it is seen that as the oxygen partial pressure falls below 10^{-16} atm. the conductivity becomes almost independent of the oxygen pressure, particularly at high concentrations of lanthanum [1 and 2 at.%] a distinct plateau is formed. Within the plateau region the conductivity increases with lanthanum content as predicted by the above compensation behavior.

Under higher oxygen partial pressure conditions, the extra charge of the lanthanum may be compensated by a lattice defect. The main compensation mechanism considered here is by the strontium vacancy model, but

since we have a ternary oxide, the additional strontium that results from the strontium vacancies may combine with oxygen to form an SrO layer which can be built into the lattice in a reasonably ordered fashion. The formation of any SrO layer would be according to the equation

$$La^{\cdot}_{Sr} + 1/2\ Sr_{Sr} + Ti'_{Ti} + 1/4\ O_2 \rightleftharpoons 1/2\ (SrO) + 1/2\ V''_{Sr} + Ti_{Ti} + La^{\cdot}_{Sr} \quad (131)$$

In this region, the donor dopant is compensated ionically by metal deficiency. This compensation mechanism has been referred to as controlled atomic imperfection,[34] self-compensation,[27,32,33] and stoichiometric compensation.[27] For large concentrations of donor dopants in transition metal oxides Eror and Smyth,[27] and Eror[92] have shown that the donor dopant is compensated ionically by metal deficiency at high oxygen activities. This means that:

$$[La^{\cdot}] \simeq 2[V''_{Sr}] = \text{constant} \quad (132)$$

Applying the quasi-chemical mass action relation to Equation (131),

$$K_{131} = \frac{[V''_{Sr}]^{1/2}}{P_{O_2}^{1/4}\,[Ti'_{Ti}]} \quad (133)$$

where $[Ti'_{Ti}]$ represents Ti^{+3} on Ti^{+4} site. $[Ti'_{Ti}]$ is the number of free electrons available for conduction process. Therefore, Equation (133) together with Equation (132) yields,

$$[n] \propto P_{O_2}^{-1/4} \quad (134)$$

For oxygen partial pressures greater than 10^{-16} atm. the observed conductivity decreases with P_{O_2} which is characteristic of n-type conduction. The slopes of log σ vs. log P_{O_2} plots in Figures 51-55 for different temperature and concentration of lanthanum (see Table XXIII) are scattered in the region (-1/4.0) - (-1/4.7). This observed oxygen pressure dependence of conductivity suggests that the lanthanum donors are predominantly compensated by doubly ionized strontium vacancies. In this region, the electron hole concentration will increase to the +1/4 power of oxygen partial pressure. At certain oxygen pressure value, the electron hole concentration will become greater than electrons and the material will become p-type. Since the p-type conduction is not observed within the experimental conditions here, we suggest that for lanthanum doped $SrTiO_3$, the electron hole contribution to the electrical conductivity should appear only at a very high oxygen pressure, well beyond P_{O_2} = 1 atm.

The activation energy of the conduction in the ionic compensation region is obtained from Arrhenius plots of the conductivity (Figures 58-61). The activation enthalpies calculated from the Arrhenius plots are given in Table XXIV for different samples investigated. The variation of mobility and density of states with temperature are neglected in evaluating the activation energy for conduction. The average values of 1.66, 1.63, 2.11, 1.90, 1.64, and 1.26 ev are obtained for the activation enthalpies for conduction for the lanthanum concentrations of 0.1, 0.2, 0.3, 0.5, 1.0, and 2.0 at.%, respectively.

Table XXIII.

P_{O_2} DEPENDENCE OF CONDUCTIVITY IN THE IONIC COMPENSATION REGION

Temperature (°C)	Amounts of La^{+3}: in at. %	m for $\sigma_n \propto P_{O_2}^{-1/m}$ 0.1	0.2	0.3	0.5	1.0	2.0
850		4.6	4.7	-	4.5	4.6	-
900		4.4	4.7	4.7	4.4	4.4	4.6
950		4.6	4.7	4.7	5.0	4.3	4.3
1000		4.5	4.5	4.7	4.5	4.5	4.3
1050		4.5	4.5	4.4	4.4	4.2	4.0

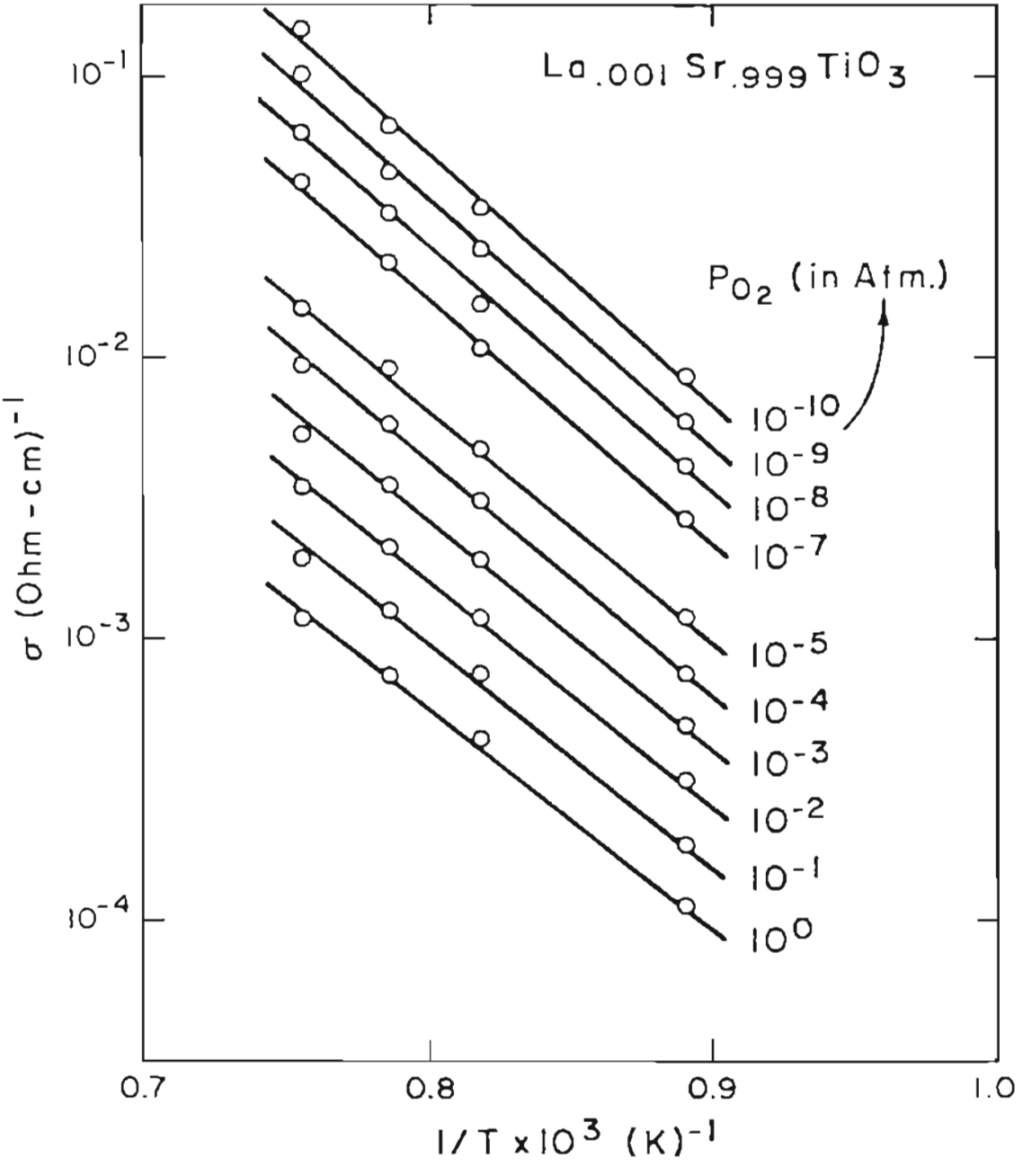

Figure 56. TEMPERATURE DEPENDENCE OF CONDUCTIVITY OF LANTHANUM DOPED $SrTiO_3$.

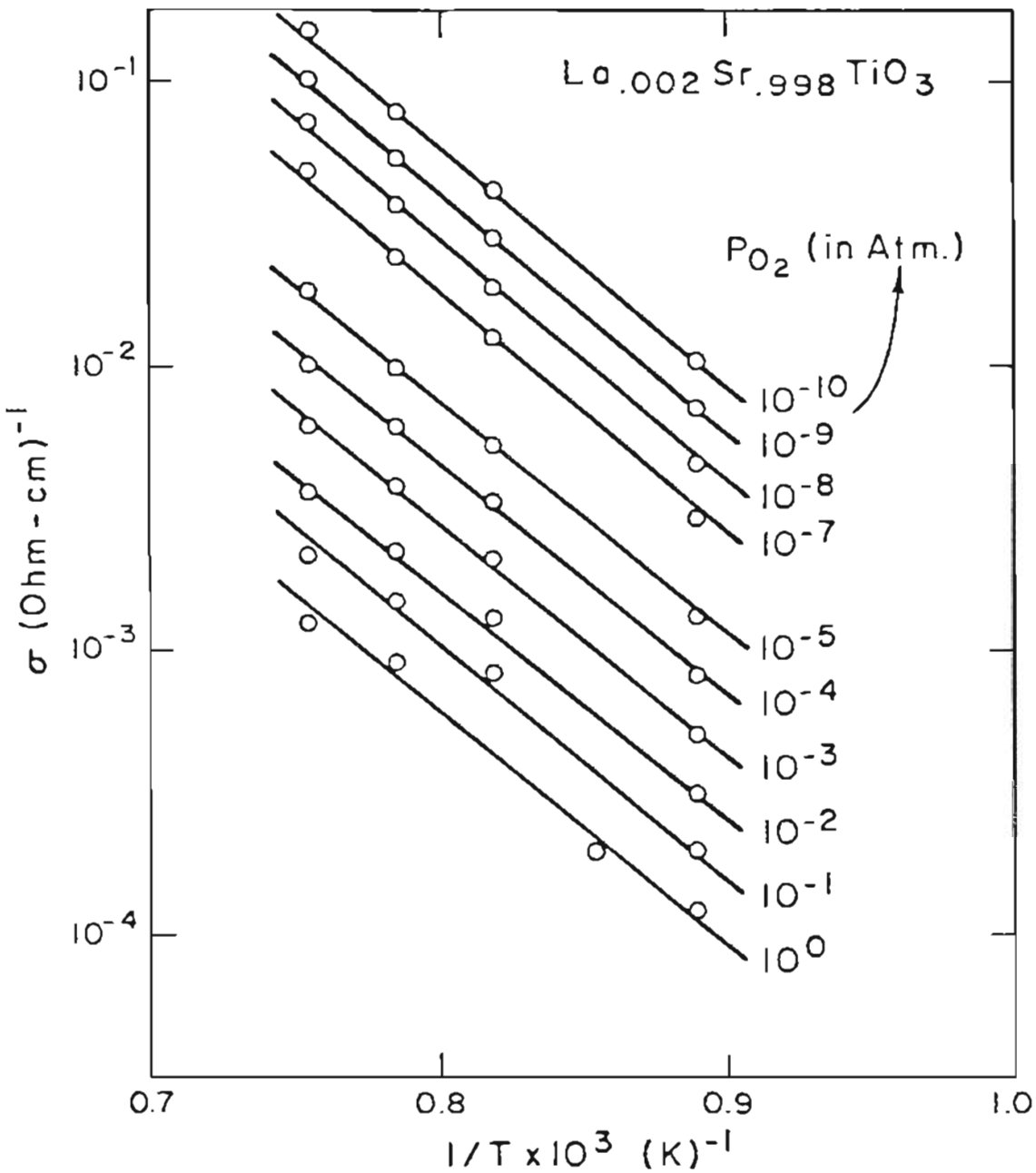

Figure 57. TEMPERATURE DEPENDENCE OF CONDUCTIVITY OF LANTHANUM DOPED $SrTiO_3$.

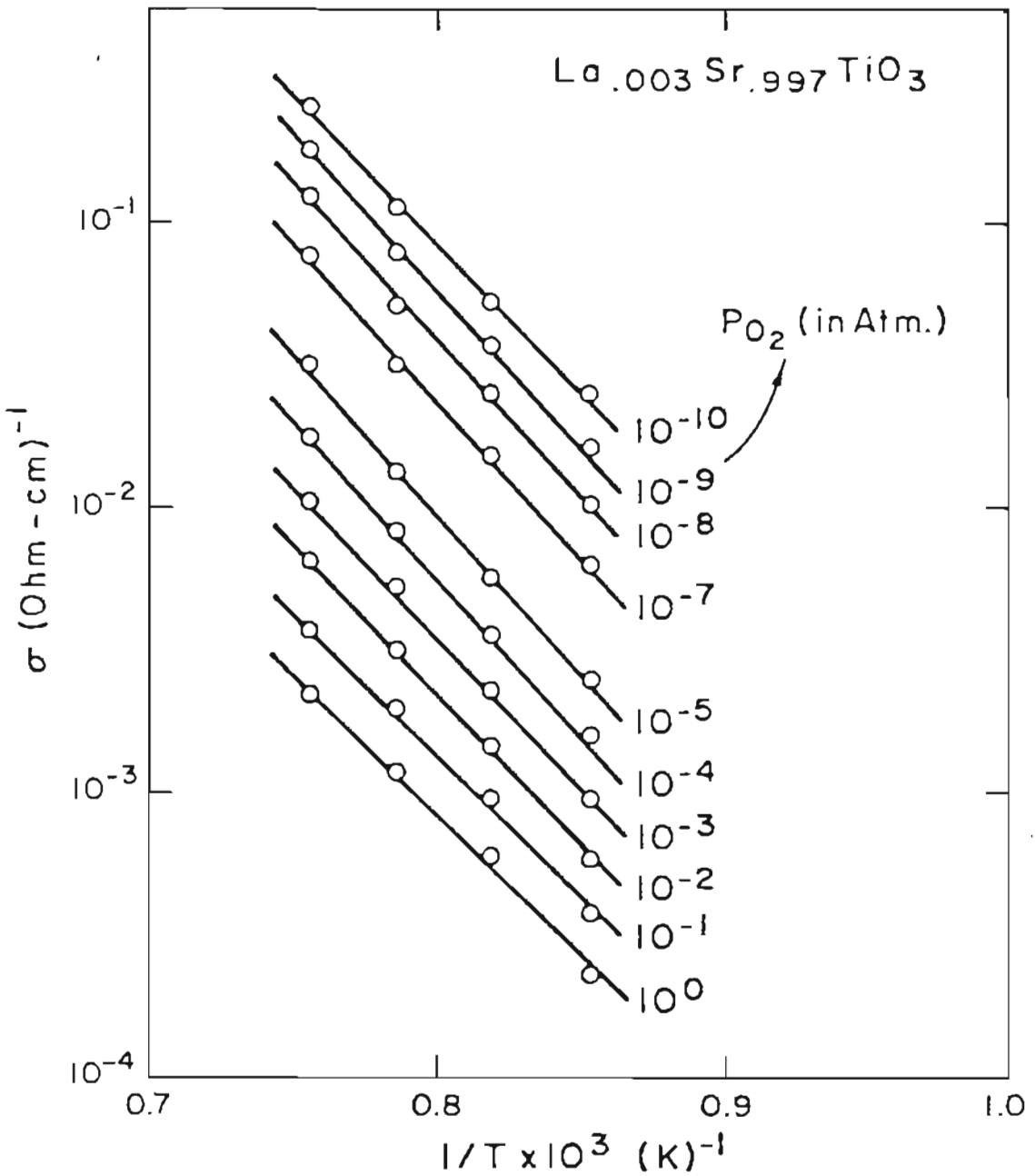

Figure 58. TEMPERATURE DEPENDENCE OF CONDUCTIVITY OF LANTHANUM DOPED $SrTiO_3$

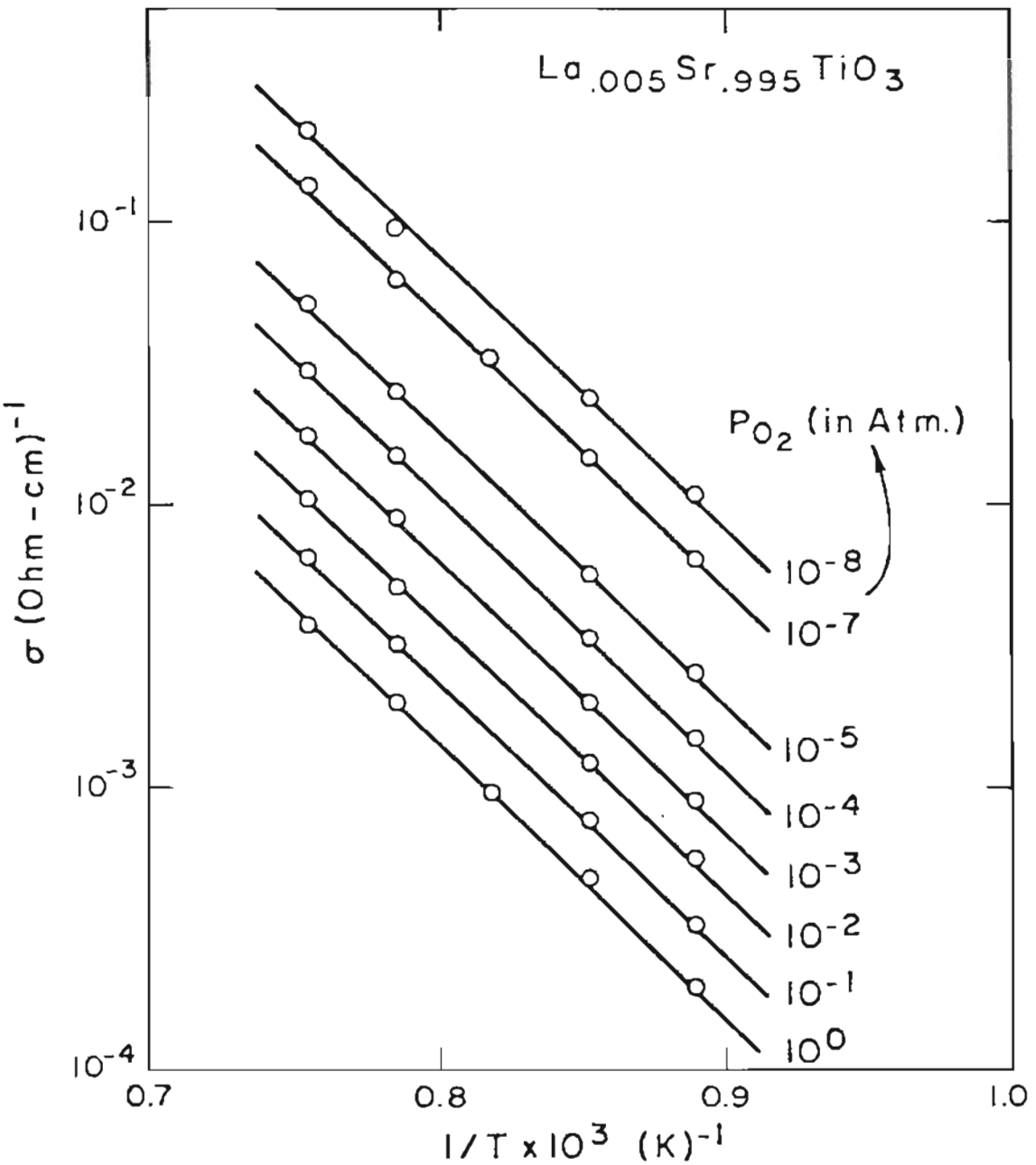

Figure 59. TEMPERATURE DEPENDENCE OF CONDUCTIVITY LANTHANUM DOPED $SrTiO_3$

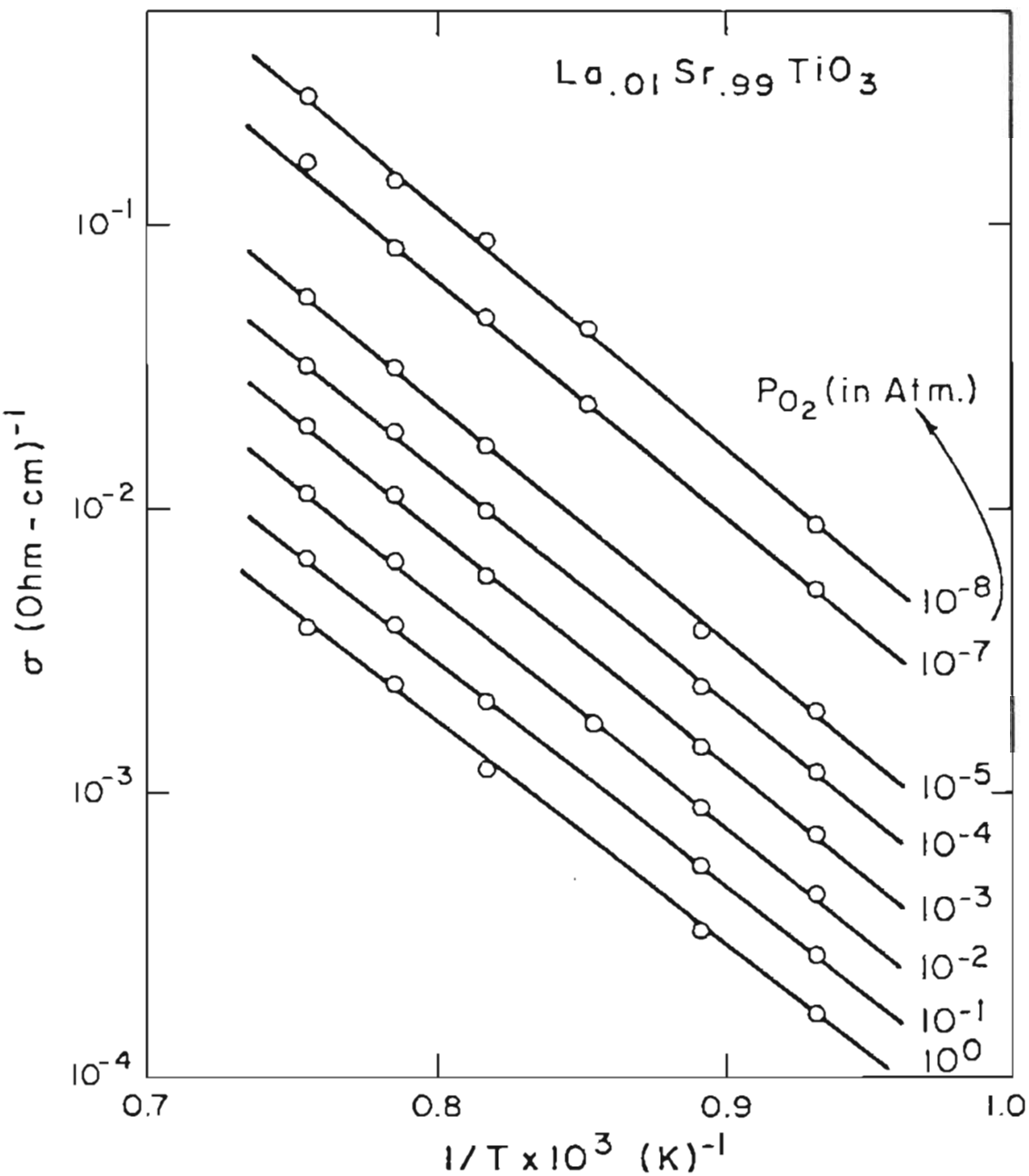

Figure 60. TEMPERATURE DEPENDENCE OF CONDUCTIVITY LANTHANUM DOPED $SrTiO_3$

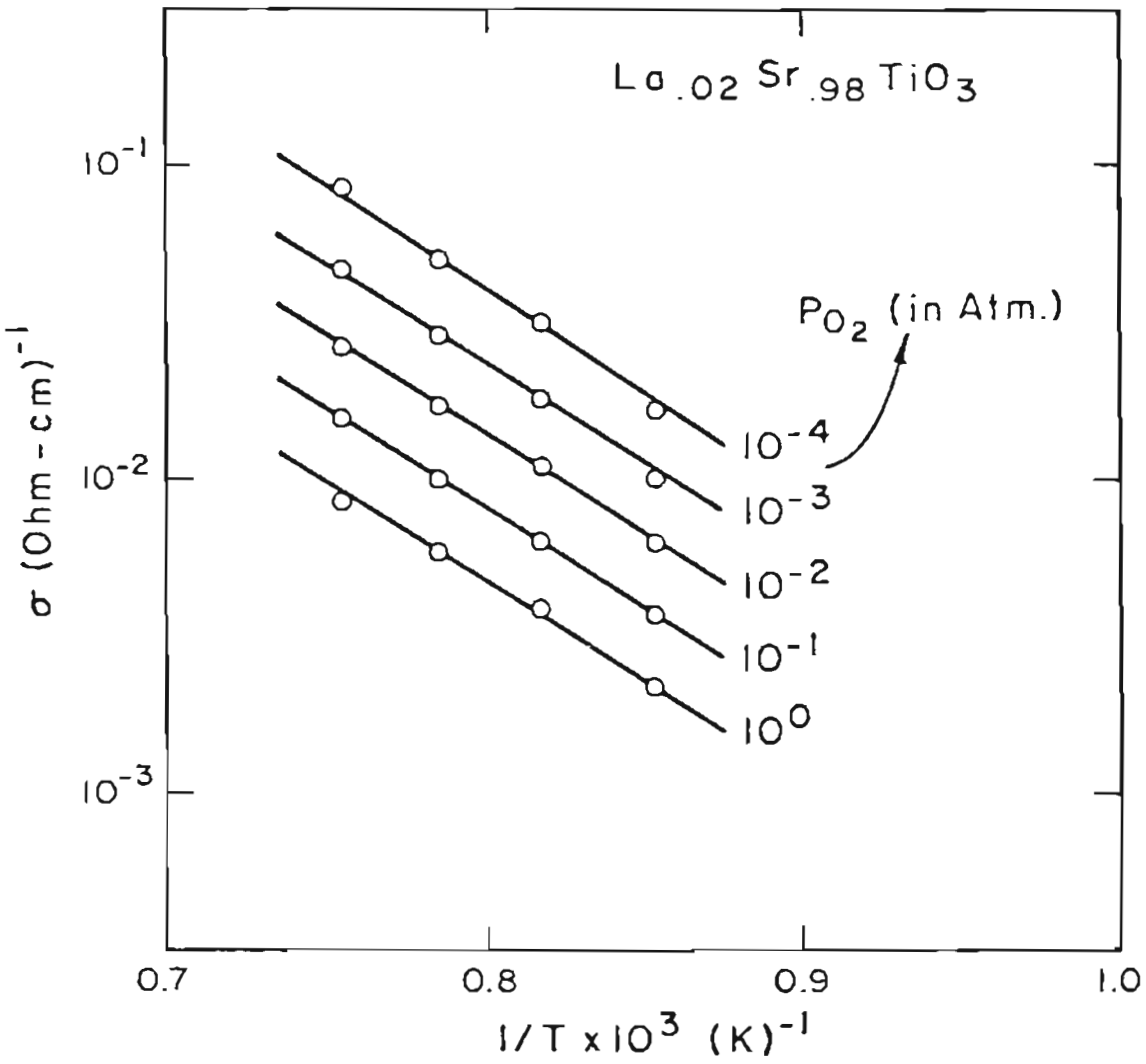

Figure 61. TEMPERATURE DEPENDENCE OF CONDUCTIVITY LANTHANUM DOPED $SrTiO_3$.

Table XXIV.

ACTIVATION ENTHALPIES FOR CONDUCTION IN THE IONIC COMPENSATION REGION

P_{O_2} (atm)	Amounts of La^{+3}: in at. %	Activation Enthalpies (Kcal/mole) 0.1	0.2	0.3	0.5	1.0	2.0
10^{0}		35.97	37.61	45.75	44.13	35.92	29.22
10^{-1}		35.98	38.14	44.01	43.55	36.49	29.16
10^{-2}		35.91	36.49	47.42	43.55	37.57	28.59
10^{-3}		37.57	37.01	49.11	43.55	38.03	28.59
10^{-4}		39.19	37.03	49.89	44.67	38.66	29.66
10^{-5}		37.64	37.05	49.99	43.55	39.20	-
10^{-7}		39.20	38.67	49.96	43.55	38.14	-
10^{-8}		40.29	38.11	49.10	43.54	38.06	-
10^{-9}		39.73	38.11	50.74	-	-	-
10^{-10}		40.29	38.09	50.86	-	-	-

5.6 Electrical Conductivity in Acceptor-Doped $SrTiO_3$

5.6.1 Iron-Doped $SrTiO_3$. The observed electrical conductivity of $SrFe_xTi_{1-x}O_3$ (x = 0.036, 0.1, and 0.5 at.%) as a function of P_{O_2} at different temperatures are shown in Figures 62-64. For three selected temperatures (950, 1000, and 1050°C) the conductivity of iron-doped and undoped $SrTiO_3$ are shown in Figures 65-67. For the iron-doped samples, no region where (-1/6)th dependence of conductivity on P_{O_2} were observed. Instead, only two distinct regions were found. The observed data were proportional to (-1/4)th power of oxygen partial pressure for the pressure $<10^{-10}$ atm., and proportional to $P_{O_2}^{+1/4}$ for the oxygen partial pressure range $>10^{-5}$ atm. As the concentration of iron increased, there is an appreciable increase in the value of p-type conduction at high oxygen partial pressures and a shift in the minimum of the conductivity, σ_{min}, towards lower oxygen partial pressure (see Figures 62-64). It will be assumed that the added iron substitute for titanium on normal lattice sites because of their close ionic radii.

In the n-type region the conductivity is less than in the undoped specimen (Figures 65-67). The minima of the conductivity of 0.5 at.% Fe doped sample is shifted by more than three orders of magnitude to the lower oxygen partial pressures in comparison with the undoped $SrTiO_3$. The conductivity minima shifts to higher P_{O_2} as the temperature is increased for any given iron concentration (Figures 62-64).

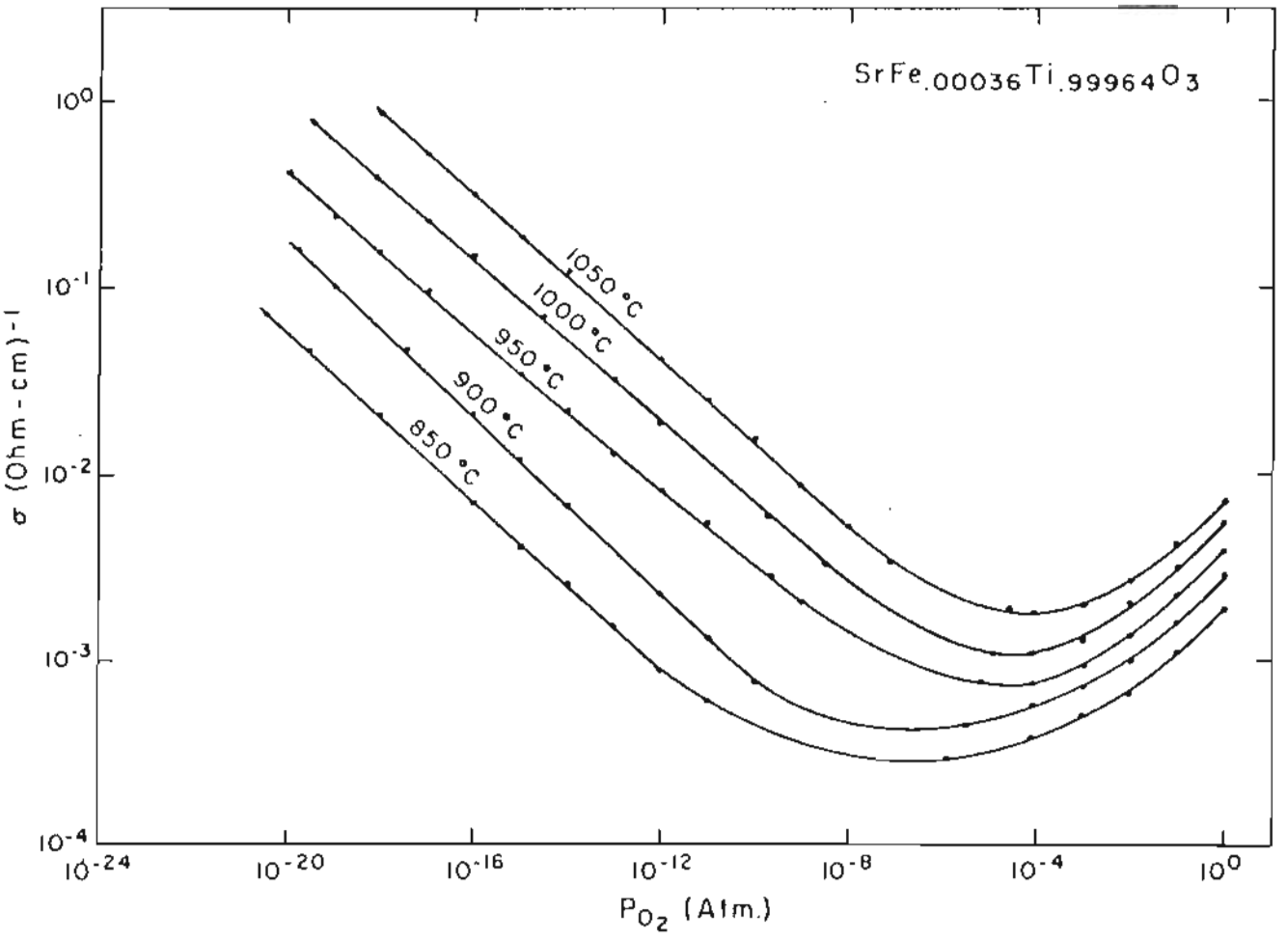

Figure 62. ELECTRICAL CONDUCTIVITY IN $SrFe_{.00036}Ti_{.99964}O_3$.

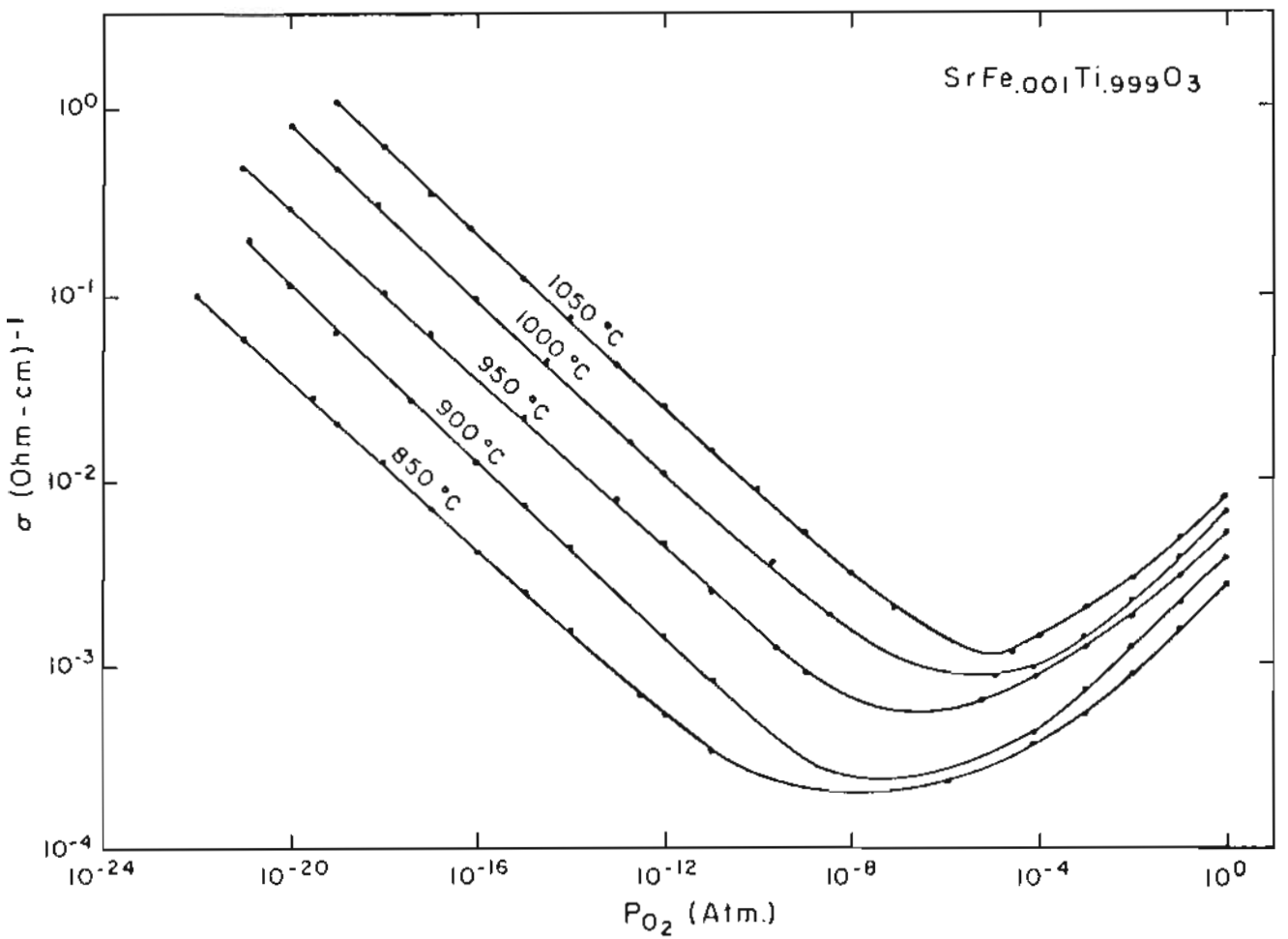

Figure 63. ELECTRICAL CONDUCTIVITY IN $SrFe_{.001}Ti_{.999}O_3$.

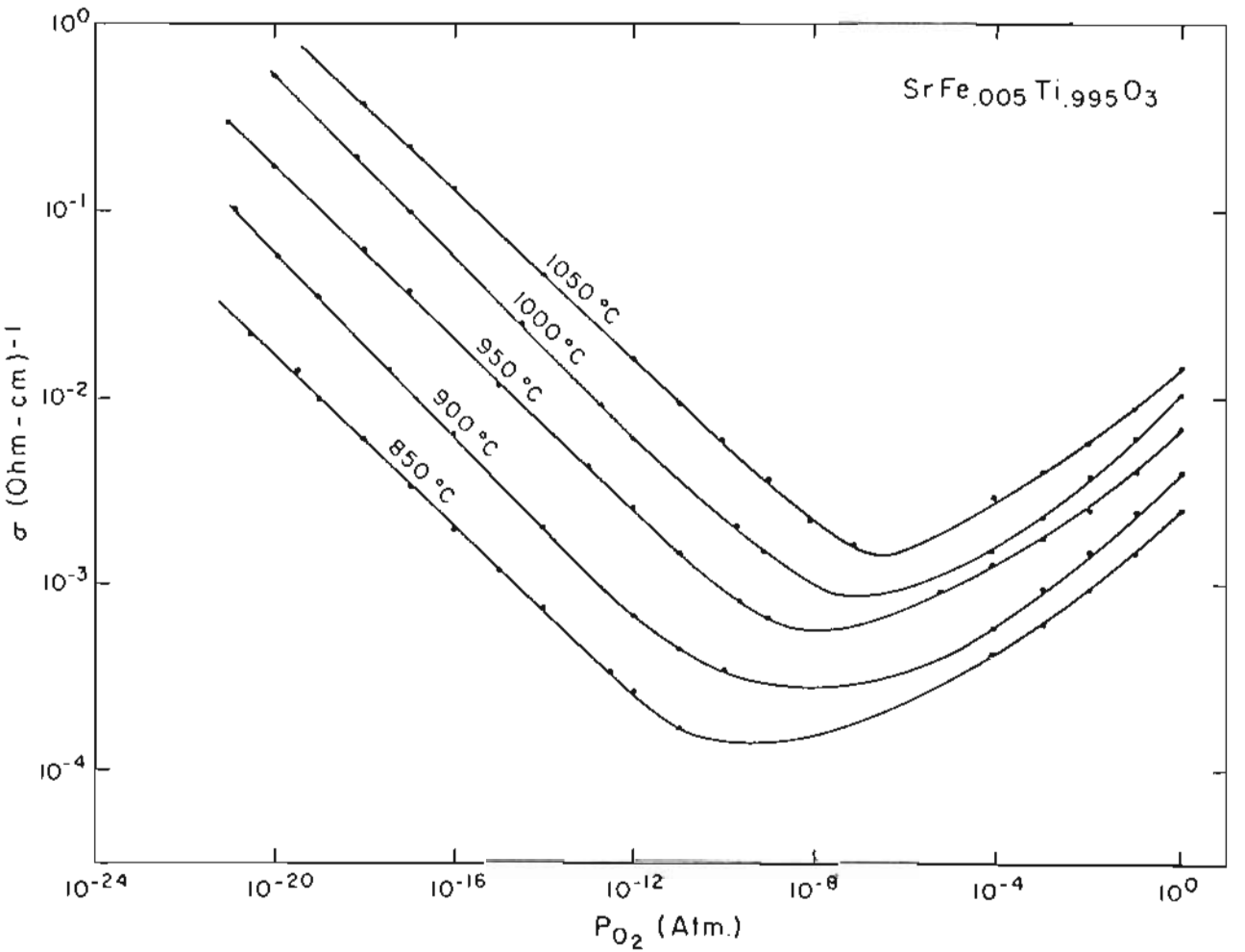

Figure 64. ELECTRICAL CONDUCTIVITY IN $SrFe_{.005}Ti_{.995}O_3$.

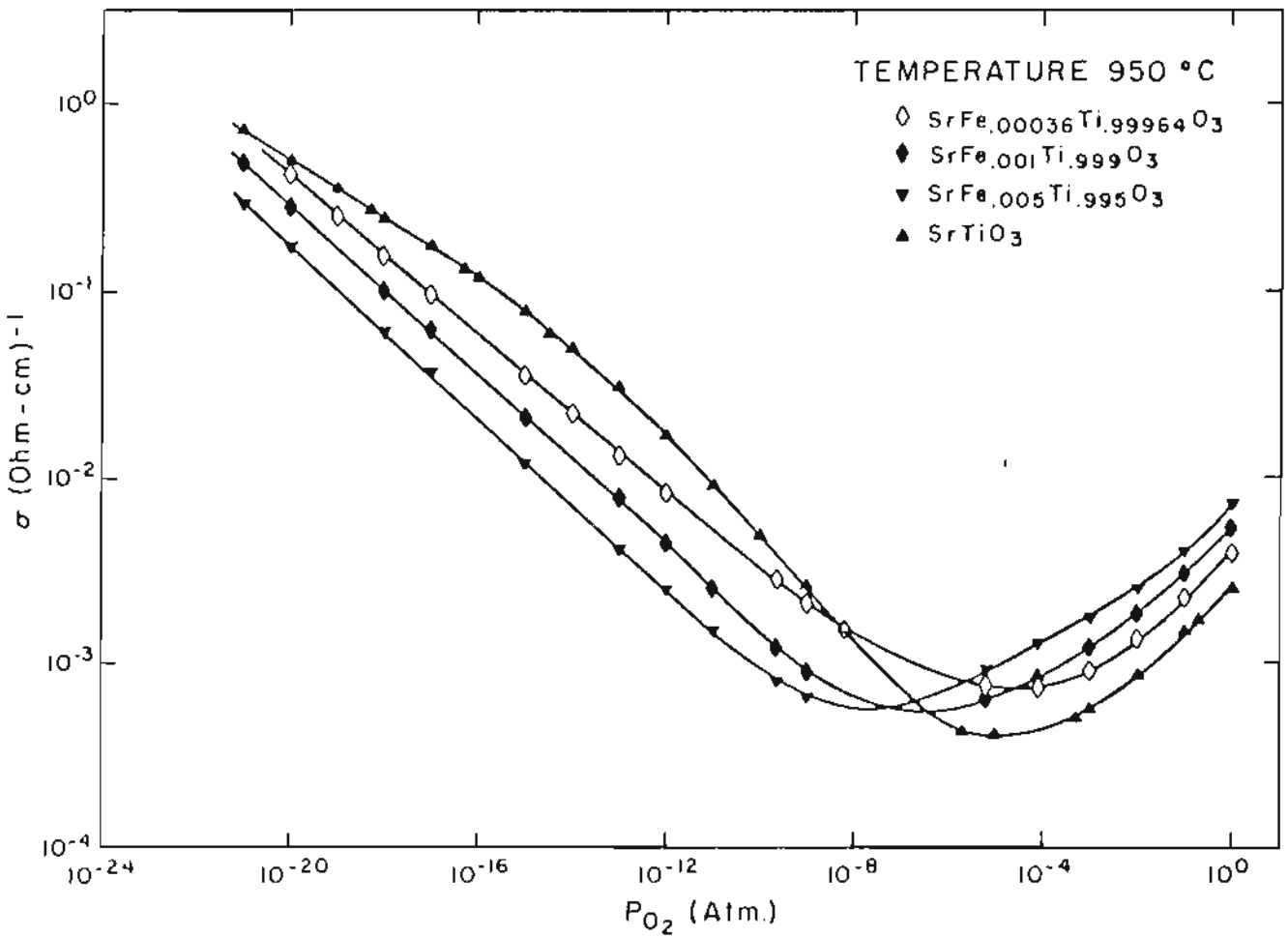

Figure 65. ELECTRICAL CONDUCTIVITY OF $SrTiO_3$ AND IRON-DOPED $SrTiO_3$ AT 950°C.

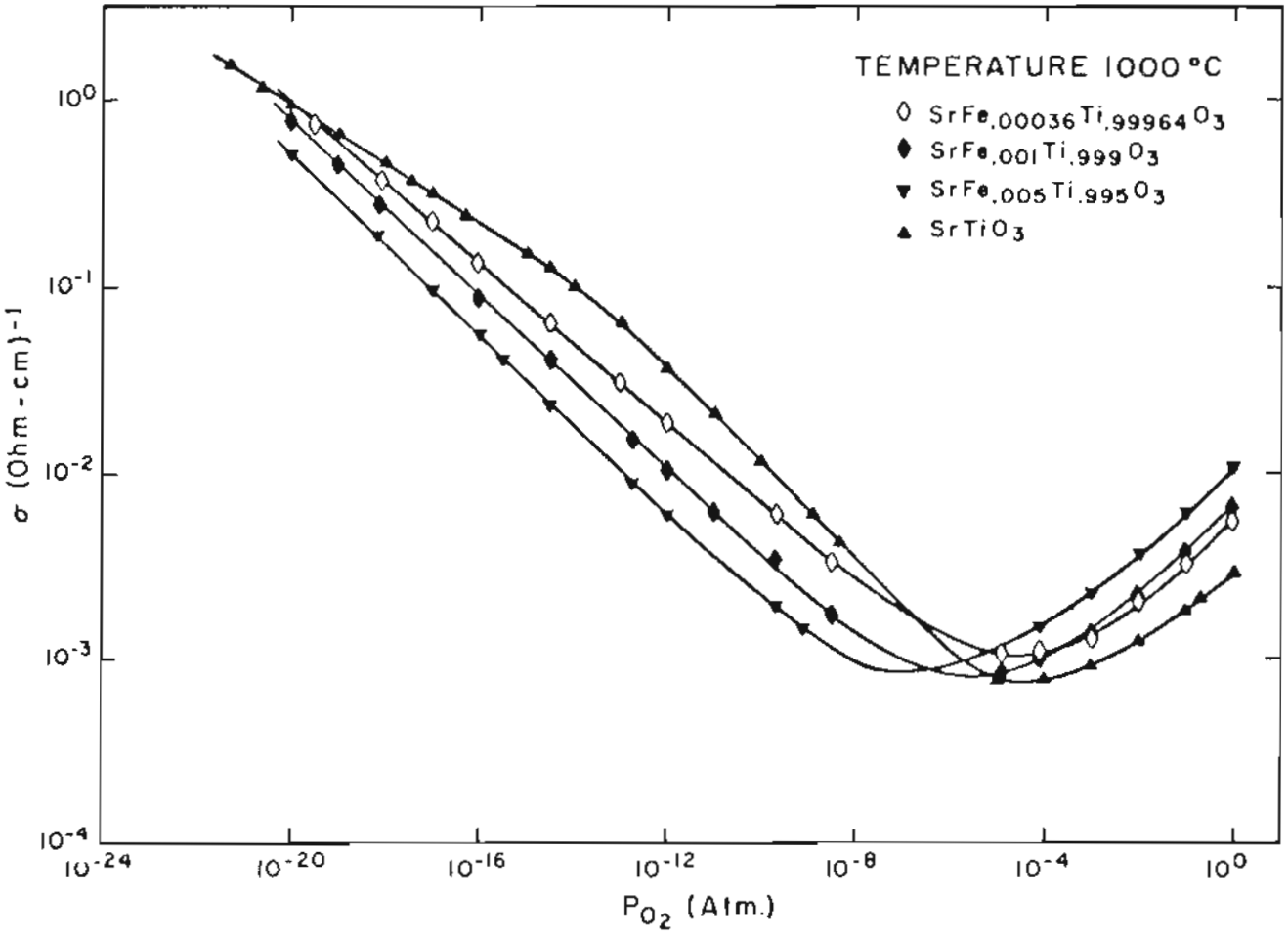

Figure 66. ELECTRICAL CONDUCTIVITY OF UNDOPED AND IRON-DOPED $SrTiO_3$ at 1000°C.

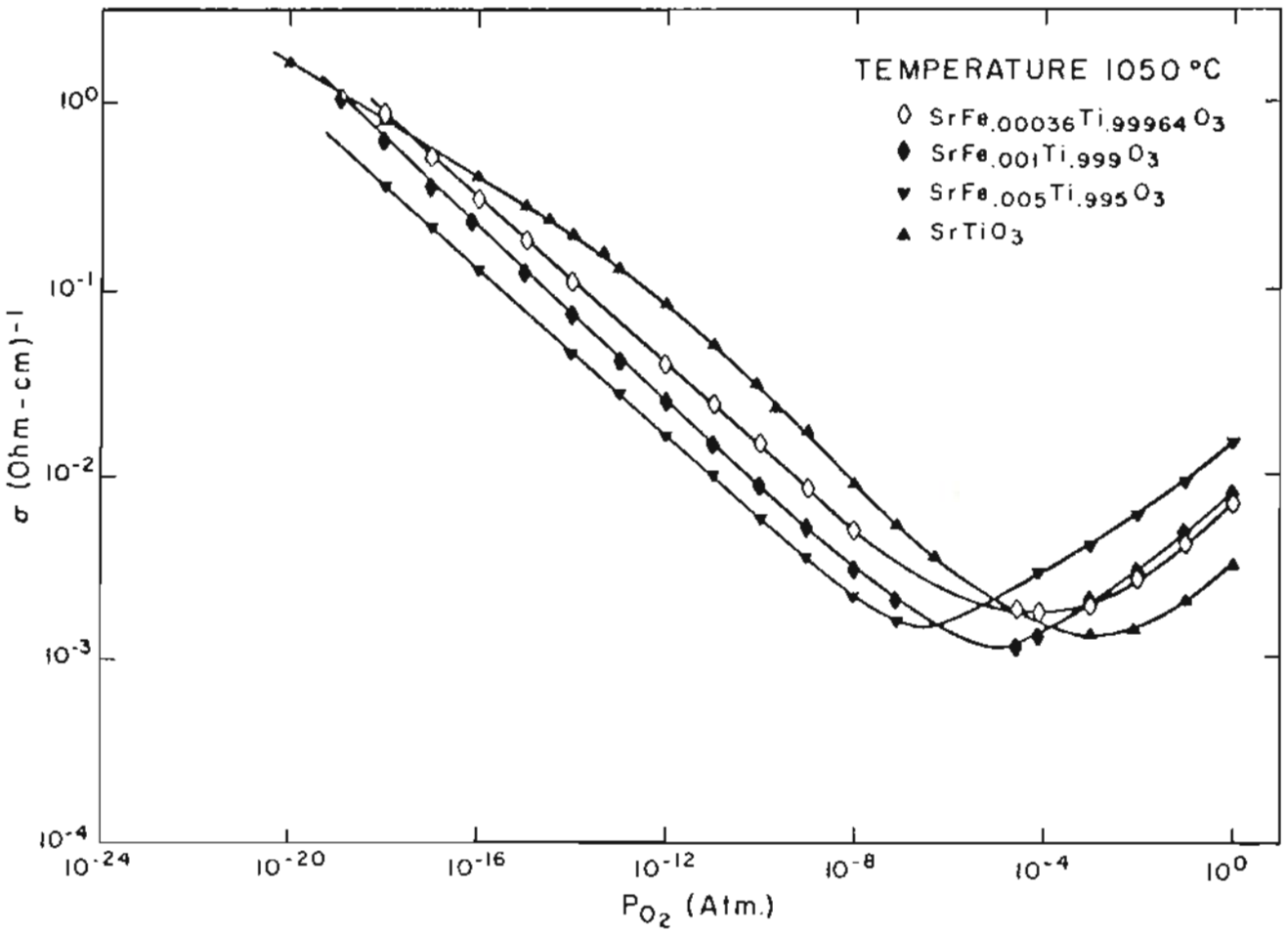

Figure 67. ELECTRICAL CONDUCTIVITY OF UNDOPED AND IRON-DOPED $SrTiO_3$.

The slopes of the log σ vs log P_{O_2} plots in the n-type region are given in Table XXV for the different concentrations of iron in $SrTiO_3$. The values of m in $\sigma_n \propto P_{O_2}^{-1/m}$ in this region are in the range 4-4.7, similar to the values obtained in the case of undoped $SrTiO_3$. The charge neutrality condition in this region is the same as used in the undoped sample, namely,

$$[A'] \simeq 2[V_O^{\cdot\cdot}] = \text{constant} \tag{97}$$

Iron exists in two valence states, namely ferric (Fe^{+3}) and ferrous (Fe^{+2}). Under reducing conditions a considerable portion of the added iron will be in the divalent (ferrous) state. Hence, the neutrality condition will be of the type

$$[A''] \simeq [V_O^{\cdot\cdot}] = \text{constant} \tag{135}$$

where A'' represents a doubly ionized acceptor impurity and in the present case it will represent the Fe^{+2} on Ti^{+4} site, i.e., Fe''_{Ti}. This charge neutrality condition (135) along with the mass-action expression for the oxygen extraction reaction (117) gives,

$$[n] \propto P_{O_2}^{-1/4} \tag{136}$$

The conductivity should, therefore, vary as -1/4th power of oxygen partial pressure. The observed data are close to the value of -1/4. The different valence state of iron will not change the results except for the change in magnitude of the conductivity values. An estimation of the activation enthalpy for conduction can be obtained from the temperature

Table XXV.

P_{O_2} DEPENDENCE OF CONDUCTIVITY IN $SrFe_xTi_{1-x}O_3$, IN THE n-TYPE REGION

		m for $\sigma_n \propto P_{O_2}^{-1/m}$		
T(°C)	x in atom % :	0.036	0.1	0.5
850		4.32	4.3	4.3
900		4.21	4.2	4.05
950		4.7	4.3	4.2
1000		4.6	4.2	4.15
1050		4.5	4.2	4.3

dependence of conductivity (Figures 68-70). The calculated average values of the activation energy for conductance are 4.78 ev (110.16 Kcal/mole), 4.90 ev (112.95 Kcal/mole) and 5.44 ev (125.49 Kcal/mole) for the 0.036, 0.1 and 0.5 at.% Fe doped $SrTiO_3$ samples, respectively (Table XXVI).

The added iron impurities serve to compensate partly for the oxygen vacancies formed during equilibration at low oxygen partial pressures. Due to this, the electron concentration is decreased and hence the conductivity is less than that observed in the undoped sample for the same oxygen partial pressure in the n-type region.

In the p-type region, the observed slopes of log σ vs log P_{O_2} plots are shown in Table XXVII for various iron-doped samples. The slopes are in the range (1/4.0) - (1/4.6). The activation energies for conduction in this region deduced from the Arrhenius slopes (Figures 71-73) are given in Table XXVIII. The average values are 1.67 (38.56 Kcal/mole), 1.47 ev (33.85 Kcal/mole) and 2.25 ev (52 Kcal/mole) for 0.036, 0.1, and 0.5 at.% Fe doped samples respectively.

As the P_{O_2} value is increased, most of the added iron will exist as Fe^{+3}. If one assumes that all the iron added are in the Fe^{+3} state in the P_{O_2} range where p-type conductivity is observed then the charge neutrality condition would be:

$$[A'] \simeq 2[V_o^{\cdot\cdot}] = \text{constant} \qquad (105)$$

where [A'] represents the Fe^{+3} on Ti^{+4} site, i.e., a single level acceptor on Ti site, Fe'_{Ti}. Always there will be some Fe^{+2} ions present, especially in the lowest P_{O_2} value in the p-type region. For the reduced neutrality

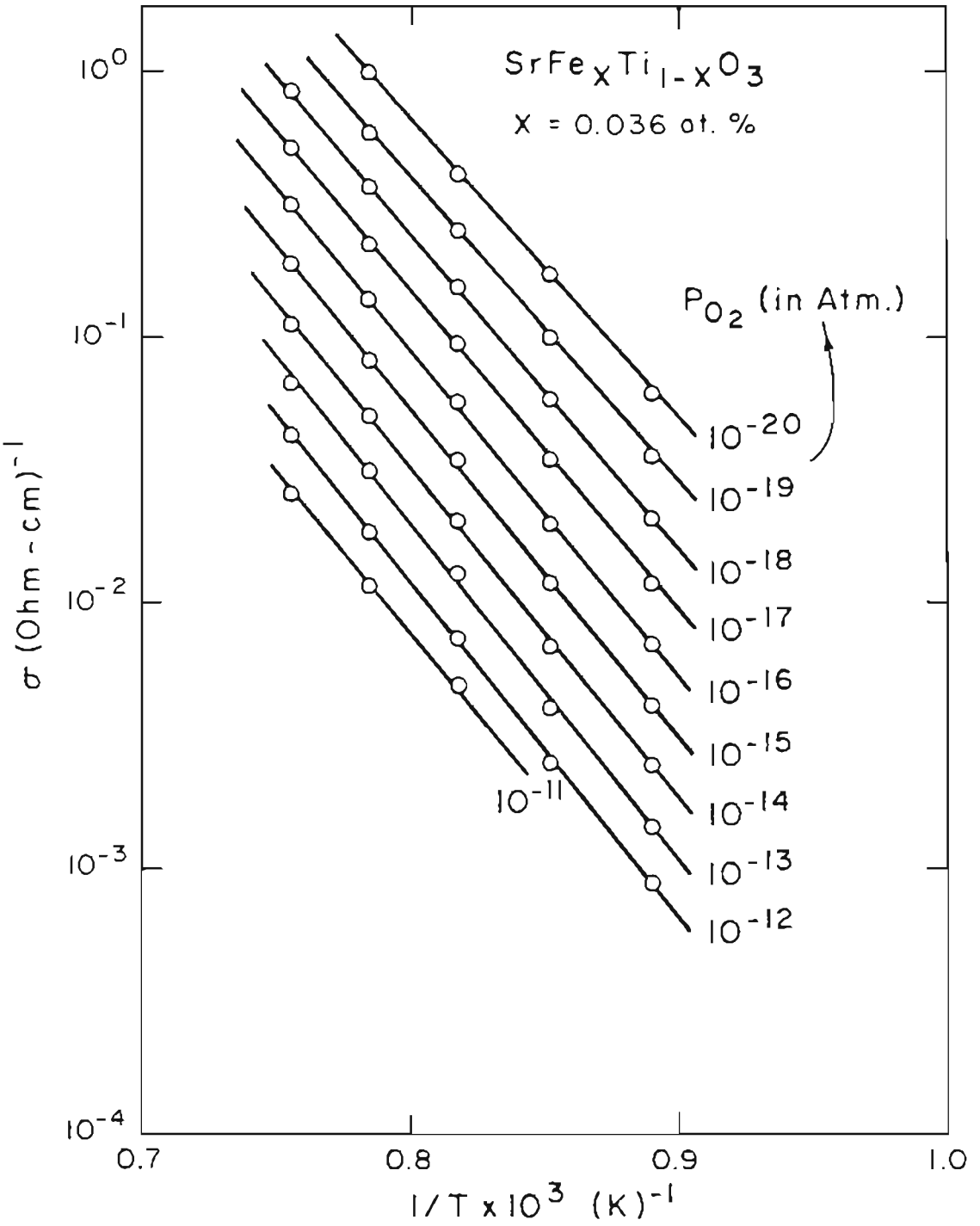

Figure 68. TEMPERATURE DEPENDENCE OF CONDUCTIVITY IN $SrFe_xTi_{1-x}O_3$ [x = 0.036 at.%] IN THE n-TYPE REGION.

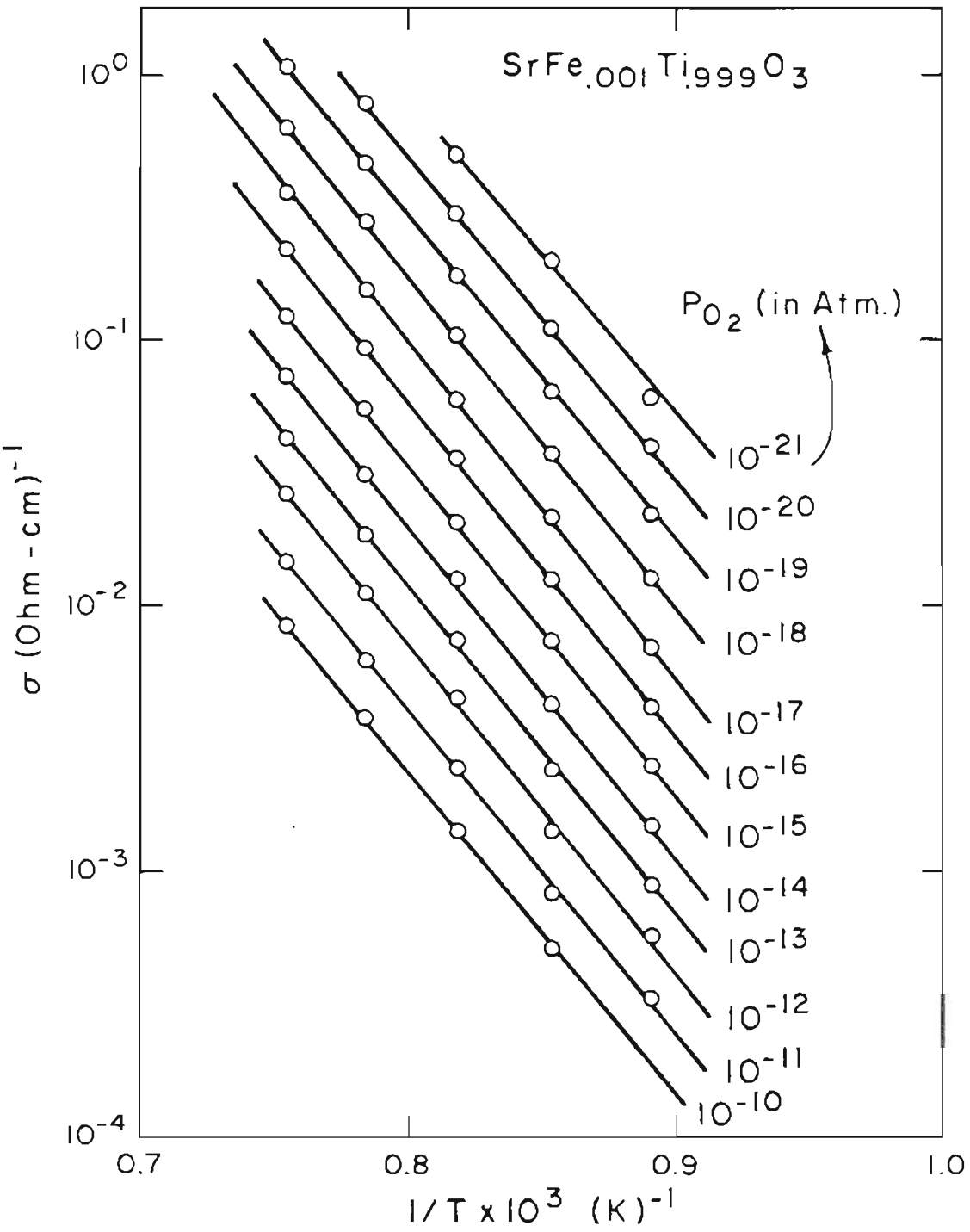

Figure 69. TEMPERATURE DEPENDENCE OF CONDUCTIVITY IN $SrFe_{.001}Ti_{.999}O_3$ IN THE n-TYPE REGION.

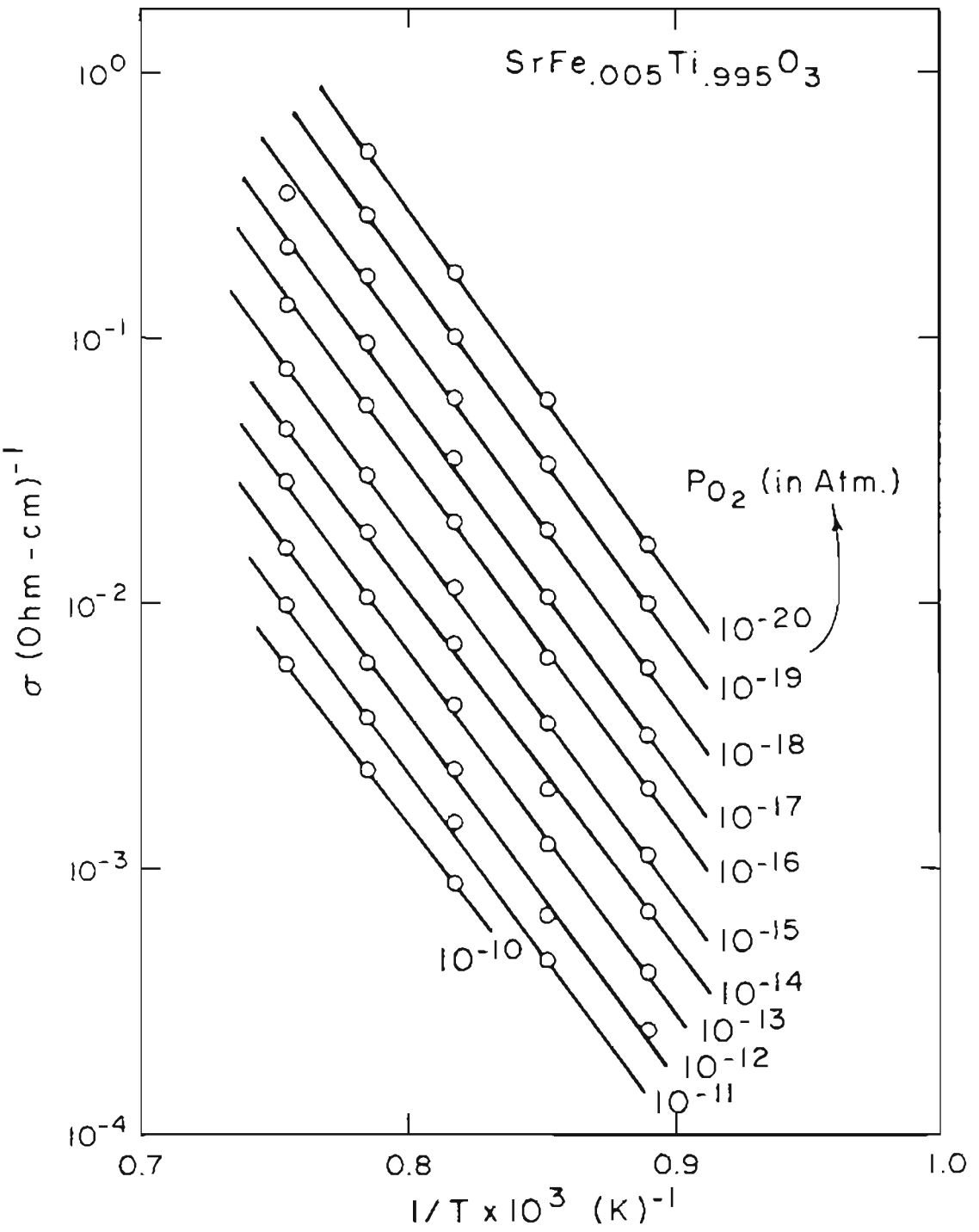

Figure 70. TEMPERATURE DEPENDENCE OF CONDUCTIVITY OF $SrFe_{.005}Ti_{.995}O_3$ IN THE n-TYPE REGION.

Table XXVI.

ACTIVATION ENTHALPIES FOR CONDUCTION IN $SrFe_xTi_{1-x}O_3$ IN THE n-TYPE REGION

		Activation Enthalpies (Kcal/mole)		
P_{O_2}(atm.)	x in atom.% :	0.036	0.1	0.5
10^{-21}			108.23	
10^{-20}		103.17	111.58	128.41
10^{-19}		104.26	110.85	128.04
10^{-18}		107.92	114.32	128.04
10^{-17}		109.38	116.52	127.58
10^{-16}		111.58	115.24	125.30
10^{-15}		112.49	114.32	124.38
10^{-14}		113.41	114.32	121.64
10^{-13}		115.24	113.04	125.30
10^{-12}		114.32	113.77	125.85
10^{-11}		109.80	111.58	125.30
10^{-10}			111.58	120.51

Table XXVII.

P_{O_2} DEPENDENCE OF CONDUCTIVITY IN $SrFe_xTi_{1-x}O_3$, IN THE p-TYPE REGION

		m for $\sigma_p \propto P_{O_2}^{+1/m}$		
T(°C)	x in atom % :	0.036	0.1	0.5
850		4.38	4.1	4.56
900		4.32	4.2	4.6
950		4.21	4.2	4.2
1000		4.15	4.05	4.44
1050		4.57	4.3	4.57

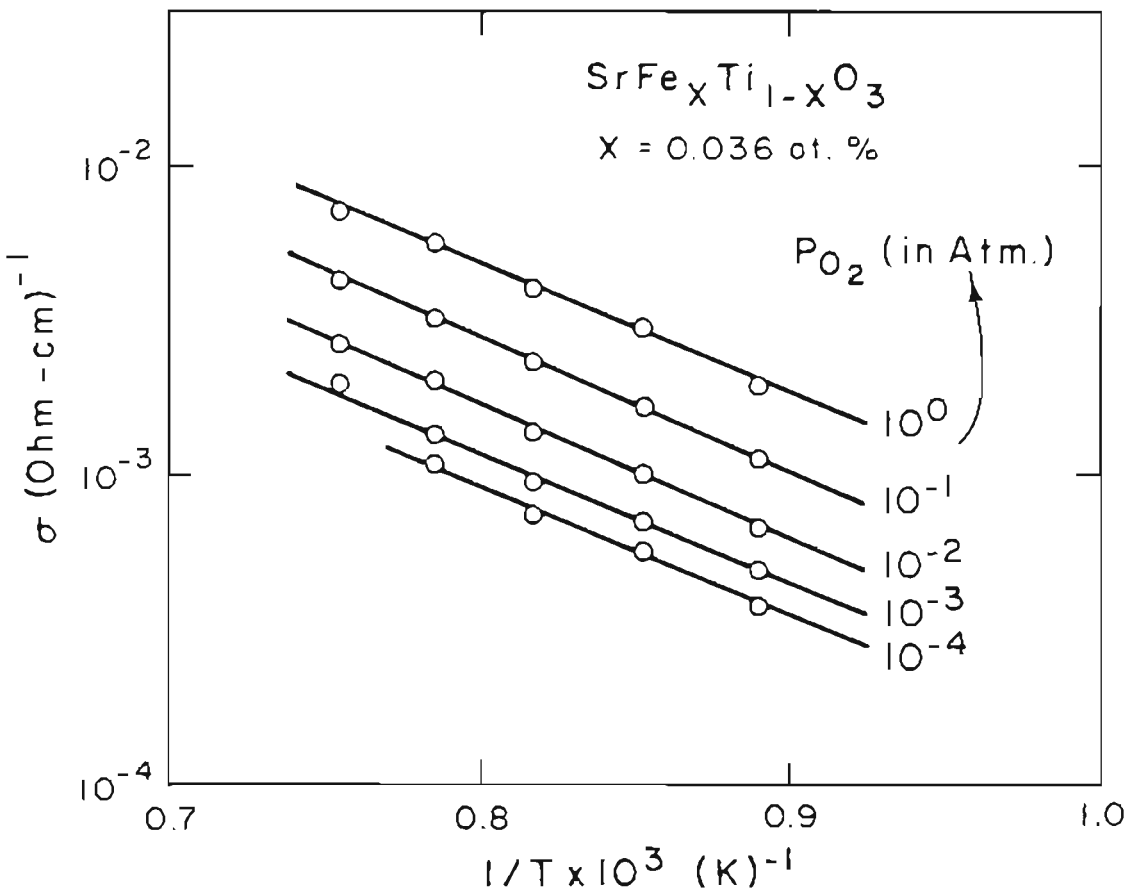

Figure 71. ARRHENIUS PLOTS FOR $SrFe_{.00036}Ti_{.99964}O_3$ IN THE p-TYPE REGION.

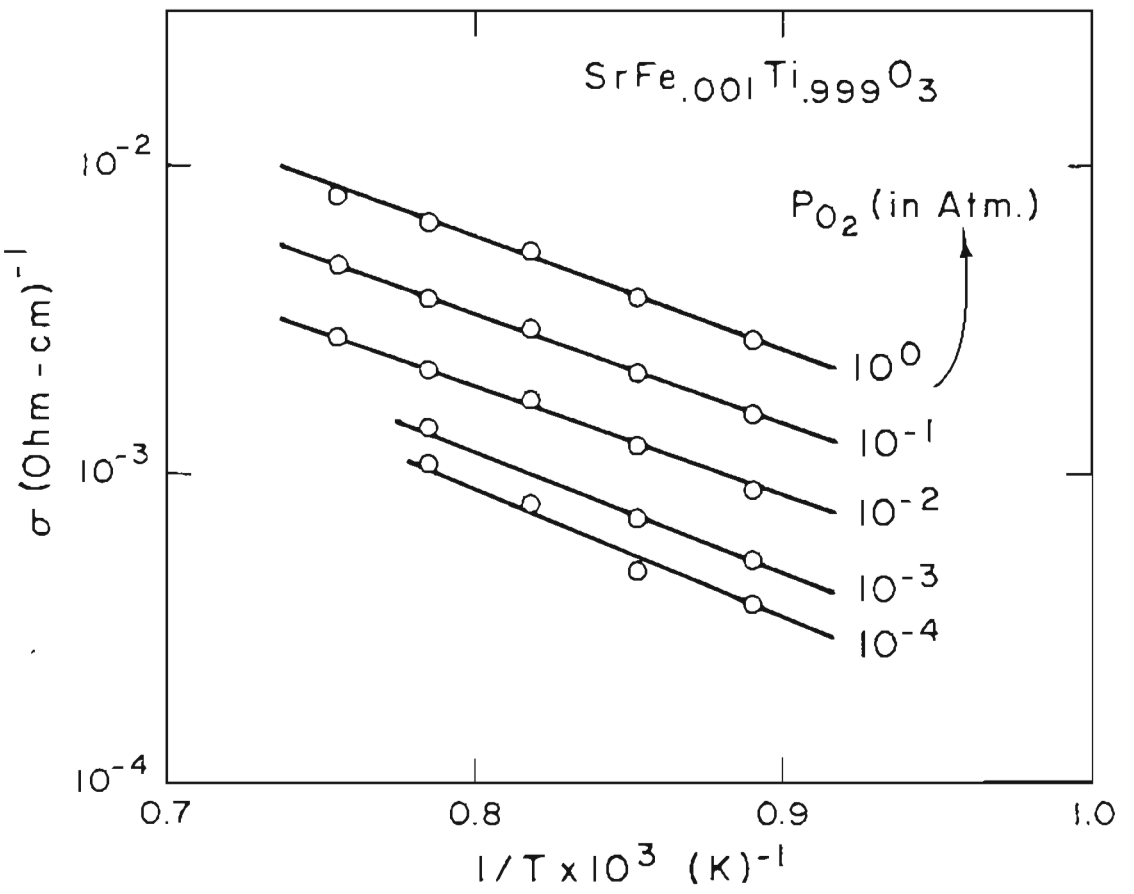

Figure 72. TEMPERATURE DEPENDENCE OF CONDUCTIVITY IN $SrFe_{.001}Ti_{.999}O_3$ IN THE p-TYPE REGION.

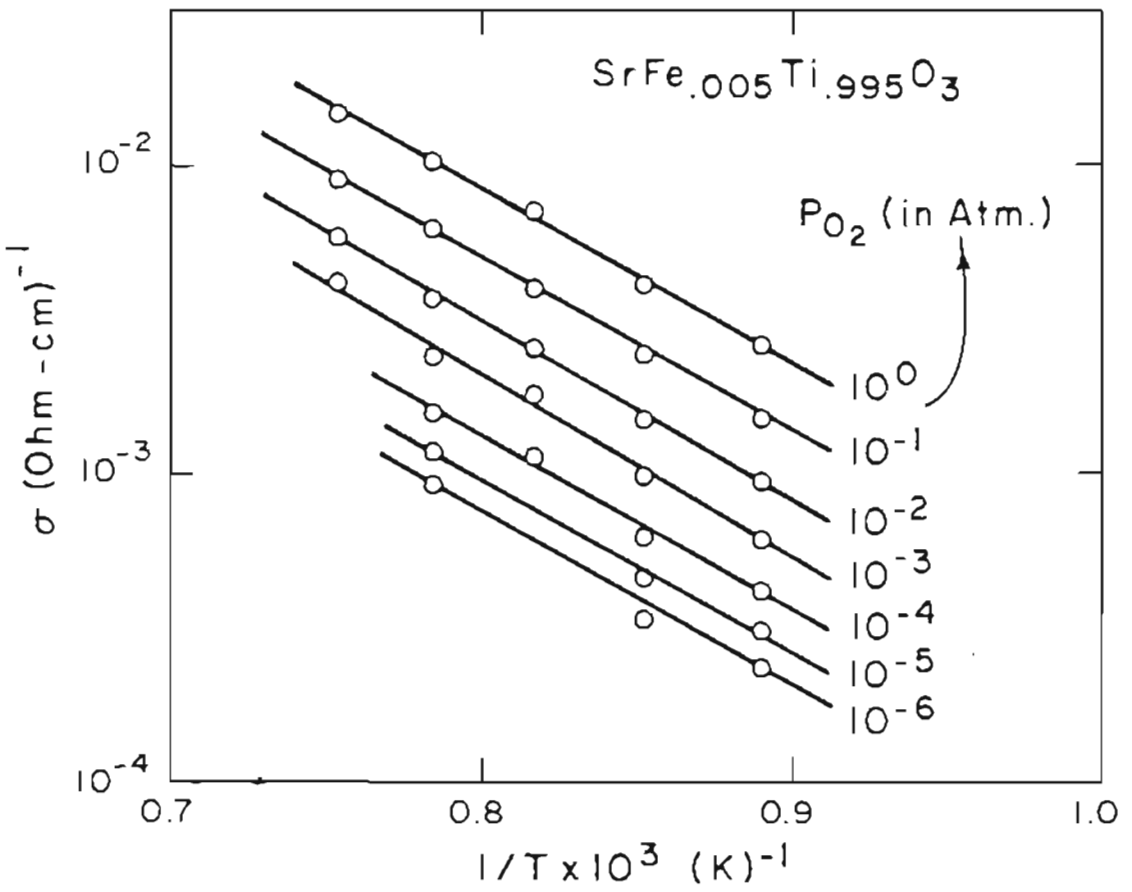

Figure 73. ARRHENIUS PLOTS FOR $SrFe_{.005}Ti_{.995}O_3$ IN THE p-TYPE REGION.

Table XXVIII.

ACTIVATION ENTHALPIES FOR CONDUCTION IN $SrFe_xTi_{1-x}O_3$ IN THE p-TYPE REGION

		Activation Enthalpies (Kcal/mole)		
P_{O_2}(atm.)	x in atom.% :	0.036	0.1	0.5
10^0		38.23	33.86	51.77
10^{-1}		39.33	31.92	51.40
10^{-2}		39.33	32.01	53.05
10^{-3}		38.41	35.44	53.95
10^{-4}		37.50	36.04	51.77
10^{-5}				50.30
10^{-6}				51.76

condition where the acceptor-impurities (whether deliberately added or accidentally present) are related to oxygen vacancies, the electron concentration varies as -1/4th power and hole concentration varies as +1/4th power of oxygen partial pressure (see Figure 13). Finally the hole concentration becomes equal to the acceptor impurity concentration, which is constant and hence the conductivity independent of P_{O_2} as shown in Figure 13. But before that stage is reached, [p] becomes greater than [n] and the conductivity also changes to p-type (Figure 13). The experimental observations as shown in Figures 62-64 are in agreement with the predicted model (Introduction part and Figure 13). The p-type conductivity is due to partial filling of the iron-related oxygen vacancies. Increase in iron concentration gives rise to higher conductivity values in the p-type region and lower values in the n-type region. This leads to the n to p-type transition to move to lower P_{O_2} values as the iron concentration is increased in $SrTiO_3$.

5.6.2 Aluminum-doped $SrTiO_3$. Aluminum was selected as another acceptor impurity since, like iron, it could be expected to give rise to higher electrical conductivity in the p-type region and low conductivity in the n-type region as compared with the undoped $SrTiO_3$. But, unlike iron, the aluminum ion is believed to exist in only one valence (trivalent) state. Figure 74 gives the conductivity as a function of oxygen partial pressure at the indicated temperatures for $SrAl_{.003}Ti_{.997}O_3$ (0.3 at.% Al). The P_{O_2} dependence of conductivity in this sample in both types of conductivity regions are given in Tables XXIX and XXX. The general

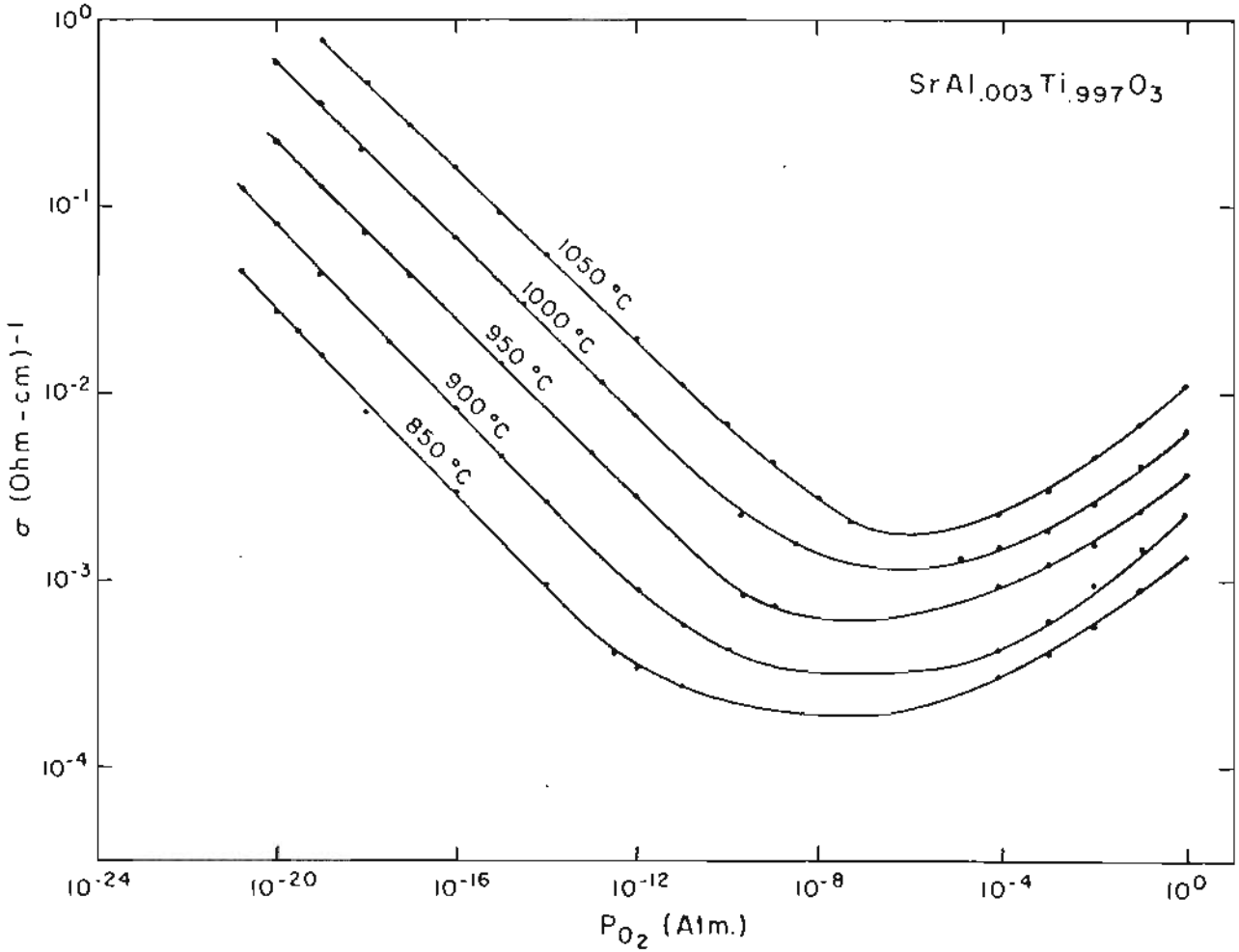

Figure 74. THE ELECTRICAL CONDUCTIVITY OF $SrAl_{.003}Ti_{.997}O_3$.

Table XXIX.

P_{O_2} DEPENDENCE OF CONDUCTIVITY IN $SrAl_{.003}Ti_{.997}O_3$ IN THE n-TYPE REGION

T(°C)	m for $\sigma_n \propto P_{O_2}^{-1/m}$
850	4.0
900	4.05
950	4.27
1000	4.15
1050	4.32

Table XXX.

P_{O_2} DEPENDENCE OF CONDUCTIVITY IN $SrAl_{.003}Ti_{.997}O_3$ IN THE p-TYPE REGION

T(°C)	m for $\sigma_p \propto P_{O_2}^{+1/m}$
850	5.2
900	5.0
950	5.16
1000	4.92
1050	5.0

shape of the curves is similar to the one observed for iron-doped $SrTiO_3$. Since aluminum ion exist only in trivalent state, the charge neutrality condition in both n- and p-type region will be

$$[A'] = 2[V_o^{\cdot\cdot}] = \text{constant} \tag{105}$$

where A' now represents Al^{+3} on Ti^{+4} site, i.e., Al'_{Ti}. This charge neutrality condition explains the observed slopes as shown in Tables XXIX and XXX.

The conductivity in the n-type region for the 0.3 at.% Al doped sample is lower than that observed in $SrFe_{.001}Ti_{.999}O_3$ and higher than in $SrFe_{.005}Ti_{.995}O_3$. In the p-type region the conductivity of the 0.3 at.% Al doped sample is higher than in $SrFe_{.001}Ti_{.999}O_3$ but lower than in $SrFe_{.005}Ti_{.995}O_3$. This observation is consistent with the expected levels of the conductivity values for the acceptor dopant concentrations considered in this work. The conductivity of the undoped and aluminum doped $SrTiO_3$ at 1050°C is shown in Figure 75. From Figure 75 it can be seen that the region in which the conductivity varies as -1/4th power of P_{O_2} due to presence of some unknown acceptor impurity in the undoped sample, is extended much further by deliberately doping with aluminum impurities. Again, there is no region where -1/6th dependence for conductivity on P_{O_2} is observed in the aluminum doped sample. The conductivity minimum is shifted by about three orders of magnitude to the low P_{O_2} by doping with 0.3 at.% Al, as compared with the undoped $SrTiO_3$ which also accounts for the crossover seen in Figure 78.

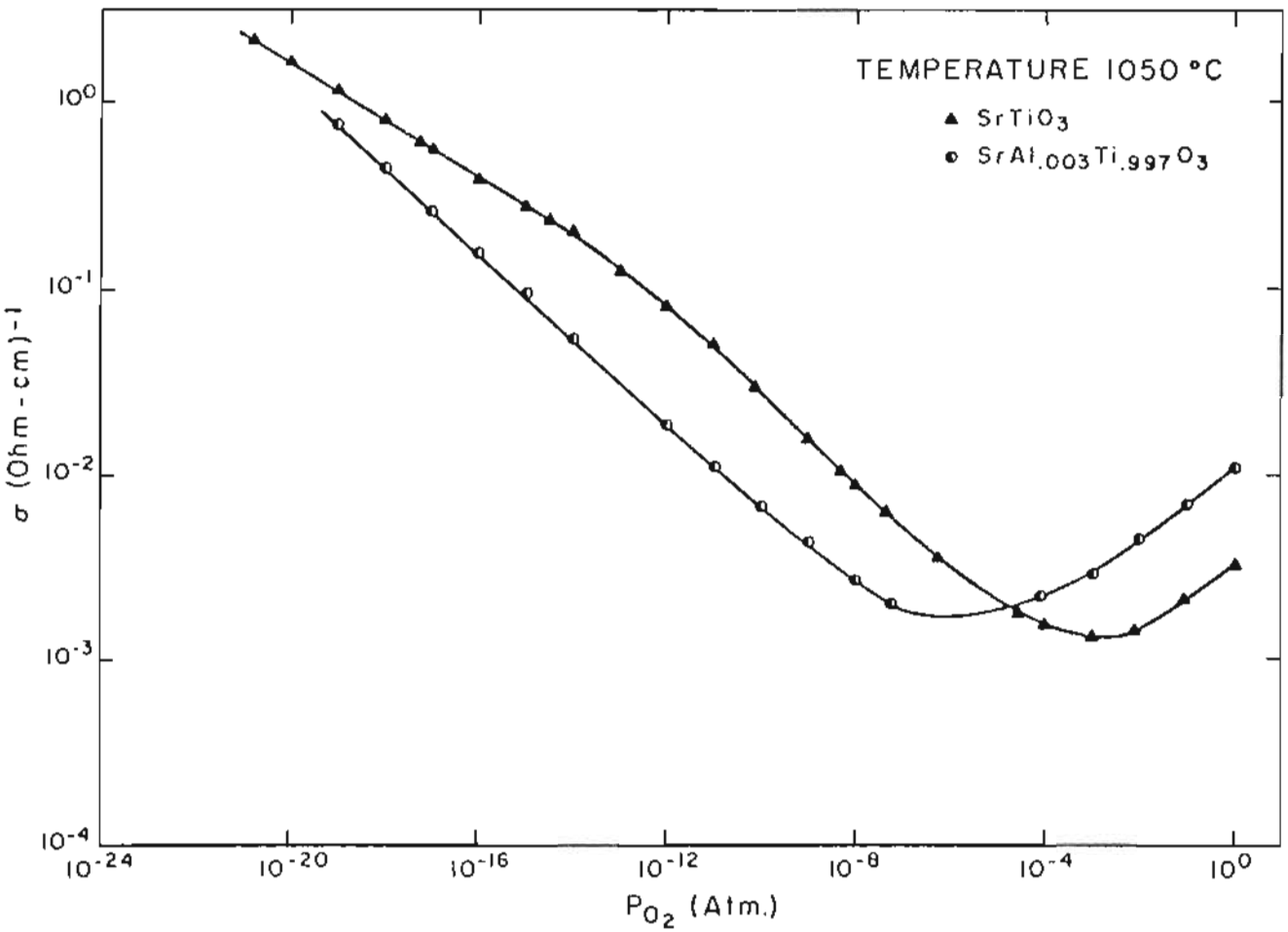

Figure 75. THE ELECTRICAL CONDUCTIVITY OF UNDOPED AND ALUMINUM DOPED $SrTiO_3$ AT 1050°C.

The temperature dependence of electrical conductivity in $SrAl_{.003}Ti_{.997}O_3$ is given in Figures 76 and 77 for both n- and p-type conductivity region, respectively. From these plots, the activation enthalpy for conduction is estimated and shown in Tables XXXI and XXXII. An average value of 5.07 ev (116.96 Kcal/mole) is obtained for n-type region and 2.69 ev (62 Kcal/mole) for the p-type region of conduction.

5.7 Raman Spectra of $SrTiO_3$

The Raman spectra of polycrystalline $SrTiO_3$ are given in Figures 78 and 79. Figure 78 shows the complete spectra at various temperatures as far as we have been able to detect. These spectra were run with a scan rate of 4 cm^{-1}/sec and slit width of 4 cm^{-1}. The spectra in Figure 79 were run with a lower scan rate (1 cm^{-1}/sec) in order to show more detail near the exciting line. The relative intensity of all of the graphs is linear and the scale is essentially the same for all of them but slightly displaced for optimum display. Each spectrum is a sum of as many as ten scans at a given temperature. Table XXXIV shows the temperature dependence of the principal peaks for the spectra of polycrystalline $SrTiO_3$ plotted in Figure 78. For comparison, the room temperature spectrum of clear, single crystal $SrTiO_3$ (growth method unknown) is given in Figure 80. All of the Raman bands observed in the single crystal sample are also seen in the spectrum of the powder samples.

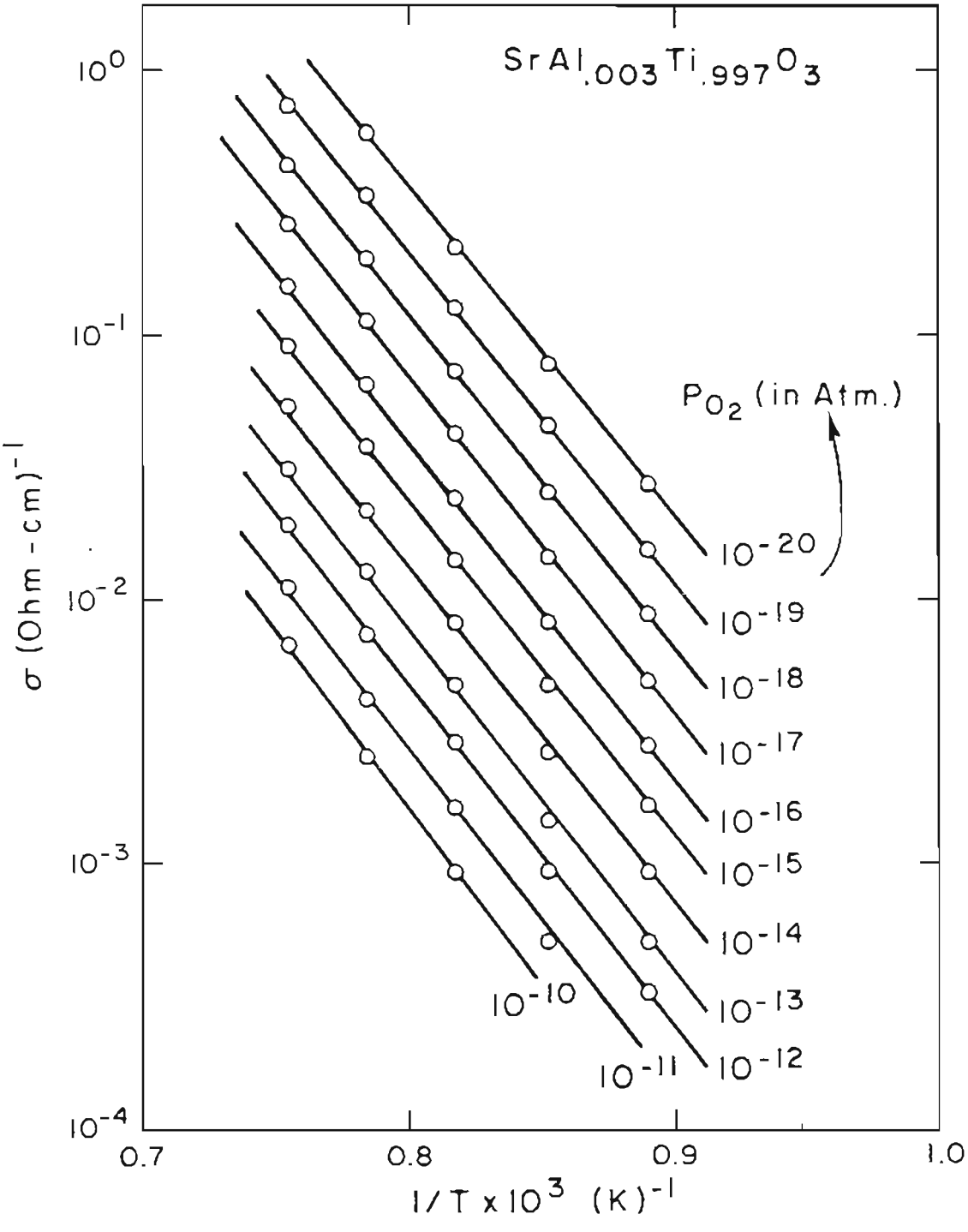

Figure 76. TEMPERATURE DEPENDENCE OF CONDUCTIVITY IN $SrAl_{.003}Ti_{.997}O_3$, IN THE n-TYPE REGION.

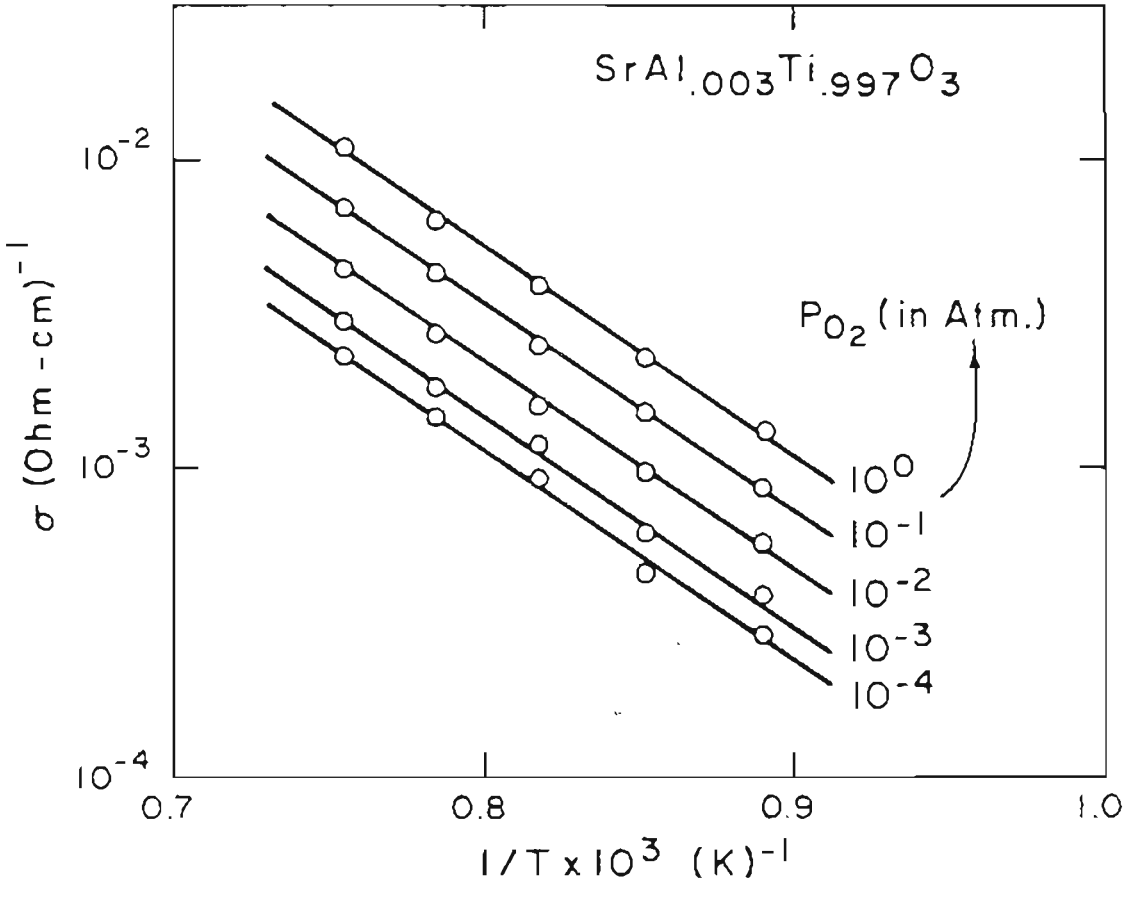

Figure 77. TEMPERATURE DEPENDENCE OF CONDUCTIVITY IN $SrAl_{.003}Ti_{.997}O_3$ IN THE p-TYPE REGION.

Table XXXI.

ACTIVATION ENTHALPIES FOR CONDUCTION IN $SrAl_{.003}Ti_{.997}O_3$ IN THE n-TYPE REGION

10^{-20}	114.14
10^{-19}	115.24
10^{-18}	115.24
10^{-17}	117.07
10^{-16}	116.52
10^{-15}	116.15
10^{-14}	116.70
10^{-13}	117.71
10^{-12}	117.98
10^{-11}	118.88
10^{-10}	120.94

Table XXXII.

ACTIVATION ENTHALPIES FOR CONDUCTION IN $SrAl_{.003}Ti_{.997}O_3$ IN THE p-TYPE REGION

P_{O_2} (atm.)	Activation Enthalpies [Kcal/mole]
10^{0}	62.19
10^{-1}	62.50
10^{-2}	60.97
10^{-3}	62.19
10^{-4}	62.19

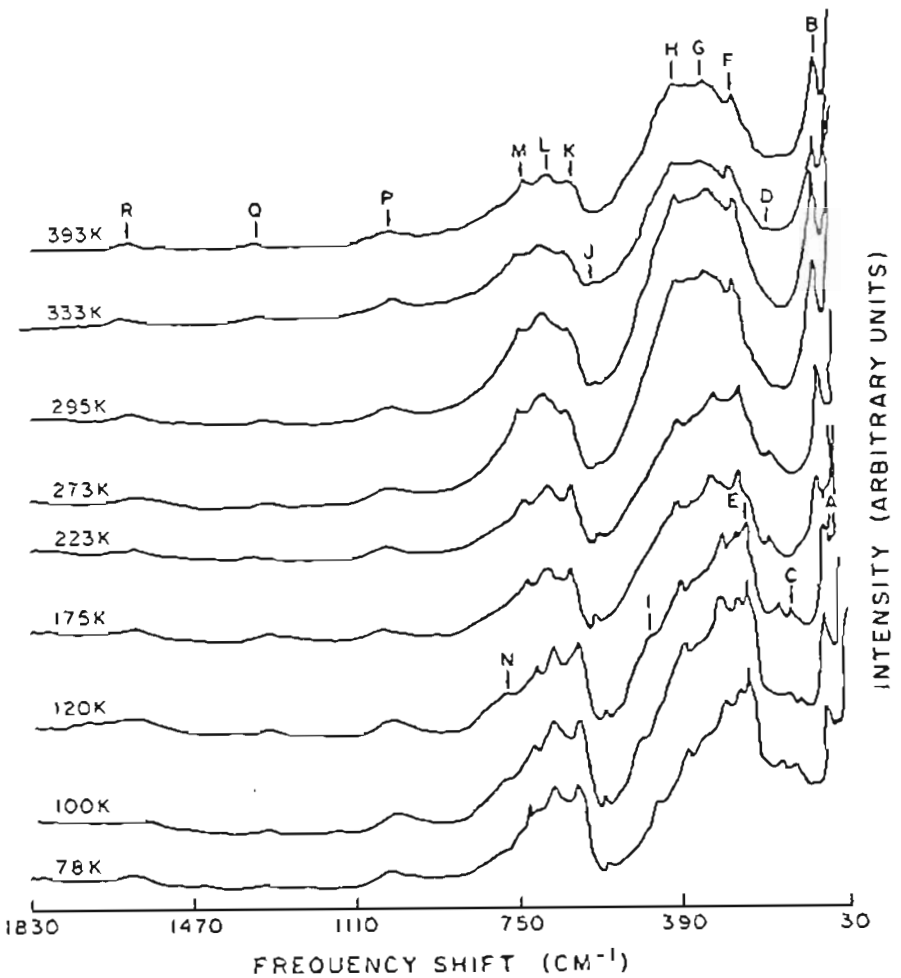

Figure 78. RAMAN SPECTRA OF POLYCRYSTALLINE $SrTiO_3$ AS A FUNCTION OF TEMPERATURE USING 4880Å LASER LINE.

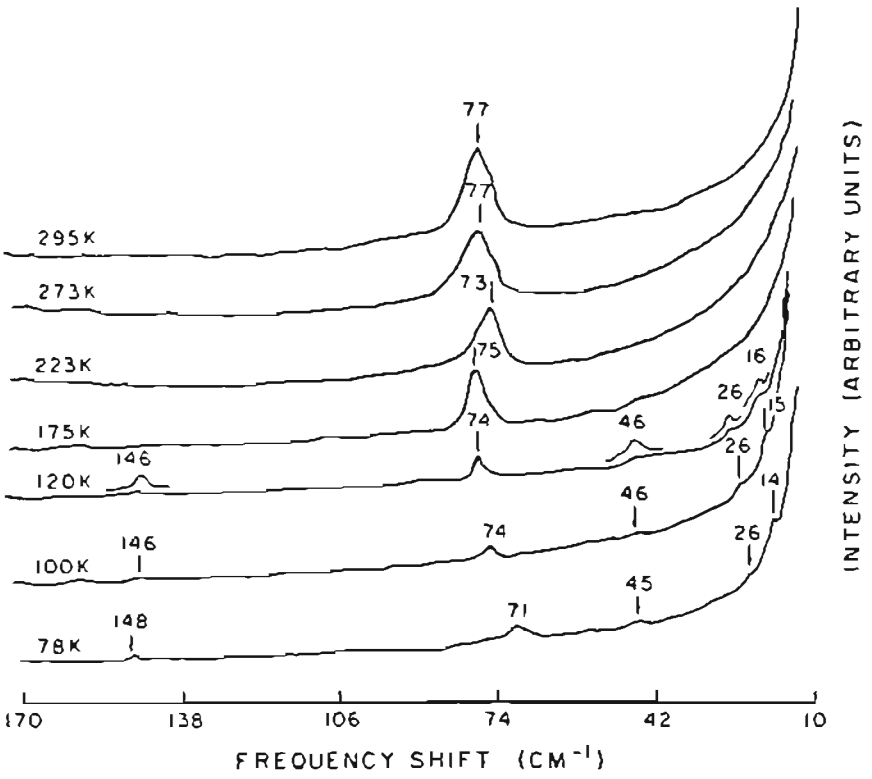

Figure 79. RAMAN SPECTRA OF POLYCRYSTALLINE $SrTiO_3$ AS A FUNCTION OF TEMPERATURE, SHOWING THE GREATER DETAIL AROUND THE EXCITING LINE.

Table XXXIII.

RAMAN BANDS OBSERVED IN $SrTiO_3$ AS A FUNCTION OF TEMPERATURE (FREQUENCIES ARE ALL IN cm^{-1})

	78K	100K	120K	175K	223K	273K	295K	333K	393K
A	48	48	49						
B	71	73	73	75	75	77	77	81	83
C	148	146	146						
D	169	169	172	174	170	171	171	170	
E	235	238	236						
F	255	255	253	250	250	250	250	252	256
G	293	297	299	305	308	311	313	316	320
H	378	372	370	368	372	374	375	380	381
I	450	450	450						
J	561	562	561	560	561	561	561	561	561
K	620	616	617	619	619	620	620	620	623
L	676	674	678	680	680	678	678	678	678
M	719	718	714	716	720	721	723	725	725
N	784	779	793						
P	1040	1043	1046	1040	1038	1033	1036	1040	1040
Q	1320	1312	1315	1316	1318	1320	1320	1320	1320
R	1620	1600	1600	1606	1610	1610	1607	1610	1610

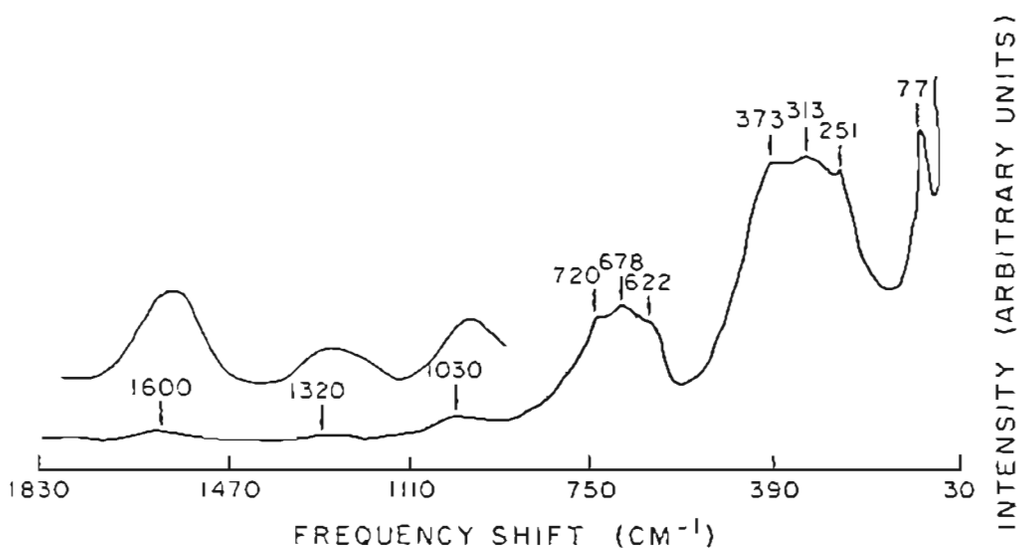

Figure 80. RAMAN SPECTRUM OF SINGLE CRYSTAL $SrTiO_3$.

As the temperature is reduced to 120 K, five sharp lines appear in the spectrum which have energy shifts of 16, 26, 146, 236 and 450 cm^{-1}. These lines undoubtedly appear as a result of the phase transition at 120 K and are essentially unaltered as the temperature is lowered. In addition to these five bands there is yet another band at 793 cm^{-1} (120 K) which appear only in the tetragonal phase. This band (793 cm^{-1}) and the small peaks at 171 and 561 cm^{-1} are attributed to impurities. An impurity induced band corresponding to the ferroelectric T_{1u} soft mode is seen at 46 cm^{-1} (100 K).

Strontium titanate at room temperature is paraelectric and has an ideal cubic perovskite structure (Figure 17) with space group $pm3m[O_h^1]$. Each unit cell contains one formula unit of $SrTiO_3$ and each ion occupies a site with inversion symmetry.

There are 3N degrees of freedom for a crystal containing N atoms in the primitive cell. Of the 3N degrees of freedom, three represent pure translations and appear as the acoustic modes involved in the propagation of sound waves through the crystal. The remaining 3N-3 modes are distributed between internal (molecular) modes, translatory (lattice vibration) modes and rotatory modes (which would become free rotations in the limit of zero interaction of groups within the structure).

There are 15 total degrees of freedom for $SrTiO_3$ in the cubic phase because it has five atoms in a cell. It is important to determine which vibrational modes are Raman and infrared spectroscopically active. The factor group method of classifying fundamental vibrational modes of crystals, as developed by Bhagavantam and Venkatarayudu[119] has been a laborious

procedure fraught with difficulty and with many points of indecision. Among the latter is the choice of the primitive cell and the correct site symmetry of each atom. However, there is a short, straightforward, fool proof correlation method[120] to obtain the vibrational selection rules. There has been little recent discussion of the correlation method in the spectroscopy literature. For this reason, a brief outline of the correlation method in obtaining the normal modes of vibration for $SrTiO_3$ is illustrated in Appendix I (a). In order to show how laborious the Bhagavantam and Venkatarayudu method is, we have outlined that method, too, in the Appendix I(b).

The group-theoretical analysis shows that the acoustic modes in cubic $SrTiO_3$ belong to a triply degenerate T_{1u} species and the optical modes to three triply degenerate T_{1u} species plus one triply degenerate T_{2u} species [see Appendix I (a) & (b)].

The T_{2u} mode is a "silent" mode; i.e., neither IR active nor Raman active. In this silent mode, only the oxygen atoms vibrate, with the titanium and strontium atoms fixed. The remaining three sets of T_{1u} modes represent the Sr-(TiO_3) oscillation, the Ti-O stretching and bending oscillations. The T_{1u} modes are infrared active but Raman inactive. All first-order Raman modes are, therefore, forbidden and the observed bands in the cubic phase are second-order from combinations of phonons at various points in the Brillouin zone. Some of the earlier investigators have attempted to interpret the room temperature spectrum of $SrTiO_3$ as first-order.[55,121-123] We find the spectra of $SrTiO_3$ at room temperature to be entirely second-order.

Second-order Raman scattering is the inelastic scattering of light by a crystal, during which the radiation is scattered by an interaction in which two phonons are either created or annihilated. In the case of Stokes components, overtone bands are obtained from the creation of two phonons from the same vibrational branch, addition combination bands from the creation of two phonons from different branches, and difference combination bands from the creation of one phonon and destruction of another phonon of lower energy. The anti-Stokes components are obtained by interchanging the roles of creation and destruction processes. The wave-vectors of these phonons are restricted by the condition that the total crystal momentum is conserved. In first-order Raman scattering processes, the phonon can only originate from a point near the zone center. Since the wave-vector of the phonon is very small compared with the dimensions of the Brillouin zone the phonon wave-vector must be small to conserve the momentum. The momentum conservation in the second-order scattering process requires effectively that the wave-vectors of the two phonons should be equal in magnitude but opposite in sign. The two phonons can originate anywhere in the zone provided their wave-vectors add up to approximately zero. Because of this difference in satisfying momentum conservation, first-order spectra are made up of discrete lines from individual branches in the vibrational spectrum, whereas the second-order spectra tend to be continuous.

The general space-group selection rules for two-phonon Raman scattering for any crystal lattice possessing inversion symmetry has been derived by Loudon.[124,125] As $SrTiO_3$ possesses inversion symmetry, the

selection rules can be summarized in the following manner. At a general wave-vector in the Brillouin zone, two-phonon combination states (two phonons belonging to different branches) are active in both Raman scattering and infrared absorption, while two-phonon overtone states (two phonons belonging to the same branch) are active only in the Raman process but forbidden in the infrared absorption. Since near the zone boundary the density of states becomes quite large, our interpretation of the second-order spectra will be in terms of phonon energies near the zone boundary.

At the zone edge, there are four doubly degenerate transverse optic modes (TO_1, TO_2, TO_3 and TO_4), four longitudinal optical modes (LO_1, LO_2, LO_3 and LO_4), a doubly degenerate transverse acoustic mode (TA), and a single longitudinal acoustic mode (LA). This results in ten discrete phonon branches to contribute to the multi-phonon process seen in the Raman spectrum of $SrTiO_3$.[57] According to Loudon's[124,125] selection rule analysis, at the zone boundary alone 45 summation bands, 45 difference bands, and 10 overtone bands are possible to contribute to the second-order Raman spectrum. Fortunately, the temperature-dependent study eliminates a large number of difference processes and with the available experimental and theoretical results for $SrTiO_3$ it is possible to interpret the Raman spectrum in terms of phonon pairs at the zone boundary where the density-of-states is maximum.

Our assignment of bands in the room temperature Raman spectrum of $SrTiO_3$ is given in Table XXXIV. The bands are identified by their room

Table XXXIV.

ASSIGNMENT OF THE SECOND-ORDER RAMAN BANDS FOR $SrTiO_3$ AT ROOM TEMPERATURE

Observed second-order energy shift (cm^{-1})	Assignment	Calculated energy shift (cm^{-1})
77	$TO_2 - TA$	74
	$TO_2 - TO_1$	74
250	2 TA	244
	2 TO_1	244
	$TO_1 + TA$	244
	TA + LA	269
313	$TO_2 + TA$	318
	$TO_2 + TO_1$	318
	$TO_4 - TO_2$	312
375	$TO_1 + LO_1$	355
	$TO_2 + LA$	343
	$LO_1 + TA$	355
	$TO_4 - TO_1$	386
	$TO_4 - TA$	386
	2 TO_2	392
620	$TO_4 + TA$	630
	$TO_4 + TO_1$	630
678	2 TO_3	678
	$TA + LO_3$	698
	$TO_1 + LO_3$	698
723	$TO_4 + TO_2$	704
	$LA + LO_3$	723
1036	2 TO_4	1016
	2 LO_2	1036
	$LO_1 + LO_4$	1037
1320	$LO_4 + TO_4$	1312
	$LO_4 + LO_3$	1380
1607	2 LO_4	1608

temperature energy shifts given in Figure 78. The observation of spectra at different temperatures below room temperature helps to distinguish overtones and addition combination bands from difference combination bands. The difference combination band should decrease in intensity relative to the other bands as the temperature is decreased. The band at 77 cm^{-1} decreases in intensity as the temperature is lowered, and hence it is obviously a difference combination band. In contrast, the band at 250 cm^{-1} does not decrease in intensity as the temperature is reduced and must, therefore, be either an overtone or addition combination band. The temperature dependence of the energy of 77 cm^{-1} band is not the same as the ferroelectric "soft" mode observed by Barker and Tinkham[63] and by Cowley[53] for $SrTiO_3$ and so it does not appear to be a fundamental of the TO_1 mode at the center of the zone, being Raman active due to distortion from cubic symmetry. We assign the 77 cm^{-1} band to the TO_2-TA and TO_2-TO_1 combinations and the 250 cm^{-1} band to the overtones 2TA and $2TO_1$ and the addition combination TO_1 + TA and TA + LA. The 250 cm^{-1} band gives the single-phonon energy of TA and TO_1 modes as 125 cm^{-1} at the zone boundary as compared to 126 cm^{-1} from the measurements of Nilsen and Skinner.[58]

The intensity of band at 313 cm^{-1} decreases only slightly as the temperature is lowered. This band is assigned to both sum and difference combination bands, namely TO_2 + TA, TO_2 + TO_1, and TO_4 - TO_2 band. From the $TO_2 \pm$ TA and $TO_2 \pm TO_1$ combinations, the TA and TO_1 phonon energies are estimated to be 118 cm^{-1} and the TO_2 energy to be 195 cm^{-1} at the zone boundary. These values are in excellent agreement with the neutron diffraction[56] values of 117 and 194 cm^{-1}. The band at 375 cm^{-1} behaves

qualitatively in the same manner as the 313 cm^{-1} band. The following combinations are allotted for this band: $TO_1 + LO_1$, $TO_2 + LA$, $LO_1 + TA$, $TO_4 - TA$, $TO_4 - TO_1$, and $2\ TO_2$. The $2\ TO_2$ overtone yields a single-phonon energy of 188 cm^{-1} for TO_2.

The bands in the region 620-723 cm^{-1} remain reasonably intense and maintain the band contour as the temperature is decreased. For this reason, no difference combination band should be present in this region of the spectrum, and the bands are attributed to addition combination and overtones only. The 620 cm^{-1} band is assigned to $TO_4 + TA$, and $TO_4 + TO_1$. From this and the assignment for 375 cm^{-1} band yield single-phonon energies of 498 cm^{-1} for TO_4 mode and 123 cm^{-1} for the TA and TO_1 modes at the zone boundary. The single-phonon energy for TO_3 mode is estimated as 339 cm^{-1} from the $2\ TO_3$ overtone given to the 678 cm^{-1} band. This energy is in good agreement with 328 cm^{-1} from the neutron diffraction work for the TO_3 mode. The addition combination bands $TO_4 + TO_2$ and $LA + LO_3$ are responsible for the observed band at 723 cm^{-1}. The $TO_4 \pm TO_2$ combination yields phonon energies of 518 cm^{-1} and 205 cm^{-1} for the TO_4 and TO_2 modes. The $LA + LO_3$ combination for 723 cm^{-1} band along with the combination bands for 678 cm^{-1} and 250 cm^{-1} yield 576 cm^{-1} for the LO_3 mode at the zone boundary.

The bands at 1036, 1320, and 1607 cm^{-1} all remain reasonably intense and maintain their band shape as the temperature is lowered. The band at 1036 cm^{-1} is assigned to $2\ LO_2$, $2\ TO_4$ and $LO_1 + LO_4$; 1320 cm^{-1} band to $LO_4 + TO_4$, and $LO_4 + LO_3$; and the 1607 cm^{-1} band to the $2\ LO_4$ overtone.

These band assignments yield 518 cm^{-1} and 804 cm^{-1} as the energies of LO_2 and LO_4 modes, respectively. We find that the bands at 171 cm^{-1} and 561 cm^{-1} are strongly sample dependent in the Raman spectra. These bands are absent in the clear, single crystal $SrTiO_3$ sample (see Figure 80). Lines at these frequencies have been consistently reported in the infrared and neutron spectra both in the cubic and tetragonal phase of $SrTiO_3$. Since there are no first-order Raman active modes in cubic $SrTiO_3$, we believe that these two bands are the result of impurity-induced Raman scattering. Further, we have evidence from the high temperature electrical conductivity studies, for the presence of small amounts of acceptor impurities (Al, Fe, or Cr on Ti site) in the sample [see Section 5.3]. The frequencies of the phonon branches at the zone boundary for $SrTiO_3$ deduced from this Raman measurements are listed in Table XXXV.

Raman scattering in the tetragonal phase

As the temperature is decreased to 120 K, new lines appear with energy shifts at 16, 26, 46, 146, 236, 450 and 793 cm^{-1}. These bands appear only in the tetragonal phase and are presumably forbidden by symmetry in the cubic perovskite phase. It was thought that some or all of these indistinct bands were attributable to local impurity modes[58] until Fleury, et al.[9] associated most of them with proper first-order modes of the tetragonal structure. The presence of acceptor impurities raised the transition temperature to 120 K from 110 K (as reported for single crystal $SrTiO_3$) for the present samples.

Table XXXV.

FREQUENCIES (cm^{-1}) OF PHONON BRANCHES AT THE EDGE OF THE BRILLOUIN ZONE FOR $SrTiO_3$ (295 K)

Phonon Branch	Present work (average value)	Published work[53,57]
TO_1	122	117, 120
TO_2	196	194, 190
TO_3	339	328, 330
TO_4	508	544, 540
LO_1	233	270
LO_2	518	473
LO_3	576	550
LO_4	804	807
TA	122	117, 110
LA	147	150

The cubic to tetragonal phase transition involves only a small rotation of the oxygen octahedron. The displacements which yield the tetragonal phase are illustrated in Figure 81. The TiO_6 octahedra rotate around a cubic [111] axis,[126] but the sense of rotation is reversed in adjacent unit cells, because in the perovskite structure the BO_6 octahedra have common oxygen corners and half of them rotate by an angle $+\Theta$ and the other half by an angle $-\Theta$. The tetragonal unit cell is double the size of the cubic cell. Because of the doubling of the unit cell, the zone boundary of the cubic phase now becomes the zone center of the tetragonal phase. The space group of $SrTiO_3$ in the low temperature, tetragonal phase was first correctly determined by the EPR studies of Unoki and Sakudo,[127] who determined it as D_{4h}^{18} [I_4/mcm] with two formula groups per primitive unit cell.

A group theoretical analysis for tetragonal $SrTiO_3$ predicts seven Raman-active modes [$A_{1g} + 3\ E_g + 2\ B_{2g} + B_{1g}$]. Taylor and Murray[60] have shown from polarization study of single crystal $SrTiO_3$ that the two E_g and B_{2g} pairs have nearly the same frequency, to the accuracy of the experiment. In other perovskites, however, such as $KMnF_3$ and $RbCaF_3$, the E_g and B_{2g} pairs are clearly separated in frequency.[128,129] Allowing for the coincidence in frequency of the two E_g - B_{2g} pairs, there should be five distinct first-order modes active in the Raman spectrum of tetragonal $SrTiO_3$. The bands observed at 16, 26, 146, 236 and 450 cm^{-1} are the five Raman active modes as predicted by symmetry for the tetragonal structure of $SrTiO_3$. The triply degenerate silent T_{2u} soft mode of the cubic phase splits into two zone-center modes: a doublet (E_g) with rotation axes

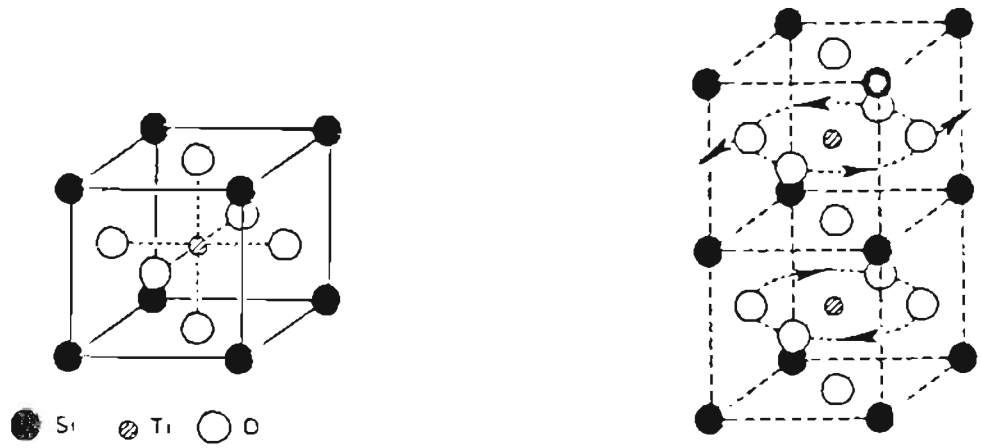

(a) (b)

Figure 81. (a) CRYSTAL STRUCTURE OF CUBIC $SrTiO_3$
(b) DISPLACEMENTS YIELDING THE TETRAGONAL PHASE OF $SrTiO_3$ FROM THE CUBIC PHASE.

perpendicular to the four fold axis and a singlet (A_{1g}) with rotation axis parallel to the four fold axis. The zone-center frequencies for the tetragonal phase obtained from the Raman spectra are compared with frequencies obtained by other techniques in Table XXXVI.

In addition to the impurity induced bands at 172 and 561 cm^{-1}, there is yet another small peak at 793 cm^{-1} which we believe is also due to impurities. This particular impurity mode appears only in the tetragonal phase and it might not be in correct symmetry to show any Raman activity in the cubic phase. This impurity mode is not reported in the literature. Presence of the impurities should also show an impurity induced peak corresponding to the ferroelectric T_{1u} soft mode which has been observed at 40 cm^{-1} (80 K) by EFIRS (Electric field induced Raman scattering) and neutron scattering. A close examination of Figure 82 shows this to be the case; there is a weak peak at 46 cm^{-1} (100 K) in this spectrum.

5.8 Ruddlesden-Popper [$nSrTiO_3 \cdot SrO$] Phases

Figure 82 gives the crystallographic unit cell containing two formula units of the compounds for the first six values of n by stacking required numbers of cubic $SrTiO_3$ perovskite blocks and a SrO layer. The x-ray powder diffraction results obtained for the first three members in this series prepared by liquid mix technique are shown in Table XXXVII. For the compounds Sr_2TiO_4, $Sr_3Ti_2O_7$, and $Sr_4Ti_3O_{10}$ there is a gradual increase in the lattice constants along the c-axis. It should be mentioned that

Table XXXVI. Zone-center phonon frequencies in tetragonal $SrTiO_3$ [cm^{-1}]

Raman:									
100 K[a]	15	26	46*	146	169*	235	450	562*	779*
	(E_g)	(A_{1g})		(B_{2g} + E_g)		(B_{1g})	(B_{2g} + E_g)		
95 K[b]	9	28	40*	142	171*	260	444	543*	
80 K[c]		39		148	172*	247	453	551*	
30 K[d]	15	48		145			459		
Neutron:[e]	12	33	40		168	262	452		
	(80 K)	(80 K)	(80 K)		(90 K)	(90 K)	(90 K)		
EFIRS:[f]		40			171	268		560	
		(80 K)			(47 K)	(10 K)		(47 K)	
Infrared:[g]					172			544	
					(80 K)			(80 K)	

(a) present work
(b) Taylor and Murray[60]
(c) Nilsen and Skinner[58]
(d) Fleury, Scott and Worlock[59]
(e) Stirling[130], Shirane and Yamada[131]
(f) Fleury and Worlock[59]
(g) Barker[66]
* Impurity induced mode

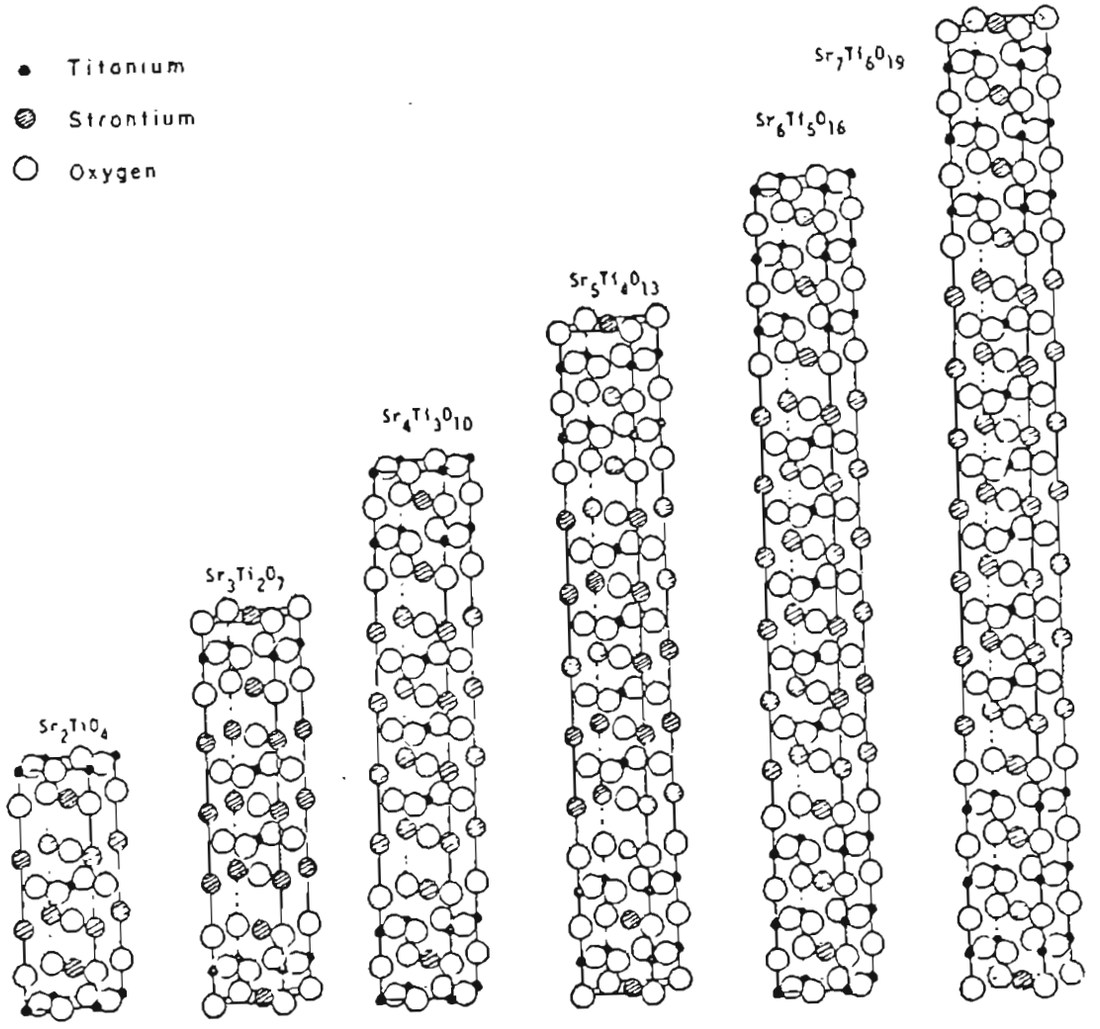

Figure 82. STRUCTURES OF RUDDLESDEN-POPPER [$nSrTiO_3 \cdot SrO$] PHASES FOR n UP TO 6.

Table XXXVII.

LATTICE CONSTANTS FOR $SrTiO_3$, Sr_2TiO_4, $Sr_3Ti_2O_7$, and $Sr_4Ti_3O_{10}$

Compound	aÅ	cÅ
$SrTiO_3$	3.905	
Sr_2TiO_4	3.882	12.600
$Sr_3Ti_2O_7$	3.907	20.454
$Sr_4Ti_3O_{10}$	3.900	28.124

single phase compounds of the above members are obtained by heating the glassy material obtained in the liquid mix technique to only 800°C for about 10 hours, and there is no change in the x-ray powder pattern when the samples are heated to still higher temperatures (1200, 1350°C) for prolonged periods of time. It was mentioned in Chapter II that a pure $Sr_4Ti_3O_{10}$ was prepared for the first time by MacCarthy et al.[80] by firing appropriate amounts of TiO_2 and SrO for a week at 1475°C, with several intermediate regrindings. Since the mixing is carried out in the liquid state in our preparation technique, diffusion is not a problem and we are able to get the homogeneous single phase material by firing at 800°C for about ten hours.

The x-ray diffraction pattern for compounds with n = 4, 5, and 6 are all similar to cubic $SrTiO_3$ phase. There was no evidence of any second phase in the x-ray diffraction pattern for these three compounds. As the value of n increases, the number of cubic perovskite ($SrTiO_3$) blocks between the SrO layers [Figure 82] also increases. The powder x-ray diffraction technique might not be sensitive enough to pick up the (SrO) layers along with large numbers of $SrTiO_3$ blocks sandwiched between the (SrO) layers. Raman spectroscopy is a much more sensitive technique and so we used that technique to study these phases in more detail.

The observed Raman spectra of the compounds with n = 1 to 6 are shown in Figure 83 and the observed frequency shifts (cm^{-1}) are listed in Table XXXVIII. The factor group analysis for the Ruddlesden-Popper phases for n up to 25 were made by the correlation method [see Appendix

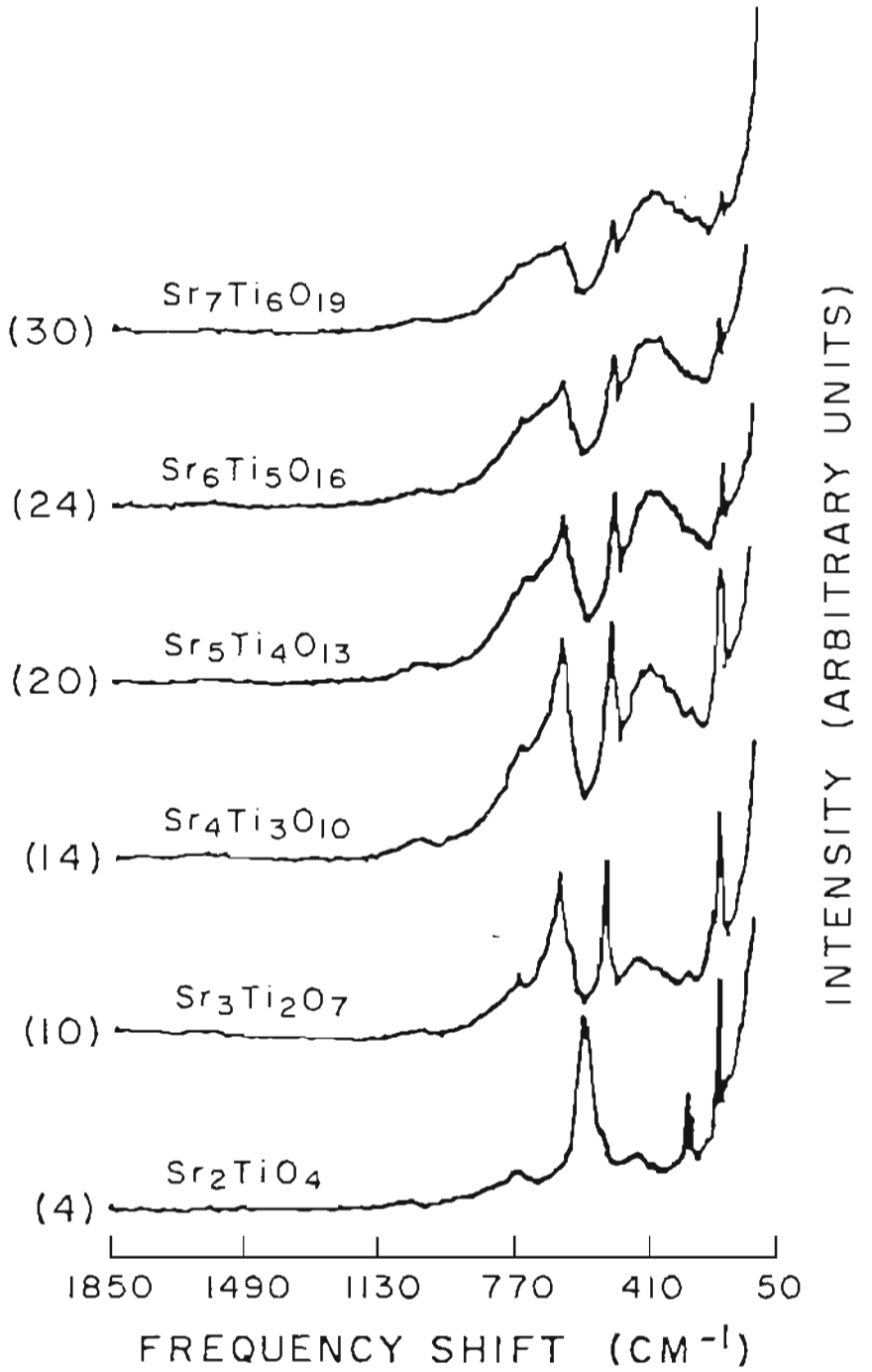

Figure 83. RAMAN SPECTRA FOR THE FIRST SIX COMPOUNDS IN THE RUDDLESDEN-POPPER [$nSrTiO_3 \cdot SrO$] SERIES.

Table XXXVIII.

OBSERVED FREQUENCY SHIFT [cm^{-1}] IN THE RUDDLESDEN-POPPER PHASES

Compound	cm^{-1}	Compound	cm^{-1}	Compound	cm^{-1}
	203		180		181
	284		273		270
Sr_2TiO_4	388	$Sr_3Ti_2O_7$	347	$Sr_4Ti_3O_{10}$	320
	426		415		381
	502		498		486
	574		631		630
	630		735		734
	748		1030		1026
	1040				1600
	187		187		187
	273		270		261
	352		360		378
$Sr_5Ti_4O_{13}$	383	$Sr_6Ti_5O_{16}$	382	$Sr_7Ti_6O_{19}$	482
	486		486		631
	628		630		673
	736		671		725
	1027		732		1018
	1602		1017		1600
			1590		

II]. Tables XXXIX and XL give the site symmetry for strontium, titanium, and oxygen atoms and the results of the factor group analysis, respectively.

The space group is determined for the first three compounds of the Ruddlesden-Popper phases as D_{4h}^{17} [I4/mmm]. Since the other members of this series seem to have the same type of stacking [see Figure 82] with different numbers of perovskite blocks, the space group for the whole series of members in the family $nSrTiO_3 \cdot SrO$ can be treated under the same space group, D_{4h}^{17} [I4/mmm]. As the number of perovskite blocks increases, there is change only in the c-axis. It must be remembered that no first-order modes are allowed to be active in Raman scattering in the cubic $SrTiO_3$, with space group O_h^1 [Pm3m]. Similarly, SrO has no first-order Raman active modes.

First-order Raman scattering is allowed in the Ruddlesden-Popper phases as can be seen from Table XL which also gives the infrared absorption modes. The factor group analyses does not show a simple band multiplicity of Raman active modes as the value of n is increased even though the space group D_{4h}^{17}, I4/mmm is preserved by stacking the cubic $SrTiO_3$ blocks. This is because of change in the sites occupied by strontium, titanium and oxygen atoms as n is changed. An enlargement of the primitive cell, without a change in space group symmetry will cause an increase in the number of allowed modes usually by some multiplicity factor only if there is no change in the site symmetry of atom species involved. Such a simple band multiplicity effect is seen in $ZnSb_2O_6$,[81] trirutile structure with space group D_{4h}^{14} [P42/mmm]. Trirutile structure is one in

Table XXXIX.

SITE SYMMETRY FOR THE ATOMS IN $nSrTiO_3.SrO$

Atom	Site	n=1	2	3	4	5	6	7	8	9	10
	D_{4h} (1)	*		*		*		*		*	
	C_{4v} (2)		*	*	*	*	*	*	*	*	*
Ti					*	*	*	*	*	*	*
							*	*	*	*	*
									*	*	*
											*
	D_{4h} (1)		*		*		*		*		*
	C_{4v} (2)	*	*	*	*	*	*	*	*	*	*
				*	*	*	*	*	*	*	*
Sr						*	*	*	*	*	*
								*	*	*	*
										*	*
	D_{4h} (1)		*		*		*		*		*
	D_{2h} (2)	*		*		*		*		*	
	C_{4v} (2)	*	*	*	*	*	*	*	*	*	*
O				*	*	*	*	*	*	*	*
						*	*	*	*	*	*
								*	*	*	*
										*	*
	C_{2v} (4)		*	*	*	*	*	*	*	*	*
					*	*	*	*	*	*	*
							*	*	*	*	*
									*	*	*
											*

Table XL.

FACTOR GROUP ANALYSES FOR THE RUDDLESDEN-POPPER [$nSrTiO_3$.SrO] PHASES

SPACE GROUP D_{4h}^{17}, $I4/mmm$.NO. OF MOLECULES IN A PRIMITIVE CELL = 1

n	A_{1g}	B_{1g}	E_g	A_{2u}	B_{2u}	E_u	Raman active modes	I.R active modes	
1	2	0	2	4	1	5	4	7	
2	4	1	5	6	1	7	10	11	
3	6	1	7	8	2	10	14	16	
4	8	2	10	10	2	12	20	20	
5	10	2	12	12	3	15	24	25	
6	12	3	15	14	3	17	30	29	
7	14	3	17	16	4	20	34	34	
8	16	4	20	18	4	22	40	38	
9	18	4	22	20	5	25	44	43	$\Gamma_{acoustic} = A_{2u} + E_u$
10	20	5	25	22	5	27	50	47	
11	22	5	27	24	6	30	54	52	B_{2u} is inactive
12	24	6	30	26	6	32	60	56	
13	26	6	32	28	7	35	64	61	
14	28	7	35	30	7	37	70	65	
15	30	7	37	32	8	40	74	70	
16	32	8	40	34	8	42	80	74	
17	34	8	42	36	9	45	84	79	
18	36	9	45	38	9	47	90	83	
19	38	9	47	40	10	50	94	88	
20	40	10	50	42	10	52	100	92	
21	42	10	52	44	11	55	104	97	
22	44	11	55	46	11	57	110	101	
23	46	11	57	48	12	60	114	106	
24	48	12	60	50	12	62	120	110	
25	50	12	62	52	13	65	124	115	

which 3-fold increase in the size of the unit cell is obtained by stacking three rutile cells along the c-axis. A tripled unit cell with no change in symmetry or site population simply triple the number of modes appearing in each irreducible representation. The twelve predicted Raman active modes are observed in $ZnSb_2O_6$.[81]

The total number of Raman active modes increase in steps of 10 for even and odd values of n, respectively, in the Ruddlesden-Popper phases. This becomes clear when the site symmetries for the atoms are considered for even and odd values of n. Atoms lying on site symmetries D_{4h} and D_{2h} do not give any Raman active modes [see Appendix II]; atoms on site symmetry C_{4v} give two; and those on C_{2v} sites give four Raman active modes. For even values of n, for each increase in n there are two more titanium atoms involved and they occupy the C_{4v} sites. This gives rise to two new Raman active modes. Similarly, there are two more new strontium and six oxygen atoms involved. The two strontium atoms go to C_{4v} sites and contribute two new Raman modes. Four oxygens occupy C_{2v} site and the remaining two go to C_{4v} site thus increasing the Raman active modes by six. Altogether, therefore, ten new Raman active modes are created for each respective increase in the even values of n. Similar site arrangements increase the Raman active modes by ten for each increase in the odd values of n.

The B_{2u} mode in the group D_{4h} is inactive, i.e., neither active in Raman scattering nor infrared absorption. The three acoustic modes have $A_{2u} + E_u$ symmetry. The Raman, infrared active modes, the inactive modes

along with three acoustic modes account for the total degrees of freedom for each compound.

Not all the Raman active modes predicted by group theoretical analysis are actually observed and this may be due to poor linkage between the individual segments in the enlarged unit cell. Because of this weak linkage, no coupling between the vibrational motions of the segments would exist. Such a reasoning for weak linkage between NbO_6 octahedra has been applied in the past for the observed 26 Raman bands[132] in $Ca_2Nb_2O_7$ even though the group theoretical analysis predicts 129 normal modes of vibration, all of which are active in both Raman and infrared absorption spectra.

White and Keramidas[81] observed a single band at 579 cm^{-1} in Sr_2TiO_4, two bands in $Sr_3Ti_2O_7$, and three bands in $Sr_4Ti_3O_{10}$. The spectra reported in this work (Figure 83) for these three compounds are not quite as simple as reported by White and Keramidas.[81] Many bands appear close to each other and some weak bands may easily have been overlooked when they appear next to strong bands. White and Keramidas[81] concluded that the new bands appearing in the Raman spectra of Ruddlesden-Popper phases have no counterparts in the parent structures. But our observation indicates that the broad bands in the region 360-380 cm^{-1} and the band at 630 cm^{-1} are also present in the parent $SrTiO_3$ spectra (Figures 78 and 80).

It is not possible to give a firm assignment of the spectra since not all the predicted modes are observed and secondly no polarization data from single crystal studies are available. Of great interest are the strong bands in the range 500-700 cm^{-1}. The A_{1g} modes should be the most

intense and should correspond to a symmetric stretch of the TiO_6 octahedra. The band around 180 cm^{-1} is due to Sr-(TiO_3) vibration. The frequency of this particular vibration is found to be at 178 cm^{-1} in $SrTiO_3$ by far-infrared dielectric dispersion experiments.[64]

Group theoretical analysis predicts 2 A_{1g} modes (Raman active) for Sr_2TiO_4. A close examination of the strong band at 574 cm^{-1} shows that it is made up of two bands very close to each other. This strong band splits into two for higher values of n. It is possible for many of the Raman active modes to have nearly the same energy and the bands therefore overlap one another.

The striking features of the spectra are the growth in intensity of the broad band in the region 360-380 cm^{-1} and broadening of the band at 630 cm^{-1} as n is increased. These broad bands have counterparts in the spectrum of $SrTiO_3$ (see Figures 78 and 80). The observed spectrum in $SrTiO_3$ was interpreted as second-order in terms of phonon energies near the Brillouin zone boundary[133] (see Section 5.7). It is seen from Figures 78 and 80 that the broad band in the region 250-380 cm^{-1} is stronger in intensity than the band at 680 cm^{-1}. Therefore, the behavior of the bands in the region 360-380 cm^{-1} and 630 cm^{-1} in the Ruddlesden-Popper phases as n is increased signifies that more second-order scattering from individual $SrTiO_3$ blocks become more predominant. The weak bands at 1030 and 1600 cm^{-1} found in Figure 83 are due to second-order scattering as observed in $SrTiO_3$. In addition to general features found in the spectra for the Ruddlesden-Popper phases and $SrTiO_3$, there are additional bands at ≈185 and 485 cm^{-1} even in the spectrum for $Sr_7Ti_6O_{19}$. The Raman spectra

show the additional bands along with the second-order broad bands for all the compounds investigated in this work (Table XL and Figure 83). This suggests the existence of the compounds in the series n $SrTiO_3$'SrO with n > 3.

6. CONCLUSIONS

6.1 Solubility of Lanthanum in $SrTiO_3$

a) The compound $La_xSr_{1-x}TiO_3$ with x up to 40 at.% was observed to be homogeneous by microscopic examination.

b) The observed x-ray powder pattern corresponds to the cubic perovskite structure and the plot of lattice constant a_o vs x indicates a Vegards law dependence within the experimental error.

c) These results indicate that Tofield and Scott's[26] conclusion as to the absence of a significant range of solubility for lanthanum in $SrTiO_3$ is incorrect.

6.2 Self-Compensation in Lanthanum-Doped $SrTiO_3$

a) Gravimetric measurements on lanthanum doped $SrTiO_3$ have shown that the reversible change of oxygen content, between specified states of oxidation and reduction is proportional to the dopant concentration.

b) These measurements indicate that the donor dopants are compensated ionically by additional oxygen uptake in the oxidized state.

c) The range of this reversible change in oxygen stoichiometry is up to more than an order of magnitude larger than the oxygen nonstoichiometry of the undoped $SrTiO_3$.

d) The gravimetric measurements are explained by a model involving shear structure in which the SrO formed in the oxidized condition are accommodated in an ordered fashion in the structure, in the way that Ruddlesden-Popper phases, $nSrTiO_3 \cdot SrO$ are formed.

e) The gravimetric observation suggests a bridge between two separate schools of thought on non-stoichiometry: The case of random, point defects in which aliovalent cations are incorporated into the host lattice without a change in either structure or cation-anion ratio, and the case of extended defect structures in which all cations retain their normal oxidation states and the resulting change in cation-anion ratio is accommodated by subtle structural changes.[134-136]

6.3 Electrical Conductivity in $SrTiO_3$

a) The electrical conductivity of polycrystalline $SrTiO_3$ has been measured over the oxygen partial pressure range of 10^0 to 10^{-22} atm in the temperature range of 800-1050°C. The electrical conductivity has been observed to be proportional to the -1/6th power of the oxygen partial pressure

in the oxygen pressure range 10^{-15} to 10^{-22} atm. Hence, Equation (99),

$$O_o \rightleftharpoons 1/2\ O_2 + V_o^{\cdot\cdot} + 2e' \qquad (99)$$

describes nonstoichiometric disorder in $SrTiO_3$ in the low oxygen partial pressure range.

b) For $P_{O_2} > 10^{-15}$ atm the defect chemistry of $SrTiO_3$ is dominated by accidental acceptor impurities and their related oxygen vacancies. Because of the presence of unknown acceptor impurities, a region in which a $P_{O_2}^{-1/4}$ dependence for the conductivity has been observed.

c) The conductivity changes from n- to p-type as the P_{O_2} is increased beyond 10^{-4} atm. The p-type conductivity observed results from a stoichiometric excess of oxygen which occupies the impurity related oxygen vacancies according to the reaction,

$$V_o^{\cdot\cdot} + 1/2\ O_2 \rightleftharpoons O_o + 2h^{\cdot} \qquad (108)$$

A stoichiometric excess of oxygen is achieved even while not all the available oxygen sites are occupied.

d) The concentration of acceptor impurities in the undoped $SrTiO_3$ is estimated to be roughly 170 ppm (atomic). The possible acceptor impurities are: Al, Fe, Mg, Cr or Ga on titanium sites or alkali metals like Li, Na, or K on strontium sites.

e) The activation enthalpies for conduction in the three distinct regions are calculated from the Arrhenius slopes and are shown in Tables VII, VIII, and X. The ready availability of impurity related oxygen vacancies result in low enthalpy for the oxygen incorporation reaction in the p-type region.

f) Grain boundaries have no significant effect on electronic transport in the range of experimental conditions considered here.

6.4 Electrical Conductivity in $SrTiO_3$ with (Sr/Ti) < 1

a) The electrical conductivity of strontium titanate with Sr/Ti = 0.996 and 0.99 was found to be similar to that obtained in $SrTiO_3$ with an ideal cationic ratio. The observed data were proportional to the -1/6th power of oxygen partial pressure for the $P_{O_2} < 10^{-15}$ atm, proportional to $P_{O_2}{}^{-1/4}$ for the pressure range 10^{-8} - 10^{-15} atm, and proportional to $P_{O_2}{}^{+1/4}$ for $P_{O_2} > 10^{-4}$ atm.

b) The absolute values of the conductivity did not change significantly as the Sr/Ti ratio was changed for all the three regions. These observations indicate that defects related to the deviation from ideal cation/cation ratio are associated in to neutral vacancy pairs (V''_{Sr} $V^{\cdot\cdot}_{o}$).

c) In the p-type region the observed conductivity is due to fractional filling of the impurity related oxygen vacancies,

$$V_O^{\cdot\cdot} + 1/2\ O_2 \rightleftharpoons O_O + 2h^{\cdot} \qquad (108)$$

and the defects present due to the deviation from ideal cationic ratios has no significant role in influencing the observed conductivity.

d) The activation enthalpies estimated from the Arrhenius slopes (Tables XVII through XXII) were found to be close, within the experimental error, to be the values obtained for $SrTiO_3$ with Sr/Ti = 1.

6.5 Electrical Conductivity in Donor-Doped $SrTiO_3$

a) The electrical conductivity of $SrTiO_3$ doped with 0.1 - 2 at.% lanthanum indicated two types of charge compensation according to the oxygen partial pressure, namely electronic and ionic.

b) Under highly reducing conditions ($P_{O_2} < 10^{-16}$ atm.) the carrier concentration is fixed by the amount of donor (La) added and hence the conductivity was found to be independent of oxygen partial pressure. A plateau region (electronic compensation) was found for the samples with higher lanthanum contents (see Figures 51 to 55) at

temperatures 1000°C and above. These high temperature regimes can probably be retained by quenching at room temperature. Use of such a semiconductor in the studies of photolysis of water should yield a well-defined electrode.

c) For $P_{O_2} > 10^{-16}$ atm, the observed conductivity varied as -1/4th power of oxygen partial pressure. In this region, the extra charge of lanthanum is compensated by doubly ionized strontium vacancies (ionic compensation). The additional strontium that results from the strontium vacancies may combine with oxygen to form SrO layers which can be built into the lattice in an ordered fashion.

6.6 Electrical Conductivity in Acceptor-Doped $SrTiO_3$

a) Electrical conductivity of $SrFe_xTi_{1-x}O_3$ with x = 0.036, 0.1 and 0.5 at.% was found to be proportional to ≈-1/4th power of P_{O_2} in the n-type region and proportional to +1/4 power of P_{O_2} in the p-type region. Similar behavior was observed in $SrAl_{0.003}Ti_{0.997}O_3$. Iron exists in two possible valence states (Fe^{+2}, Fe^{+3}) and the charge neutrality condition under reducing conditions, assuming that all the added iron is present as Fe^{+2} is,

$$[Fe''_{Ti}] = [V_O^{\cdot\cdot}] = \text{constant}$$

and in the range where iron is present predominantly as Fe^{+3}, the charge neutrality condition is,

$$[Fe'_{Ti}] = 2\,[V_O^{\cdot\cdot}]$$

b) The added acceptor impurities partly compensate the oxygen vacancies that are formed during reduction and decrease the electron concentration. Hence, the observed conductivity in the acceptor doped samples is less than that of the undoped sample in the n-type region.

c) Since the concentration of the acceptor-related oxygen vacancies in the deliberately doped samples is higher than that in the undoped $SrTiO_3$, more amount of oxygen will occupy these vacancies in the acceptor doped samples. This gives rise to observed higher electrical conductivity values in the p-type region for the acceptor doped samples as compared to undoped $SrTiO_3$.

d) The activation enthalpies for conduction in the acceptor (Fe, Al)-doped samples deduced from the Arrhenius slopes are given in Tables XXVI, XXVIII, XXXI and XXXII for both the regions of conduction.

6.7 Raman Spectra of $SrTiO_3$

a) The room temperature Raman spectrum of $SrTiO_3$ has been interpreted in terms of second-order scattering processes

taking place mainly at the Brillouin zone boundary. In agreement with the selection rules for the cubic perovskite structure, no first-order Raman spectra were detected. The temperature-dependent Raman spectra of $SrTiO_3$ have been used to differentiate between possible combination and summation processes and difference processes which contribute to the multiphonon spectrum of the cubic phase. From the observed energy shifts in the room temperature spectrum, the single-phonon energies at the zone boundary are deduced for the ten different phonon branches used for the peak assignments.

b) The new lines which appear at 16, 26, 146, 236 and 450 cm^{-1} in the spectra taken below 120 K are attributed to the first-order modes allowed by symmetry in the tetragonal structure. A new impurity related peak at 793 cm^{-1} is reported in addition to other impurity induced peaks at 172 and 561 cm^{-1} observed by earlier investigators. An impurity induced band corresponding to the ferroelectric soft mode is observed at 46 cm^{-1} (100 K). The deduced zone-center phonon frequencies in the tetragonal phase is compared with the results of neutron scattering, infrared absorption, and electric field induced Raman scattering experiments.

c) All the main bands observed in the single crystal $SrTiO_3$ are present in the Raman powder spectrum. All the energy shifts reported in this work are compared with the available

data obtained from single crystals. There is excellent agreement between the data obtained in this experiment using powder samples and the results from single crystal. Although there is no alternative to the wealth of information that can be obtained by single-crystal studies, in some systems much of the same information can be realized from the powder method as exemplified by the cubic and tetragonal phase of $SrTiO_3$.

6.8 Ruddlesden-Popper ($nSrTiO_3 \cdot SrO$) Phases

a) Single-phase material of composition $Sr_4Ti_3O_{10}$ was obtained by heating the samples obtained by the liquid mix technique to 800°C for about 10 hours.

b) The lattice constant increases along the c-axis for the compounds Sr_2TiO_4, $Sr_3Ti_2O_7$ and $Sr_4Ti_3O_{10}$. The lattice constant along the a-axis is essentially the same (≈3.90Å) for all compounds.

c) For compounds with $n > 3$, no evidence of the presence of second phase is seen. This suggests the existence of homogeneous, single phase materials of compositions with $n > 3$.

d) Factor-group analysis made for $nSrTiO_3 \cdot SrO$ up to $n = 25$ did not give a simple band multiplicity even though the space group D_{4h}^{17} (I4/mmm) was preserved by stacking the $SrTiO_3$ blocks.

e) For both even and odd values of n, the number of Raman active modes increases by ten for each increase in the value of n. This is because the number of strontium, titanium and oxygen atoms entering into correct site symmetries to give Raman active modes increased in an ordered fashion.

f) Not all the predicted Raman active modes were observed in the spectra for compounds up to n = 6, and this may be due to poor coupling of the vibrations between the individual segments in the enlarged unit cell obtained by stacking different number of $SrTiO_3$ blocks.

7. RECOMMENDATIONS FOR FUTURE WORK

a) It is suggested that the donor-dopants in the system $SrTiO_3$ are compensated in the ionic compensation region by the formation of SrO which is built in the structure in an ordered fashion. This suggested model could be tested experimentally by lattice image techniques, using high resolution electron microscope. Lattice images are formed by the interference of the direct and the diffracted beams. The accommodation of SrO layer in the ordered fashion in lanthanum doped $SrTiO_3$ samples should also be studied by Raman spectral measurements.

b) The structures (see Figure 82) of the higher members of the series $nSrTiO_3 \cdot SrO$ are proposed as the stacking of the different numbers of cubic $SrTiO_3$ blocks between the SrO layers. The existences of these compounds can also be studied by the lattice image technique. The compounds Sr_2TiO_4, and $Sr_3Ti_2O_7$ have been studied by Tilley[137] using the above mentioned technique. He was not able to prepare single phase compound of either $Sr_4Ti_3O_{10}$ or any other members (with $n > 2$) in the series $nSrTiO_3 \cdot SrO$ using the solid state reaction sample preparation techniques.

c) It is assumed that the added lanthanum substitutes for strontium atoms in the lattice because of its close size factor. A change in cation site occupied by lanthanum dopant, i.e., part of lanthanum going into titanium site and acting as acceptor, is discounted because of the unlikely possibility of the creation of titanium vacan-

cies in the perovskite structure that are required to compensate donor-dopants like tantalum and niobium substituted for Ti^{+4}. The electron spin resonance (EPR) experiment in the reduced $SrTiO_3$ containing La^{+3} should be performed to test the validity of our assumption.

In a structural analog $BaTiO_3$, EPR measurements have revealed that the paramagnetic center in $BaTiO_3$ is an F-center, i.e., a single electron trapped at an oxygen vacancy, and not a Ti^{+3} ion as observed in reduced TiO_2.[138] An introduction of trivalent ions into Ti^{+4} sites will also form F-centers in reduced $BaTiO_3$. Takeda and Watanabe[105] examined EPR measurements in reduced $BaTiO_3$ ceramic samples containing La^{+3} ions. For a certain value of the Ba/Ti ratio, which is larger than unity, a characteristic F-center signal was observed. This observation means that some fraction of doped rare earth ions act certainly as acceptors and this means that La^{+3} ions will be at Ti^{+4} sites.

Therefore, a similar EPR measurement on reduced $SrTiO_3$ containing La^{+3} will help one to find out whether added lanthanum is going to titanium sites in addition to strontium sites.

d) The composition of strontium titanate at 1 atm of oxygen partial pressure is taken as $SrTiO_3$, even though it is expected to be of the form $SrTiO_{3-\delta}$ ($\delta << 1$). The electrical conductivity measurements in the undoped $SrTiO_3$ showed three different regions where the conductivity varied as -1/6, -1/4 and +1/4th power of P_{O_2}. The -1/4th and 1/4th behavior are attributed to the presence of acceptor impurities.

If one had ideally pure material, then the conductivity should be of n-type for the entire P_{O_2} range with -1/6th dependence on P_{O_2} if the true composition is $SrTiO_{3-\delta}$ even at 1 atm oxygen pressure. The oxygen vacancies will be doubly ionized to give this P_{O_2} dependence. In ideally pure strontium titanate, one can obtain the value of δ by measuring the weight of the sample at various P_{O_2} values at several temperatures. The plot of the weight vs $P_{O_2}^{-1/6}$ should be a straight line (because the electrical conductivity varies as $P_{O_2}^{-1/6}$) and the intercept of each isotherm of the plot will give the weight (W_0) if it were stoichiometric. From the weight W_0 and w, the weight at 1 atm oxygen pressure, one can calculate the amount of oxygen vacancies and hence the value of δ.

REFERENCES

1. J. Frenkel, Z. Physik., 35, 652 (1926).
2. W. Schottky, Halbleiter probl., 4, 235 (1958).
3. W. Schottky, and C. Wagner, Z. Phys. Chem., B11, 163 (1931).
4. F. A. Kroger and H. J. Vink, Solid State Phys., 3, 307 (1956).
5. H. Schmalzried and C. Wagner, Z. Phys. Chem., B31, 198 (1962).
6. J. E. Schooley, W. R. Hosler and M. L. Cohen, Phys. Rev. Lett., 12, 474 (1964).
7. J. E. Schooley, W. R. Hosler and E. Ambler, Phys. Rev. Lett., 14, 305 (1965).
8. C. S. Koonce, M. L. Cohen, J. E. Schooley, W. R. Hosler, and E. R. Pfeiffer, Phys. Rev., 163, 380 (1967).
9. P. A. Fleury, J. F. Scott, and J. M. Worlock, Phys. Rev. Lett., 21, 16 (1968).
10. T. S. Chang, J. S. Holzrichter, G. F. Imbusch and A. L. Schawlow, Solid State Comm., 8, 1179 (1970).
11. F. Seitz, in "Imperfections in Nearly Perfect Crystals," Ed. by Schooley, p. 3, Wiley, New York, 1952.
12. G. Brouwer, Philips. Res. Rept., 9, 366 (1954).
13. W. Koch and C. Wagner, Z. Physik Chem., B38, 295 (1937).
14. J. Teltow, Ann. Physik, 5, 63 (1949).
15. E. J. W. Verway, P. W. Haayman and F. C. Romeyn, Chem. Weekblad, 44, 705 (1948).

16. E. J. W. Verway, P. W. Haayman, F. C. Romeyn, and G. W. van Oosterhout, Philips. Res. Rept., 5, 173 (1950).

17. F. A. Kroger and J. J. Vink, Physica, 20, 950 (1954).

18. D. M. Smyth, J. Solid State Chem., 16, 73 (1976).

19. D. M. Smyth, J. Solid State Chem., 20, 359 (1977).

20. N. G. Eror and D. M. Smyth, J. Solid State Chem., 24, 235 (1978).

21. S. A. Long, and R. N. Blumenthal, J. Amer. Ceram. Soc., 54, 515 (1971).

22. N. -H. Chan, and D. M. Smyth, J. Electrochem. Soc., 123, 1584 (1976).

23. U. Balachandran, and N. G. Eror, Extended Abstracts, American Ceramic Society Fall meeting, October, 1980.

24. T. Y. Tien and F. A. Hummel, Trans. Brit. Ceram. Soc., 66, 233 (1967).

25. J. Bouwma, K. J. Devries, and A. J. Burggraaf, Phys. Stat. Sol. (a), 35, 281 (1976).

26. B. C. Tofield, and W. R. Scott, J. Solid State Chem., 10, 183 (1974).

27. N. G. Eror, and D. M. Smyth, in "The Chemistry of Extended Defects in Non-Metallic Solids," p. 62-74, Ed. by L. Eyring and M. O'Keefe, North-Holland Pub. Co., Amsterdam (1970).

28. D. Hennings, Mat. Res. Bull., 6, 329 (1971).

29. D. Hennings and K. H. Hardtl, Phys. Stat. Sol. (a), 3, 465 (1970).

30. E. J. W. Verwey, Philips Res. Rept., 5, 173 (1950).

31. R. F. Brebrick, "Progress in Solid State Chemistry", vol. III, Pergamon Press, Oxford and New York (1966).

32. G. Mandel, Phys. Rev., 134, A1073 (1964).

33. G. Mandel, Phys. Rev., 136, A136 (1964).

34. F. A. Kroger, "Physical Chemistry, an Advanced Treatise," Vol. X, 229, Ed. by H. Eyring, Academic Press, New York (1970).

35. R. S. Roth and L. W. Coughanour, J. Res. NBS., 55, 209 (1955).

36. M. Itakura, N. Niizeki, H. Toyoda and H. Iwasaki, Jap. J. Appl. Phys., 6, 311 (1967).

37. H. P. R. Frederikse, W. R. Thurber, and W. R. Hosler, Phys. Rev., 134, A442 (1964).

38. A. H. Kahn and A. J. Leyendecker, Phys. Rev., 135, A1321 (1964).

39. H. W. Gandy, Phys. Rev., 113, 795 (1959).

40. A. E. Paladino, L. G. Rubin, and J. S. Waugh, J. Phys. Chem. Solids, 26, 391 (1965).

41. L. C. Walters and R. E. Grace, J. Phys. Chem. Solids., 28, 245 (1967).

42. A. E. Paladino, Bull. Am. Ceram. Soc., 48, 476 (1965).

43. L. C. Walters and R. E. Grace, J. Phys. Chem. Solids, 28, 239 (1967).

44. H. Yamada and G. R. Miller, J. Solid State Chem., 6, 169 (1973).

45. H. Veith, Z. Angew Phys., 20, 16 (1965).

46. F. Fosek, and H. Arend, Phys. Status. Solidi, 24, K69 (1967).

47. S. A. Long, and R. N. Blumenthal, J. Amer. Ceram. Soc., 54, 577 (1971).

48. A. M. J. H. Seuter, Philips. Res. Rept. Suppl., No. 3, (1974).

49. O. N. Tufte and P. W. Chapman, Phys. Rev., 155, 796 (1967).

50. H. P. R. Frederikse and W. R. Hosler, Phy. Rev., 161, 822 (1967).

51. J. Daniels, Philips. Res. Repts., 31, 505 (1976).

52. W. Cochran, Advan. Phys., 9, 387 (1960).

53. R. A. Cowley, Phys. Rev., 134, A981 (1964).

54. R. Loudon, Advan. Phys., 13, 423 (1964).

55. P. S. Narayanan and K. Vedam, Zeit. fur Physik., 163, 158 (1961).

56. A. L. Stekhanov and Z. A. Grabrichidze, Soviet Phys. Solid State, 5, 972 (1963).

57. C. H. Perry, J. H. Fertel and T. F. McNelly, J. Chem. Phys., 47, 1619 (1967).

58. W. G. Nelson and J. G. Skinner, J. Chem. Phys., 48, 2240 (1968).

59. P. A. Fleury and J. M. Worlock, Phys. Rev., 174, 613 (1968).

60. W. Taylor and A. F. Murray, Solid State Comm., 31, 937 (1979).

61. Y. Yamada and G. Shirane, J. Phy. Soc. Japan, 26, 396 (1969).

62. L. J. Last, Phys. Rev., 105, 1740 (1957).

63. A. S. Barker and M. Tinkham, Phys. Rev., 125, 1527 (1962).

64. W. G. Spitzer, R. C. Miller, D. A. Kleinman and L. E. Howard, Phys. Rev., 126, 1710 (1962).

65. A. S. Barker and J. J. Hopfield, Phys. Rev., 135, 1732 (1964).

66. A. S. Barker, Phys. Rev., 145, 391 (1966).

67. H. D. Megaw, Proc. Phys. Soc. London, 58, 133 (1946).

68. H. D. Megaw, in "Ferroelectricity", Methuen Co., London, (1957).

69. A. F. Wells, "Structural Inorganic Chemistry", p. 375-377, Clarendon Press, (1950).

70. I. K. Hulm, Proc. Phys. Soc. London, 63, 1184 (1950).

71. E. Weaver, J. Phys. Chem. Solids., 11, 274 (1959).

72. E. Poindexterand, and A. A. Giardini, Phys. Rev., 110, 1069 (1958).

73. J. B. Wachtman, and S. Marzullo, J. Res. Natl. Bur. Std., 67A, 193 (1963).

74. K. A. Muller, Phys. Rev. Lett., 2, 341 (1959).

75. W. I. Dobrov, R. F. Vieth, and M. E. Browne, Phys. Rev., 115, 79 (1959).

76. L. Rimai and G. A. deMars, Phys. Rev., 127, 702 (1962).

77. F. W. Lytle, J. Appl. Phys., 35, 2212 (1964).

78. S. N. Ruddlesden and P. Popper, Acta Cryst., 10, 538 (1957).

79. S. N. Ruddlesden and P. Popper, Acta Cryst., 11, 54 (1958).

80. G. J. MacCarthy, W. B. White and R. Roy, J. Amer. Ceram. Soc., 52, 463 (1969).

81. W. B. White and V. G. Keramidas, Nat. Bur. Stands., NO. 364, Proceedings of the 5th Materials Research Symp., 113 (1972).

82. P. Tarte, Nature, 191, 1002 (1961).

83. M. Pechini, U. S. Patent 3,330,697, July 11, (1967).

84. Marcilly, P. Courty and B. Delmon, J. Amer. Ceram. Soc., 53, 56 (1970).

85. H. Schmalzried, Prog. Solid State Chem., 2, 265 (1965).

86. M. Pechini, U. S. Patent 3,231,328, Jan. 25, (1966).

87. J. S. Smith, T. R. Dolloff, and K. S. Mazdiyasni, J. Amer. Ceram. Soc., 53, 91 (1970).

88. JANAF, Joint Army, Navy, and Air Force Thermochemical Tables, Ed. by D. R. Stull, Dow Chemical Co., Midland, Michigan (1965).

89. B. M. French, Rev. Geophys., 4, 223 (1966).

90. J. B. Nelson and D. P. Railey, Proc. Phys. Soc. London., 57, 160 (1945).

91. J. B. MacChesney and A. Sauer, J. Amer. Ceram. Soc., 45, 416 (1962).

92. N. G. Eror, J. Solid State Chem., 37, March (1981).

93. DeVeries, K. Keizer, J. Bouma and A. J. Burggraaf, Sci. Ceramics, 8, 187 (1975).

94. H. Reiss, C. S. Fuller and A. J. Pietruszkiewicz, J. Chem. Phys., 25, 650 (1956).

95. U. Balachandran, and N. G. Eror, Presented at the 82nd Annual Meeting of the Amer. Ceram. Soc., April (1980).

96. E. C. Subbarao and G. Shirane, J. Amer. Ceram. Soc., 42, 279 (1959).

97. J. B. MacChesney, P. K. Gallagher and F. V. D. Marcello, J. Amer. Ceram. Soc., 46, 197 (1963).

98. G. H. Jonker, Solid State Elec., 7, 895 (1964).

99. O. Saburi, J. Phys. Soc. Japan, 14, 1159 (1959).

100. M. Abe and K. Uchino, Mat. Res. Bull., 9, 147 (1974).

101. M. Kestingian and R. Ward, J. Amer. Ceram. Soc., 77, 6199 (1955).

102. D. Hennings and G. Rosenstein, Mat. Res. Bull., 7, 1505 (1972).

103. W. Kwestroo and H. A. M. Paping, J. Amer. Ceram.Soc., 42, 292 (1959).

104. T. Murakami, T. Miyashita, M. Nakahara, and E. Sekine, J. Amer. Ceram. Soc., 56, 294 (1973).

105. T. Takeda, and A. Watanabe, Jap. J. Appl. Phys., 7, 232 (1968).

106. W. L. George and R. E. Grace, J. Phys. Chem. Solids., 30, 881 (1969).

107. J. Daniels and K. H. Hardtl, Philips. Res. Repts., 31, 489 (1976).

108. J. H. Becker and H. P. R. Frederikse, J. Appl. Phys., 33, 447 (1962).

109. T. A. Noland, Phys. Rev., 94, 724 (1954).

110. M. Cardona, Phys. Rev., 140, A651 (1965).

111. M. I. Cohen and R. F. Blunt, Phys. Rev., 168, 929 (1968).

112. U. Balachandran, and N. G. Eror, J. Amer. Ceram. Soc., April, 1981.

113. F. A. Kroger, "Chemistry of Imperfect Crystals", Chap. 9, 12, 15, 16, North-Holland Publishing Co., Amsterdam (1964).

114. A. D. Franklin, in "Point Defects in Solids", vol. I., Chap. I, (Ed. by J. H. Crawford and L. M. Slifkin) Plenum Press, New York (1972).

115. F. G. Fuller, in "Point Defects in Solids", Vol. II, Chap. 2 (Ed. by J. H. Crawford and L. M. Slifkin) Plenum Press (1972).

116. W. J. Minford and V. S. Stubican, J. Amer. Ceram. Soc., 57, 363 (1974).

117. R. A. Ferkins and R. A. Rapp, Met. Trans., 4, 193 (1973).

118. P. Kofstad, "Non Stoichiometry, Diffusion, and Electrical Conductivity in Binary Metal Oxides", Chaps. 11-12, Wiley Interscience, New York (1972).

119. S. Bhagavantam, and T. Venkatarayudu, Pro. Indian Acad. Sci., 9A, 224 (1939).

120. W. G. Fately, F. R. Dollish, N. T. McDevitt and F. F. Bentley in "Infrared and Raman Selection Rules for Molecular and Lattice Vibrations", Wiley-Interscience, New York, (1972).

121. L. Rimai, J. L. Parsons, and A. L. Cederquist, Bull. Amer. Phys. Soc., 12 60 (1967).

122. L. Rimai and J. L. Parsons, Solid State Comm., 5, 387 (1967).

123. D. C. O'Shea, R. V. Kolluri, and H. Z. Cummins, Solid State Comm., 5, 241 (1967).

124. R. Loudon, Advan. Phys., 14, 423 (1960).

125. R. Loudon, Phys. Rev., 137, A1784 (1965).

126. K. A. Muller, E. Bruns, B. Derighetti, J. E. Drumheller, and F. Waldner, Phys. Letters., 9, 223 (1964).

127. H. Unoki and T. Sakudo, J. Phys. Soc. Japan, 23, 546 (1967).

128. D. J. Lockwood, and B. H. Torrie, J. Physics, C., 7, 2729 (1974).

129. C. Ridou, M. Rousseau, Y. J. Gesland, J. Nouet and A. Zarembowitch, Ferroelectrics, 12, 199 (1976).

130. W. G. Sirling, J. Phys. C., 5, 2711 (1972).

131. G. Shirane and Y. Yamada, Phys. Rev., 177, 858 (1969).

132. S. D. Ross, Spectrochimica Acta., 32A, 1331 (1976).

133. U. Balachandran and N. G. Eror, in Extended Abstracts, 158th Meeting of the Electrochemical Society, Hollywood (1980).

134. A. Magneli, Arkiv. Kemi., 1, 513 (1950).

135. A. D. Wadsley, Acta Cryst., 14, 660 (1961).

136. J. S. Anderson, Advances in Chemistry, Vol. 39, American Chem. Soc., Washington, D.C. (1963).

137. R. J. D. Tilley, J. Solid State Chem., 21, 293 (1977).

138. P. F. Chester, J. Appl. Phys., 32, 2233 (1961).

139. International Tables for X-ray Crystallography, Vol. I, Ed. by N. F. M. Henry and K. Lonsdale, Birmingham, England, (1965).

140. R. W. C. Wyckoff, Crystal Structures, Vol. I & II, Wiley-Interscience, New York, (1964).

APPENDIX I(a).

Factor-Group Analyses for the Cubic $SrTiO_3$ by the Correlation Method

First, we shall outline some practical rules for the use of the simple correlation method to derive the vibrational selection rules for crystals. We have chosen not to review the theory of the correlation procedure but to proceed directly to a demonstration of its use, and that of the correlation tables, to obtain the vibrational selection rules.

a. Crystal Structure: The crystal structure of the sample must be known. Alternatively a structure can be assumed and predictions made for the vibrations, which can then be compared with observations to prove or disprove the assumed structure. It is far better, however, to know the structure in advance.

Crystallographic information may be obtained from references 139 and 140.

b. Molecules per Bravais Space Cell: The Bravais cell is used by molecular spectroscopists to obtain the irreducible representation for the lattice vibrations. The crystallographic unit cell may be identical with the Bravais cell or it may be larger by some simple multiple. This can be ascertained from the capital letter in the x-ray symbol for the crystal structure. For all crystal structures designated by a symbol containing P (for primitive) the crystallographic unit cell and the Bravais unit cell

are identical (an example is Pm3m for $SrTiO_3$). Crystal structure designated by other capital letters (B, C, I, etc.) have crystallographic unit cells that contain two, three, or four Bravais cells. The irreducible representations obtained from these crystallographic unit cells will contain two, three, or four times as many vibrations as are needed to represent the lattice vibrations of the crystal. This problem of including too many Bravais cells in the crystallographic cell can be eliminated by dividing the number of molecules per unit crystallographic cell by a small integer which is identical to the number of lattice points (LP) in a crystallographic cell of specific symmetry, as designated by the capital letter in its symbol.

In summary,

$$\left.\begin{matrix}\text{number of molecules} \\ \text{in the Bravais cell}\end{matrix}\right\} = \frac{Z}{(LP)} = \frac{\text{Number of molecules in crystallographic unit cell}}{\text{Number of lattice points}} = Z^B$$

c. Site symmetry of each atom in the Bravais cell: The equilibrium position of each atom lies on a site that has its own symmetry. This site symmetry, a subgroup of the full symmetry of the Bravais unit cell must be ascertained correctly for each atom. It is easy to do so in some cases, difficult in others.

From the number of molecules, and hence the number of atoms in a Bravais cell, one can find out the number of equilivalent atoms of each kind of atom that constitutes the molecule under consideration. Next we turn to the table in the International Tables giving all possible site symmetries for the space group of the molecule under investigation. As

an example, for the space group O_h^4 (e.g., Cu_2O) the site symmetries are written as $T_d(2)$, $2D_{3d}(4)$, $D_{2d}(6)$, ... They represent all the possible kinds of site for an O_h^4 crystal, but most of them will not be occupied in a specific crystal.

The most useful information is the number contained in parentheses, for it represents the number of equivalent atoms which have that particular site symmetry; for example, $T_d(2)$ indicates that there are two equivalent atoms occupying sites of symmetry T_d; similarly, $D_{3d}(4)$ indicates the presence of four equivalent atoms on D_{3d} sites.

Some of the site symmetries have numerical coefficients, such as $2D_{3d}(4)$. The coefficient 2 indicates the presence of two different and distinct kinds of D_{3d} sites in the unit cell. Each can accommodate four equivalent atoms. In a given crystal there may be atoms on one or both sites or on neither. Now we have to find out the site symmetries of each kind of atoms in the crystal. This is done by matching the number of equivalent atoms of one kind and a site symmetry that can accommodate that many equivalent atoms. When selecting the site symmetry, we must always have the number of equivalent atoms equal to the accommodational value of the site symmetry.

d. Correlation of the site group to the Factor group: Once the site symmetry for each atom in the lattice is found, then the symmetry species are identified for each equivalent set of atom displacements in the site. The displacements we describe will become the lattice vibrations in the crystal. These site species for the displacements are re-

lated to the species of the factor group using the correlation tables. This correlation explicitly identifies the species of the lattice vibration in the crystal and further allows the predictions of infrared or Raman activity.

Now we identify the lattice modes in $SrTiO_3$ by obtaining the irreducible representation that contains the number and species of the lattice vibrations.

$SrTiO_3$ is cubic at room temperature and has the space group Pm3m (O_h^1). There is only one molecular formula unit in a Bravais cell ($Z^B=1$). There are, therefore, one equivalent strontium atom, one equivalent titanium atom and three equivalent oxygen atoms in the Bravais cell. The space group Pm3m (O_h^1) contains the following site symmetries: $2O_h(1)$; $2C_{4v}(6)$; $2D_{4h}(3)$; $C_{3v}(8)$; $3C_{2v}(12)$; $3C_s(24)$; $C_1(48)$. From this we see that the strontium and titanium atom should be in O_h sites and the three oxygen atoms are in the D_{4h} sites. Each set of equivalent atoms is treated separately.

Strontium atom

The vibrational displacements of the strontium atoms in the lattice can be described as simple motions parallel to the x, y, or z-axis. The displacement of strontium atoms in x-direction will have the same character of the x-displacement vector in the point group O_h (i.e., translational vector in the x-direction in O_h). A complete character table for the point group O_h is given in Table XLI. From this table we see that the

Table XLI.

A COMPLETE CHARACTER TABLE FOR THE POINT GROUP O_h.

O_h	E	$8C_3$	$3C_2$	$6C_4$	$6C_2'$	i	$8S_6$	$3\sigma_h$	$6S_4$	$6\sigma_d$		
A_{1g}	1	1	1	1	1	1	1	1	1	1		$\alpha_{xx} + \alpha_{yy} + \alpha_{zz}$
A_{2g}	1	1	1	−1	−1	1	1	1	−1	−1		
E_g	2	−1	2	0	0	2	−1	2	0	0		$(\alpha_{xx} + \alpha_{yy} - 2\alpha_{zz}, \alpha_{xx} - \alpha_{yy})$
T_{1g}	3	0	−1	1	−1	3	0	−1	1	−1	(R_x, R_y, R_z)	
T_{2g}	3	0	−1	−1	1	3	0	−1	−1	1		$\alpha_{xy}, \alpha_{xz}, \alpha_{yz}$
A_{1u}	1	1	1	1	1	−1	−1	−1	−1	−1		
A_{2u}	1	1	1	−1	−1	−1	−1	−1	1	1		
E_u	2	−1	2	0	0	−2	1	−2	0	0		
T_{1u}	3	0	−1	1	−1	−3	0	1	−1	1	(T_x, T_y, T_z)	
T_{2u}	3	0	−1	−1	1	−3	0	1	1	−1		

translation T_x belongs to the species T_{1u} of the site group. Similarly, the displacements of strontium atoms along the y- and z-axis will have the same character as T_y and T_z and will belong to species T_{1u}. It is important to note that this approach, which classifies the lattice vibrations as excursions in x, y, and z directions, is no different from the descriptions used for the molecular vibrations such as bond stretching, bending, and twisting.

When the species of the site group is identified for each excursion of an equivalent set of atoms, this information is integrated via the correlation tables to the species of the crystal that contain this lattice vibration. To begin this correlation procedure, Table XLII lists the O_h site species of the translations T_x, T_y, and T_z. Since the lattice vibrations have the same character as the translations, the species that contain these vibrations can readily be identified and this information is presented in Table XLII. Before applying the correlations of site to factor group we define some useful terms:

t^γ = Number of translations in a site species γ. This number can take the value of zero, one, two, or three, depending on whether none, one, two, or three translations are contained in the site species γ, respectively.

f^γ = Degree of vibrational freedom present in each site species γ for an equivalent set of atoms, ions, or molecules.

$t^\gamma n = f^\gamma \cdot n \downarrow$ number of atoms in an equivalent set.

Table XLII.

SPECIES OF THE SITE GROUP O_h AND THE TRANSLATIONS

O_h Site of Sr Atom Species	Translation Species	Sr Atoms Excursion
A_{1g}		
A_{2g}		
E_g		
T_{1g}		
T_{2g}		
A_{1u}		
A_{2u}		
E_u		
T_{1u}	$T_{x,y,z}$	Motions Parallel to x, y, & z axes
T_{2u}		

a_γ = Degree of freedom contributed by each site species γ to a factor group species ζ.

$f^\gamma = a_\gamma \Sigma_\zeta^\gamma c_\zeta$

c_ζ = The degeneracy of the species ζ of the factor group

a_ζ = Number of lattice vibrations of the equivalent set of atoms in species ζ of factor group $[= \Sigma_\gamma a_\gamma]$

The above definitions are utilized in listing the degrees of vibrational freedom for each species of the site group O_h for equivalent set of strontium atom (see Table XLIII). Table XLIII indicates the presence of strontium lattice vibrations designated as degrees of freedom in species T_{1u}. The next step is to correlate the T_{1u} species of the site group O_h to the O_h factor group species. In this particular case, it is simple because the site group and the factor group are the same. Table XLIV shows this correlation and identifies the species of the lattice vibration in the crystal.

The strontium atoms' irreducible representation for the factor group is obtained using the following equation:

$$\Gamma = \Sigma_\zeta a_\zeta \cdot \zeta$$

Therefore, the species of the factor group that contains lattice vibration involving the strontium atom can be written as the following irreducible representation Γ_{Sr}.

$$\Gamma_{Sr} = 1 \cdot T_1u = T_1u$$

Table XLIII.

Sr ATOMS ON SITE O_h--THE DEGREES OF VIBRATIONAL FREEDOM FOR EACH SPECIES (n = 1 ATOM/EQUIVALENT SET)

O_h Species	Translation	t^γ	Degree of Vibrational Freedom $f^\gamma = n \cdot t^\gamma$
A_{1g}		0	0
A_{2g}		0	0
E_g		0	0
T_{1g}		0	0
T_{2g}		0	0
A_{1u}		0	0
A_{2u}		0	0
E_u		0	0
T_{1u}	$T_{(x,y,z)}$	3	3
T_{2u}		0	0

Table XLIV.

THE CORRELATION FOR THE LATTICE VIBRATIONS OF THE STRONTIUM ATOMS IN $SrTiO_3$ CRYSTAL BETWEEN THE SITE GROUP O_h AND FACTOR GROUP O_h

f^γ	t^γ	O_h Site Species γ	Correlation	O_h Factor Group Species ζ	C_ζ	$a_\zeta=\Sigma_\gamma a_\gamma$
3	3	T_{1u}	⟶	T_{1u}	3	1

Titanium atom

By following the same procedure we can obtain the irreducible representation Γ_{Ti} for the equivalent set of titanium atoms. A summary of the necessary information is given in Table XLV.

$$\Gamma_{Ti} = \Sigma_{\zeta} a_{\zeta} \cdot \zeta$$

$$\Gamma_{Ti} = 1 \cdot T_{1u} = T_{1u}$$

Correlation Table for the Point Group D_{4h} to O_h

The three equivalent oxygen atoms occupy the D_{4h} sites in $SrTiO_3$. In order to determine the lattice vibrations of the oxygen atoms we need to have a correlation table between the point groups D_{4h} and O_h. We are outlining a method to obtain the correlation table in a simple situation like C_{3v} to D_{3h} point group. First, we write the point group C_{3v}:

	Operations		
C_{3v}	E	$2C_3(z)$	$3\sigma_v$
A_1	1	1	1
A_2	1	1	−1
E	2	−1	0

We note that C_{3v} is a subgroup of D_{3h}. This property is easily recognized, for we see that D_{3h} contains the same symmetry operations as C_{3v}, i.e., E, $2C_3(z)$, $3\sigma_v$ plus additional operations σ_h, $2S_3$, and $3C_2$. To obtain the

Table XLV.

TABULATIONS OF THE TERMS AND CORRELATIONS NECESSARY TO CALCULATE THE LATTICE VIBRATIONS OF THE TITANIUM ATOM IN $SrTiO_3$.

f^γ	r^γ	O_h Site Symmetry Species Containing Translation	Correlation	O_h Factor Group Species	c_ζ	a_ζ
3	3	T_{1u}	⟶	T_{1u}	3	1

species of C_{3v} that correlate with the species of D_{3h} we need only to compare the character of the operations common to both point groups D_{3h} and C_{3v}, which in this case are E, $2C_3(z)$, and $3\sigma_v$. To do this we simply write the partial character table of D_{3h}, including only the operations common to both C_{3v} and D_{3h}:

Species of the D_{3h} point group	Operation E	$2C_3(z)$	$3\sigma_v$	Species of the C_{3v} point group
A_1'	1	1	1	A_1
A_1''	1	1	−1	A_2
A_2'	1	1	−1	
A_2''	1	1	1	A_1
E'	2	−1	0	E
E''	2	−1	0	

	Character of the operation E	$2C_3(z)$	$3\sigma_v$
Point group D_{3h}: species A_1'	1	1	1
Point group C_{3v}: species A_1	1	1	1

Therefore the correlation is ${}^{C_{3v}}A_1$ to ${}^{D_{3h}}A_1'$.

	Character of the operation E	$2C_3(z)$	$3\sigma_v$
Point group D_{3h}: species A_1''	1	1	−1
Point group C_{3v}: species A_2	1	1	−1

The correlation is ${}^{C_{3v}}A_2$ to ${}^{D_{3h}}A''$.

The other correlations found are summarized below:

D_{3h}	C_{3v}	D_{3h}	C_{3v}
A_1'	A_1	A_2''	A_2
A_1''	A_2	E'	E
A_2'	A_2	E''	E

By following the similar procedure, correlation is obtained between the point groups D_{4h} and O_h. This correlation is given in Table XLVI.

Oxygen Atoms

Table XLVII gives the necessary information to obtain the lattice vibrations of the oxygen atoms in $SrTiO_3$.

The total representation of the crystal, Γ^{SrTiO_3}, is the sum of the individual irreducible representation for each set of equivalent atoms, or

$$\Gamma^{SrTiO_3} = \Gamma_{Sr} + \Gamma_{Ti} + \Gamma_O$$
$$= T_{1u} + T_{1u} + 2T_{1u} + T_{2u}$$
$$= 4T_{1u} + T_{2u}$$

The acoustical vibrations are included in the irreducible representation given above. Of the 3N degrees of vibrational freedom, three of these vibrations are acoustical modes. When we consider only those vibrations

Table XLVI.

CORRELATION TABLE BETWEEN POINT GROUPS D_{4h} AND O_h

O_h	D_{4h}
A_{1g}	A_{1g}
A_{2g}	B_{1g}
E_g	$A_{1g} + B_{1g}$
T_{1g}	$A_{2g} + E_g$
T_{2g}	$B_{2g} + E_g$
A_{1u}	A_{1u}
A_{2u}	B_{1u}
E_u	$A_{1u} + B_{1u}$
T_{1u}	$A_{2u} + E_u$
T_{2u}	$B_{2u} + E_u$

Table XLVII.

n = 3 atoms/equivalent set

TABULATIONS OF TERMS AND CORRELATIONS NECESSARY TO CALCULATE THE LATTICE VIBRATIONS OF THE OXYGEN ATOMS IN $SrTiO_3$ CRYSTAL

f^γ	t^γ	D_{4h} SITE SYMMETRY SPECIES CONTAINING TRANSLATION	CORRELATION	O_h FACTOR GROUP SPECIES	c_ζ	$a_\zeta = \Sigma_\gamma a_\gamma = a_{A_{2u}} + a_{E_u}$
3	$1(T_z)$	A_{2u}		A_{1g}	1	0 = 0 + 0
6	$2(T_{x,y})$	E_u		A_{2g}	1	0 = 0 + 0
				E_g	2	0 = 0 + 0
				T_{1g}	3	0 = 0 + 0
				T_{2g}	3	0 = 0 + 0
				A_{1u}	1	0 = 0 + 0
				A_{2u}	1	0 = 0 + 0
				E_u	2	0 = 0 + 0
				T_{1u}	3	2 = 1 + 1
				T_{2u}	3	1 = 0 + 1

$$\therefore \Gamma_{oxy} = \Sigma_\zeta a_\zeta \cdot \zeta$$
$$= 2 \cdot T_{1u} + 1 \cdot T_{2u} = 2\,T_{1u} + T_{2u}$$

at the center of the Brillouin zone, i.e., $K \rightarrow 0$, the three acoustical vibrations have near zero frequency. Since vibrations with near zero frequency are of no physical interest in the vibrational spectrum of a solid, these acoustical vibrations can be subtracted from the irreducible representation.

$$\Gamma_{vib}^{SrTiO_3} = \Gamma^{SrTiO_3} - \Gamma^{acoustical}$$

The acoustical modes are readily identifiable in factor groups, since they have the same character as the translation. The irreducible representation of the acoustical vibrations

$$\Gamma^{acoustical} = T_{1u}$$

$$\therefore \quad \Gamma_{vib}^{SrTiO_3} = 3T_{1u} + T_{2u}$$

The activity of each mode is determined from the character table for the group O_h. The modes having Raman polarizability tensor are active in Raman scattering. In order to be active in infrared absorption a mode should have a translation vector in its irreducible representation. One vibration, T_{2u}, will be inactive in both the infrared and Raman spectrum. The T_{1u} modes are active only in the infrared and forbidden in Raman. Hence, none of the first order modes are allowed in the cubic $SrTiO_3$.

APPENDIX I(b).

Since $SrTiO_3$ has already been treated by the correlation method, it would be worthwhile to repeat this calculation, using the method proposed by Bhagavantam and Venkatarayudu,[119] to determine (a) whether both methods give the same result, and (b) to demonstrate the simplicity of the correlation method. Only a simple outline of the Bhagavantam and Venkatarayudu method is given in this Appendix. For more detailed description of this method the reader is referred to the reference 119.

I. The irreducible representation for $SrTiO_3$ is obtained as follows:

By definition ω_R = the number of atoms left invariant under operation R

χ_R = the character of the operation R, obtained in the following manner

$$\chi_R = \omega_R(\pm 1 + 2\cos\theta)$$

The angle θ is defined as follows:

(a) where E is a proper rotation, $\theta = 0°$;

(b) $(+)$ used for proper rotations, C_n, $\theta = \frac{360}{P}$;

(c) $(-)$ used for improper rotations, S_n, $\theta = \frac{360}{P}$;

(d) σ_h is an improper rotation with $\theta = 0°$;

(e) i is an improper rotation with $\theta = 180°$.

Next, each operation is considered in obtaining ω_r and χ_p. First the crystal structure with atoms in the position of the unit cell shown in Figure 84 must be considered. This same unit cell is used throughout this Appendix.

In the unit cell of this crystal structure (see Figure 84)

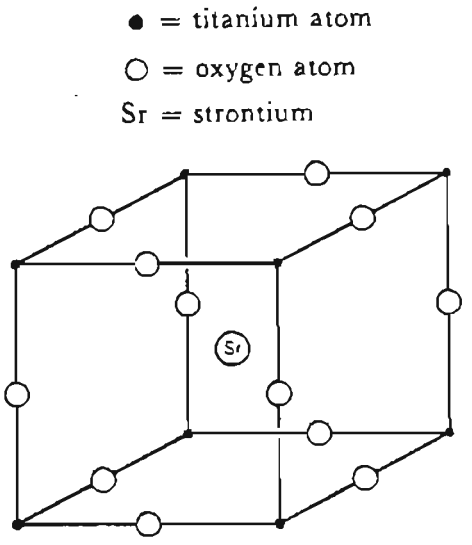

Figure 84. THE CRYSTALLOGRAPHIC UNIT CELL OF $SrTiO_3$.

Note: (a) Each Ti is shared by 8 Sr; (b) there are 12 oxygen around 1 Sr. To check:

Atom

Ti-8 per cell, each contributing $\frac{1}{8}$ to the unit cell:

$$\therefore \qquad 8 \times \tfrac{1}{8} = 1\ \text{Ti}$$

oxy-12 atoms, each oxy contributed $\frac{1}{4}$ to unit cell;

$$\therefore \qquad 12 \times \tfrac{1}{4} = 3\ \text{O}$$

Sr-1 atom in middle of cell

$\therefore$ 1 Sr atom per unit cell = 1 Sr

Total $\omega_R = SrTiO_3$ for $Z = 1$.

A. E Operation: Character and number of atoms invariant under E operations can be found as follows:
All the atoms remained unchanged: $\therefore \omega_R = 5$ (i.e., 1 Sr + 1 Ti + 3 oxy), $\chi_p = 5(+1 + 2\cos 0°) = 5 \cdot 3 = 15$.

B. C_3 Operation: The illustration that follows shows some of the C_3 elements of symmetry in the unit cell. The list that accompanies it is a tabulation of the number of atoms left invariant under all the C_3 operations and the irreducible representation χ_p.

Comment

There are 7 C_3's passing through this unit (Figure 85): all are parallel to one another (note that this is <u>not</u> the 8 C_3 operation that appear in the character table, but only one of these eight operations).

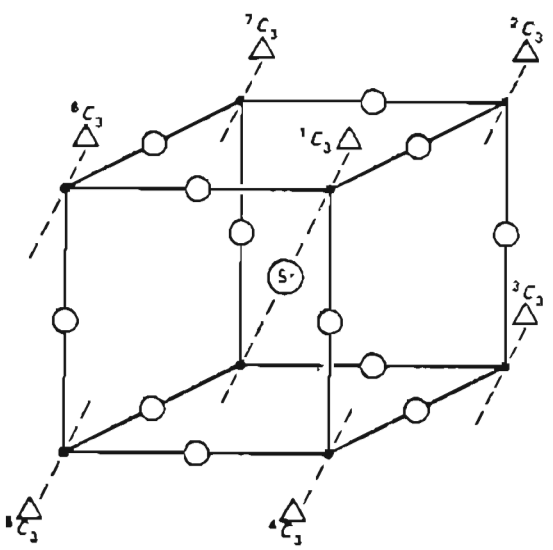

Figure 85. A C_3 OPERATION IN $SrTiO_3$.

Operation	Number of atoms invariant, ω_R
$^1C_2$	1 Sr + 2 · ½ Ti
$^2C_3$	⅓ Ti
$^3C_3$	⅓ Ti
$^4C_3$	⅓ Ti
$^5C_3$	⅓ Ti
$^6C_3$	⅓ Ti
$^7C_3$	⅓ Ti
Total atoms	1 Sr + 1 Ti

$$\therefore \quad \sum \omega_R = 2$$

However, for all C_3 operations $1 + 2\cos\theta$ (where $\theta = 120) = 0$, where $\theta = 120°$.

$$\therefore \quad \omega_R(1 + 2\cos\theta) = 0$$

C. Since this example illustrates the procedure followed on each symmetry operation, only the essentials are presented in the discussion for obtaining the ω_R and χ_P for each operation. (see Figure 86).

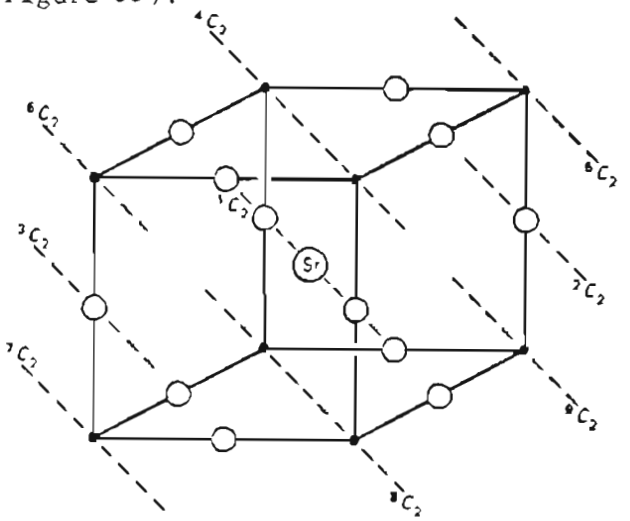

Figure 86. THE C_2 OPERATION IN $SrTiO_3$.

Operation	Number of atoms invariant, ω_R
$^1C_2$	1 Sr + 2 · ½ oxy
$^2C_2$	½ oxy
$^3C_2$	½ oxy
$^4C_2$	2 · ⅛ Ti
$^5C_2$	⅛ Ti
$^6C_2$	⅛ Ti
$^7C_2$	⅛ Ti
$^8C_2$	2 · ⅛ Ti
$^9C_2$	⅛ Ti

Total atoms = 1 Sr + 1 oxy + 1 Ti

$\therefore \quad \sum \omega_R = 3$

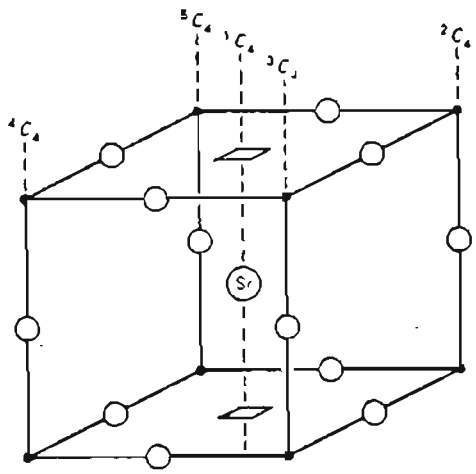

Figure 87. THE C_4 OPERATION IN $SrTiO_3$.

D.

Operation	ω_R
$^1C_4$	1 Sr
$^2C_4$	2 · ⅛ Ti + ½ oxy
$^3C_4$	2 · ⅛ Ti + ½ oxy
$^4C_4$	2 · ⅛ Ti + ½ oxy
$^5C_4$	2 · ⅛ Ti + ½ oxy

(see Figure 87)

$\therefore \quad \sum \omega_R = 1\,\text{Sr} + 1\,\text{Ti} + 1\,\text{O} = 3$

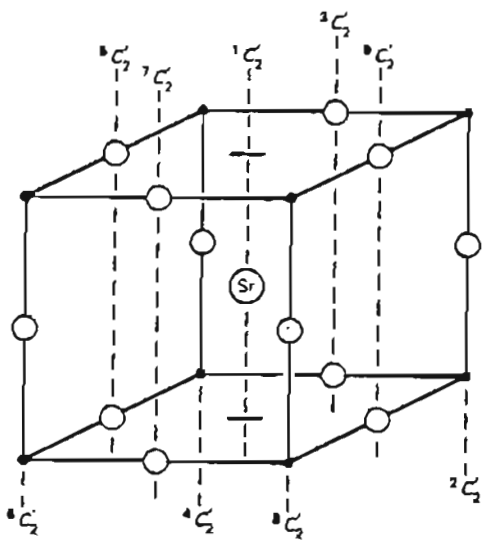

Figure 88. THE C_2' OPERATION IN $SrTiO_3$.

E.

Operation	ω_R
$^1C_2'$	1 Sr
$^2C_2'$	$2 \cdot \frac{1}{8}$ Ti + $\frac{1}{4}$ oxy
$^3C_2'$	$2 \cdot \frac{1}{4}$ oxy
$^4C_2'$	$2 \cdot \frac{1}{8}$ Ti + $\frac{1}{4}$ oxy
$^5C_2'$	$2 \cdot \frac{1}{4}$ oxy
$^6C_2'$	$2 \cdot \frac{1}{8}$ Ti + $\frac{1}{4}$ oxy
$^7C_2'$	$2 \cdot \frac{1}{4}$ oxy
$^8C_2'$	$2 \cdot \frac{1}{8}$ Ti + $\frac{1}{4}$ oxy
$^9C_2'$	$2 \cdot \frac{1}{4}$ oxy

(see Figure 88)

$\therefore \quad \sum \omega_R = \text{Sr} + \text{Ti} + 3\,\text{oxy} = 5$

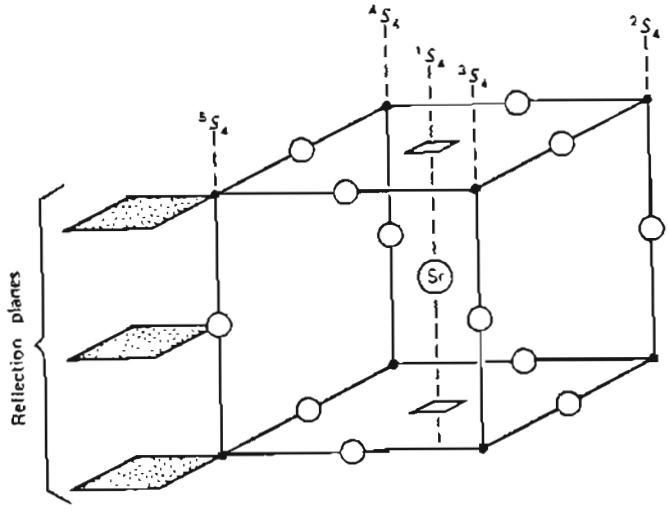

Figure 89. THE S_4 OPERATION (IMPROPER) IN $SrTiO_3$.

F. *i*-operation

There is a center of symmetry at every atom in the unit; therefore all the atoms remain invariant under *one* of the many *i*-inversion operations, i.e., 1 Sr + 1 Ti + 3 oxy, for $\sum \omega_R = 5$.

G. Comment

The S_4 operation yields the same result as the C_4 operation, even though there is the additional reflection. If we note that there are three reflection planes in the unit cell and all the atoms lie on one of these reflection planes and the S_4 axis, we find $\omega_R = 3$ (see Figure 89).

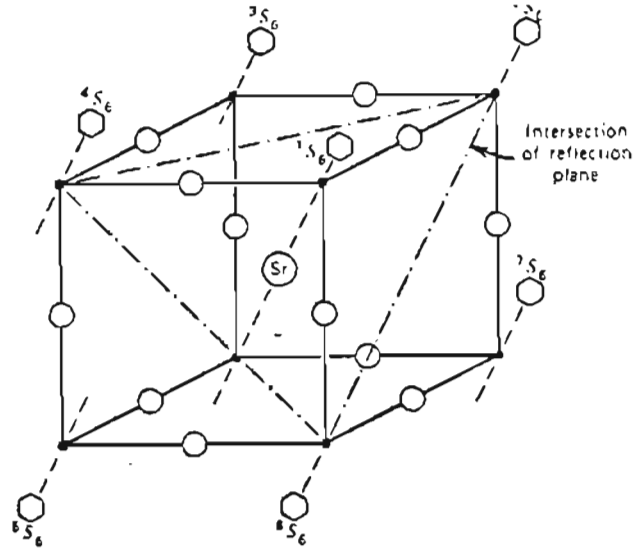

Figure 90. THE S_6 OPERATION.

H.

Operation	ω_R
$^1S_6$	1 Sr + 2 · $\frac{1}{8}$ Ti
$^2S_6$	$\frac{1}{8}$ Ti
$^3S_6$	$\frac{1}{8}$ Ti
$^4S_6$	$\frac{1}{8}$ Ti
$^5S_6$	$\frac{1}{8}$ Ti
$^6S_6$	$\frac{1}{8}$ Ti
$^7S_6$	$\frac{1}{8}$ Ti

(see Figure 90)

$$\therefore \quad \sum \omega_R = 2$$

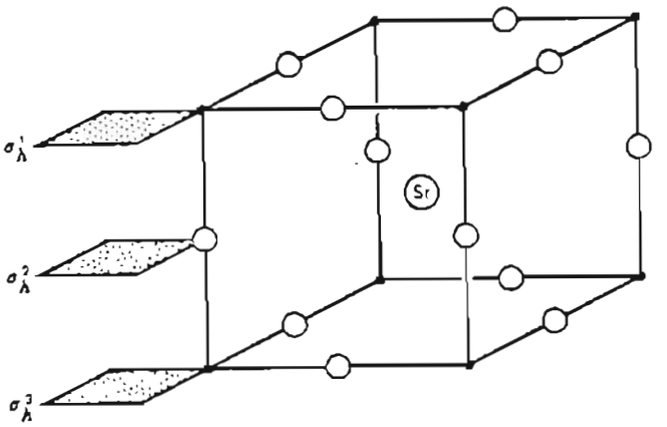

Figure 91. THE σ_h OPERATION.

I. All atoms are invariant under σ_h: (see Figure 91)

$$\therefore \quad \sum \omega_R = 5$$

J.

Operation	ω_R (see Figure 92)
$^1\sigma_d$	$2 \cdot \frac{1}{8}$ Ti + $\frac{1}{4}$ oxy
$^2\sigma_d$	$4 \cdot \frac{1}{8}$ Ti + $2 \cdot \frac{1}{4}$ oxy + Sr
$^3\sigma_d$	$2 \cdot \frac{1}{8}$ Ti + $\frac{1}{4}$ oxy

$$\therefore \quad \sum \omega_R = 3$$

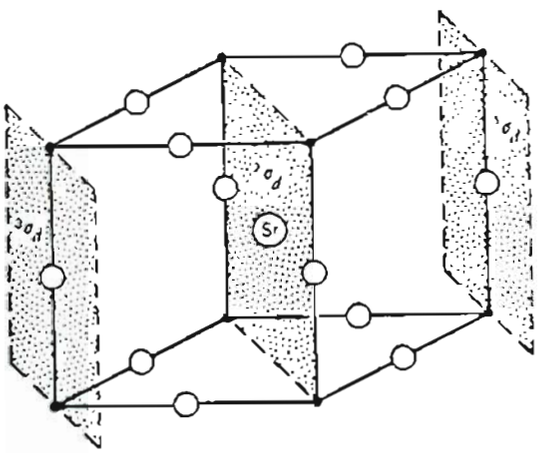

Figure 92. THE σ_d OPERATION IN $SrTiO_3$.

The results can be summarized in tabular form:

Class (O_h factor group)	ω_R	χ_{P_i}
E	5	15
$8\,C_3$	2	0
$6\,C_2$	3	−3
$6\,C_4$	3	3
$3\,C_2'$	5	−5
i	5	−15
$6\,S_4$	3	−3
$8\,S_6$	2	0
$3\,\sigma_h$	5	5
$6\,\sigma_d$	3	3

II. Calculation of the number of modes in each of the species.

$n^{(\gamma)}$ = number of modes in each species, γ

g = order of the group, $g = \sum_i g_i$

g_i = number of elements in each class

$\chi_i^{(\gamma)}$ = the character for the class i and irreducible representation Γ_γ

χ_{P_i} = character of the irreducible representation, derived and tabulated above

$$n^{(\gamma)} = \frac{1}{g}\sum_i g_i \chi_i^{(\gamma)} \chi_{P_i}$$

Example of its use:

1. A_{1g} Species

O_h	E	$8C_3$	$6C_2$	$6C_4$	$3C_2'$	i	$6S_4$	$8S_6$	$3\sigma_h$	$6\sigma_d$
$\chi_i^{A_{1g}}$ =	1	1	1	1	1	1	1	1	1	1
χ_{P_i} =	15	0	−3	3	−5	−15	−3	0	5	3
g_i =	1	8	6	6	3	1	6	8	3	6

$$\frac{\sum \chi_i^{A_{1g}} \chi_{P_i} \cdot g_i}{g = 48} = 15 + 0 - 18 + 18 - 15 - 15 - 18 + 0 + 15 + 18 = 0$$

Therefore there are no lattice vibrations in A_{1g} species.

2. T_{1u} species

	E	$8C_3$	$6C_2$	$6C_4$	$3C_2'$	i	$6S_4$	$8S_6$	$3\sigma_h$	$6\sigma_d$
$\chi_1^{T_{1u}}$	= 3	0	−1	1	−1	−3	−1	1	1	1
χ_p	= 15	0	−3	3	−5	−15	−3	0	5	3
g_i	= 1	8	6	6	3	1	6	8	3	6

$$\frac{\sum_i \chi_i \chi_{p_i} \cdot g_i}{g = 48} = 45 + 0 + 18 + 18 + 15 + 45 + 18 + 0 + 15 + 18 = 4$$

Therefore there are $4T_{1u}$ irreducible representations.

3. T_{2u} species

	E	$8C_3$	$6C_2$	$6C_4$	$3C_2'$	i	$6S_4$	$8S_6$	$3\sigma_h$	$6\sigma_d$
$\chi_1^{T_{2u}}$	= 3	0	1	−1	−1	−3	1	0	1	−1
χ_p	= 15	0	−3	3	−5	−15	−3	0	5	3
g_i	= 1	8	6	6	3	1	6	8	3	6

$$\frac{\sum_i \chi_i \chi_{p_i} \cdot g_i}{g = 48} = 45 + 0 - 18 - 18 + 15 + 45 - 18 + 0 + 15 - 18 = 1$$

Therefore there is $1T_{2u}$ irreducible representation.

4. All the other species of O_h give zero irreducible representations.

5. *Summary:*

$$\Gamma^{cryst} = 4T_{1u} + T_{2u}$$

$$\Gamma_{vib}^{cryst} = \Gamma^{cryst} - \Gamma^{acoust} = 4T_{1u} + T_{2u} - T_{1u}$$

$$\Gamma_{vib}^{cryst} = 3T_{1u} + T_{2u}$$

This checks the result in the Appendix I (a).

It is now easy to compare the two methods to establish that the correlation method takes only minutes, whereas this procedure involves much more time.

APPENDIX II.

In this Appendix, we outline the factor group analysis for the compound Sr_2TiO_4 having the space group D_{4h}^{17} (I4/mmm) by the correlation method.

The crystallographic unit cell contains two molecular formula units (Z = 2) and, hence, the Bravais cell contains one formula unit of Sr_2TiO_4 since the space group is I4/mmm (D_{4h}^{17}) [LP=2]. It is important to realize that in a crystal the observed fundamentals arise from identical movements within every Bravais unit cell in the crystal. Thus, in the factor group analysis only one Bravais cell is to be considered. Since there are seven atoms in a cell, the total number of degrees of freedom is 21. There are two equivalent strontium atoms, one titanium atom and four oxygen atoms in the primitive cell. To consider the site symmetries of each set of atoms, it is enough to consider the layer marked by the bracket in Figure 93. From this, we can assign that strontium atoms lie on sites of C_{4v} symmetry, titanium on D_{4h} site and two oxygens (Ti-plane) on D_{2h} and the other two oxygens (Sr-plane) on sites of C_{4v} symmetry.

The symmetry species are now identified for each equivalent set of atom displacements in the site. Each set of equivalent atoms is treated separately and the vibrational modes of the crystal are obtained by summing up the individual sets.

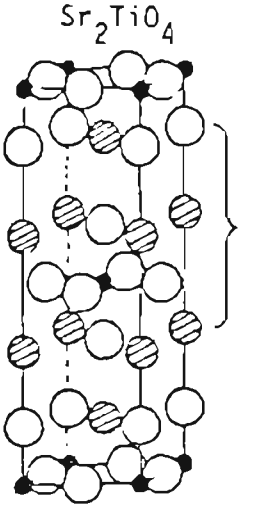

Figure 93. STRUCTURE OF Sr_2TiO_4.

Strontium atoms:

First, the vibrational displacements of the strontium atoms in the lattice can be described as simple motions parallel to the x, y, and z axis as we did for the Sr atom in $SrTiO_3$.

The translation T_z belongs to the species A_1 of the site group C_{4v}. Therefore, the atom displacements parallel to the z-axis will also belong to the A_1 species. Similarly, the displacements of strontium atoms along the x-axis will have the same character as T_x and will belong to species E. Now to begin the correlation procedure, Table XLVIII lists a portion of the C_{4v} site group and identifies the species of the transitions T_x, T_y, and T_z.

Table XLVIII.

SPECIES OF THE SITE GROUP C_{4v} AND THE TRANSLATIONS

C_{4v} site of strontium atom species	Translation Species	Sr atom Excursion
A_1	T_z	Motions parallel to z-axis
A_2		
B_1		-
B_2		
E	$T_{x,y}$	Motions parallel to x and y axis.

Utilizing the definition given in Appendix I(a), we list in Table XLIX the degrees of vibrational freedom for each species of the site group C_{4v} for the equivalent set of strontium atoms. Table L indicates the presence of the strontium lattice vibrations designated as degrees of freedom in species A_1 and E. The next step is to correlate the A_1 and E species of the site group C_{4v} to the D_{4h} factor group species.

Table XLIX.

STRONTIUM ATOMS ON SITE C_{4v}. THE DEGREES OF VIBRATIONAL FREEDOM FOR EACH SPECIES (n = 2)

C_{4v} species	Translation	t^γ	Degree of vibrational freedom $f^\gamma = n \cdot t^\gamma$
A_1	T_z	1	2
A_2		0	0
B_1		0	0
B_2		0	0
E	T_x, T_y	2	4

Table L.

THE CORRELATION FOR THE LATTICE VIBRATIONS OF THE STRONTIUM ATOMS IN Sr_2TiO_4 CRYSTAL BETWEEN THE SITE GROUP C_{4v} AND FACTOR GROUP D_{4h}

t^γ	f^γ	C_{4v} site species γ	correlation →	D_{4h} factor group species, ζ	c_ζ	a_ζ
1	2	A_1 (T_z)	→	A_{1g}	1	1
			→	A_{2u}	1	1
2	4	E (T_x,T_y)	→	E_g	2	1
			→	E_u	2	1

Since only the site species A_1 and E contain translations which are like the lattice vibrations in the crystal, the correlations relating these species to those in this factor group are of immediate interest. By integrating the site species which contain the translations into the factor group by use of the correlation tables it is easy to identify these lattice vibrations in the factor group species. Table L shows this correlation and identifies the species of the lattice vibration in the crystal.

The strontium atom's irreducible representation for the factor group is obtainable with the equation

$$\Gamma = \Sigma_{\zeta} a_{\zeta} \cdot \zeta$$

Therefore, the species of the factor group that contains lattice vibration involving the strontium atom can be written as the following irreducible representation Γ_{Sr}

$$\Gamma_{Sr} = 1 \cdot A_{1g} + 1 \cdot A_{2u} + 1 \cdot E_{g} + 1 \cdot E_{u}$$

Titanium atom

By following the same procedure we can obtain the irreducible representation Γ_{Ti} for the titanium atom. A summary of necessary information is given in Table LI.

Table LI.

TABULATIONS OF TERMS AND CORRELATIONS NECESSARY TO CALCULATE THE LATTICE VIBRATIONS OF THE TITANIUM ATOM IN Sr_2TiO_4. (n = 1)

t^{γ}	f^{γ}	D_{4h} site species	correlation →	D_{4h} factor group species, ζ	c_{ζ}	a_{ζ}
1	1	A_{2u} (T_z)	⟶	A_{2u}	1	1
2	2	E_u (T_x,T_y)	⟶	E_u	2	1

Therefore, $\Gamma_{Ti} = A_{2u} + E_u$

Oxygen atoms

We have one equivalent set of oxygen atoms on D_{2h} site and another equivalent set on C_{4v} site. Table LII (a,b) gives the necessary information to obtain the irreducible representation Γ_0 for the two different site symmetries.

Table LII (a).

TABULATION OF TERMS AND CORRELATIONS NECESSARY TO CALCULATE THE LATTICE VIBRATIONS OF THE OXYGEN ATOMS ON D_{2h} SITE IN Sr_2TiO_4

(n = 2)

t^γ	f^γ	D_{2h} site species	correlation →	D_{4h} factor group species, ζ	c_ζ	a_ζ
1	2	B_{1u} (T_z)	→	A_{2u}	1	1
			→	B_{2u}	1	1
1	2	B_{2u} (T_y)	→	E_u	2	2
1	2	B_{3u} (T_x)	→			

$$\Gamma_0\ [D_{2h}\ \text{site}] = A_{2u} + B_{2u} + 2\ E_u$$

Table LII (b).

TABULATION OF TERMS AND CORRELATIONS NECESSARY TO CALCULATE THE LATTICE VIBRATIONS OF THE OXYGEN ATOMS ON C_{4v} SITE IN Sr_2TiO_4

(n = 2)

t^γ	f^γ	C_{4v} site species	correlation →	D_{4h} factor group species, ζ	c_ζ	a_ζ
1	2	A_1 (T_z)	→	A_{1g}	1	1
			→	A_{2u}	1	1
2	4	E (T_x,T_y)	→	E_g	2	1
			→	E_u	2	1
		Γ_O [C_{4v} site] = $A_{1g} + A_{2u} + E_g + E_u$				

The total representation of the Sr_2TiO_4, $\Gamma^{Sr_2TiO_4}$ can be calculated by summing the irreducible representation for each type of atom in Sr_2TiO_4,

$$\text{i.e., } \Gamma^{Sr_2TiO_4} = \Gamma_{Sr} + \Gamma_{Ti} + \Gamma_O$$

$$= 4A_{2u} + 5E_u + 2A_{1g} + 2E_g + B_{2u}$$

This accounts for 21 degrees of freedom for Sr_2TiO_4. The acoustical vibrations are included in the irreducible representation, $\Gamma^{Sr_2TiO_4}$ given above. By subtracting the acoustical modes, one obtains the internal vibrational modes as shown on the next page.

$$\Gamma_{vib}^{Sr_2TiO_4} = \Gamma^{Sr_2TiO_4} - \Gamma^{acoustic}$$

The irreducible representation of the acoustical vibrations in the point group D_{4h} is readily obtained from the character table for the point group D_{4h}, and is shown as,

$$\Gamma^{acoustic} = A_{2u} + E_u$$

$$\text{and} \quad \therefore \quad \Gamma_{vib}^{Sr_2TiO_4} = 3A_{2u} + 4E_u + 2A_{1g} + 2E_g + B_{2u}$$

The four fundamental Raman active lattice vibrations allowed by selection rule are, two A_{1g} and two doubly degenerate E_g modes. Seven fundamental lattice vibrations are allowed in the infrared absorption spectrum. They are three A_{2u} and four doubly degenerate E_u modes. One vibration, B_{2u}, will be inactive in both infrared and Raman spectrum. Also, there are no coincidences, i.e., the same vibration mode which is active and observable by both Raman effect and in the infrared absorption spectrum.

BIOGRAPHICAL NOTE

U. Balachandran was born March 15, 1952, in Jalakantapuram, Tamil-nadu, India. He graduated from high school in 1969 in that city. He received his B.E. (Honours) degree in Metallurgy in 1975 from Madras University and his M.E. degree in 1977 from Indian Institute of Science, Bangalore, India. In September 1977, he enrolled at the Oregon Graduate Center for Study and Research at Beaverton, Oregon. He completed the requirements for his Ph.D. in Materials Science in December, 1980.